On the Viscoelastic Deformation of the Earth

Ophelia Crawford

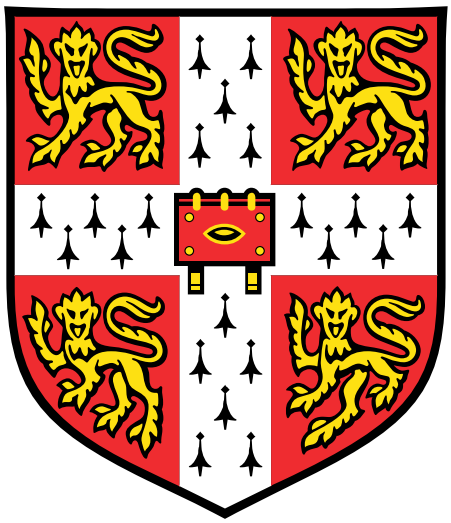

This dissertation is submitted for the degree of Doctor of Philosophy.

Girton College
University of Cambridge
August 2018

Declaration

This dissertation is the result of my own work and includes nothing which is the outcome of work done in collaboration except as specified in the text. It is not substantially the same as any that I have submitted, or, is being concurrently submitted for a degree or diploma or other qualification at the University of Cambridge or any other university or similar institution. I further state that no substantial part of my dissertation has already been submitted, or, is being concurrently submitted for any such degree, diploma or other qualification at the University of Cambridge or any other university or similar institution. It does not exceed the prescribed page limit.

Ophelia Crawford
August 2018

Summary

Post-seismic deformation and glacial isostatic adjustment are two processes by which the Earth deforms viscoelastically. In both cases, the details of the deformation depend on the rheological structure of the Earth as well as the forcing, which is the earthquake and further movement on the fault in the case of post-seismic deformation, and the change in load on the surface of the Earth due to the redistribution of water and ice mass in the case of glacial isostatic adjustment. It is therefore possible to learn about the Earth's rheological structure and the processes' respective forcings from measurements of the deformation.

In order to use measurements in this way, it is first necessary to have a method of forward modelling the processes, that is, calculating the deformation due to a given forcing and in an earth model with a given structure. Given this, a way of calculating derivatives of measurements of the deformation with respect to the parameters of interest is then desirable. In this dissertation, the adjoint method is used. This, for the first time, enables efficient calculation of continuous derivatives, which have many potential applications. Firstly, they can be used within a gradient-based optimisation method to find a model which minimises some data misfit function. The derivatives can also be used to quantify the uncertainty in such a model and hence to provide understanding of which parts of the model are well constrained. Finally, they enable construction of measurements which provide sensitivity to a particular part of the model space.

In this dissertation, new methods for forward modelling both post-seismic deformation and glacial isostatic adjustment are presented. The adjoint method is also applied to both problems. Numerical examples are presented in spherically symmetric earth models and, in the case of glacial isostatic adjustment, models with laterally varying rheological structure. Such examples are used to illustrate the potential applications of the developments made within this dissertation.

Publications

Arising from this dissertation:

Crawford, O., Al-Attar, D., Tromp, J., & Mitrovica, J. X. (2017). Forward and inverse modelling of post-seismic deformation. *Geophys. J. Int.*, **208**(2), 845–876. doi:10.1093/gji/ggw414.

Crawford, O., Al-Attar, D., Tromp, J., Mitrovica, J. X., Austermann, J., & Lau, H. C. P. (2018). Quantifying the sensitivity of post-glacial sea level change to laterally varying viscosity. *Geophys. J. Int.*, **214**(2), 1324–1363. doi:10.1093/gji/ggy184.

Arising through other work:

Al-Attar, D. & Crawford, O. (2016). Particle relabelling transformations in elastodynamics. *Geophys. J. Int.*, **205**(1), 575–593. doi:10.1093/gji/ggw032.

Lau, H. C. P., Mitrovica, J. X., Austermann, J., Crawford, O., Al-Attar, D., & Latychev, K. (2016). Inferences of mantle viscosity based on ice age data sets: Radial structure. *J. Geophys. Res.*, **121**(10), 6991–7012. doi:10.1002/2016JB013043.

Al-Attar, D., Crawford, O., Valentine, A. P., & Trampert, J. (2018). Hamilton's principle and normal mode coupling in an aspherical planet. *Geophys. J. Int.*, **214**(1), 485–507. doi:10.1093/gji/ggy141.

Lau, H. C. P., Austermann, J., Mitrovica, J. X., Crawford, O., Al-Attar, D., & Latychev, K. (2018). Inferences of mantle viscosity based on ice age data sets: the bias in radial viscosity profiles due to neglect of laterally heterogeneous viscosity structure. *J. Geophys. Res.*, **123**(9), 7237–7252. doi:10.1029/2018JB015740.

Acknowledgements

First and foremost, my sincerest thanks to my supervisor, David Al-Attar, for his assistance, patience and encouragement during my PhD. He has been very generous with his time and has never been anything but extremely supportive. Conversations with him have contributed significantly to my geophysics, mathematics and American television education. I could not have asked for a better supervisor.

I gratefully acknowledge funding from NERC, the Girdler studentship and a CASE award with the British Antarctic Survey which facilitated my PhD. Through the CASE award, I have benefitted from conversations with Richard Hindmarsh and Robert Arthern.

Bullard has been a wonderful place to have spent the last four years, and I am very grateful to everyone who has been a part of it. Thanks to all of my office mates – Karen Lythgoe, Jenny Jenkins, Prin Eksinchol, Frank Syvret, Matthew Maitra and Zhi Li. In particular, thanks to Jenny for being my front office companion for more than three years, and for sharing my interest in BBC News, cats and biscuits. A mention must also go to "Bullard cat", our honorary office member, whose company and muddy paw prints were greatly appreciated. It has been lovely to have had an expanded group for the last year of my PhD – I am grateful to Frank, Matthew and Li for making me no longer an only PhD child.

I have been fortunate to have had some excellent collaborators. Jerry Mitrovica has been very supportive and extremely welcoming when I have visited him, including generously allowing me to stay with him. I have benefitted greatly from conversations with him and the rest of his group. Jacky Austermann and Harriet Lau in particular have been wonderful colleagues and friends. It has also been a great privilege to have worked with Jeroen Tromp, and I am very grateful for his contributions to and comments on my work.

Thanks to Camilla Penney for being a part of what makes Cambridge home and for many shared meals, cakes and crosswords. I am also very grateful to Dave Lyness for accommodating me for the last few months of my PhD and beyond, and for many interesting conversations.

Finally, thanks to my family for their unwavering support and interest in my work, particularly my Mum, my brother, Arthur, and our cats, Zeus and Ziva.

Contents

Chapter 1

Introduction

1.1 Summary

This dissertation includes the study of two processes – post-seismic deformation and post-glacial deformation. Both relate to the viscoelastic response of the Earth, and there are a number of similarities between them, particularly the motivation for their study. However, there are also significant differences in, for example, how the processes are modelled.

In this introduction, we mostly focus on aspects that the processes have in common. An important reason for considering both processes is in order to learn about the rheology of the Earth; we give an overview of what is known about the rheology and why improving out knowledge of it is important in section 1.2. Another commonality is the approach that we take to the inverse problem in both cases, and we discuss this, and other approaches, in detail. In section 1.3, we also outline several methods that are used throughout this work. More specific introductions are given in the relevant chapters.

1.2 Overview

1.2.1 The rheology and deformation of the Earth

The nature of the time-dependent response of the Earth to geological forces acting on it depends on the time scale of the force involved. On short time scales, of order seconds to hours, such as those over which seismic wave propagation occurs, the Earth largely behaves elastically. In contrast, over millions of years, the Earth behaves like a viscous fluid, as for mantle convection. For processes which occur on intermediate time scales, from years to thousands of years, both elastic and viscous effects are significant and the Earth is said to behave viscoelastically. Two such processes are post-seismic and post-glacial deformation, and this work is concerned with the study of these processes.

Post-seismic deformation is the time-dependent movement of the solid Earth following an earthquake. The exact nature of the deformation depends on the earthquake forcing, any afterslip that occurs and the rheological structure of the Earth. Post-glacial deformation, or glacial isostatic adjustment (GIA), is the equivalent response of the Earth to the loss and growth of ice sheets on its surface. It depends on the location and timing of the ice sheet change as well as the rheological structure of the Earth. Therefore, measurements of the deformations can be used to learn about their respective forcings as well as the rheology of the Earth.

The rheology of the Earth is not fully understood. The time-scale dependent nature of the Earth's

response is indicative of it having a frequency-dependent rheology. It is clear that, as all these processes occur on the same Earth, there must be a consistent way of describing the behaviour across time scales; however, it is not yet obvious how this should be done. Even on short time scales, viscoelasticity is apparent through seismic attenuation. The rheology in the frequency range of seismology is thought to be that of an absorption band solid (Anderson *et al.*, 1977), which has longterm strength and for which the deformation has a continuous range of time scales of response. In convection studies, the mantle is considered to be a fluid, with no elastic component. Its behaviour can be described by a viscosity. In typical studies of post-seismic and post-glacial deformation, the rheology is considered to be a Maxwell solid, which has an initial elastic response but does not support long-term stresses. It can be described by one time scale. This time scale can be associated with a viscosity; however, it is not clear whether this viscosity is the "same" as is observed in the mantle convection case, nor how seismic attenuation can be related to viscosity. It would therefore be desirable to further our understanding of the rheological structure of the Earth across time scales.

Even within a small range of time scales, the Earth's rheology is not well known. Whilst the nature of the rheologies considered for post-seismic and post-glacial deformation are similar, the details can be very different – post-seismic deformation typically requires a much thinner elastic lid and lower viscosities below it than post-glacial deformation. Therefore, there remain questions about how these rheologies can be reconciled. Within either of these two fields, the range of proposed rheologies is quite broad-ranging in depth variation, lateral variation, the existence of transient rheologies and the existence of non-linear rheologies. There is therefore further work to be done in understanding the Earth's rheology even within the smaller range of time scales on which post-seismic and post-glacial deformation occur.

1.2.2 Motivation and relevance

As mentioned above, the details of post-seismic and post-glacial deformation depend on the rheological structure of the Earth and the forcing. Improving our knowledge of these aspects of the Earth has implications for other important processes, and some of these are discussed below. It is also important to recall that developing understanding of one of the aspects will enhance our ability to constrain the other.

Firstly, the viscosity structure affects the dynamics of the Earth's interior and in particular, the pattern of mantle convection (e.g., Bunge *et al.*, 1996; Cserepesa *et al.*, 2000; Nakagawa & Tackley, 2011). There are also a number of more specific effects on, for example, the form of upwelling and downwellings (Zhong *et al.*, 2000), plate tectonics (Tackley, 2000; Stadler *et al.*, 2010), the cause of slab stagnation and plume deflection in the mid-mantle (Rudolph *et al.*, 2015) and the thermal evolution of the mantle (van den Berg *et al.*, 2005) and core (Nakagawa & Tackley, 2004). Whilst, as mentioned above, we would not necessarily expect the viscosities obtained from viscoelastic studies to be the same as those which matter in mantle convection, improved understanding of the Earth's rheology more generally could inform mantle convection processes. Furthermore, it has been suggested that both post-glacial and convection data can be reconciled by the same viscosity structure (Forte & Mitrovica, 1996).

It is clear that understanding how the Earth's ice sheets varied with time in the past will provide insight into the Earth's climate. An event of particular interest is Meltwater Pulse 1A (MWP-1A). Between approximately 15000 and 14000 years ago, 20 m of sea level rise occured in less than 500 years.

The precise timing of the event is unknown, with estimates of the onset ranging from approximately 14200 (Bard *et al.*, 1990) to 14600 (Deschamps *et al.*, 2012) years ago. The source of the meltwater (in particular, the relative contributions of Antarctica and the northern hemisphere ice sheets) is also of considerable debate. Different studies argue the data can be explained by entirely or predominantly northern hemisphere sources (Peltier, 2005; Gregoire *et al.*, 2012; Gomez *et al.*, 2015), similar volumes of northern hemisphere and Antarctic melt (Rohling *et al.*, 2004) or significant or total Antarctic sources (Clark *et al.*, 2002; Weaver *et al.*, 2003; Carlson, 2009). Others argue the data considered does not constrain the Antarctic component either way (Bassett *et al.*, 2007; Liu *et al.*, 2016). At around the same time as MWP-1A, Bølling-Allerød warming occurred. This was a rise in temperature of at least 5 K in northern hemisphere air temperature in just a few decades. However, the uncertainty in the timing and source of MWP-1A means its relationship with Bølling-Allerød warming is unclear. For example, Weaver *et al.* (2003) argue MWP-1A caused the warming while Carlson *et al.* (2012) argue the converse. Improving our knowledge of MWP-1A would further our understanding of the interaction between the ice sheets, oceans and atmosphere on Earth.

Uncertainties in the past ice history also affect our knowledge of the present day climate. Estimates of present day mass-loss from ice sheets are typically calculated from satellite gravity measurements; however, such measurements also depend on the Earth's continued isostatic adjustment due to ice mass loss over the last glacial cycle. As a consequence, estimates of present day ice mass loss can vary considerably and have significant uncertainties, often of the same order as the estimate itself (e.g., Chen *et al.*, 2009; Velicogna, 2009; Zwally & Giovinetto, 2011; King *et al.*, 2012; Ivins *et al.*, 2013; Van der Wal *et al.*, 2015). Therefore, in order to estimate accurately the ice melt that is currently occurring, and so further our knowledge about the Earth's response to present climate, it is necessary to improve our knowledge of the Earth's ice history and viscosity structure.

Finally, constraining aspects of earthquake afterslip, such as the temporal and spatial evolution and the moment release, provides insight into some aspects of the earthquake cycle such as fault frictional behaviour (Miyazaki *et al.*, 2004; Barbot *et al.*, 2009).

1.2.3 Approaching the post-seismic and post-glacial inverse problems

An inverse problem involves using some measurements of a process to learn about the model parameters that govern it. In the case of post-seismic and post-glacial deformation, the parameters are typically the rheological structure of the Earth and the processes' respective forcings. The typical inverse problem is to seek model parameters which fit some given data, and there are several ways to approach this problem.

One way to tackle an inverse problem is to run a suite of forward models with different model parameters and assess how well each fits the data. This works particularly well if the main aim is to find a model which fits the data, and it has the advantage that the entire misfit surface is mapped for the parameters chosen. However, as discretisation of the model space is required, which may not capture the full range of true models, it is likely that any uncertainties will be underestimated. A further drawback is that the number of forward calculations required scales exponentially with the number of model parameters and so this method can quickly become unfeasible. As a result, studies which use such grid-search methods to investigate the Earth's viscosity structure typically split it into a handful of homogeneous layers – e.g., Lambeck *et al.* (2014) and Nakada *et al.* (2015) in the post-glacial case and Diao *et al.* (2014) and Nishimura & Thatcher (2003) in the post-seismic case, with the

latter considering a viscoelastic half space rather than a defined layer. The effects of lateral viscosity variations are also sometimes considered, though often only on a regional scale (e.g., Milne *et al.*, 2018), and typically with large homogeneous areas. Such discretisation naturally raises questions of how such a best-fitting structure relates to the true continuously heterogeneous Earth.

There are a few possible ways to reduce the number of forward calculations required. One would be to use a sampling algorithm such as Markov Chain Monte Carlo, which reduces the number of calculations required to build up an accurate picture of the misfit surface. However, the number required is still usually prohibitively high for many applications. In some studies of post-seismic deformation, the number of calculations has been limited by only varying a few parameters simultaneously (Freed *et al.*, 2017) or by considering misfits in only a small region to find the best-fitting viscosity in that area (Li *et al.*, 2017b). While such alterations can be sufficient to make the problem tractable in some cases, the number of parameters that can be considered is still limited. Li *et al.* (2018), when studying GIA, invert for a simple scaling between s-wave speed and viscosity structure, which limits the number of parameters they consider to two whilst retaining a continuous viscosity structure; however, this assumes firstly that the seismic velocity structure is correct and secondly that there exists a direct relationship between the two properties. In the context of ice sheet history, Tarasov & Peltier (2004) used a limited number of parameters to describe the Laurentide ice sheet. They applied an ice sheet evolution model to ensure the physicality of their results, but it could be argued that the number of parameters was not sufficient to capture all the details. To summarise, whilst grid-search methods offer a number of directions for investigating the post-seismic and post-glacial inverse problems, we would like to consider other methods so that we can explore models with higher, or even infinite, dimensions and develop more understanding of the uncertainties involved.

An alternative is to use gradient-based optimisation to update the model iteratively and approach a minimum of the misfit surface. In order to do this, we require a method of calculating the derivative of the misfit with respect to the model parameters. One way is to use finite-differencing methods, whereby derivatives are constructed by perturbing each of the model parameters in turn and calculating the change in misfit. This method has commonly been used in GIA studies, particularly in inversions for the radial viscosity structure (e.g., Peltier, 2004; Lau *et al.*, 2016). The number of forward calculations required to construct the derivative increases only linearly with the number of model parameters; however, this still makes calculations with large numbers of model parameters, particularly in three-dimensional earth models, difficult.

The adjoint method (discussed further in section 1.3.3) provides an alternative way of calculating the derivatives, and requires just one solution of the forward problem and one of the so-called adjoint problem in order to construct the entire derivative. Typically, the adjoint problem is very similar to the forward problem and so the adjoint method provides significant advantages over the methods discussed above. The adjoint method originated in control theory (Lions, 1970) and since then has had applications in many fields. Tarantola (1984) first used the method in solid Earth geophysics, applying it to acoustic wave propagation, and other seismological applications were presented over the following two decades (e.g., Mora, 1987; Crase *et al.*, 1990; Pratt, 1999). There was also limited use in other areas, such as mantle convection (Bunge *et al.*, 2003). The method rose to prominence in solid Earth geophysics through Tromp *et al.* (2005), by which time computational advances had made the use of the adjoint method in the full seismological elastic problem possible. Since then, it has been used extensively in global seismology (e.g. Fichtner *et al.*, 2009; Tape *et al.*, 2009; Zhu *et al.*, 2012;

Chen *et al.*, 2013) as well as other fields, such as geomagnetism (Li *et al.*, 2011) and mantle convection (Li *et al.*, 2017a).

Having a method to calculate derivatives also allows derivatives of other measurements, not just a data misfit function, to be considered. For example, the derivative of a particular piece of data provides insight into the sensitivity of the measurement to different parts of the model, and can help with resolution quantification. These have also been calculated in the context of GIA using finite differencing for one-dimensional (e.g., Lau *et al.*, 2016) and three-dimensional (e.g., Paulson *et al.*, 2005) viscosity structures, as well as for ice sheet history (Mitrovica *et al.*, 2018). Again, this method requires discretisation of the model space with a limited number of model parameters, particularly in the case of a three-dimensional viscosity structure, but the adjoint method provides a significantly more efficient alternative.

1.2.4 Further constraints on post-seismic and post-glacial parameters

As well as using GIA data to constrain ice sheet histories, it is also possible to use geological data on ice extent and thicknesses. Such data is often combined with ice sheet modelling in order to build a physically sensible model (e.g., Clark *et al.*, 1996; Whitehouse *et al.*, 2012).

As mentioned above, mantle convection is affected by the viscosity structure. Therefore, the viscosity structure of the Earth can be investigated using measurements of mantle convection such as surface plate velocities, the geoid and dynamic topography (e.g., Hager, 1984; Forte & Peltier, 1987; King & Masters, 1992; Corrieu *et al.*, 1994; Panasyuk & Hager, 2000; Čadek & Fleitout, 2003; Rolf *et al.*, in press). To what extent we expect a viscosity obtained in this manner to match those obtained from post-seismic or post-glacial deformation remains unclear, due to the different time-scales of the processes; however, it has been argued that mantle convection and post-glacial observations can be matched simulataneously without needing to invoke transient or non-linear rheologies (Forte & Mitrovica, 1996).

1.3 Methods

1.3.1 The spectral element method

Throughout this work, we expand the fields as a function of depth using a radial mesh and expand laterally using spherical harmonics (see section 1.3.2). For the radial mesh, we use the spectral element method (e.g., Patera, 1984; Komatitsch & Tromp, 1999).

Using this method, the radius, r, is split into n_s elements, Ω_b, for $1 \leq b \leq n_s$. Each of these contains a number of control nodes, n_c, which are the locations at which the parameters and fields are stored. The upper boundary of one element coincides with the lower boundary of the next. There exists a unique mapping to each radial element from a reference element, which is defined in terms of the coordinate ξ with $-1 \leq \xi \leq 1$. The radial elements are defined in terms of the n_c control nodes located at $r_a = r(\xi_a)$ for $1 \leq a \leq n_c$ and n_c shape functions, $N_a(\xi)$ for $1 \leq a \leq n_c$. The relationship between a point r in a radial element and a point ξ in the reference element can be written

$$r(\xi) = \sum_{a=1}^{n_c} N_a(\xi) r_a. \tag{1.1}$$

The shape functions are Lagrange polynomials of degree $n_l = n_c - 1$ which we write as $\ell_\alpha^{n_l}$. They satisfy

$$\ell_\alpha^{n_l}(\xi_\beta) = \delta_{\alpha\beta}, \tag{1.2}$$

where δ is the Kronecker delta.

We will now expand some of the required fields using this formulation. First, the control nodes ξ_α for $0 \leq \alpha \leq n_l$ are chosen to be the $n_l + 1$ Gauss-Lobatto-Legendre points, which are the roots of

$$(1 - \xi^2)P'_{n_l}(\xi) = 0, \tag{1.3}$$

where P'_{n_l} is the derivative of the Legendre polynomial of degree n_l. A scalar field can be expressed in terms of the Lagrange polynomials of degree $n_l + 1$ as

$$f(r(\xi), t) \approx \sum_{\alpha=0}^{n_l} f^\alpha(t)\ell_\alpha(\xi), \tag{1.4}$$

where $f^\alpha(t) = f(r(\xi_\alpha), t)$. The derivative of such a field with respect to r can be seen to be

$$\frac{\partial f}{\partial r}(r(\xi), t) \approx \sum_{\alpha=0}^{n_l} f^\alpha(t)\frac{\partial l_\alpha}{\partial \xi}(\xi)\frac{\partial \xi}{\partial r}(\xi), \tag{1.5}$$

where $\frac{\partial r}{\partial \xi}$ is the Jacobian for the particular radial element. It can also be shown that the integral with respect to r over a particular element Ω_b is given by

$$\int_{\Omega_b} f(r, t)\mathrm{d}\, r = \int_{-1}^{1} f(r(\xi), t)\frac{\partial r}{\partial \xi}\mathrm{d}\, \xi \tag{1.6}$$

$$\approx \sum_{\alpha=0}^{n_l} w_\alpha f^\alpha(t)\frac{\partial r}{\partial \xi}(\xi_\alpha), \tag{1.7}$$

where w_α is the weight associated with the ξ_α Gauss-Lobatto-Legendre point.

We take $n_c = 5$ and choose N_s by considering the wavelength of the expected deformation and by ensuring all internal discontinuities lie on an element boundary.

1.3.2 Generalised spherical harmonics

At a particular depth, we expand the fields in terms of generalised spherical harmonics (Phinney & Burridge, 1973). Using this approach, a scalar field, ϕ can simply be written

$$\phi = \sum_{l,m} \phi_{lm} Y_{lm}^0, \tag{1.8}$$

where Y_{lm}^N are the generalised spherical harmonics defined in appendix C of Dahlen & Tromp (1998) and here, and in what follows, the summation is over integer values for $0 \leq l \leq \infty$ and $-l \leq m \leq l$. In

considering higher order fields, we first recall the canonical basis vectors (Phinney & Burridge, 1973),

$$\hat{\mathbf{e}}_- = \frac{1}{\sqrt{2}}(\hat{\boldsymbol{\theta}} - i\hat{\boldsymbol{\phi}}), \tag{1.9}$$

$$\hat{\mathbf{e}}_0 = \hat{\mathbf{r}} \tag{1.10}$$

$$\hat{\mathbf{e}}_+ = -\frac{1}{\sqrt{2}}(\hat{\boldsymbol{\theta}} + i\hat{\boldsymbol{\phi}}), \tag{1.11}$$

defined relative to the basis vectors in spherical polar coordinates. The so-called contravariant components of a vector, $\mathbf{u}$, in this basis are

$$u^- = \frac{1}{\sqrt{2}}(u_\theta + iu_\phi), \tag{1.12}$$

$$u^0 = u_r, \tag{1.13}$$

$$u^+ = -\frac{1}{\sqrt{2}}(u_\theta - iu_\phi). \tag{1.14}$$

In order to expand these components using generalised spherical harmonics, we write

$$u^\alpha_{lm} = \sum_{l,m} u^\alpha_{lm} Y^\alpha_{lm}. \tag{1.15}$$

We can also write a second-order tensor field, $\mathbf{T}$, as

$$\mathbf{T} = \sum_{l,m} T^{\alpha\beta}_{lm} Y^{\alpha+\beta}_{lm} \hat{\mathbf{e}}_\alpha \otimes \hat{\mathbf{e}}_\beta, \tag{1.16}$$

where $\otimes$ is the tensor product.

We include further expansions in the main chapters of this work as required.

1.3.3 The adjoint method

When considering the inverse problem, a simple approach is to calculate derivatives using a finite differencing method (e.g., Mitrovica & Peltier, 1991; Paulson *et al.*, 2005). For an n-dimensional parameter space, construction of the derivative using such a method requires $n + 1$ solutions of the forward problem. For laterally varying earth models, which require a large number of model parameters and time-consuming forward calculations, it clearly becomes prohibitively computationally expensive to calculate kernels in this way. In contrast, the adjoint method allows the exact derivative to be constructed using just one solution of the forward problem and one of the corresponding adjoint problem, even for an infinite-dimensional model space. Here, we will briefly present the theory of the adjoint method and illustrate it schematically.

We consider an observable, J, of which we wish to calculate the derivative with respect to a model parameter. This will typically be a function of the forward variables, $\mathbf{u}$ (displacement), ϕ (gravity perturbation) and, in the post-glacial case, SL (sea level), but may also involve an explicit dependence on model parameters (for example, through a regularisation term). We call J the objective functional, and, schematically, can write $J(u, p)$ where u represents the forward variables and p the model parameters. As the forward variables depend on the model parameters through the equations

of motion, we can define the reduced objective functional through

$$\hat{J}(p) = J(\hat{u}(p), p), \tag{1.17}$$

where $\hat{u}(p)$ is the value of u obtained for a given p. It is the derivative of this reduced objective functional with respect to p that we wish to calculate. We will write this derivative as $D\hat{J}$, and it is defined such that

$$\hat{J}(p + \delta p) = \hat{J}(p) + \langle D\hat{J}(p), \delta p \rangle + O(\delta p^2), \tag{1.18}$$

where $\langle \cdot, \cdot \rangle$ is an appropriate inner product. From this definition, $\delta\hat{J}(p)$, the linearised change $\hat{J}(p)$ due to a perturbation of p, is given by

$$\delta\hat{J}(p) = \langle D\hat{J}(p), \delta p \rangle. \tag{1.19}$$

However, this derivative is difficult to calculate directly. Instead, we calculate the derivative of the objective functional $J(u, p)$ subject to the constraint that the forward variables are solutions of the equations of motion. For the class of problems we wish to consider, these constraints can be written schematically as $a(u, p) = 0$ for all p. Therefore, in order to calculate $D\hat{J}(p)$, we introduce a Lagrangian functional

$$L(u, u^\dagger, p) = J(u, p) + \langle a(u, p), u^\dagger \rangle, \tag{1.20}$$

where $u^\dagger$ is a Lagrange multiplier used to enforce the constraint $a(u, p) = 0$. It can be shown (e.g., Tröltzsch, 2005, and outlined below) that

$$D\hat{J}(p) = D_p L(u, u^\dagger, p), \tag{1.21}$$

provided

$$D_u L = 0, \tag{1.22}$$

$$D_{u^\dagger} L = 0, \tag{1.23}$$

where $D_p L$ is the partial derivative of L with respect to p, and similarly for $D_u L$ and $D_{u^\dagger} L$.

This can be proved as follows. Expanding equation (1.20) in terms of u (and retaining only first order terms after the first line), we find

$$\begin{aligned}
L(u + \delta u, u^\dagger, p) &= J(u + \delta u, p) + \langle a(u + \delta u, p), u^\dagger \rangle && (1.24)\\
&\approx J(u, p) + \langle D_u J(u, p), \delta u \rangle + \langle a(u, p) + D_u a\, \delta u, u^\dagger \rangle && (1.25)\\
&= L(u, u^\dagger, p) + \langle D_u J(u, p), \delta u \rangle + \langle D_u a\, \delta u, u^\dagger \rangle && (1.26)\\
&= L(u, u^\dagger, p) + \langle D_u J(u, p) + (D_u a)^*\, u^\dagger, \delta u \rangle && (1.27)\\
&\equiv L(u, u^\dagger, p) + \langle D_u L(u, p), \delta u \rangle, && (1.28)
\end{aligned}$$

where * indicates the adjoint of an operator. We can therefore see that

$$D_u L = D_u J + (D_u a)^*\, u^\dagger, \tag{1.29}$$

and so, provided equation (1.22) holds and assuming $D_u a$ is invertible, we find

$$u^\dagger = -(D_u a)^{-*} D_u J, \tag{1.30}$$

where $^{-*}$ indicates the inverse of the adjoint. We can similarly expand equation (1.20) in terms of p to give

$$\begin{aligned} L(u, u^\dagger, p + \delta p) &= J(u, p + \delta p) + \langle a(u, p + \delta p), u^\dagger \rangle && (1.31)\\ &\approx J(u, p) + \langle D_p J, \delta p \rangle + \langle a(u, p) + D_p a\, \delta p, u^\dagger \rangle && (1.32)\\ &= L(u, u^\dagger, p) + \langle D_p J, \delta p \rangle + \langle D_p a\, \delta p, u^\dagger \rangle && (1.33)\\ &= L(u, u^\dagger, p) + \langle D_p J + (D_p a)^*\, u^\dagger, \delta p \rangle && (1.34)\\ &\equiv L(u, u^\dagger, p) + \langle D_p L, \delta p \rangle, && (1.35) \end{aligned}$$

and so

$$D_p L = D_p J + (D_p a)^*\, u^\dagger. \tag{1.36}$$

Using equation (1.30), we therefore see that

$$D_p L = D_p J - (D_p a)^*\, (D_u a)^{-*}\, D_u J. \tag{1.37}$$

We need to show that this result is equal to $D\hat{J}$. Using the chain rule, it is clear that

$$\begin{aligned} \hat{J}(p + \delta p) &= J(\hat{u}(p + \delta p), p + \delta p) && (1.38)\\ &\approx \hat{J}(p) + \langle D\hat{J}(p), \delta p \rangle && (1.39)\\ &= \hat{J}(p) + \langle D_u J, D_p \hat{u}\, \delta p \rangle + \langle D_p J, \delta p \rangle && (1.40)\\ &= \hat{J}(p) + \langle (D_p u)^* D_u J + D_p J, \delta p \rangle, && (1.41) \end{aligned}$$

and so

$$D\hat{J} = (D_p u)^* D_u J + D_p J. \tag{1.42}$$

Provided equation (1.23) holds, we have $a(u, p) = 0$ for all p. Expanding this with respect to p, we find

$$\begin{aligned} a(\hat{u}(p + \delta p), p + \delta p) &\approx a(\hat{u}(p) + D_p \hat{u}(p)\, \delta p, p + \delta p) && (1.43)\\ &\approx a(u, p) + D_u a(u, p)\, D_p \hat{u}(p)\, \delta p + D_p a(u, p)\, \delta p && (1.44)\\ &= [D_u a(u, p) D_p \hat{u}(p) + D_p a(u, p)]\, \delta p && (1.45)\\ &= 0. && (1.46) \end{aligned}$$

Therefore

$$D_u a\, D_p \hat{u} + D_p a = 0, \tag{1.47}$$

and upon rearranging, we find

$$D_p \hat{u}(p) = -(D_u a)^{-1} D_p a. \tag{1.48}$$

Substituting this into equation (1.42) gives

$$D\hat{J} = D_p J - (D_p a)^* (D_u a)^{-*} D_u J \tag{1.49}$$

and so, as stated above, equation (1.21) is true provided equations (1.22) and (1.23) hold.

Evaluation of equation (1.23) will simply return the forward equations and equation (1.22) gives the corresponding adjoint equations. Therefore, in order to calculate $D\hat{J}(p)$, we see that we must

1. for the given observable, write down $J(u, p)$;
2. construct the Lagrangian using equation (1.20);
3. solve the forward equations which are given by equation (1.23);
4. solve the adjoint equations which are given by equation (1.22);
5. calculate $D\hat{J}(p)$ using equation (1.21). $D_p L(u, u^\dagger, p)$ will in general be some function of the solutions of the forward and adjoint equations.

The choice of J only changes the force terms in the adjoint equations, and so we do not have to rederive the entire set of equations for each type of measurement.

1.3.4 The conjugate gradient method

In this dissertation, we perform several inversions to find the model parameters that best fit some given data. In order to do this, we take an iterative approach. We calculate the derivate of the misfit function with respect to the model parameters and use the non-linear conjugate gradient method to update the model parameters. This is repeated until the model no longer changes significantly or a sufficiently low value of the misfit is reached. We follow Tape *et al.* (2007) for the algorithmic details of the conjugate gradient method. Using our notation, the steps are:

1. For some initial model, p_0 calculate the initial misfit, $\hat{J}_0 = \hat{J}(p_0)$ and the initial kernel (derivative), $K_0 = K_p(p_0)$;
2. Set the initial descent direction, $p_0 = -K_0$;
3. Set $k = 0$ and, while the termination criteria has not been reached:
   (a) Calculate α_k, the step length (see below);
   (b) Calculate the new model, $p_{k+1} = p_k + \alpha_k\, p_k$;
   (c) Calculate the new misfit, $\hat{J}_{k+1} = \hat{J}(p_{k+1})$, and kernel, $K_{k+1} = K_p(p_{k+1})$;
   (d) Calculate
   $$\beta_{k+1} = \frac{\langle K_{k+1}, K_{k+1} - K_k \rangle}{\langle K_k, K_k \rangle}, \tag{1.50}$$
   where $\langle \cdot, \cdot \rangle$ is some suitably defined inner product;
   (e) Update the descent direction, $p_{k+1} = -K_{k+1} + \beta_{k+1}\, p_k$;
   (f) Set $k = k + 1$;

At each iteration, α_k can be calculated by performing a line search in the p_k direction to find the value which minimises the misfit in this direction. In practice, we find the minimum approximately by assuming the misfit is quadratic with respect to α_k. Again, we follow Tape *et al.* (2007).

Let us write

$$\tilde{\hat{J}}_k(\alpha) = \hat{J}(p_k + \alpha\, p_k), \tag{1.51}$$

$$\tilde{g}_k(\alpha) = \langle K_p(p_k + \alpha\, p_k), p_k \rangle. \tag{1.52}$$

We therefore wish to find α_k such that $\tilde{g}_k(\alpha_k) \approx 0$. We have $\tilde{\hat{J}}_k(0)$ and $\tilde{g}_k(0)$, but require the value of the function (or its derivative) at one other location in order to be able to perform a quadratic interpolation. We therefore calculate $\tilde{\hat{J}}_k(\alpha_k^t)$ where $\alpha_k^t = -\frac{2\tilde{\hat{J}}_k(0)}{\tilde{g}_k(0)}$. As we are assuming that the misfit is quadratic with respect to α_k, we can write

$$\tilde{\hat{J}}_k(\alpha) = A\alpha^2 + B\alpha + C, \tag{1.53}$$

and so

$$\tilde{\hat{J}}_k(0) = C, \tag{1.54}$$

$$\tilde{g}_k(0) = B, \tag{1.55}$$

$$\tilde{\hat{J}}_k(\alpha_k^t) = A(\alpha_k^t)^2 + B\alpha_k^t + C, \tag{1.56}$$

and α_k satisfies

$$2A\alpha_k + B = 0. \tag{1.57}$$

From equations (1.54) – (1.56), we find

$$C = \tilde{\hat{J}}_k(0), \tag{1.58}$$

$$B = \tilde{g}_k(0), \tag{1.59}$$

$$A = \frac{\tilde{\hat{J}}_k(\alpha_k^t) - \tilde{\hat{J}}_k(0) - \tilde{g}_k(0)\alpha_k^t}{(\alpha_k^t)^2}, \tag{1.60}$$

and so

$$\alpha_k = -\frac{B}{2A} = \frac{\tilde{g}_k(0)(\alpha_k^t)^2}{\tilde{\hat{J}}_k(0) - \tilde{\hat{J}}_k(\alpha_k^t) + \tilde{g}_k(0)\alpha_k^t}. \tag{1.61}$$

1.4 The dissertation

In chapter 2, we present a new method of modelling post-seismic deformation in spherical, continuously heterogeneous, self-gravitating and compressible earth models, which can have a variety of linear rheologies. The method can be extended to non-linear rheologies as discussed in Crawford *et al.* (2017). We show benchmarking exercises to confirm the validity of the method and its numerical implementation. Examples of numerical calculations carried out in spherically symmetric earth models are presented.

In chapter 3, we apply the adjoint method to the post-seismic inverse problem. We derive the form of the sensitivity kernels for afterslip and both radial and laterally varying rheological parameters.

Again, numerical examples are presented in spherically symmetric background models. These examples include viscosity kernels for measurements of displacement as well as example viscosity inversions using synthetic data. We consider the effect of data errors on the inversion results as well as presenting a method of resolution analysis to quantify how well any obtained model is constrained.

In chapter 4, we turn our attention to the post-glacial problem. A new method for forward modelling gravitationally self-consistent post-glacial sea level change in fully heterogeneous earth models with a variety of linear rheologies is presented. Again, the method can also be extended to non-linear rheologies. The so-called sea level equation is typically used when modelling GIA; our formulation does not involve its use, which allows us, in chapter 5, to apply the adjoint method to the inverse problem. Our formulation is validated through a benchmarking exercise with another GIA code. We present numerical examples calculated in both spherically symmetric earth models and those with laterally varying viscosity.

In chapter 5, we consider the post-glacial inverse problem. We apply the adjoint method to calculate kernels with respect to ice sheet history, viscosity structure and initial sea level. The last of these, whilst not usually considered part of the inverse problem, is an unknown parameter on which measurements of GIA depend. It is common to adjust the initial sea level until the present day sea level matches current observations; we present a method of doing so systematically using the adjoint method. We also present numerical examples of ice sheet and viscosity sensitivity kernels calculated in spherically symmetric earth models and, in the case of the latter, models with laterally varying viscosity. We finally present an example of an inversion for three-dimensional viscosity structure using synthetic data.

In chapter 6, we present our conclusions and discuss some possible applications of the results of this dissertation.

Chapter 2

Forward modelling of post-seismic deformation

2.1 Introduction

It is well known that after an earthquake the Earth continues to deform over a period of months to years. There are three main processes that contribute to this time dependent deformation – afterslip, poroelastic rebound and viscoelastic rebound. Afterslip is continued aseismic movement on the original fault plane or neighbouring fault planes. Poroelastic rebound arises due to flow of fluid through rocks, which is driven by pressure changes associated with the coseismic motion. Lastly, there is further flow at depth due to viscoelastic relaxation in the Earth's crust and mantle. If we can isolate the deformation due to this final aspect, we can use measurements of the deformation to place constraints on the viscoelastic structure of the Earth.

However, the form of the Earth's rheology is not well known. The simplest viscoelastic rheology is that of a Maxwell solid, which has historically been considered sufficient to explain the form of post-seismic deformation and other viscoelastic processes such as post-glacial deformation. However, more recent studies have argued that some measurements of post-seismic deformation show evidence of a more complex rheology, such as a transient rheology with multiple decay times (e.g., Pollitz, 2003) or a non-linear rheology (e.g., Pollitz *et al.*, 2001; Freed & Bürgmann, 2004). The different orders of magnitude of the viscosities obtained from studies post-seismic and post-glacial displacements gives further suggestion of this.

In order to use measurements of post-seismic deformation to learn about the rheological structure of the Earth, a method of forward modelling the process is first required. Given an earth model and earthquake source, this enables the surface deformations to be calculated. There are, however, a number of challenges associated this.

Firstly, it is common when forward modelling to solve the equations of motion in the Laplace transform domain. However, this method is not well suited to lateral variations in structure nor to radial structures that are not piecewise continuous (e.g., Fang & Hager, 1995; Han & Wahr, 1995; Boschi *et al.*, 1999). As the Earth's rheological structure will be pressure and temperature dependent, quantities that vary continuously, it would be preferable to be able to permit continuous structure variation in the model. There is also recent evidence for the effect of lateral variations in structure on post-seismic deformation (e.g., Pollitz, 2015). A further difficulty relates to the inclusion of self-

gravitation. Some studies ignore its effect completely or include only an approximation to it (e.g., Pollitz *et al.*, 2006; Wang *et al.*, 2006). Another approximation that is sometimes made is that the Earth is incompressible (e.g., Boschi *et al.*, 2000).

In this chapter, we present a method for modelling post-seismic deformation in a fully heterogeneous, compressible, self-gravitating Earth, which allows for both linear rheologies with multiple decay times and non-linear rheologies. We illustrate both the forward method with several numerical examples using spherically symmetric earth models, but emphasise again that the theory allows for lateral variations in model structure.

2.2 Deformation of the solid Earth

We wish to formulate the equations of motion that describe post-seismic deformation in a self-gravitating, viscoelastic earth model. Our approach will be similar to that used in Al-Attar & Tromp (2014) to describe post-glacial deformation, but with the addition of a body force through the stress glut. Furthermore, whilst it is often considered sufficient to model the Earth's response as a Maxwell solid in the post-glacial case, we extend the equations to include other linear rheologies that are of interest in the post-seismic case. Non-linear rheologies can be included in a similar manner through extensions presented in Crawford *et al.* (2017).

2.2.1 Equations of motion

Following Al-Attar & Tromp (2014) and making use of Dahlen & Tromp (1998), Dahlen (1974) and Tromp & Mitrovica (1999), we can formulate the equations of motion. We have an earth model that occupies a volume $M \subseteq \mathbb{R}^3$ with external boundary ∂M. The model has a number of fluid and solid regions, the former denoted by M_F and the latter by M_S, that are separated by smooth, non-intersecting, closed surfaces called internal boundaries. The union of all boundaries, both internal and external, is denoted by Σ, with the internal boundaries consisting of four subsets – Σ_{SS}, Σ_{SF}, Σ_{FS} and Σ_{FF}. Here, the first subscript denotes whether the region on the inside of the boundary is solid (S) or fluid (F), and the second subscript refers to the region on the outside of the surface. Neglecting inertial terms, the quasi-static momentum equation for a non-rotating, self-gravitating, hydrostatically pre-stressed, compressible and laterally heterogeneous earth model is

$$-\nabla \cdot \mathbf{T} + \nabla(\rho \mathbf{u} \cdot \nabla \Phi) - \nabla \cdot (\rho \mathbf{u}) \nabla \Phi + \rho \nabla \phi = -\nabla \cdot \mathbf{\Gamma}, \tag{2.1}$$

where $\mathbf{u}$ is the displacement, ρ is the density, $\mathbf{T}$ is the Lagrangian-Cauchy stress tensor, Φ is the reference gravitational potential, ϕ is the gravitational potential perturbation and $\mathbf{\Gamma}$ is the stress glut (Backus & Mulcahy, 1976). Φ satisfies Poisson's equation,

$$\nabla^2 \Phi = 4\pi G \rho, \tag{2.2}$$

and, following Dahlen (1974), ϕ satisfies the modified Poisson's equation,

$$(4\pi G)^{-1}\nabla^2\phi = \begin{cases} -\nabla\cdot(\rho\mathbf{u}), & \mathbf{x}\in M_S, \\ g^{-1}\phi\partial_n\rho, & \mathbf{x}\in M_F, \\ 0, & \mathbf{x}\in\mathbb{R}^3\setminus M, \end{cases} \tag{2.3}$$

where g is the gravitational acceleration and ∂_n is the directional derivative along the outward normal to the level surfaces of density. The stress glut is a body force that arises due to the localised failure of the assumed constitutive relation due to a seismic source (e.g., Dahlen & Tromp, 1998). It is defined as

$$\boldsymbol{\Gamma} = \mathbf{T}_{model} - \mathbf{T}_{true}, \tag{2.4}$$

where $\mathbf{T}_{model}$ is the stress defined using the assumed constitutive relation, and $\mathbf{T}_{true}$ is the physical or true stress. For many applications, it is sufficient to consider the earthquake to be a point source, for which the stress glut can be written as

$$\boldsymbol{\Gamma}(\mathbf{x}) = \mathbf{M}\ \delta(\mathbf{x}-\mathbf{x_0})\mathrm{H}(t), \tag{2.5}$$

where $\mathbf{M}$ is the moment tensor, $\mathbf{x_0}$ the hypocentral location and $\mathrm{H}(t)$ is the Heaviside step function. Finite sources can be built up by the superposition of multiple point sources.

We further need the boundary conditions for the system, which, again following Al-Attar & Tromp (2014) but generalising to include the stress glut, are

$$\hat{\mathbf{n}}\cdot\mathbf{T} = \hat{\mathbf{n}}\cdot\boldsymbol{\Gamma}, \quad \mathbf{x}\in\partial M, \tag{2.6}$$

$$[\hat{\mathbf{n}}\cdot\mathbf{T}]^+_- = [\hat{\mathbf{n}}\cdot\boldsymbol{\Gamma}]^+_-, \quad \mathbf{x}\in\Sigma_{\mathrm{SS}}, \tag{2.7}$$

$$\hat{\mathbf{n}}\cdot\mathbf{T}^+ = \rho^-[\mathbf{u}^+\cdot\nabla\Phi+\phi]\hat{\mathbf{n}} + \hat{\mathbf{n}}\cdot\boldsymbol{\Gamma}^+, \quad \mathbf{x}\in\Sigma_{\mathrm{FS}}, \tag{2.8}$$

$$\hat{\mathbf{n}}\cdot\mathbf{T}^- = \rho^+[\mathbf{u}^-\cdot\nabla\Phi+\phi]\hat{\mathbf{n}} + \hat{\mathbf{n}}\cdot\boldsymbol{\Gamma}^-, \quad \mathbf{x}\in\Sigma_{\mathrm{SF}}, \tag{2.9}$$

$$[\mathbf{u}]^+_- = \mathbf{0}, \quad \mathbf{x}\in\Sigma_{\mathrm{SS}}, \tag{2.10}$$

$$[\phi]^+_- = 0, \quad \mathbf{x}\in\Sigma, \tag{2.11}$$

$$\left[(4\pi G)^{-1}\hat{\mathbf{n}}\cdot\nabla\phi\right]^+_- - \rho^-\hat{\mathbf{n}}\cdot\mathbf{u}^- = 0, \quad \mathbf{x}\in\partial M, \tag{2.12}$$

$$\left[(4\pi G)^{-1}\hat{\mathbf{n}}\cdot\nabla\phi + \rho\hat{\mathbf{n}}\cdot\mathbf{u}\right]^+_- = 0, \quad \mathbf{x}\in\Sigma_{\mathrm{SS}}, \tag{2.13}$$

$$\left[(4\pi G)^{-1}\hat{\mathbf{n}}\cdot\nabla\phi\right]^+_- + [\rho]^+_-\hat{\mathbf{n}}\cdot\mathbf{u}^+ = 0, \quad \mathbf{x}\in\Sigma_{\mathrm{FS}}, \tag{2.14}$$

$$\left[(4\pi G)^{-1}\hat{\mathbf{n}}\cdot\nabla\phi\right]^+_- + [\rho]^+_-\hat{\mathbf{n}}\cdot\mathbf{u}^- = 0, \quad \mathbf{x}\in\Sigma_{\mathrm{SF}}, \tag{2.15}$$

where $^+$ and $^-$ indicate whether a term is evaluated on the upper or lower side of a discontinuity respectively. We further require the gravity perturbation to tend to 0 as $\mathbf{x}$ tends to infinity, which we can write as

$$\lim_{\|\mathbf{x}\|\to\infty}\phi = 0. \tag{2.16}$$

2.2.2 Linear viscoelasticity

In order to formulate the equations for the problem, we require a constitutive equation to specify the relationship between stress ($\mathbf{T}$) and strain ($\mathbf{e}$). In this section, we will consider linear viscoelasticity.

In Crawford *et al.* (2017), we demonstrate how the theory can be extended to include non-linear viscoelasticity. For a classical, linear elastic solid, the constitutive equation is given by Hooke's law,

$$\mathbf{T} = \mathbf{C} : \mathbf{e}, \tag{2.17}$$

where $\mathbf{C}$ is the fourth-order elastic tensor and $\mathbf{e}$ is given by

$$\mathbf{e} = \frac{1}{2}\left[\nabla\mathbf{u} + (\nabla\mathbf{u})^{\mathrm{T}}\right]. \tag{2.18}$$

In the case of an isotropic solid, equation (2.17) simplifies to

$$\mathbf{T}(t) = \kappa\nabla\cdot\mathbf{u}(t)\mathbf{I} + 2\mu\mathbf{d}(t), \tag{2.19}$$

where κ and μ are the bulk and shear moduli respectively and $\mathbf{d}$ is the deviatoric strain,

$$\mathbf{d} = \mathbf{e} - \frac{1}{3}\mathrm{tr}(\mathbf{e})\mathbf{I}. \tag{2.20}$$

Extending equation (2.19) to an isotropic linear viscoelastic material using the Boltzmann superposition principle, we have

$$\mathbf{T}(t) = \kappa\nabla\cdot\mathbf{u}(t)\mathbf{I} + 2\int_0^t \mu(t-t')\dot{\mathbf{d}}(t')\ \mathrm{d}t', \tag{2.21}$$

where $\mu(t)$ is now the time-dependent relaxation function and we have neglected bulk viscoelasticity, which is thought to be a valid simplification (e.g., Wu & Peltier, 1982). We could, however, include bulk viscoelasticity and, more generally, anisotropy through a simple extension of the internal variables method described below (Simo & Hughes, 1998). Integrating the second term in equation (2.21) by parts, we find

$$\mathbf{T}(t) = \kappa\nabla\cdot\mathbf{u}(t)\mathbf{I} + 2\mu_0\mathbf{d}(t) + 2\int_0^t \dot{\mu}(t-t')\mathbf{d}(t')\ \mathrm{d}t', \tag{2.22}$$

where $\mu_0 = \mu(0)$ is, as we will see below, a measure of the elastic response of the material. For a wide class of linear viscoelastic materials, we can write $\mu(t)$ in the general Maxwell form

$$\mu(t) = \sum_i \mu_i e^{-t/\tau_i}, \tag{2.23}$$

where each term in the sum represents a Maxwell element (Simo & Hughes, 1998). We note that a relaxation function of this form allows only for linear rheologies with discrete decay times, and so we could not, for example, model an absorption band solid. However, the theory does include most linear rheologies of interest, and we will next demonstrate its equivalence to the formulation in the Laplace domain more commonly used in post-seismic literature (e.g., Piersanti *et al.*, 1995; Pollitz, 1997).

We recall that the Laplace transform, $\widetilde{f}(s)$, of a function $f(t)$ is defined as

$$\widetilde{f}(s) = \int_0^\infty f(t)e^{-st}\ \mathrm{d}t, \tag{2.24}$$

where s is the transform parameter. It can be seen that the Laplace transform of equation (2.21) is

$$\widetilde{\mathbf{T}}(s) = \kappa\nabla\cdot\widetilde{\mathbf{u}}(s)\mathbf{I} + 2s\widetilde{\mu}(s)\widetilde{\mathbf{d}}(s), \tag{2.25}$$

and the Laplace transform of equation (2.23) is

$$\widetilde{\mu}(s) = \sum_i \frac{\mu_i}{s + \frac{1}{\tau_i}}. \tag{2.26}$$

Using equation (2.26), equation (2.25) becomes

$$\widetilde{\mathbf{T}}(s) = \kappa \nabla \cdot \widetilde{\mathbf{u}}(s)\mathbf{I} + 2\sum_i \frac{s\mu_i}{s + \frac{1}{\tau_i}} \widetilde{\mathbf{d}}(s). \tag{2.27}$$

We can illustrate the equivalence with several simple examples of linear rheologies commonly used in post-seismic deformation. We shall first consider the case of a Maxwell solid. The relaxation function of such a material is given by

$$\mu(t) = \mu e^{-t/\tau}, \tag{2.28}$$

and so its Laplace transform is

$$\widetilde{\mu}(s) = \frac{\mu}{s + \frac{1}{\tau}}. \tag{2.29}$$

Substituting equation (2.29) into equation (2.25) gives

$$\widetilde{\mathbf{T}}(s) = \kappa \nabla \cdot \widetilde{\mathbf{u}}(s)\mathbf{I} + \frac{2\mu s \widetilde{\mathbf{d}}(s)}{s + \frac{1}{\tau}}. \tag{2.30}$$

Comparing equation (2.30) to, for example, equations (6) and (7) in Peltier (1974) shows that equation (2.28) is indeed the relaxation function of a Maxwell solid.

We can further consider a Burgers body rheology, which is also commonly used in post-seismic literature (e.g., Pollitz, 2003; Pollitz *et al.*, 2006). This is the simplest transient rheology – it has two different time scales of decay. The relaxation function of a Burgers solid is

$$\mu(t) = \mu_1 e^{-t/\tau_1} + \mu_2 e^{-t/\tau_2}, \tag{2.31}$$

with Laplace transform

$$\widetilde{\mu}(s) = \frac{\mu_1}{s + \frac{1}{\tau_1}} + \frac{\mu_2}{s + \frac{1}{\tau_2}}. \tag{2.32}$$

Through some simple algebra (e.g., Müller, 1986), it is possible to show that equations (2.25) and (2.32) are indeed equivalent to the more common formulation of a Burgers body rheology in the Laplace domain (e.g., Pollitz, 2003).

Examination of equation (2.27) in the high and low s limits enables us to see the short and long term behaviour of a linear viscoelastic material described using equation (2.23). Considering first the situation where $s \gg \frac{1}{\tau_i}\ \forall i$ (i.e., $t \ll \tau_i\ \forall i$), we see that in this limit, equation (2.27) becomes

$$\widetilde{\mathbf{T}}(s) \approx \kappa \nabla \cdot \widetilde{\mathbf{u}}(s)\mathbf{I} + 2\sum_i \mu_i \widetilde{\mathbf{d}}(s), \tag{2.33}$$

and so when the inverse Laplace transform is applied, we have

$$\mathbf{T}(t) \approx \kappa \nabla \cdot \mathbf{u}(t)\mathbf{I} + 2\sum_i \mu_i \mathbf{d}(t), \tag{2.34}$$

which is the constitutive relation for a linear elastic solid with shear modulus

$$\mu_0 = \sum_i \mu_i. \tag{2.35}$$

If we instead consider the situation where $s \ll \frac{1}{\tau_i}\ \forall i$ (i.e., $t \gg \tau_i\ \forall i$), we see that for deformations that are slow relative to the relaxation times, equation (2.27) becomes

$$\widetilde{\mathbf{T}}(s) \approx \kappa \nabla \cdot \widetilde{\mathbf{u}}(s)\mathbf{I} + 2\sum_i s\mu_i\tau_i\widetilde{\mathbf{d}}(s), \tag{2.36}$$

and when inverse Laplace transformed,

$$\mathbf{T}(t) \approx \kappa \nabla \cdot \mathbf{u}(t)\mathbf{I} + 2\sum_i \mu_i\tau_i\dot{\mathbf{d}}(t). \tag{2.37}$$

This is the constitutive relation for a compressible Newtonian fluid with viscosity

$$\eta = \sum_i \mu_i\tau_i. \tag{2.38}$$

We therefore see that a material with shear relaxation function given by equation (2.23) behaves like a linear elastic solid for deformations that are fast relative to its decay times and like a Newtonian fluid for deformations that are slow relative to its decay times. Its exact behaviour on time scales between these two limits depends on the number of terms in equation (2.23) and the relative magnitudes of the μ_is and τ_is.

We will now discuss how we can use the form of the relaxation function given in equation (2.23) to model linear viscoelastic materials in the time domain. This is useful for numerical calculations and circumvents the issues with the Laplace transform method of modelling continuous variation in model parameters (e.g., Fang & Hager, 1995; Han & Wahr, 1995; Boschi *et al.*, 1999). We define internal variables, $\mathbf{m}_i$, (e.g., Simo & Hughes, 1998) such that

$$\mathbf{m}_i(t) = \frac{1}{\tau_i}\int_0^t e^{-\frac{(t-t')}{\tau_i}}\mathbf{d}(t')\ \mathrm{d}t'. \tag{2.39}$$

These are seen to satisfy

$$\dot{\mathbf{m}}_i + \frac{1}{\tau_i}(\mathbf{m}_i - \mathbf{d}) = 0, \tag{2.40}$$

and using this result, we can write equation (2.22) as

$$\mathbf{T} = \kappa \nabla \cdot \mathbf{u}\mathbf{I} + \sum_i 2\mu_i(\mathbf{d} - \mathbf{m}_i). \tag{2.41}$$

As $\mathbf{d}$ is a trace-free tensor, the same is true of $\mathbf{m}_i$, and the deviatoric stress, $\overline{\mathbf{T}}$, is given by

$$\overline{\mathbf{T}} = \sum_i 2\mu_i(\mathbf{d} - \mathbf{m}_i). \tag{2.42}$$

2.2.3 Rate formulation

In order to incorporate time dependence and a viscoelastic rheology into equation (2.1), the momentum equation, we follow the method of Al-Attar & Tromp (2014). Differentiating equation (2.1) with respect to time and using equations (2.40) and (2.41), we obtain a rate formulation of the problem,

$$\nabla \cdot (\kappa \nabla \cdot \dot{\mathbf{u}}\mathbf{I} + 2\mu_0 \dot{\mathbf{d}}) + 2\sum_i \nabla \cdot \left[\frac{\mu_i}{\tau_i}(\mathbf{m}_i - \mathbf{d})\right] - \nabla(\rho \dot{\mathbf{u}} \cdot \nabla \Phi) + \nabla \cdot (\rho \dot{\mathbf{u}} \nabla \Phi) - \rho \nabla \dot{\phi} = \nabla \cdot \dot{\mathbf{\Gamma}}. \quad (2.43)$$

We can similarly differentiate equations (2.6) – (2.15) to obtain the rate formulated boundary conditions. These equations, along with equation (2.40) and the initial conditions

$$\mathbf{u}(\mathbf{x}, 0) = \mathbf{0}, \quad \phi(\mathbf{x}, 0) = 0, \quad \mathbf{m}_i(\mathbf{x}, 0) = \mathbf{0}, \quad (2.44)$$

constitute the strong form of the problem. We now have a system of equations that implicitly give the time derivatives $\dot{\mathbf{u}}$, $\dot{\phi}$ and $\dot{\mathbf{m}}_i$ at time t as a function of the current state $\mathbf{u}$, ϕ, $\mathbf{m}_i$ and $\mathbf{\Gamma}$. We can therefore calculate the time derivatives at a given time, and use them along with some time-stepping scheme to calculate the state of the system at a future time. This approach is equivalent to other time-domain methods in the geophysical literature (e.g., Hanyk *et al.*, 1995; Zhong *et al.*, 2003; Latychev *et al.*, 2005), although it differs due to the introduction of internal variables. Furthermore, we have avoided explicitly introducing a numerical scheme for time-stepping, which allows for greater flexibility.

2.3 Weak formulation of the post-seismic problem

In order to implement equation (2.43) and the associated boundary conditions numerically using a finite-element-type method, we derive the so-called weak form of the problem. We can introduce test functions $\mathbf{u}'$, ϕ' and $\mathbf{m}_i'$, where we require that

$$[\mathbf{u}']^+_- = \mathbf{0}, \quad \mathbf{x} \in \Sigma_{\mathrm{SS}}, \quad (2.45)$$

$$[\phi']^+_- = 0, \quad \mathbf{x} \in \Sigma, \quad (2.46)$$

and $\phi' \to 0$ as $\|\mathbf{x}\| \to \infty$. Multiplying equations (2.43) and (2.40) by these test functions and integrating by parts with respect to V, we obtain the weak form,

$$\mathcal{A}(\dot{\mathbf{u}}, \dot{\phi} | \mathbf{u}', \phi') - \int_{M_S} \sum_i 2\mu_i \left[\dot{\mathbf{m}} : \mathbf{m}' + \frac{1}{\tau_i}(\mathbf{d} - \mathbf{m}_i) : (\mathbf{d}' - \mathbf{m}_i')\right] \, \mathrm{d}V - \int_{M_S} \dot{\mathbf{\Gamma}} : \nabla \mathbf{u}' \, \mathrm{d}V = 0, \quad (2.47)$$

which for a symmetric stress glut can be written as

$$\mathcal{A}(\dot{\mathbf{u}}, \dot{\phi} | \mathbf{u}', \phi') - \int_{M_S} \sum_i 2\mu_i \left[\dot{\mathbf{m}} : \mathbf{m}' + \frac{1}{\tau_i}(\mathbf{d} - \mathbf{m}_i) : (\mathbf{d}' - \mathbf{m}_i')\right] \, \mathrm{d}V - \int_{M_S} \dot{\mathbf{\Gamma}} : \mathbf{e}' \, \mathrm{d}V = 0, \quad (2.48)$$

where $\mathbf{e}'$ is the strain tensor given by

$$\mathbf{e}' = \frac{1}{2}[\nabla \mathbf{u}' + (\nabla \mathbf{u}')^{\mathrm{T}}]. \quad (2.49)$$

Henceforth, we will assume that the stress glut is symmetric and so we can use the weak form in equation (2.48). As derived in appendix B of Al-Attar & Tromp (2014), $\mathcal{A}$ is given by

$$\begin{aligned}\mathcal{A}(\mathbf{u},\phi|\mathbf{u}',\phi') = &\int_{M_S} \kappa\nabla\cdot\mathbf{u}\,\nabla\cdot\mathbf{u}'\,\mathrm{d}V + \int_{M_S} 2\mu\mathbf{d}:\mathbf{d}'\mathrm{d}V + \frac{1}{2}\int_{M_S}\rho\left[\nabla(\mathbf{u}\cdot\nabla\Phi)\cdot\mathbf{u}' + \nabla(\mathbf{u}'\cdot\nabla\Phi)\cdot\mathbf{u}\right]\mathrm{d}V \\ &- \frac{1}{2}\int_{M_S}\rho\left(\nabla\cdot\mathbf{u}\nabla\Phi\cdot\mathbf{u}' + \nabla\cdot\mathbf{u}'\nabla\Phi\cdot\mathbf{u}\right)\mathrm{d}V + \int_{M_S}\rho(\nabla\phi\cdot\mathbf{u}' + \mathbf{u}\cdot\nabla\phi')\mathrm{d}V \\ &+ \frac{1}{4\pi G}\int_{\mathbb{R}^3}\nabla\phi\cdot\nabla\phi'\mathrm{d}V + \int_{M_F} g^{-1}\phi\phi'\partial_n\rho\mathrm{d}V + \int_{\Sigma_{\mathrm{FS}}}\rho^- g\hat{\mathbf{n}}\cdot\mathbf{u}\,\hat{\mathbf{n}}\cdot\mathbf{u}'\mathrm{d}S \\ &- \int_{\Sigma_{\mathrm{SF}}}\rho^+ g\hat{\mathbf{n}}\cdot\mathbf{u}\,\hat{\mathbf{n}}\cdot\mathbf{u}'\mathrm{d}S + \int_{\Sigma_{\mathrm{FS}}}\rho^-(\phi\mathbf{u}' + \mathbf{u}\phi')\cdot\hat{\mathbf{n}}\mathrm{d}S - \int_{\Sigma_{\mathrm{SF}}}\rho^+(\phi\mathbf{u}' + \mathbf{u}\phi')\cdot\hat{\mathbf{n}}\mathrm{d}S.\end{aligned} \tag{2.50}$$

We notice that $\mathcal{A}$ is symmetric under interchange of ($\mathbf{u}$,ϕ) and ($\mathbf{u}'$,ϕ'). It may be shown that all $\mathbf{u}$, ϕ and $\mathbf{m}_i$ that are solutions of this weak form are also solutions of the strong form, and vice versa.

2.4 Numerical implementation in spherically symmetric earth models

To illustrate the forward method, we will consider our equations in spherically symmetric earth models. This allows the equations to be reduced to a system of one-dimensional equations in the radial coordinate. In order to do this, we expand the fields in generalised spherical harmonics, as discussed in section 1.3.2, which results in total decoupling of the radial expansion functions for each spherical harmonic of degree l and order m. We therefore need only construct a radial mesh, and then solve the radial equations using the Spectral Element Method, as discussed in section 1.3.1.

2.4.1 Generalised spherical harmonic expansions

In order to describe the displacement, we will find it useful to define the coefficients U_{lm}, V_{lm} and W_{lm} such that

$$u^0_{lm} = U_{lm}, \tag{2.51}$$

$$u^{\pm}_{lm} = \frac{k}{\sqrt{2}}(V_{lm} \pm iW_{lm}), \tag{2.52}$$

where

$$k = \sqrt{l(l+1)}. \tag{2.53}$$

For such a displacement, we find that $\nabla\mathbf{u}$ has components

$$\partial^0 u^0_{lm} = \partial_r U_{lm}, \tag{2.54}$$

$$\partial^0 u^\pm_{lm} = \frac{k}{\sqrt{2}}(\partial_r V_{lm} \pm i\partial_r W_{lm}), \tag{2.55}$$

$$\partial^\pm u^0_{lm} = \frac{k}{\sqrt{2}r}(U_{lm} - V_{lm} \mp iW_{lm}), \tag{2.56}$$

$$\partial^\pm u^\pm_{lm} = \frac{k\sqrt{k^2-2}}{2r}(V_{lm} \pm iW_{lm}), \tag{2.57}$$

$$\partial^\pm u^\mp_{lm} = \frac{k^2}{2r}(V_{lm} \mp iW_{lm}) - \frac{1}{r}U_{lm}, \tag{2.58}$$

and so the strain, $\mathbf{e}$, given by equation (2.18), has components

$$e^{00}_{lm} = \partial_r U_{lm}, \tag{2.59}$$

$$e^{0\pm}_{lm} = e^{\pm 0}_{lm} = \frac{k}{2\sqrt{2}r}(r\partial_r V_{lm} - V_{lm} + U_{lm}) \pm \frac{ik}{2\sqrt{2}r}(r\partial_r W_{lm} - W_{lm}), \tag{2.60}$$

$$e^{\pm\pm}_{lm} = \frac{k\sqrt{k^2-2}}{2r}(V_{lm} \pm iW_{lm}), \tag{2.61}$$

$$e^{\pm\mp}_{lm} = \frac{k^2}{2r}V_{lm} - \frac{1}{r}U_{lm}. \tag{2.62}$$

Furthermore, the deviatoric strain, $\mathbf{d}$, which is given by equation (2.20), has components

$$d^{00}_{lm} = \frac{2}{3r}\left(r\partial_r U_{lm} - U_{lm} + \frac{k^2}{2}V_{lm}\right), \tag{2.63}$$

$$d^{0\pm}_{lm} = d^{\pm 0}_{lm} = \frac{k}{2\sqrt{2}r}(r\partial_r V_{lm} - V_{lm} + U_{lm}) \pm \frac{ik}{2\sqrt{2}r}(r\partial_r W_{lm} - W_{lm}), \tag{2.64}$$

$$d^{\pm\pm}_{lm} = \frac{1}{2r}(V_{lm} \pm iW_{lm}), \tag{2.65}$$

$$d^{\pm\mp}_{lm} = \frac{k\sqrt{k^2-2}}{3r}\left(r\partial_r U_{lm} - U_{lm} + \frac{k^2}{2}V_{lm}\right). \tag{2.66}$$

As $\mathbf{d}$ is a trace-free tensor, the same is true of the internal variables, $\mathbf{m}_i$. We can therefore write the components of $\mathbf{m}_i$ as

$$m^{\pm\pm}_{ilm} = \frac{1}{2r}k\sqrt{k^2-2}(M_{ilm} \pm iN_{ilm}), \tag{2.67}$$

$$m^{00}_{ilm} = \frac{2}{3r}R_{ilm}, \tag{2.68}$$

$$m^{0\pm}_{ilm} = \frac{k}{2\sqrt{2}r}(S_{ilm} \pm iT_{ilm}), \tag{2.69}$$

$$m^{\pm\mp}_{ilm} = \frac{1}{3r}R_{ilm}, \tag{2.70}$$

where we have introduced new coefficients M_{ilm}, N_{ilm}, R_{ilm}, S_{ilm} and T_{ilm}.

2.4.2 Derivation of the weak form in generalised spherical harmonics

The expansion in generalised spherical harmonics of the first two terms in equation (2.47) is given in appendix D of Al-Attar & Tromp (2014). Here, we will derive the form of the third term,

$$\int_{M_S} \mathbf{\Gamma} : \nabla \mathbf{u}'^{*} \, \mathrm{d}V, \tag{2.71}$$

where $\mathbf{u}'^{*}$ will be expanded in terms of the complex conjugates of the generalised spherical harmonics. We will first do this for a general, non-symmetric moment-tensor source and then show how the result can be simplified in the case of a symmetric moment tensor to give the third term in equation (2.48). For a moment tensor point source, we can write the stress glut as

$$\mathbf{\Gamma} = \mathbf{M}\delta(r - r_0) \, \frac{\delta(\theta - \theta_0) \, \delta(\phi - \phi_0)}{\sin\theta} \mathrm{H}(t), \tag{2.72}$$

where $\mathbf{M}$ is the moment tensor of a source located at (r_0,θ_0,ϕ_0) in spherical polar coordinates, and $\mathrm{H}(t)$ is the Heaviside step function. A general, non-symmetric $\mathbf{M}$ can be expanded as

$$\begin{aligned} \mathbf{M} =& M_{rr}\hat{\mathbf{r}} \otimes \hat{\mathbf{r}} + M_{r\theta}\hat{\mathbf{r}} \otimes \hat{\boldsymbol{\theta}} + M_{\theta r}\hat{\boldsymbol{\theta}} \otimes \hat{\mathbf{r}} + M_{r\phi}\hat{\mathbf{r}} \otimes \hat{\boldsymbol{\phi}} + M_{\phi r}\hat{\boldsymbol{\phi}} \otimes \hat{\mathbf{r}} & (2.73) \\ &+ M_{\theta\theta}\hat{\boldsymbol{\theta}} \otimes \hat{\boldsymbol{\theta}} + M_{\theta\phi}\hat{\boldsymbol{\theta}} \otimes \hat{\boldsymbol{\phi}} + M_{\phi\theta}\hat{\boldsymbol{\phi}} \otimes \hat{\boldsymbol{\theta}} + M_{\phi\phi}\hat{\boldsymbol{\phi}} \otimes \hat{\boldsymbol{\phi}}. & (2.74) \end{aligned}$$

Using equations (1.9) – (1.11) and rearranging, equation (2.74) becomes

$$\begin{aligned} \mathbf{M} =& M_{rr}\hat{\mathbf{e}}_0 \otimes \hat{\mathbf{e}}_0 + \frac{1}{\sqrt{2}}(M_{r\theta} + iM_{r\phi})\hat{\mathbf{e}}_0 \otimes \hat{\mathbf{e}}_- + \frac{1}{\sqrt{2}}(M_{\theta r} + iM_{\phi r})\hat{\mathbf{e}}_- \otimes \hat{\mathbf{e}}_0 \\ &+ \frac{1}{\sqrt{2}}(-M_{r\theta} + iM_{r\phi})\hat{\mathbf{e}}_0 \otimes \hat{\mathbf{e}}_+ + \frac{1}{\sqrt{2}}(-M_{\theta r} + iM_{\phi r})\hat{\mathbf{e}}_+ \otimes \hat{\mathbf{e}}_0 \\ &+ \frac{1}{2}(M_{\theta\theta} + iM_{\theta\phi} + iM_{\phi\theta} - M_{\phi\phi})\hat{\mathbf{e}}_- \otimes \hat{\mathbf{e}}_- + \frac{1}{2}(M_{\theta\theta} - iM_{\theta\phi} - iM_{\phi\theta} - M_{\phi\phi})\hat{\mathbf{e}}_+ \otimes \hat{\mathbf{e}}_+ \\ &- \frac{1}{2}(M_{\theta\theta} + M_{\phi\phi} + iM_{\phi\theta} - iM_{\theta\phi})\hat{\mathbf{e}}_- \otimes \hat{\mathbf{e}}_+ - \frac{1}{2}(M_{\theta\theta} + M_{\phi\phi} - iM_{\phi\theta} + iM_{\theta\phi})\hat{\mathbf{e}}_+ \otimes \hat{\mathbf{e}}_-. \end{aligned} \tag{2.75}$$

We can therefore see that the components of $\mathbf{M}$ in the canonical basis are

$$M^{00} = M_{rr}, \tag{2.76}$$

$$M^{0\pm} = \frac{1}{\sqrt{2}}(\mp M_{r\theta} + iM_{r\phi}), \tag{2.77}$$

$$M^{\pm 0} = \frac{1}{\sqrt{2}}(\mp M_{\theta r} + iM_{\phi r}), \tag{2.78}$$

$$M^{\pm\pm} = \frac{1}{2}(M_{\theta\theta} - M_{\phi\phi} \mp iM_{\theta\phi} \mp iM_{\phi\theta}), \tag{2.79}$$

$$M^{\pm\mp} = \frac{1}{2}(-M_{\theta\theta} - M_{\phi\phi} \pm iM_{\phi\theta} \mp iM_{\theta\phi}). \tag{2.80}$$

In the canonical basis, equation (2.71) can be expanded as

$$\begin{aligned} \int_{M_S} \mathbf{\Gamma} : \nabla \mathbf{u}'^{*} \, \mathrm{d}V = \int_{M_S} (&\Gamma^{--}\partial^- u'^{*-} + \Gamma^{-0}\partial^- u'^{*0} + \Gamma^{-+}\partial^- u'^{*+} + \Gamma^{0-}\partial^0 u'^{*-} + \Gamma^{00}\partial^0 u'^{*0} \\ &+ \Gamma^{0+}\partial^0 u'^{*+} + \Gamma^{+-}\partial^+ u'^{*-} + \Gamma^{+0}\partial^+ u'^{*0} + \Gamma^{++}\partial^+ u'^{*+}) \, \mathrm{d}V. \end{aligned} \tag{2.81}$$

Using equations (2.54) – (2.58), (2.72) and (2.76) – (2.80), and after some rearrangement, we find that

$$
\begin{aligned}
&\int_{M_S} \mathbf{\Gamma} : \nabla \mathbf{u}'^{*} \, \mathrm{d}V \\
&= \sum_{l,m} \int_{I_S} \int_{\phi=0}^{2\pi} \int_{\theta=0}^{\pi} \left\{ \frac{k\sqrt{k^2-2}}{4r} (M_{\theta\theta} + iM_{\theta\phi} + iM_{\phi\theta} - M_{\phi\phi})(V'^{*}_{lm} + iW'^{*}_{lm}) Y^{-2*}_{lm} \right. \\
&\qquad + \frac{k}{2} \left[\frac{1}{r} (M_{\theta r} + iM_{\phi r})(U'^{*}_{lm} - V'^{*}_{lm} - iW'^{*}_{lm}) + (M_{r\theta} + iM_{r\phi})(\partial_r V'^{*}_{lm} + i\partial_r W'^{*}_{lm}) \right] Y^{-*}_{lm} \\
&\qquad + \left[\frac{1}{r} (M_{\theta\theta} + M_{\phi\phi}) \left(U'^{*}_{lm} - \frac{k^2}{2} V'^{*}_{lm} \right) + \frac{k^2}{2r} (M_{\theta\phi} - M_{\phi\theta}) W'^{*}_{lm} + M_{rr} \partial_r U'^{*}_{lm} \right] Y^{0*}_{lm} \\
&\qquad + \frac{k}{2} \left[\frac{1}{r} (-M_{\theta r} + iM_{\phi r})(U'^{*}_{lm} - V'^{*}_{lm} + iW'^{*}_{lm}) + (-M_{r\theta} + iM_{r\phi})(\partial_r V'^{*}_{lm} - i\partial_r W'^{*}_{lm}) \right] Y^{+*}_{lm} \\
&\qquad \left. + \frac{k\sqrt{k^2-2}}{4r} (M_{\theta\theta} - iM_{\theta\phi} - iM_{\phi\theta} - M_{\phi\phi})(V'^{*}_{lm} - iW'^{*}_{lm}) Y^{+2*}_{lm} \right\} \\
&\qquad \mathrm{H}(t) \; \delta(\theta - \theta_0) \; \delta(\phi - \phi_0) \; \delta(r - r_0) \; \mathrm{d}\theta \; \mathrm{d}\phi \; \mathrm{d}r, \qquad (2.82)
\end{aligned}
$$

where I_S is the set of all radii within solid regions. Considering the definition of the generalised spherical harmonics, we can see that (Dahlen & Tromp, 1998)

$$
\int_{\Omega} Y^{N*}_{lm} \delta(\theta - \theta_0) \; \delta(\phi - \phi_0) \; \mathrm{d}\theta \; \mathrm{d}\phi = Y^{N*}_{lm}(\theta_0, \phi_0) = (-1)^{m+N} Y^{-N}_{l-m}(0,0) = \left(\frac{2l+1}{4\pi} \right)^{1/2} (-1)^{m+N} \delta_{Nm}, \qquad (2.83)
$$

where we have defined our coordinate system such that $\phi_0 = 0$ and $\theta_0 = 0$. Substituting equation (2.83) into equation (2.82), we have

$$
\begin{aligned}
\int_{M_S} \mathbf{\Gamma} : \nabla \mathbf{u}'^{*} \, \mathrm{d}V = \sum_{l=0}^{\infty} \int_{I_S} &\left\{ \frac{k\sqrt{k^2-2}}{4r} (M_{\theta\theta} + iM_{\theta\phi} + iM_{\phi\theta} - M_{\phi\phi})(V'^{*}_{l,-2} + iW'^{*}_{l,-2}) \right. \\
&+ \frac{k}{2} \left[\frac{1}{r} (M_{\theta r} + iM_{\phi r})(U'^{*}_{l,-1} - V'^{*}_{l,-1} - iW'^{*}_{l,-1}) + (M_{r\theta} + iM_{r\phi})(\partial_r V'^{*}_{l,-1} + i\partial_r W'^{*}_{l,-1}) \right] \\
&+ \frac{1}{r} (M_{\theta\theta} + M_{\phi\phi}) \left(U'^{*}_{l,0} - \frac{k^2}{2} V'^{*}_{l,0} \right) + \frac{k^2}{2r} (M_{\theta\phi} - M_{\phi\theta}) W'^{*}_{l,0} + M_{rr} \partial_r U'^{*}_{l,0} \\
&+ \frac{k}{2} \left[\frac{1}{r} (-M_{\theta r} + iM_{\phi r})(U'^{*}_{l,1} - V'^{*}_{l,1} + iW'^{*}_{l,1}) + (-M_{r\theta} + iM_{r\phi})(\partial_r V'^{*}_{l,1} - i\partial_r W'^{*}_{l,1}) \right] \\
&\left. + \frac{k\sqrt{k^2-2}}{4r} (M_{\theta\theta} - iM_{\theta\phi} - iM_{\phi\theta} - M_{\phi\phi})(V'^{*}_{l,2} - iW'^{*}_{l,2}) \right\} \qquad (2.84) \\
&\left(\frac{2l+1}{4\pi} \right) \; \mathrm{H}(t) \; \delta(r - r_0) \; \mathrm{d}r. \qquad (2.85)
\end{aligned}
$$

For a symmetric moment tensor, as would usually be the case, this reduces to

$$\begin{aligned}\int_{M_S} \mathbf{\Gamma} : \nabla \mathbf{u}'^{*} \, \mathrm{d}V &= \int_{M_S} \mathbf{\Gamma} : \mathbf{e}'^{*} \, \mathrm{d}V \\ &= \sum_{l=0}^{\infty} \int_{I_S} \left[\frac{k\sqrt{k^2-2}}{4r}(M_{\theta\theta} + 2iM_{\theta\phi} - M_{\phi\phi})(V'^{*}_{l,-2} + iW'^{*}_{l,-2}) \right. \\ &\quad + \frac{k}{2}(M_{r\theta} + iM_{r\phi}) \left(\frac{U'^{*}_{l,-1}}{r} - \frac{V'^{*}_{l,-1}}{r} - \frac{iW'^{*}_{l,-1}}{r} + \partial_r V'^{*}_{l,-1} + i\partial_r W'^{*}_{l,-1} \right) \\ &\quad + \frac{1}{r}(M_{\theta\theta} + M_{\phi\phi}) \left(U'^{*}_{l,0} - \frac{k^2}{2} V'^{*}_{l,0} \right) + M_{rr}\partial_r U'^{*}_{l,0} \\ &\quad + \frac{k}{2}(-M_{r\theta} + iM_{r\phi}) \left(\frac{U'^{*}_{l,1}}{r} - \frac{V'^{*}_{l,1}}{r} + \frac{iW'^{*}_{l,1}}{r} + \partial_r V'^{*}_{l,1} - i\partial_r W'^{*}_{l,1} \right) \\ &\quad \left. + \frac{k\sqrt{k^2-2}}{4r}(M_{\theta\theta} - 2iM_{\theta\phi} - M_{\phi\phi})(V'^{*}_{l,2} - iW'^{*}_{l,2}) \right] \left(\frac{2l+1}{4\pi} \right) \mathrm{H}(t) \, \delta(r - r_0) \, \mathrm{d}r. \end{aligned} \tag{2.86}$$

2.4.3 Details of implementation

Our equations are implemented in an earth model with a solid elastic inner core, a compressible inviscid outer core, a viscoelastic mantle with a linear rheology of the form given in equation (2.23) and an elastic lid. Our implementation allows for discontinuities between model layers, but also for continuous variation in model parameters within these layers. This is in contrast to the more common implementation in the Laplace domain, for which problems arise unless the model is piecewise continuous (e.g., Fang & Hager, 1995; Han & Wahr, 1995; Boschi *et al.*, 1999).

At each time point, we use the current fields to calculate their time derivatives by solving equation (2.48) and time step using an explicit second order Runge-Kutta integration scheme (e.g., Press *et al.*, 1986). The time step is taken to be half the shortest decay time in the model, which is sufficient for numerical stability and to obtain the desired level of accuracy.

Unless otherwise stated, in the examples below our source is a thrust fault earthquake at 15 km depth, striking North and with a dip of 30°. Our source is an approximation to a point source - its spatial distribution is a delta function in θ and ϕ, but a Gaussian with a standard deviation of 2.0 km in the radial direction. This is chosen for convenience, and we note that it would be possible to choose any other radial function. We use the elastic structure of the Preliminary Reference Earth Model (PREM) (Dziewonski & Anderson, 1981), with a 19 km thick elastic lid and a viscosity of 6×10^{18} Pa s from below this layer to a depth of 400 km, 5×10^{20} Pa s from a depth of 400 km to 670 km and 5×10^{21} Pa s from 670 km to the core-mantle boundary. The shallowest viscosity is taken from Huang *et al.* (2016), and the deeper values are common in post-glacial simulations; however, the post-seismic displacements are unlikely to be sensitive to these deeper viscosities. In general, we use a Maxwell solid rheology, though we include an example using a Burgers body rheology. We note again that the theory described allows for other linear and non-linear rheologies, although the latter necessarily introduces lateral heterogeneity into the problem due to the dependence of the effective viscosity on stress, a laterally varying field. Therefore, non-linear rheologies are not currently implemented.

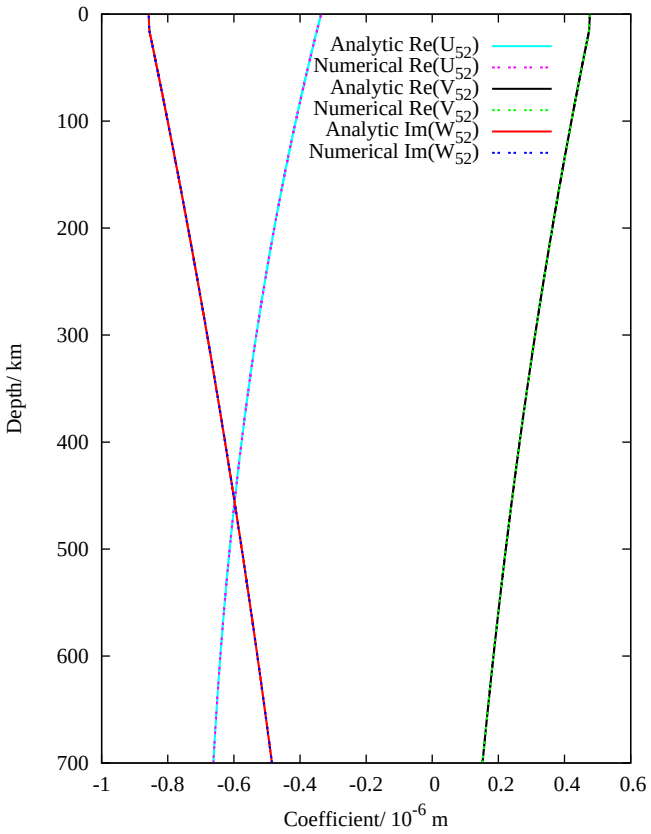

Figure 2.1: Comparison of the initial values of the displacement coefficients U_{lm}, V_{lm} and W_{lm} for $l = 5$ and $m = 2$ for both analytic and numerical solutions. The analytic solutions are derived using propagator matrix methods. The source is as described in section 2.4.3 and the earth structure as in section 2.4.4. The solutions obtained by the different methods agree very well.

2.4.4 Comparison with analytic solutions

In order to benchmark the code, we compared our numerical solutions to those obtained analytically in a few specific cases. For a non-self-gravitating, spherically symmetric earth model, it is possible to derive an analytic solution for some simple models. This can be done using propagator matrix methods (Gilbert & Backus, 1966; Woodhouse & Deuss, 2007; Al-Attar & Woodhouse, 2008). The source has the same form as described above, except that it is a delta function in the radial direction. We obtained analytic solutions for the initial values of the U_{lm} and V_{lm} coefficients and time-dependent values of the W_{lm} coefficients for a homogeneous elastic structure – the parameters from the base of the mantle to the surface are equal to the values at a depth of 19 km in PREM. The viscosity is 6×10^{18} Pa s throughout the entirety of the mantle. These solutions were compared to the numerical solutions for the earthquake described above for many values of l and m, and were found to agree to within numerical precision, except within the vicinity of the source where the fact the numerical source only approximates a delta function increases the error slightly. Examples are shown in figures 2.1 and 2.2.

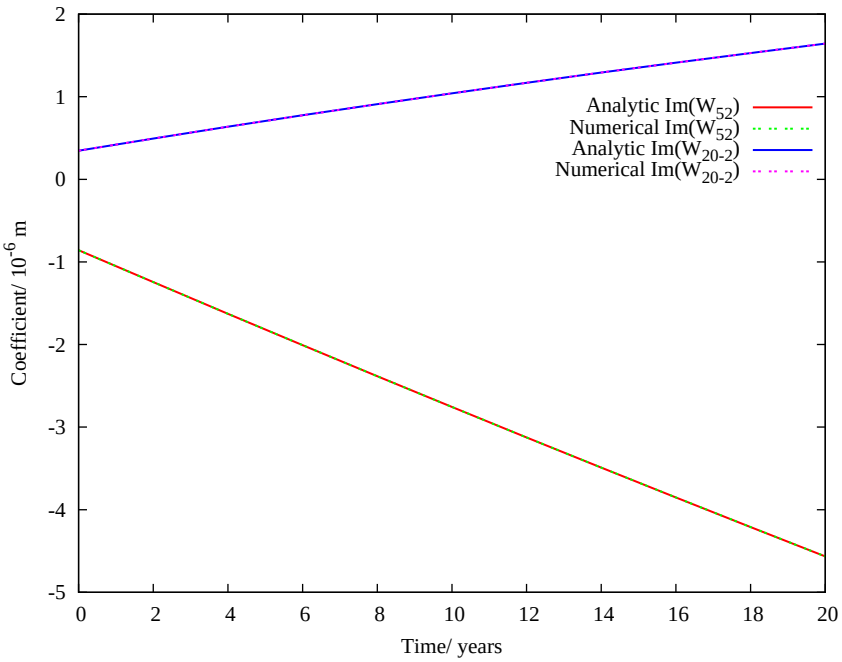

Figure 2.2: Comparison of the analytic and numerical solutions for the time dependence of the value at the surface of the displacement coefficients W_{lm} for $l = 5$ and $m = 2$, and $l = 20$ and $m = -2$. These coefficients have zero real part due to the geometry of the source. The analytic solutions are derived using propagator matrix methods. The source is as described in section 2.4.3 and the earth structure as in section 2.4.4. The solutions obtained by the different methods agree very well.

2.4.5 Comparison with Laplace domain code

Our code was further compared to an existing Laplace domain code, based on Wu & Peltier (1982), which models post-glacial deformation. For this case, we must replace the stress glut term in equation (2.48) with a term that represents a surface load; from Al-Attar & Tromp (2014), this term is

$$\int_{\partial M} (\nabla\Phi \cdot \mathbf{u}' + \phi')\dot{\sigma} \, \mathrm{d}S, \tag{2.87}$$

for some time-dependent surface load $\sigma(\mathbf{x}, t)$. The surface load used was

$$\sigma(\mathbf{x}, t) = \sum_{l=2}^{l_{max}} \left(\frac{2l+1}{4\pi}\right)^{1/2} \exp\left[\frac{-2\pi(l+1)}{L+\frac{1}{2}}\right] Y_{l0}^{0}(\theta, \phi), \tag{2.88}$$

for $t \geq 0$, where $l_{max} = 256$ and $L = 100$. Its value as a function of latitude is shown in figure 2.3. For this test, we used an earth structure with a 120 km thick elastic lid, a viscosity of 5×10^{20} Pa s in the upper mantle and a viscosity of 5×10^{21} Pa s in the lower mantle. Figure 2.4 shows the radial displacement and the gravity perturbation calculated by the two codes initially and 10000 years after the load was added. We can see that the two codes agree very well, with any differences of order 1%, in spite of the significant differences in the numerical implementations.

2.4.6 Numerical examples

In figure 2.5, we show the surface displacement at two different times for the earthquake and earth structure described above calculated using our model. Figure 2.6 shows the depth dependent displace-

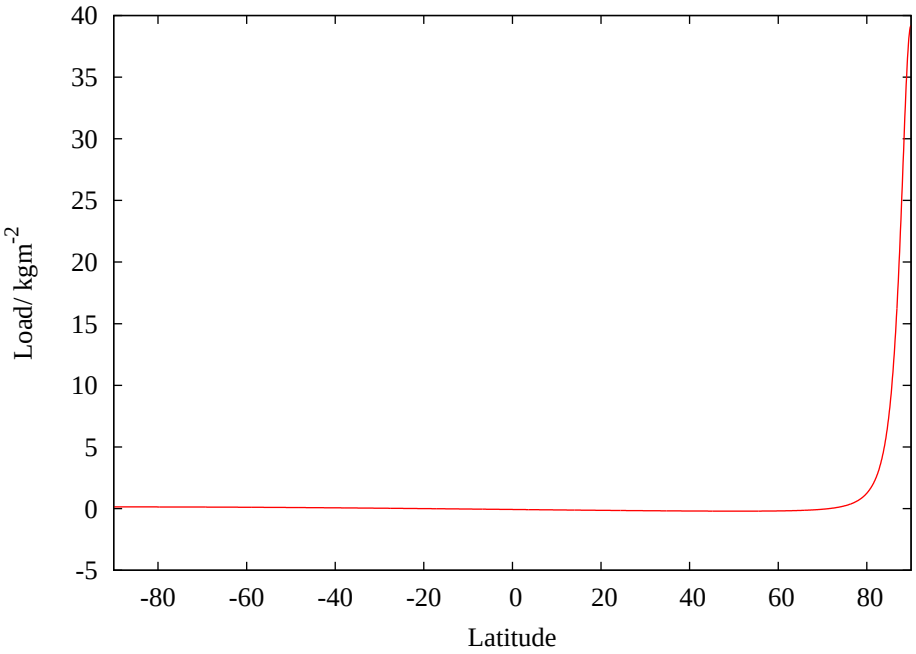

Figure 2.3: Axially symmetric surface load given by equation (2.88) used to compute the displacements in figure 2.4.

ments for a slice through the Earth for the same earthquake.

Figure 2.7 shows the horizontal displacement at the epicentre for both a Maxwell solid and Burgers solid mantle rheology. The parameters of the Burgers body relaxation function (equation (2.31)) are chosen such that the two rheologies have the same shear modulus (given by equation (2.35)) and long-term viscosity (equation (2.38)) and so, as the figure shows, the displacements will have the same initial value and long-term gradient. Using parameters similar to those found by Pollitz (2003), we have chosen $\mu_1 = \mu_2$ and $\tau_1 = 30\tau_2$.

2.5 Conclusion

In this chapter, we have presented a new method for modelling post-seismic deformation in a compressible, self-gravitating and laterally heterogeneous earth model that can have a variety of linear rheologies as well as continuous variation in structure. Non-linear rheologies can also be considered through extensions discussed in Crawford *et al.* (2017). Example forward calculations are shown for earth models with a spherically symmetric structure. One of the main advantages of this new formulation is that is allows the adjoint method to be applied to the inverse problem; this is considered in the next chapter.

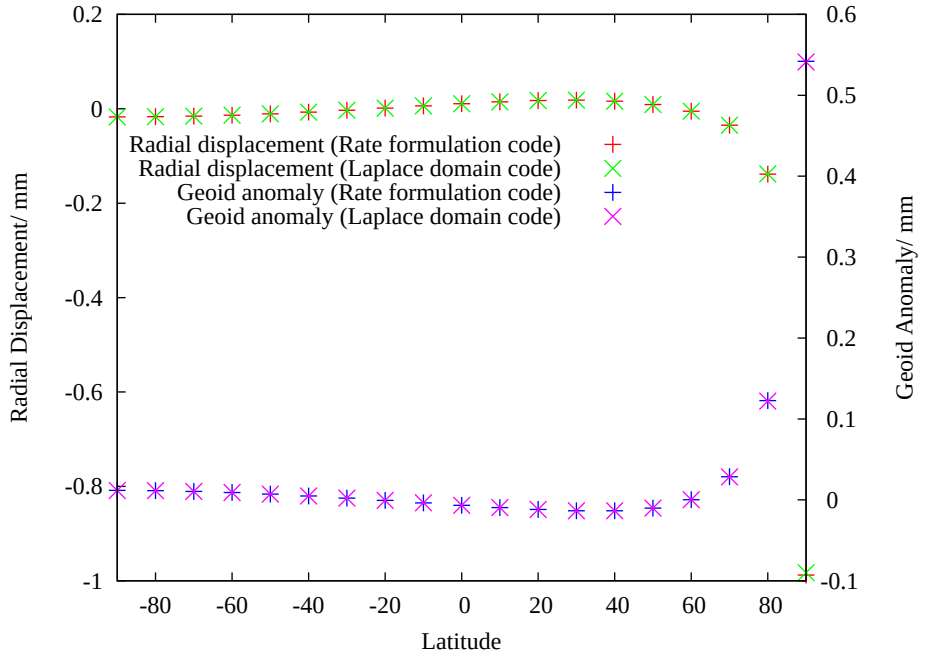

(a) $t = 0$ years

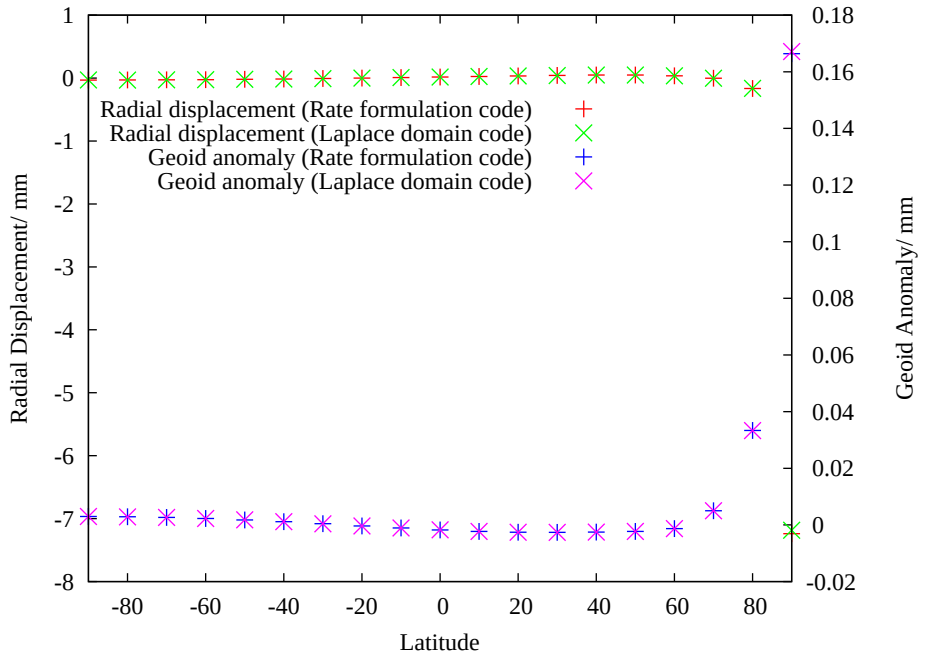

(b) $t = 10000$ years

Figure 2.4: The radial displacements and geoid anomalies as a function of latitude computed using the approach of this study and a code based on Laplace domain methods (see section 2.4.5). The green and red points are associated with the left axes, whereas the blue and pink are associated with the right. The force is an axially symmetric surface load shown in figure 2.3 and given by equation (2.88). The comparison is shown at (a) 0 years and (b) 10000 years after the load is first applied.

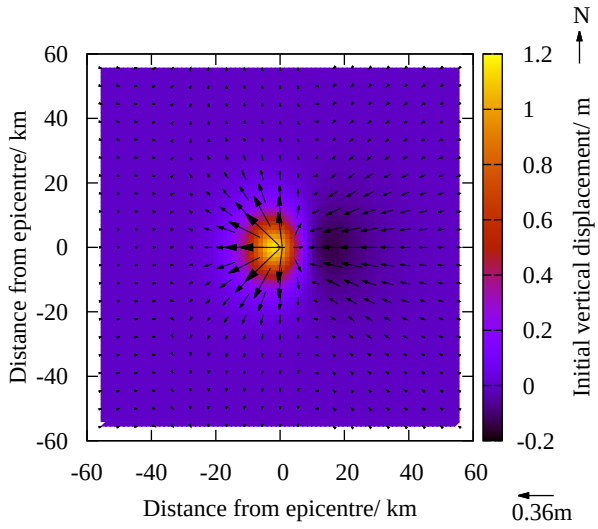

(a) Initial vertical and horizontal displacements

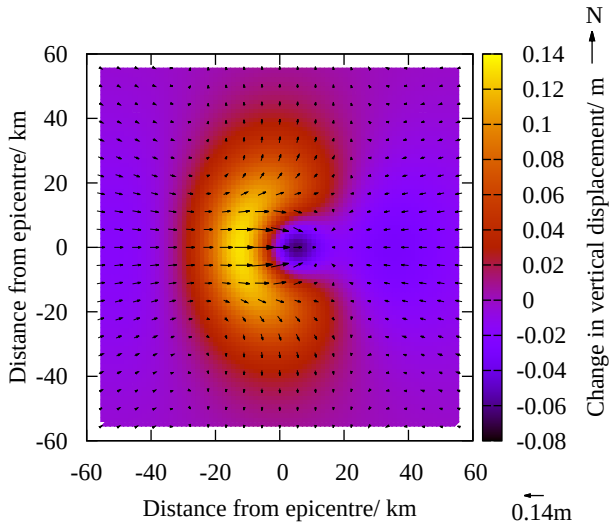

(b) Change from the initial displacements after 20 years

Figure 2.5: The surface displacements due to the dip slip earthquake described in section 2.4.3 at 15 km depth. The initial displacement is shown in (a) and the change from this displacement 20 years after the earthquake in (b). The colour gives the vertical displacement and the arrows show the direction and size of the horizontal displacement.

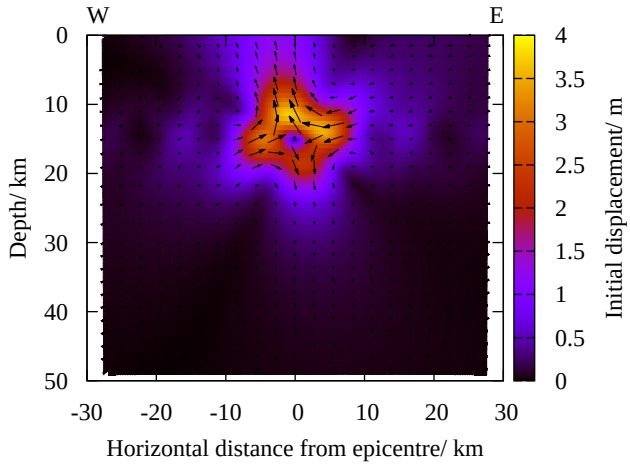

(a) Initial displacement

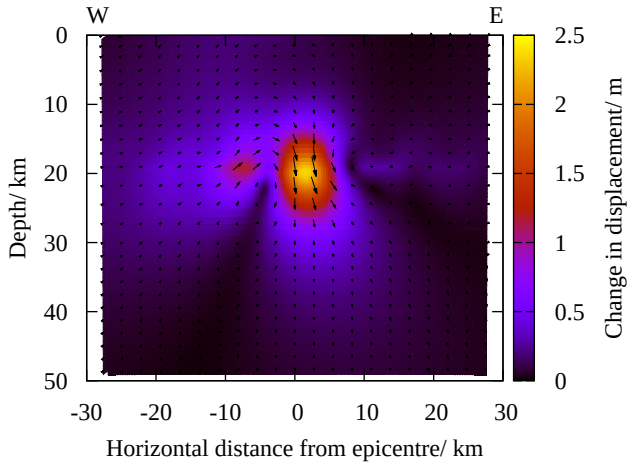

(b) Change from the initial displacement after 20 years

Figure 2.6: The displacements at depth due to the dip slip earthquake described in section 2.4.3 at 15 km depth. The initial displacement is shown in (a) and the change from this displacement 20 years after the earthquake in (b). The colour gives the magnitude of the displacement and the arrows show the direction and relative magnitude of the displacement. There is no displacement perpendicular to the plane of the figures due to the geometry of the earthquake source.

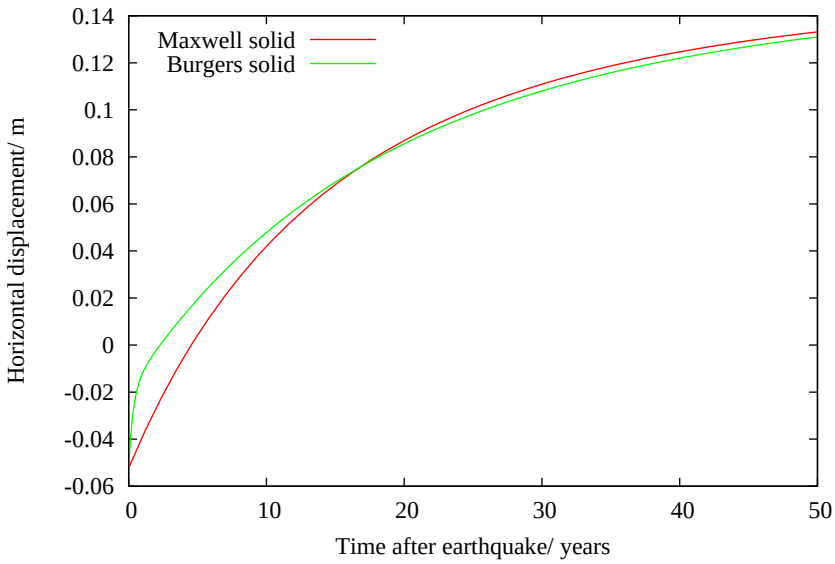

Figure 2.7: The horizontal displacement at the epicentre due to the earthquake described in section 2.4.3, for a Maxwell solid rheology and a Burgers solid rheology. The parameters for the latter are described in section 2.4.6. With the Burgers body, there is a rapid change in displacement initially, due to the short decay time. At long times, as expected, the Burgers body and Maxwell solid exhibit similar behaviour.

Chapter 3

Inverse modelling of post-seismic deformation

3.1 Introduction

In the previous chapter, we discussed how we could model post-seismic deformation in an earth model with a given structure. We will now turn our attention to the inverse problem – using measurements of post-seismic deformation to make inferences about the structure of the Earth.

One of the main difficulties associated with the post-seismic inverse problem is that of non-uniqueness. It is clear that due to the multiple processes contributing to the deformation and the wide variety of rheological structures possible, there will be many scenarios that yield essentially the same surface deformation. As an example of this, Freed *et al.* (2006) lists the variety of mechanisms that have been suggested by different studies to have caused the time-dependent surface deformation after the 1992 Landers earthquake. A variety of combinations of afterslip, poroelastic rebound and different rheological structures were all found to fit the data. This non-uniqueness emphasises the need for evaluating which features of any model obtained are robust.

When performing an inversion from post-seismic data, most studies invert for a very small number of parameters and perform a grid-search to find the best-fitting values of these parameters (e.g., Diao *et al.*, 2014; Huang *et al.*, 2016; Han *et al.*, 2016). This limits the range of models that can be explored, and so raises questions of the physical significance of the features, such as discontinuities, of these models. A wider variety of models could be included by increasing the number of parameters, but this would also increase computation time.

Another approach is to use gradient-based optimisation methods where the gradient of the misfit with respect to model parameters is calculated and used to lower the misfit iteratively (e.g., Nocedal & Wright, 1999). A common way to calculate such gradients is to use finite difference methods, although this can also become computationally unfeasible for large numbers of model parameters. The adjoint method (e.g., Lions, 1970) provides a more efficient way of calculating the gradient, and has been used for a number of geophysical applications (e.g., Bunge *et al.*, 2003; Tromp *et al.*, 2005; Li *et al.*, 2011; Al-Attar & Tromp, 2014). The exact gradient can be calculated with just one solution of the forward problem and one of the corresponding adjoint problem.

In this chapter, we consider the post-seismic inverse problem and present the first application of the adjoint method to this process in order to calculate sensitivity kernels and perform viscosity

inversions. We include illustrative examples calculated with respect to a spherically symmetric earth model with a Maxwell rheology, but, as in the previous chapter, the theory allows for lateral variations as well as transient and non-linear rheologies.

As discussed in section 1.3.3, in order to use the adjoint method we must form the Lagrangian, derive the adjoint equations and derive the form of the sensitivity kernels.

3.2 The Lagrangian

The Lagrangian for the post-seismic problem is

$$L = J(\mathbf{u},\phi)+\int_{t_0}^{t_1}\left\{\mathcal{A}(\dot{\mathbf{u}},\dot{\phi}\mid\mathbf{u}',\phi') - \int_{M_S}\sum_i 2\mu_i\left[\dot{\mathbf{m}}_i:\mathbf{m}_i' + \frac{1}{\tau_i}(\mathbf{d}-\mathbf{m}_i):(\mathbf{d}'-\mathbf{m}_i')\right]\mathrm{d}V - \int_{M_S}\dot{\mathbf{\Gamma}}:\mathbf{e}'\mathrm{d}V\right\}\mathrm{d}t \tag{3.1}$$

where J is the chosen observable and the remaining terms are the time-integrated weak form of the post-seismic problem, as given in equation (2.48) with $\mathcal{A}$ defined as in equation (2.50). We note that we are ignoring any possible explicit dependence of J on a model parameter, which is sufficient for our purposes, but could be trivially included if desired.

3.3 Deriving the adjoint equations

We will now derive the adjoint equations for our post-seismic problem. The solutions to these and the forward equations can then be used to calculate the derivatives needed for the inverse problem.

We find that equation (1.23) simply returns equation (2.48) (with our test functions $\mathbf{u}'$, ϕ' and $\mathbf{m}_i'$ replaced by $\delta\mathbf{u}'$, $\delta\phi'$ and $\delta\mathbf{m}_i'$). Evaluation of equation (1.22) gives

$$\begin{aligned}&\int_{t_0}^{t_1}\left\{\mathcal{A}(\delta\dot{\mathbf{u}},\delta\dot{\phi}\mid\mathbf{u}',\phi') - \int_{M_S}\sum_i 2\mu_i\left[\delta\dot{\mathbf{m}}_i:\mathbf{m}_i' + \frac{1}{\tau_i}(\delta\mathbf{d}-\delta\mathbf{m}_i):(\mathbf{d}'-\mathbf{m}_i')\right]\mathrm{d}V\right\}\mathrm{d}t\\ &+\int_{t_0}^{t_1}\int_{\partial M}(\dot{\mathbf{h}}_{\mathbf{u}}\cdot\delta\mathbf{u}+\dot{h}_\phi\delta\phi)\,\mathrm{d}S\,\mathrm{d}t = 0,\end{aligned} \tag{3.2}$$

where we have written the first-order perturbation of J with respect to $\mathbf{u}$ and ϕ as

$$\delta J = \int_{t_0}^{t_1}\int_{\partial M}(\dot{\mathbf{h}}_{\mathbf{u}}\cdot\delta\mathbf{u}+\dot{h}_\phi\delta\phi)\,\mathrm{d}S\,\mathrm{d}t. \tag{3.3}$$

Here, $\dot{\mathbf{h}}_{\mathbf{u}}$ is the Fréchet kernel of J with respect to $\mathbf{u}$, and $\dot{h}_\phi$ is the Fréchet kernel of J with respect to ϕ. It will now be useful to define the adjoint variables

$$\mathbf{u}^\dagger(t) = \mathbf{u}'(t_1-t+t_0), \tag{3.4}$$

$$\mathbf{m}_i^\dagger(t) = \mathbf{m}_i'(t_1-t+t_0), \tag{3.5}$$

$$\phi^\dagger(t) = \phi'(t_1-t+t_0), \tag{3.6}$$

and adjoint tractions

$$\mathbf{h}_{\mathbf{u}}^{\dagger}(t) = \mathbf{h}_{\mathbf{u}}(t_1 - t + t_0), \tag{3.7}$$

$$h_{\phi}^{\dagger}(t) = h_{\phi}(t_1 - t + t_0). \tag{3.8}$$

Integrating equation (3.2) by parts with respect to time, and using the fact that it must hold for all times, we obtain

$$\mathcal{A}(\delta\mathbf{u}, \delta\phi | \dot{\mathbf{u}}^{\dagger}, \dot{\phi}^{\dagger}) - \int_{M_S} \sum_i 2\mu_i \left[\delta\mathbf{m} : \dot{\mathbf{m}}^{\dagger} + \frac{1}{\tau_i}(\delta\mathbf{d} - \delta\mathbf{m}_i) : (\mathbf{d}^{\dagger} - \mathbf{m}_i^{\dagger}) \right] \mathrm{d}V - \int_{\partial M} (\dot{\mathbf{h}}_{\mathbf{u}}^{\dagger} \cdot \delta\mathbf{u} + \dot{h}_{\phi}^{\dagger} \delta\phi) \, \mathrm{d}S = 0, \tag{3.9}$$

where the forward variables are evaluated at time t whereas the adjoint variables are evaluated at time $t_1 - t + t_0$. The adjoint variables satisfy the initial conditions

$$\mathbf{u}^{\dagger}(\mathbf{x}, 0) = \mathbf{0}, \quad \phi^{\dagger}(\mathbf{x}, 0) = 0, \quad \mathbf{m}_i^{\dagger}(\mathbf{x}, 0) = \mathbf{0}, \tag{3.10}$$

which arise from the requirement that the boundary terms created by integrating by parts to obtain equation (3.9) vanish. This constitutes the weak form of the adjoint problem, where $\delta\mathbf{u}$, $\delta\phi$ and $\delta\mathbf{m}_i$ act as the time-independent test functions. We notice that this equation is identical in form to equation (2.48) with the exception that the force term is now dependent on the form of J through the adjoint tractions $\mathbf{h}_{\mathbf{u}}^{\dagger}$ and $h_{\phi}^{\dagger}$. This means we can use the same numerical code to solve both the forward and adjoint equations.

3.4 Sensitivity kernels

We now wish to use the solutions of the forward and adjoint equations to calculate how J changes in response to a change in a given model parameter. We will first consider the sensitivity of a particular surface measurement to changes in the model parameter and in this case, J will be the chosen measurement. We could, for example, choose J to be the displacement in a given direction at a time t_s and at a point (θ_s, ϕ_s) on the surface and so it will be given by

$$J(\mathbf{u}) = \mathbf{u}(R, \theta_s, \phi_s, t_s) \cdot \hat{\mathbf{d}} = \int_{t_0}^{t_1} \int_{\phi=0}^{2\pi} \int_{\theta=0}^{\pi} \mathbf{u}(R, \theta, \phi) \cdot \hat{\mathbf{d}} \, \frac{\delta(\theta - \theta_s)\delta(\phi - \phi_s)}{\sin\theta} \delta(t - t_s) \, \mathrm{d}\theta \, \mathrm{d}\phi \, \mathrm{d}t, \tag{3.11}$$

where $\hat{\mathbf{d}}$ is the unit vector in the direction of the displacement measurement, R is the radius of the Earth and $t_0 \leq t_s \leq t_1$. The adjoint tractions will therefore be

$$h_{\phi}^{\dagger}(t) = 0, \quad \dot{\mathbf{h}}_{\mathbf{u}}^{\dagger}(t) = \hat{\mathbf{d}} \, \frac{\delta(\theta - \theta_s)\delta(\phi - \phi_s)}{\sin\theta} \delta(t_1 - t + t_0 - t_s). \tag{3.12}$$

Calculation of sensitivity kernels gives insight into what can be learnt about the Earth from individual surface measurements. We will consider such applications further in section 3.4.3. In the following subsections, we will derive the form of the sensitivity kernels for viscosity and the time-dependence of the source, but note that it would be simple to calculate the kernels for other parameters, such as the elastic structure.

3.4.1 Viscosity kernels

When calculating the sensitivity of surface measurements to viscosity, it will be useful to consider relative changes in viscosity. We therefore write the linearised change in $\hat{J}$ as

$$\delta\hat{J} = \int_{M_S} K_{\eta_i} \frac{\delta\eta_i}{\eta_i} \mathrm{d}V, \tag{3.13}$$

where $\eta_i = \mu_i\tau_i$ is the ith component of the viscosity, $\delta\eta_i$ is the change in this component and K_{η_i} is the derivative of $\hat{J}$ with respect to η_i, which is commonly known as the sensitivity kernel. We will consider changes in η_i due to changes in τ_i only, and so assume the elastic structure does not change. Perturbing equation (3.1) with respect to η_i, we find

$$\delta\hat{J} = \int_{t_0}^{t_1} \int_{M_S} \frac{2\mu_i}{\tau_i} [\mathbf{d}(t) - \mathbf{m}_i(t)] : [\mathbf{d}^\dagger(t_1 - t + t_0) - \mathbf{m}_i^\dagger(t_1 - t + t_0)] \frac{\delta\eta_i}{\eta_i} \, \mathrm{d}V \, \mathrm{d}t, \tag{3.14}$$

and so

$$K_{\eta_i} = \int_{t_0}^{t_1} \frac{2\mu_i}{\tau_i} [\mathbf{d}(t) - \mathbf{m}_i(t)] : [\mathbf{d}^\dagger(t_1 - t + t_0) - \mathbf{m}_i^\dagger(t_1 - t + t_0)] \, \mathrm{d}t. \tag{3.15}$$

We note that equation (3.15) gives the sensitivity to the ith component of the viscosity, $\eta_i = \mu_i\tau_i$; however, we can calculate the total viscosity sensitivity kernel by summing the individual contributions.

We can therefore use the solutions of the forward and adjoint equations and equation (3.15) to calculate the sensitivity kernel at all spatial positions in the Earth. However, for some applications, it will also be useful to calculate the sensitivity to viscosity as a function of depth only. We shall denote this radial sensitivity kernel by $\overline{K}_{\eta_i}$ and it is given by

$$\overline{K}_{\eta_i} = \int_{\mathbb{S}^2} r^2 K_{\eta_i} \mathrm{d}S = \int_{t_0}^{t_1} \int_{\mathbb{S}^2} \frac{2\mu_i}{\tau_i} [\mathbf{d}(t) - \mathbf{m}_i(t)] : [\mathbf{d}^\dagger(t_1 - t + t_0) - \mathbf{m}_i^\dagger(t_1 - t + t_0)] \, r^2 \, \mathrm{d}S \, \mathrm{d}t, \tag{3.16}$$

where $\mathbb{S}^2$ is the unit two-sphere.

3.4.2 Stress glut kernels

As the stress glut is a time-dependent quantity, we will define the stress glut sensitivity kernel such that

$$\delta\hat{J} = \int_{t_0}^{t_1} \int_{M_S} K_{\dot{\mathbf{\Gamma}}} : \delta\dot{\mathbf{\Gamma}} \, \mathrm{d}V \, \mathrm{d}t. \tag{3.17}$$

We note that, given the form of equation (3.1), it is preferable to calculate the kernel with respect to $\dot{\mathbf{\Gamma}}$ rather than $\mathbf{\Gamma}$. Perturbing equation (3.1) with respect to $\dot{\mathbf{\Gamma}}$, we find

$$\delta\hat{J} = -\int_{t_0}^{t_1} \int_{M_S} \delta\dot{\mathbf{\Gamma}} : \mathbf{e}^\dagger(t_1 - t + t_0) \, \mathrm{d}V \, \mathrm{d}t, \tag{3.18}$$

and so

$$K_{\dot{\mathbf{\Gamma}}} = -\mathbf{e}^\dagger(t_1 - t + t_0), \tag{3.19}$$

where $\mathbf{e}^\dagger$ is the strain of the adjoint field (c.f. Tromp *et al.* (2005)).

3.4.3 Viscosity inversions

We will now define J to be the misfit between given displacement data and displacements calculated from our forward model. We wish to minimise this misfit in order to find the earth model that provides the best fit to our displacement data. Suppose we have displacement data at N locations on the surface, with these locations given by $\mathbf{x}_i$ for $1 \leq i \leq N$. At each location, there are N_i measurements that each give the displacement at a particular time in a particular direction. Thus u_{ij}^{obs} is the datum for the displacement at location $\mathbf{x}_i$ and time t_{ij} and in direction $\hat{\mathbf{d}}_{ij}$. We can then define the misfit between the displacement data and calculated displacements to be

$$J(\mathbf{u}) = \frac{1}{2}\sum_{i=1}^{N}\sum_{j=1}^{N_i}[\mathbf{u}(\mathbf{x}_i, t_{ij}) \cdot \hat{\mathbf{d}}_{ij} - u_{ij}^{obs}]^2 \tag{3.20}$$

where for simplicity, we ignore potential data errors. We note that we could include regularisation in the inversion by adding a term to J with an explicit dependence on model parameter, but its contribution to the gradient can be calculated directly. Perturbing equation (3.20) with respect to $\mathbf{u}$, we find that the adjoint tractions are

$$h_{\phi}^{\dagger}(t) = 0, \quad \dot{\mathbf{h}}_{\mathbf{u}}^{\dagger}(t) = \sum_{i=1}^{N}\sum_{j=1}^{N_i}\hat{\mathbf{d}}_{ij}[\mathbf{u}(R,\theta,\phi)\cdot\hat{\mathbf{d}}_{ij} - u_{ij}^{obs}]\ \frac{\delta(\theta-\theta_i)\delta(\phi-\phi_i)}{\sin\theta}\delta(t_1 - t + t_0 - t_{ij}). \tag{3.21}$$

We see that the adjoint traction, $\dot{\mathbf{h}}_{\mathbf{u}}^{\dagger}(t)$, in this case is simply the sum of the viscosity kernel tractions for the individual measurements weighted by the difference between the observed and calculated displacements. Therefore, the linearised change in the misfit, J, with viscosity is

$$\delta\hat{J} = \sum_{i=1}^{N}\sum_{j=1}^{N_i}\int_{M_S}[\mathbf{u}(R,\theta,\phi)\cdot\hat{\mathbf{d}}_{ij} - u_{ij}^{obs}]K_{\eta_k}^{ij}\frac{\delta\eta_k}{\eta_k}\ \mathrm{d}V, \tag{3.22}$$

where $K_{\eta_k}^{ij}$ is the kernel associated with the kth viscosity component for a measurement made at location $\mathbf{x}_i$ and at time t_{ij} of the displacement in the direction $\hat{\mathbf{d}}_{ij}$. The gradient of the misfit, g_k, with respect to changes in the kth viscosity component, η_k, is defined such that

$$\delta\hat{J} = \int_{M_S} g_k\ \frac{\delta\eta_k}{\eta_k}\ \mathrm{d}V, \tag{3.23}$$

and so

$$g_k = \sum_{i=1}^{N}\sum_{j=1}^{N_i}[\mathbf{u}(R,\theta,\phi)\cdot\hat{\mathbf{d}}_{ij} - u_{ij}^{obs}]K_{\eta_k}^{ij}. \tag{3.24}$$

We can also write the gradient of the misfit with respect to changes in viscosity as a function of depth only. This will be a function of the radial kernels, $\overline{K}_{\eta_k}^{ij}$, and is given by

$$\overline{g}_k = \sum_{i=1}^{N}\sum_{j=1}^{N_i}[\mathbf{u}(R,\theta,\phi)\cdot\hat{\mathbf{d}}_{ij} - u_{ij}^{obs}]\overline{K}_{\eta_k}^{ij}. \tag{3.25}$$

We can also use the adjoint method to investigate the resolution of a model obtained from a viscosity inversion. We wish to quantify which parts of the model a given measurement, or set of measurements,

can constrain, and how accurately it can do so given a level of uncertainty in our surface measurements. As we have seen, the linearised change in a surface measurement can be related to the change in viscosity, η, through

$$\delta u_i = \int_{I_S} K_i(r) \frac{\delta \eta}{\eta} \mathrm{d}r, \tag{3.26}$$

where u_i is the ith surface measurement with sensitivity kernel K_i, and I_S is the set of radii within solid regions. Here we are assuming a Maxwell solid rheology, but the method could be extended by a generalisation of what follows. We can write this relationship for all measurements as

$$\delta \mathbf{u} = \mathbf{A} \frac{\delta \eta}{\eta}, \tag{3.27}$$

where $\delta \mathbf{u}$ is a vector of all the surface measurements and $\mathbf{A}$ is a linear operator from the model to data space constructed from the sensitivity kernels. Given N measurements, we can calculate a maximum of N model parameters. However, the kernels are not necessarily linearly independent (e.g., Gilbert, 1971). A way to assess what can be resolved is to look at the singular value decomposition of $\mathbf{A}$ (e.g., Parker, 1994). A similar approach has been considered by Pollitz & Thatcher (2010) and Hines & Hetland (2016), and has also been used for post-glacial applications (e.g., Mitrovica & Peltier, 1991).

It can be shown (e.g., Golub & van Loan, 1983) that for any real matrix $\mathbf{A}$, there exist orthogonal matrices, $\mathbf{L}$ and $\mathbf{R}$, such that

$$\mathbf{L}^\dagger \mathbf{A} \mathbf{R} = \mathbf{\Lambda}, \tag{3.28}$$

where $\mathbf{\Lambda}$ is a matrix with diagonal components only. If we let $\boldsymbol{l_i}$ denote the ith column of $\mathbf{L}$ and $\boldsymbol{r}_i$ denote the ith column of $\mathbf{R}$, it is easy to see that

$$\mathbf{A}^\dagger \boldsymbol{l}_i = \lambda_i \boldsymbol{r}_i, \tag{3.29}$$

$$\mathbf{A} \boldsymbol{r}_i = \lambda_i \boldsymbol{l}_i, \tag{3.30}$$

where λ_i is the ith diagonal component of the matrix $\mathbf{\Lambda}$. We say that λ_i, $\boldsymbol{l}_i$ and $\boldsymbol{r}_i$ are the ith singular value, left singular vector and right singular vector of $\mathbf{A}$ respectively. As $\mathbf{L}$ and $\mathbf{R}$ are orthogonal matrices, it is clear that

$$\langle \boldsymbol{l}_i, \boldsymbol{l}_j \rangle = \delta_{ij}, \tag{3.31}$$

$$\langle \boldsymbol{r}_i, \boldsymbol{r}_j \rangle = \delta_{ij}, \tag{3.32}$$

where $\langle \cdot, \cdot \rangle$ are the appropriate inner products. From equations (3.29) and (3.30), we can further see that

$$\mathbf{A}\mathbf{A}^\dagger \boldsymbol{l}_i = \lambda_i^2 \boldsymbol{l}_i, \tag{3.33}$$

$$\mathbf{A}^\dagger \mathbf{A} \boldsymbol{r}_i = \lambda_i^2 \boldsymbol{r}_i. \tag{3.34}$$

In the case described by equation (3.27), each left singular vector will be a vector of length N, the number of surface measurements, whereas each right singular vector will be a continuous function of radius. We will therefore write r_i for the right singular vectors to indicate that they are continuous scalar functions. As $\mathbf{A}\mathbf{A}^\dagger$ is simply a square matrix of dimension N, we can compute its eigenvalues,

λ_i^2, and eigenvectors, $\mathbf{l}_i$, and then calculate the right singular vectors, r_i, using equation (3.29). The $\boldsymbol{l}_i$ will provide an orthonormal basis for the data space, and the r_i provide the corresponding orthonormal basis for a finite-dimensional subspace of the model space. We see that the measurements $\delta\mathbf{u}$ are only affected by relative changes in model that can be spanned by the r_i basis. We can now quantify how well we can constrain each orthogonal part of the model space given by r_i using the combination of data points given in the corresponding $\boldsymbol{l}_i$.

Suppose we have some surface displacement data and used the method described in section 3.5.4 to find a solution to the inverse problem described by this data. Given that there will be errors associated with our data, we can ask how well constrained our model is, i.e., how much we can perturb the model whilst keeping the surface displacements within the error bounds of our data. Let us consider a perturbation of the form

$$\frac{\delta\eta}{\eta} = br_i \tag{3.35}$$

for a particular i, where b is a coefficient determining the size of the perturbation and η is the viscosity structure obtained in the inversion. Using equation (3.30), the corresponding change in surface displacements will be

$$\delta\mathbf{u} = \mathbf{A}br_i = \lambda_i b\boldsymbol{l}_i, \tag{3.36}$$

where $\mathbf{A}$ is a linear operator constructed from the sensitivity kernels calculated with respect to our model, η. If this change in displacements leaves them within the error bounds of our data, then our data is unable to distinguish between the original and perturbed models. Therefore, in order for a given perturbation to be resolvable, the change in displacements must be greater than the error in the displacements. We can denote the errors in the displacement data by the vector $\boldsymbol{\epsilon}$, which we assume has zero mean and known covariance matrix, $\mathbf{C}$, which we recall is defined such that

$$\mathbf{C} = \mathbb{E}[\boldsymbol{\epsilon} \otimes \boldsymbol{\epsilon}], \tag{3.37}$$

where $\mathbb{E}[\cdot]$ is the expectation and $\otimes$ is the tensor product. It then follows that

$$\mathbb{E}[||\boldsymbol{\epsilon}||^2] = \text{tr } \mathbf{C}, \tag{3.38}$$

and so we require

$$||\delta\mathbf{u}|| > \sqrt{\text{tr } \mathbf{C}}, \tag{3.39}$$

for the perturbation to be resolvable. Using equation (3.36), we find that

$$|b| > \frac{\sqrt{\text{tr } \mathbf{C}}}{\lambda_i}. \tag{3.40}$$

We can further use this approach to say how well our model is constrained subject to perturbations of the form br_i. Say, for example, that we wish to know which perturbations we can constrain sufficiently well such that the viscosity at any point in the model cannot change by more than a fraction f. In this case, we require

$$|b|\ |R_i| < f, \tag{3.41}$$

where R_i is the maximum value of the ith right singular value, r_i. Combining this with equation (3.40),

we see that

$$\lambda_i > f^{-1}|R_i|\sqrt{\mathrm{tr}\mathbf{C}}, \tag{3.42}$$

and so for perturbations of the form of equation (3.35), only those with singular values for which equation (3.42) holds are sufficiently constrained.

3.5 Numerical implementation in spherically symmetric earth models

In order to illustrate the inverse problem, we calculate some examples in a spherically symmetric earth model. As described in section 2.4, we expand the fields in generalised spherical harmonics. Expansions of the stress fields and internal variables are as in section 2.4.1. In order to implement the adjoint tractions in equation (3.12), we also require an expansion of the delta function in generalised spherical harmonics; discussion of this expansion for delta functions in the radial direction is given in appendix E of Al-Attar & Tromp (2014) and in the tangential direction in the following section.

3.5.1 Smoothed horizontal delta function in spherical harmonics

We wish to find the expansion in generalised spherical harmonics of a delta function tangential to the surface of the Earth. Without loss of generality, we will define our coordinate system such that the delta function is in the $\hat{\theta}$ direction. In this case

$$\mathbf{u}(\theta,\phi) = \frac{\delta(\theta-\theta')\delta(\phi-\phi')}{\sin\theta}\hat{\theta}, \tag{3.43}$$

or, in the canonical basis,

$$\mathbf{u}(\theta,\phi) = \frac{\delta(\theta-\theta')\delta(\phi-\phi')}{\sin\theta}\ \frac{(\hat{\mathbf{e}}_- - \hat{\mathbf{e}}_+)}{\sqrt{2}}. \tag{3.44}$$

We now wish to find the coefficients a_{lm} and b_{lm} such that

$$\mathbf{u}(\theta,\phi) = \sum_{l,m}(a_{lm}Y^+_{lm}\hat{\mathbf{e}}_+ + b_{lm}Y^-_{lm}\hat{\mathbf{e}}_-). \tag{3.45}$$

Integrating this over the unit two-sphere with Y^{+*}_{lm} and Y^{-*}_{lm} in turn, we find that

$$a_{lm} = -Y^{+*}_{lm}(\theta',\phi'), \tag{3.46}$$

$$b_{lm} = Y^{-*}_{lm}(\theta',\phi'). \tag{3.47}$$

If we define our coordinate system such that $\theta' = \phi' = 0$, the coefficients become

$$a_{l,1} = -\left(\frac{2l+1}{4\pi}\right)^{1/2}, \tag{3.48}$$

$$b_{l,-1} = \left(\frac{2l+1}{4\pi}\right)^{1/2}, \tag{3.49}$$

and are equal to zero for all other values of m. Therefore,

$$\frac{\delta(\theta)\delta(\phi)}{\sin\theta}\hat{\theta} = \sum_{l=0}^{\infty}\left(\frac{2l+1}{4\pi}\right)^{1/2}[Y^{-}_{l,-1}(\theta,\phi)\hat{\mathbf{e}}_{-} - Y^{+}_{l,1}(\theta,\phi)\hat{\mathbf{e}}_{+}]. \tag{3.50}$$

In practice, we cannot sum to infinite l and so would have to truncate the sum in equation (3.50). However, this will lead to ringing. Therefore, we instead expand the smoothed delta function as

$$\frac{\delta(\theta)\delta(\phi)}{\sin\theta}\hat{\theta} \approx \sum_{l=0}^{l_{max}}\left(\frac{2l+1}{4\pi}\right)^{1/2}\exp\left(-2\pi\frac{l+1}{L+\frac{1}{2}}\right)[Y^{-}_{l,-1}(\theta,\phi)\hat{\mathbf{e}}_{-} - Y^{+}_{l,1}(\theta,\phi)\hat{\mathbf{e}}_{+}], \tag{3.51}$$

where L determines its width.

3.5.2 Laterally varying viscosity kernels

In order to calculate laterally varying kernels in a spherically symmetric earth model, we must

1. solve the forward equations given by (2.48) to calculate the spherical harmonic coefficients of the forward displacement field, U_{lm}, V_{lm} and W_{lm}, and of the internal variables, $\mathbf{m}_i$;

2. solve the adjoint equations given by (3.9), with adjoint tractions from equation (3.12), to calculate the spherical harmonic coefficients of the adjoint displacement field, $U^{\dagger}_{lm}$, $V^{\dagger}_{lm}$ and $W^{\dagger}_{lm}$, and of the internal variables, $\mathbf{m}^{\dagger}_i$;

3. calculate the spherical harmonic coefficients of the strain fields, $\mathbf{d}$ and $\mathbf{d}^{\dagger}$;

4. calculate the spatial dependence of $\mathbf{d}$, $\mathbf{d}^{\dagger}$, $\mathbf{m}_i$ and $\mathbf{m}^{\dagger}_i$ by expanding the spherical harmonic representation;

5. calculate the sensitivity kernel using equation (3.15).

We calculate both the forward and adjoint fields in coordinate systems defined such that their respective sources are at the North Pole. This greatly increases computational efficiency as the spherical harmonic coefficients are non-zero only for particular values of m. (For the forward fields, the coefficients are non-zero for $-2 \leq m \leq 2$ whereas for the adjoint fields, they are non-zero for $-1 \leq m \leq 1$ as the adjoint source is a vector quantity for point measurements.) The spatial dependence of the two fields is calculated using the angles between the actual locations of the sources and the North Pole.

For the source and Earth structure described in section 2.4.3, we plot the kernel for two different displacements 20 years after the earthquake – the vertical displacement at the epicentre (figure 3.1) and the displacement to the east at a point 0.1° west of the epicentre (figure 3.2).

3.5.3 Radial viscosity kernels

In order to calculate the radial kernel in a spherically symmetric earth model, we can write equation (3.16) using the generalised spherical harmonics. Using the expansions of $\mathbf{d}$ and $\mathbf{m}_i$ given by equations (2.63) – (2.66) and (2.67) – (2.70) respectively, and making use of the identity (2.83), we

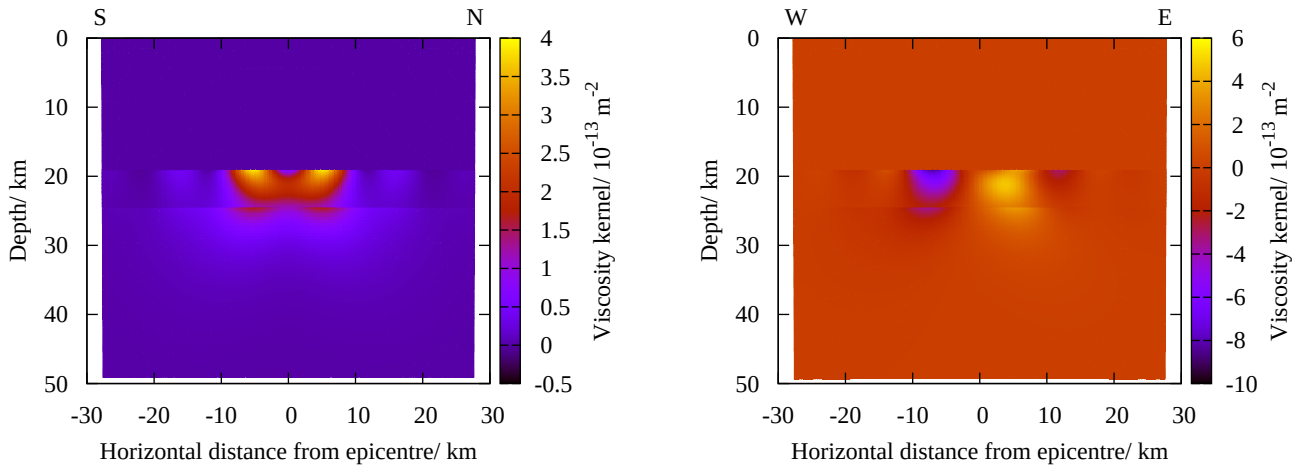

(a) Kernel for varying latitude

(b) Kernel for varying longitude

Figure 3.1: The laterally varying viscosity kernel, given by equation (3.15), for the vertical displacement at the epicentre, 20 years after the earthquake. The earthquake source and earth structure are as described in section 2.4.3. The value of the kernel is shown for (a) varying latitude and (b) varying longitude.

find that

$$\begin{aligned}\overline{K}_{\eta_i} = \int_{t_0}^{t_1} \sum_{l,m} \Bigg[&\frac{k^2}{2}(k^2-2)(V_{lm}-M_{ilm})(V_{lm}^\dagger - M_{ilm}^\dagger) + \frac{k^2}{2}(k^2-2)(W_{lm}-N_{ilm})(W_{lm}^\dagger - N_{ilm}^\dagger) \\ &+\frac{k^2}{2}(r\partial_r V_{lm} - V_{lm} + U_{lm} - S_{ilm})(r\partial_r V_{lm}^\dagger - V_{lm}^\dagger + U_{lm}^\dagger - S_{ilm}^\dagger) \\ &+\frac{k^2}{2}(r\partial_r W_{lm} - W_{lm} - T_{ilm})(r\partial_r W_{lm}^\dagger - W_{lm}^\dagger - T_{ilm}^\dagger) \\ &+\frac{2}{3}(r\partial_r U_{lm} - U_{lm} + \frac{k^2}{2}V_{lm} - R_{ilm})(r\partial_r U_{lm}^\dagger - U_{lm}^\dagger + \frac{k^2}{2}V_{lm}^\dagger - R_{ilm}^\dagger)\Bigg] \, \mathrm{d}t. \end{aligned} \tag{3.52}$$

We see that in order to calculate the radial kernel, we must

1. solve the forward equations given by (2.48) to calculate the spherical harmonic coefficients of the forward displacement field, U_{lm}, V_{lm} and W_{lm}, and of the internal variables, $\mathbf{m}_i$;

2. solve the adjoint equations given by (3.9), with adjoint tractions from equation (3.12), to calculate the spherical harmonic coefficients of the adjoint displacement field, $U_{lm}^\dagger$, $V_{lm}^\dagger$ and $W_{lm}^\dagger$, and of the internal variables, $\mathbf{m}_i^\dagger$;

3. calculate the spherical harmonic coefficients of the strain fields, $\mathbf{d}$ and $\mathbf{d}^\dagger$;

4. calculate the sensitivity kernel using equation (3.52).

In contrast to the calculation of laterally varying kernels, we require the spherical harmonic coefficients to be defined relative to the same coordinate system. We choose the coordinate system to be that which places the adjoint source at the North Pole, as this minimises the number of m values for which the spherical harmonic coefficients are non-zero. This is similar to the method used by Nissen-Meyer *et al.* (2007) for calculating seismic kernels in an axisymmetric setting.

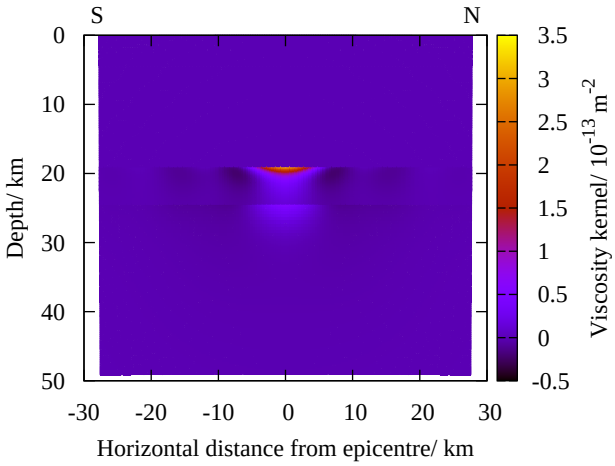

(a) Kernel for varying latitude

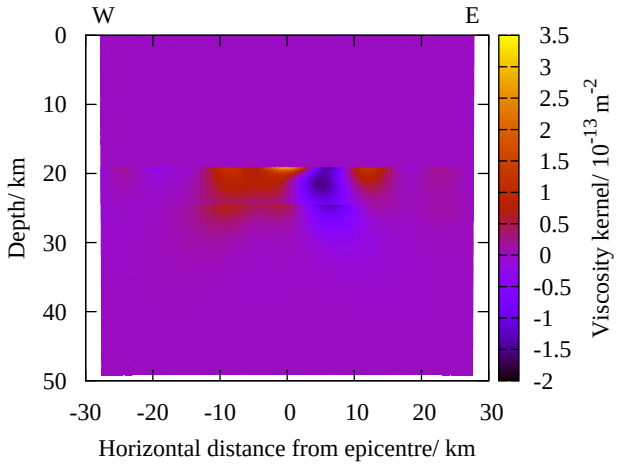

(b) Kernel for varying longitude

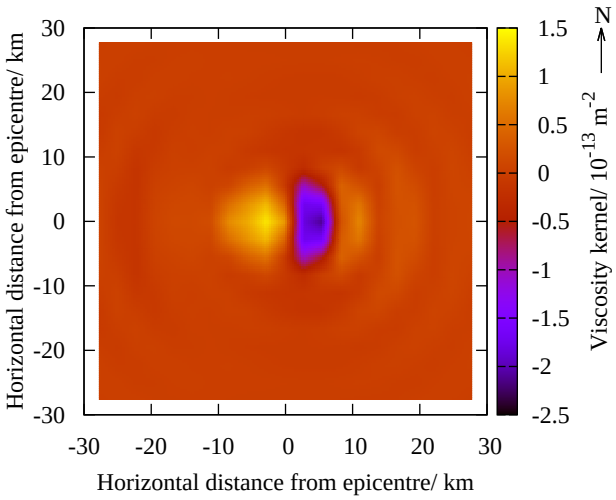

(c) Kernel for a horizontal slice through the Earth at a depth of 21 km.

Figure 3.2: The laterally varying viscosity kernel, given by equation (3.15), for the displacement to the east, 0.1° (≈ 11 km) west of the epicentre, 20 years after the earthquake. The earthquake source and earth structure are as described in section 2.4.3. The value of the kernel is shown for (a) varying latitude, (b) varying longitude and (c) variation in both latitude and longitude at a depth of 21 km.

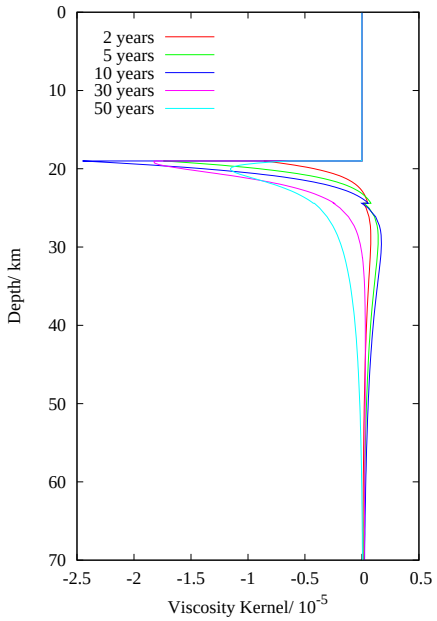

(a) Radial viscosity kernels for the vertical displacement

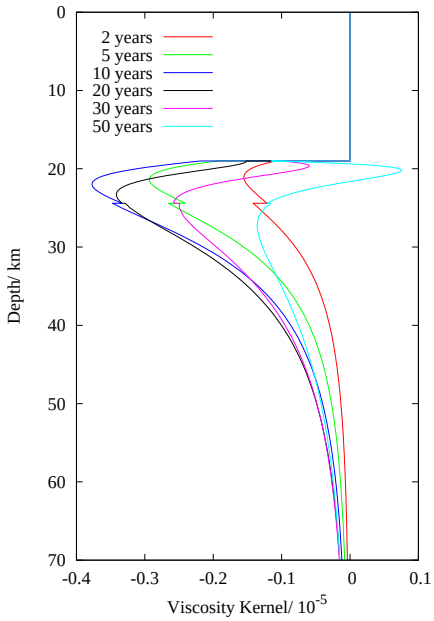

(b) Radial viscosity kernels for the displacement in the ϕ direction (to the east)

Figure 3.3: The radial viscosity kernels, given by equation (3.16), for the displacement at different times at the epicentre of the earthquake. The earthquake source and earth structure are as described in section 2.4.3. The kernels shown are for (a) the vertical displacement and (b) the displacement to the east.

In figures 3.3 and 3.4, we show several examples of radial sensitivity kernels for the earthquake source and earth structure described in section 2.4.3. Figure 3.3 shows the kernels for vertical and horizontal displacements at multiple times at the epicentre. Figure 3.4 shows the kernels for the vertical and horizontal displacements at varying locations 20 years after the earthquake.

In order to emphasise that the kernels give the linearised sensitivity of a particular measurement to change in viscosity, we compare the changes in displacement predicted by the kernel to the actual changes in displacement due to viscosity perturbations of different magnitudes. This comparison is shown in figure 3.5. We can see that the actual change in displacement is close to the linear kernel prediction for perturbations of up to approximately an order of magnitude, and that above this, the kernel is still of the correct sign, which is important for carrying out a gradient-based inversion. The linearised nature of the kernel is further shown by the dependence of the kernel on the viscosity model used to calculate it, as illustrated in figure 3.6.

3.5.4 Viscosity inversions

Given surface displacement data, we wish to find a radial viscosity profile that fits the data to within error. We can again use generalised spherical harmonics to expand the fields as described in section 2.4.3. In order to perform an inversion, we

1. calculate the surface displacements for some initial model at the locations where there are data measurements, and calculate the misfit using equation (3.20);

2. calculate the radial sensitivity kernels for each measurement, as described in section 3.5.3;

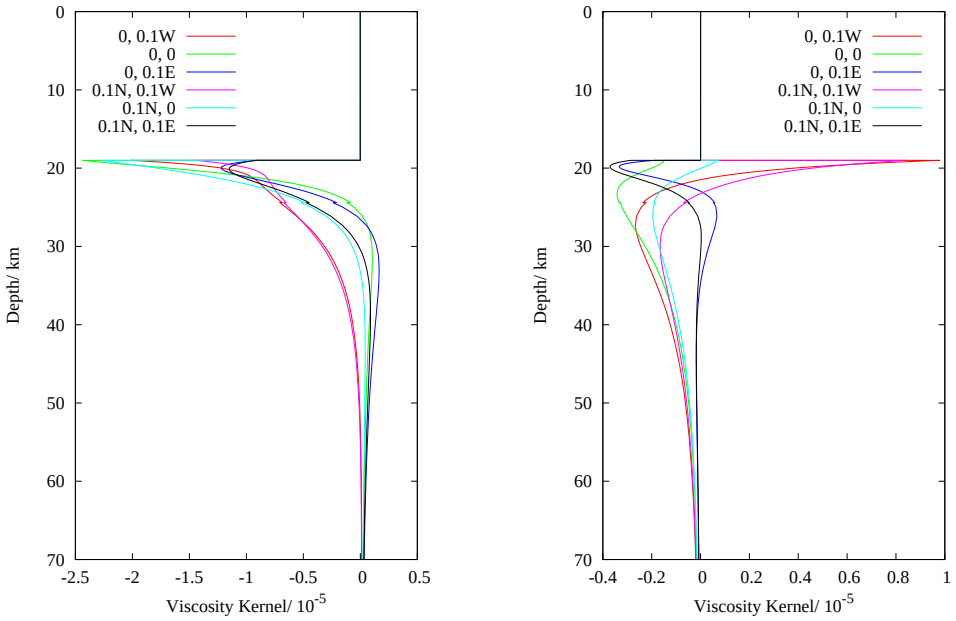

(a) Radial viscosity kernels for the vertical displacement

(b) Radial viscosity kernels for the displacement in the ϕ direction (to the east)

Figure 3.4: The radial viscosity kernels, given by equation (3.16), for the displacement at varying locations, 20 years after the earthquake. The earthquake source and earth structure are as described in section 2.4.3. The labels give the locations of the displacements in degrees relative to the epicentre of the earthquake. The kernels shown are for (a) the vertical displacement and (b) the displacement to the east. The spatial dependence of the surface displacement at this time for this earthquake is as shown in figure 2.5.

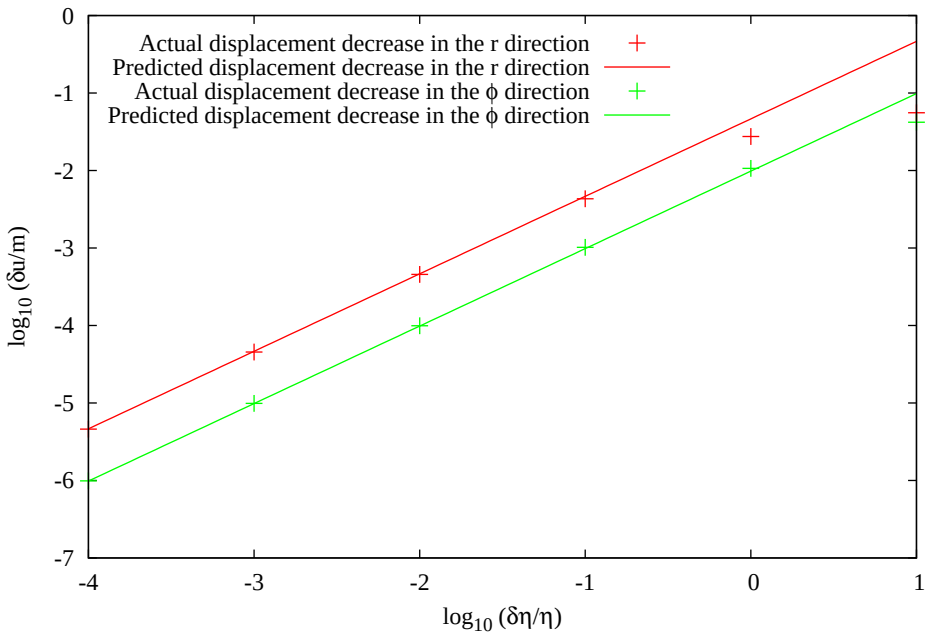

Figure 3.5: Comparison of the change in displacements predicted by the sensitivity kernels to the actual changes due to viscosity perturbations of different magnitudes between 19 km and 30 km depth. The displacement in the r direction is at the epicentre, whereas the displacement in the ϕ direction is 0.1° west of the epicentre. Both are the displacements 20 years after the earthquake. The lines show the decrease in displacements predicted by the kernels whereas the crosses shown the actual decrease in displacements.

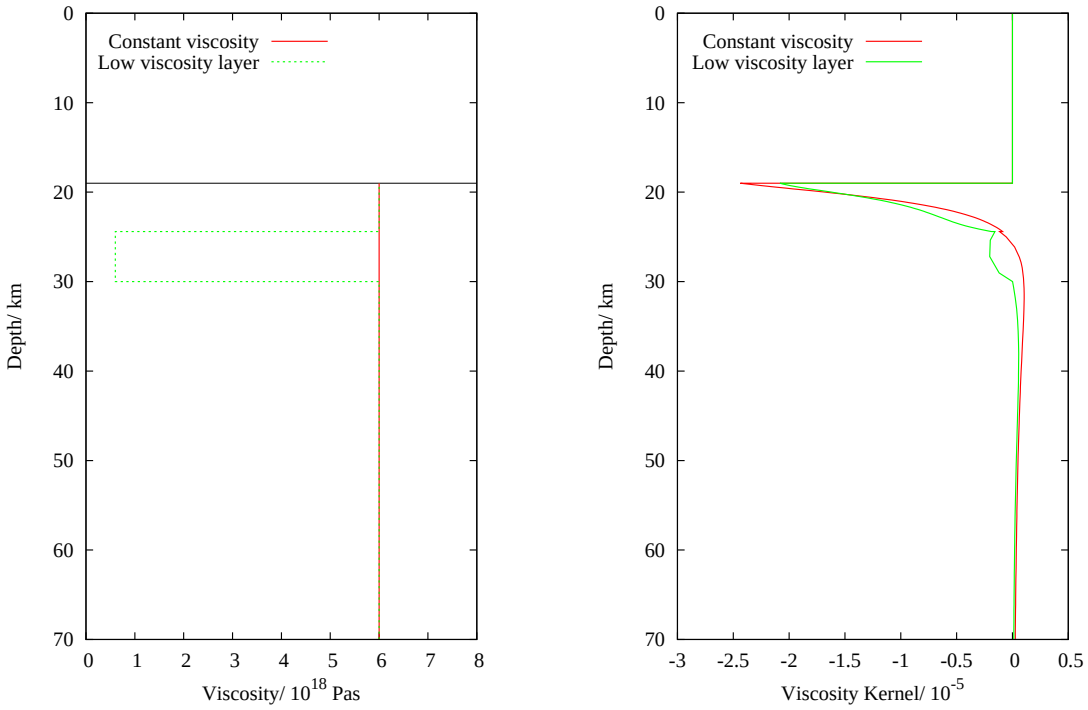

(a) Two different viscosity structures for which the kernels in (b) were calculated

(b) Radial viscosity kernels for the same measurement with two different viscosity structures

Figure 3.6: An example of the dependence of the sensitivity kernel on the background model used. The radial viscosity kernels, shown in (b), for the vertical displacement at the epicentre 20 years after the earthquake were calculated with the two different background models in (a).

3. calculate the gradient of the misfit function by evaluating the weighted sum of radial kernels given in equation (3.25);

4. calculate a model update using, for example, the conjugate gradient method (see section 1.3.4);

5. repeat steps 1 to 4 until the value of the misfit fails to decrease by some suitable amount.

In order to minimise the number of calculations required, and hence improve the computational efficiency, the adjoint equations are solved only twice at each iteration – once with a vertical traction and once with a horizontal. The location and orientation of the earthquake are then defined relative to the adjoint traction for each kernel calculation.

For several models, we have calculated synthetic data for the earthquake source described in section 2.4.3, and then inverted for viscosity structure using the method detailed above. The locations, times and directions of the displacement data used are shown in Table 3.1. Unless otherwise stated, the model chosen to begin the inversion was that described in section 2.4.3. Several examples of the actual viscosity structures and results of the inversions are shown in figures 3.7 to 3.10, along with the corresponding displacement misfits, given by equation (3.20), and viscosity misfits where appropriate. The viscosity misfit after the ith iteration of the inversion is defined to be

$$\frac{1}{2}\int_{r_1}^{r_2}[\eta_{act}(r)-\eta_i(r)]^2\,\mathrm{d}r, \tag{3.53}$$

where r_1 is the radius of the base of the mantle, r_2 is the radius of the top of the mantle, η_{act} is the actual viscosity and η_i is the viscosity obtained from the inversion after the ith iteration.

Firstly, we observe that the final models obtained in the cases shown in figure 3.7 are similar, and that both have a small final displacement misfit, despite one model having a discontinuous change in viscosity and one having a continuous change which occurs over approximately 10 km. We therefore conclude that, in this case, our data are unable to resolve sharp changes in viscosity, which is perhaps unsurprising given the physics of viscoelastic relaxation.

We have also investigated the ability of the data to resolve a discontinuous change in viscosity at different depths. In figure 3.8, we show the results of an inversion using synthetic data generated from a viscosity structure which jumps from 1.2×10^{19} Pa s to 6×10^{18} Pa s at three different depths - 30 km, 40 km and 50 km. We see that there is a substantial difference in the inverted viscosities in the case of the 30 km and 40 km discontinuities, and both have a low viscosity misfit. However, the inverted viscosity in the case of the 50 km discontinuity is very similar to that of the 40 km discontinuity, and has a significantly higher viscosity misfit, despite all three models having a very low displacement misfit (4.1×10^{-6} m^2, 1.2×10^{-5} m^2 and 7.0×10^{-5} m^2 for the 30 km, 40 km and 50 km discontinuities respectively, the largest of which corresponds to an average error per measurement of about 2 mm). We therefore conclude that in this case, the data struggles to resolve a change in viscosity at a depth of 50 km. This makes sense given the form of the sensitivity kernels in figures 3.3 and 3.4, as the kernels are very small in magnitude at depths of 50 km and below.

In order to illustrate the dependence of the inversion results on the initial viscosity structure chosen, we have performed an inversion for the same viscous structure using two different starting models, as shown in figure 3.9. It can be seen that the final viscosity structures in the two cases are very different, despite convergence having occurred as the misfit is roughly constant for the last few iterations. The misfit in one case is noticeably higher, which suggests the inversion has found a local misfit minimum.

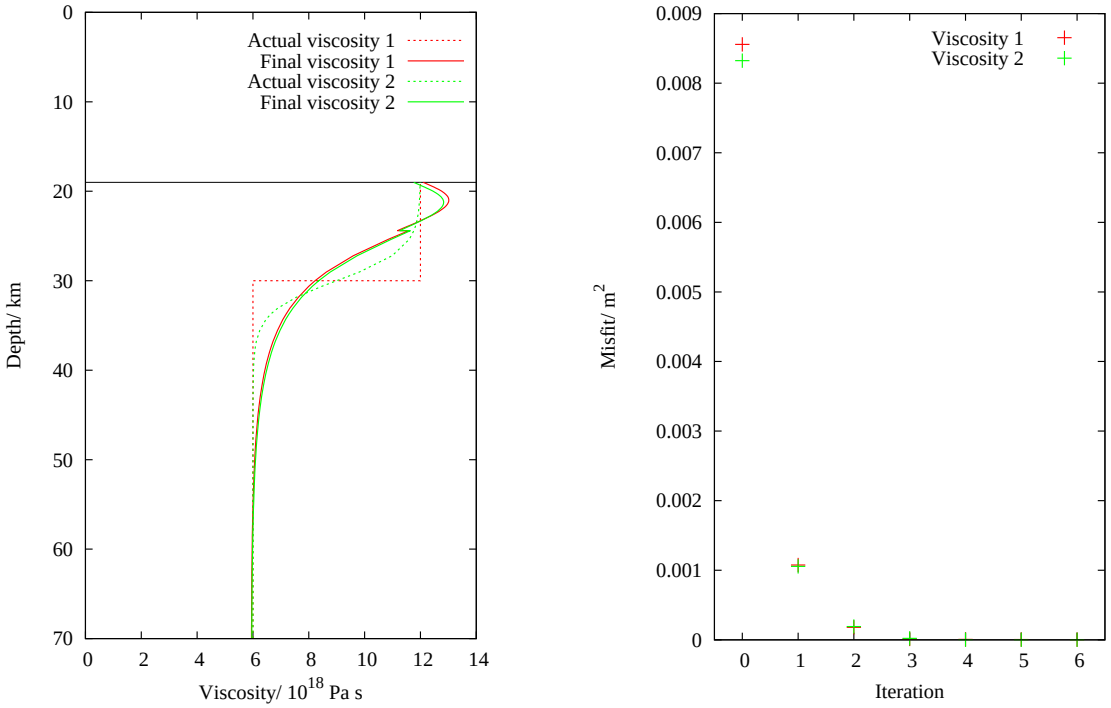

(a) Actual and final viscosities

(b) Displacement misfits

Figure 3.7: Viscosity inversions using synthetic data generated from a structure with a discontinuous change in viscosity and a continuous change occurring over approximately 10 km. The actual viscosities used to generate the synthetic data and final inverted viscosities are shown in (a), the former using dotted lines and the latter using solid lines of the same colour. The corresponding displacement misfits, given by equation (3.20), at each iteration of the inversion are shown in (b). The earthquake source and starting structure for the inversion are as described in section 2.4.3.

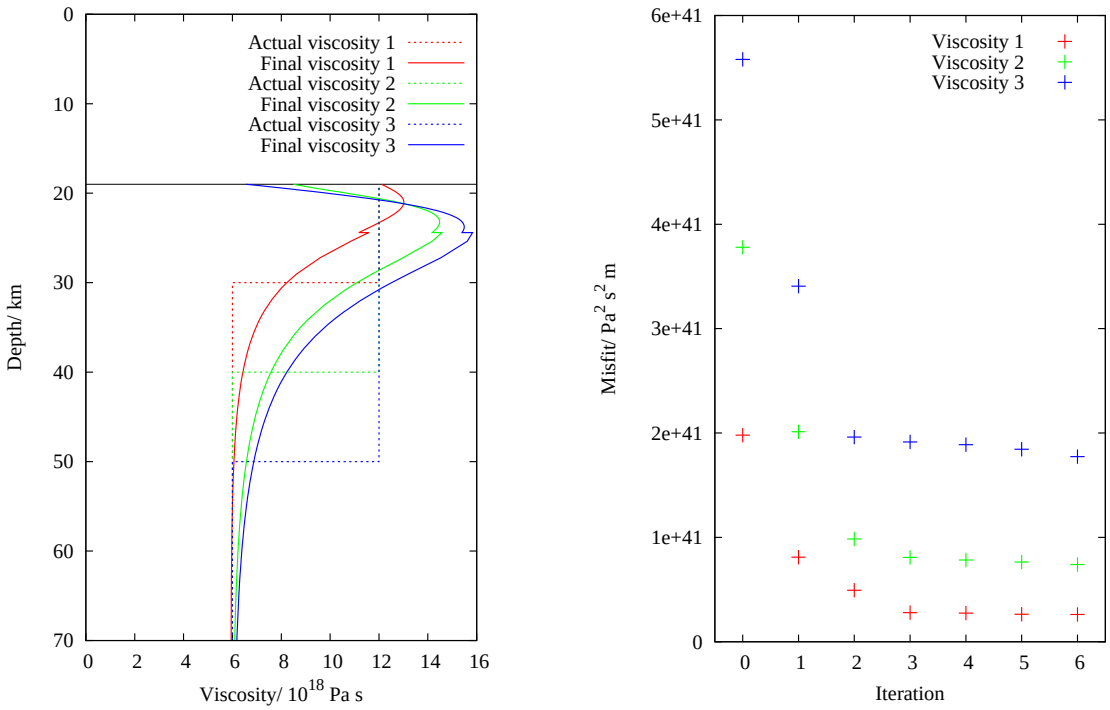

(a) Actual and final viscosities

(b) Viscosity misfits

Figure 3.8: Viscosity inversions with a viscosity discontinuity at different depths. The actual viscosities used to generate the synthetic data and the final inverted viscosities are shown in (a), the former using dotted lines and the latter using solid lines of the same colour. The corresponding viscosity misfits, given by equation (3.53), at each iteration of the inversion are shown in (b). The earthquake source and starting structure for the inversion are as described in section 2.4.3.

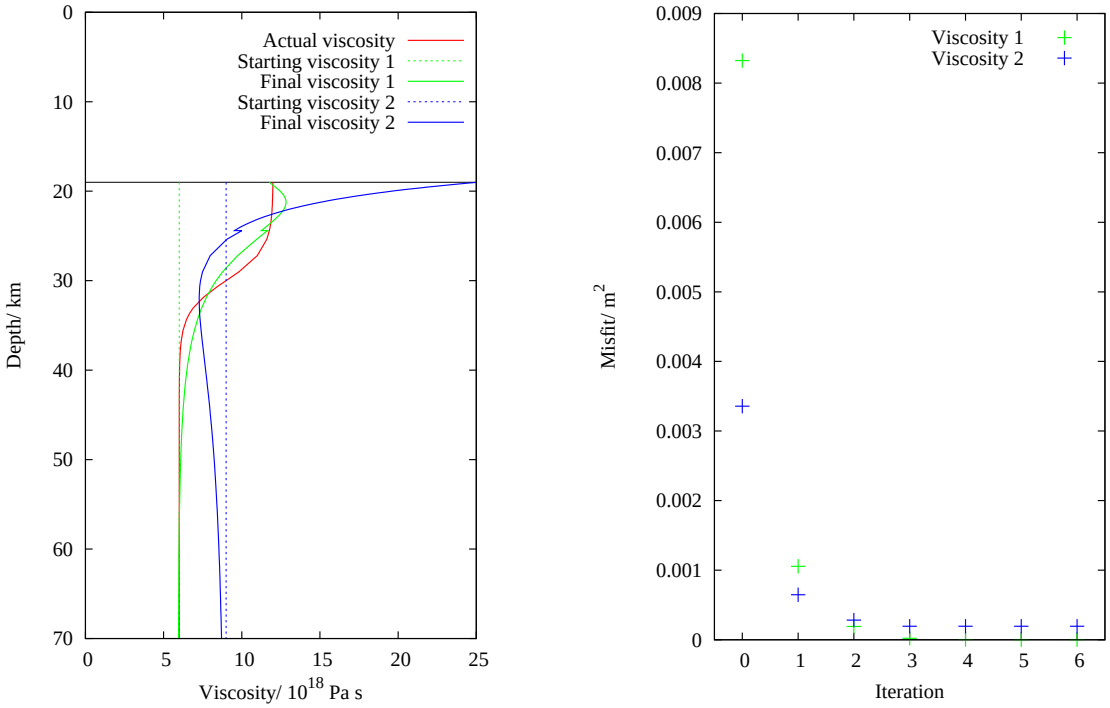

(a) Actual, starting and final viscosities

(b) Displacement misfits

Figure 3.9: Viscosity inversions using the same synthetic data but two different starting models. The actual viscosity used to generate the synthetic data, along with the starting viscosities and final viscosities in the two cases are shown in (a), the former using dotted lines and the latter using solid lines of the same colour. The corresponding displacement misfits, given by equation (3.20), in the two cases are shown in (b). The earthquake source is as described in section 2.4.3.

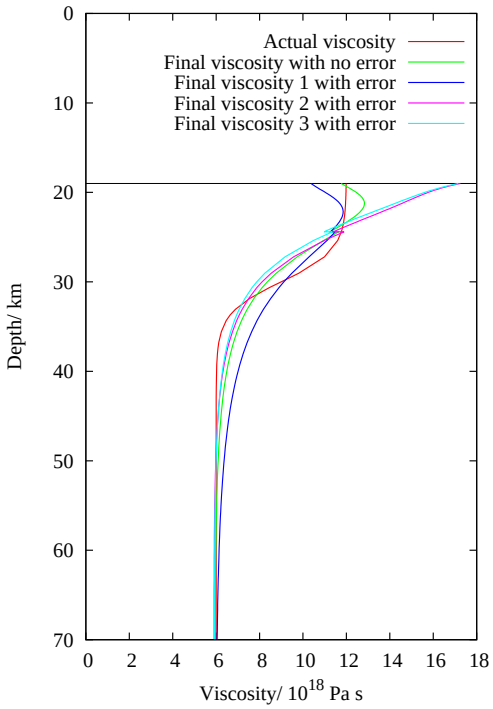

(a) Actual and final viscosities

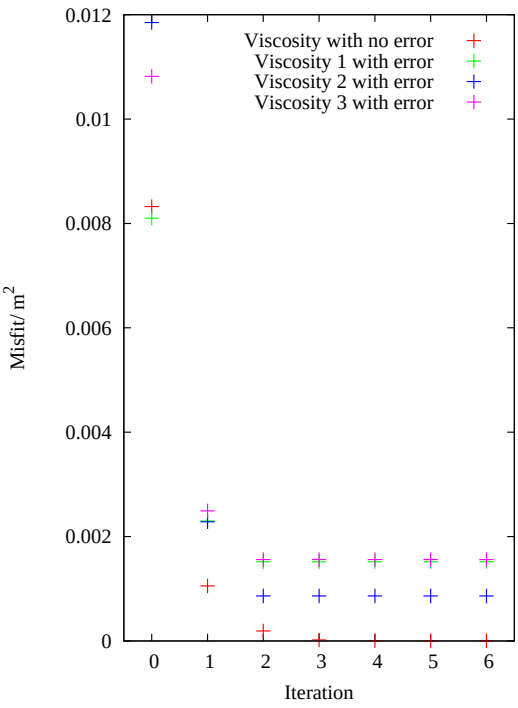

(b) Displacement misfits

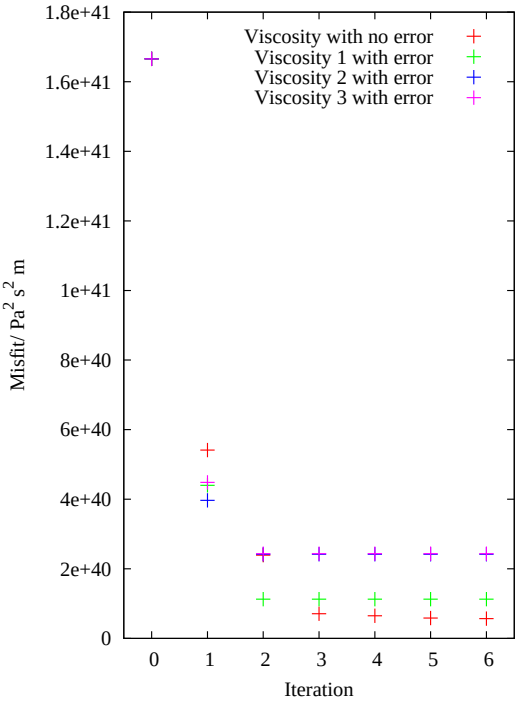

(c) Viscosity misfits

Figure 3.10: The effect on viscosity inversions of adding errors to the synthetic data. The actual viscosity and result of the inversion using the synthetic data is shown in (a) along with three inversions where the synthetic data have had random errors added from a normal distribution with a standard deviation of 1 cm. The corresponding (b) displacement misfits, given by equation (3.20), and (c) viscosity misfits, given by equation (3.53), are also shown. The earthquake source and starting structure for the inversion are as described in section 2.4.3.

Table 3.1: The locations (relative to the epicentre), times and directions of displacements used in carrying out the viscosity inversions. The displacements to the north are not used for the locations at 0° latitude as these displacements are zero due to the geometry of the source.

Latitude/ °	Longitude/ °	Directions	Times/ years
0.0	-0.1	E, z	10, 20
0.0	0.0	E, z	10, 20
0.0	0.1	E, z	10, 20
0.1	-0.1	N, E, z	10, 20
0.1	0.0	N, E, z	10, 20
0.1	0.1	N, E, z	10, 20

Despite this, the misfits in both cases are still low enough to be virtually indistinguishable, particularly given a reasonable level of uncertainty in any real surface displacements. However, we also notice that in one case, the viscosity change is very steep just below the elastic layer. Such a structure may be considered to be unphysical, and so the inversion could be improved by adding a regularisation term.

All the inversions discussed above have used synthetic data with no errors. In practice, the data will not be error free and so we have investigated the effect of errors on a particular inversion. Having generated synthetic data for the model shown by the green dotted line in figure 3.7a, we added random errors from a normal distribution with a standard deviation of 1 cm. In figure 3.10, the results for three inversions with different random errors selected from this distribution are shown. We see that the inclusion of errors results in model structures with higher viscosity misfits, although the difference is not obviously significant. Furthermore, we see that the final viscosity with the lowest displacement misfit of the three with data errors does not have the lowest viscosity misfit. As mentioned previously, adding a regularisation term could also improve these inversions.

In this section, we have investigated a variety of viscosity inversions using post-seismic data. However, these examples are intended to illustrate the potential of the adjoint method and not necessarily to demonstrate exactly how an inversion could be carried out. We note in particular the dependence of the inversion results on the initial structure chosen as shown in figure 3.9, and the possibility for adding regularisation to the inversion. We further emphasise that care must be taken in the interpretation of the inverted viscosity profile, particularly in the case of data errors, and will now illustrate the resolution analysis considered in section 3.4.3 with an example.

We will consider the resolution of the example inversion in dark blue in figure 3.10. We can calculate the sensitivity kernels for each of the surface measurements in Table 3.1 for the final model obtained in this inversion and so construct the matrix $\mathbf{A}$ and calculate the matrix $\mathbf{A}\mathbf{A}^\dagger$. From equation (3.33), we can see that the eigenvalues of this matrix will be the singular values squared and the eigenvectors will be the left singular values. Using equation (3.29), we can then calculate the right singular vectors. The λ_i are shown in figure 3.11 in order of decreasing magnitude and the right singular vectors with the four largest singular values are shown in figure 3.12. We see that the best constrained right singular vector (i.e., the one with the largest singular value) has its maximum amplitude at the top of the viscoelastic region and the amplitude decays as depth increases. Furthermore, as the singular value decreases, the associated right singular vector has a greater number of oscillations.

Let us assume, for example, that the standard deviation of the error in each surface measurement is 1 cm, and that the errors are uncorrelated. The trace of the covariance matrix will then simply be $0.01\sqrt{30} \approx 0.05$ as there are 30 displacement measurements. From figure 3.12, we can see that

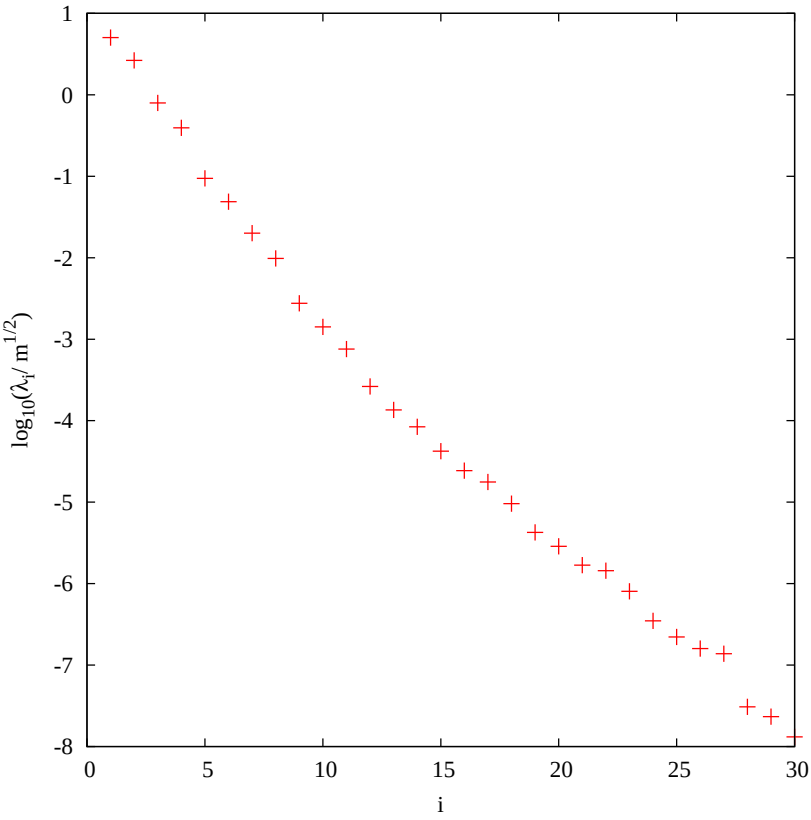

Figure 3.11: The singular values in order of decreasing magnitude of the matrix **A** whose rows are given by the sensitivity kernels calculated for the measurements in Table 3.1 with respect to the final viscosity structure shown in dark blue in figure 3.10.

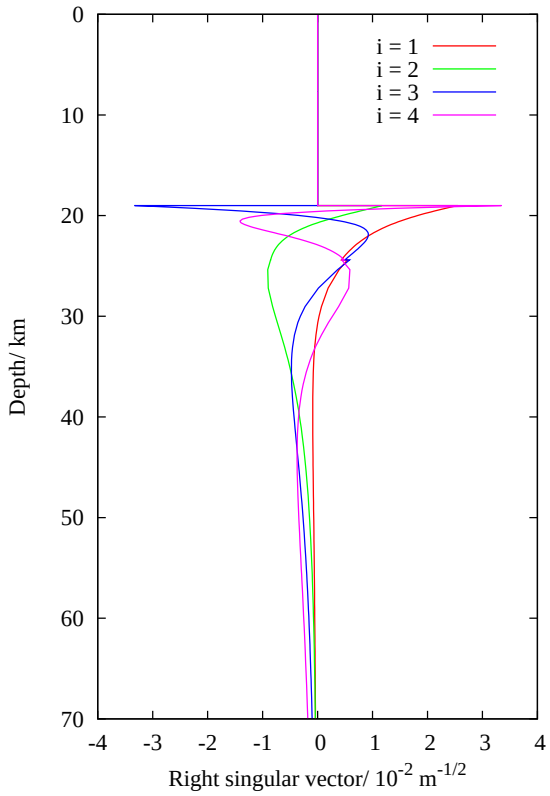

Figure 3.12: The right singular vectors, r_i, with the four highest singular values, of the matrix **A** whose rows are given by the sensitivity kernels calculated for the measurements in Table 3.1 with respect to the final viscosity structure shown in dark blue in figure 3.10.

$R_i \approx 0.03m^{-1/2}$. If we wish to find which perturbations we can constrain such that the viscosity at any point varies by up to 10%, we find from equation (3.42) that

$$\lambda_i > 0.015, \tag{3.54}$$

and so, by examining figure 3.11, we can say our model is resolved to within 10% subject to perturbations of the form of one of the right singular vectors with the seven largest singular values.

3.6 Conclusion

In this chapter, the adjoint method has been applied to the post-seismic deformation inverse problem for the first time. This enables efficient calculation of derivatives of measurements of the deformation with respect to model parameters which, for this process, are the rheological structure of the Earth and the earthquake forcing. Such derivatives have many applications, some of which are illustrated here with further possibilities discussed in chapter 6. Numerical examples are presented in models with a spherically symmetric background structure, but the theory is valid in models with continuous lateral variations.

Chapter 4

Forward modelling of post-glacial deformation

4.1 Introduction

Over glacial cycles, sea level varies in both space and time due to the melting of ice sheets. The way in which the Earth responds to such a change in surface load depends on the details of the ice sheet history and also the structure of the Earth – in particular, its viscosity structure. It is therefore possible to use measurements of the response, known as glacial isostatic adjustment (GIA), to learn about both of these aspects, and there have been many such studies, from Haskell (1935) to more recent work (e.g., Nakada & Lambeck, 1989; Mitrovica, 1996; Lambeck *et al.*, 1998; Peltier, 2004; Argus *et al.*, 2012; Nakada *et al.*, 2015; Lau *et al.*, 2016).

In order to use measurements of GIA in this way, forward modelling must first be considered, where, given an ice history and earth model, the response of the Earth is calculated. We require a method of calculating the viscoelastic deformation of the Earth due to changes in ice load that includes a number of effects. Firstly, the deformation must be coupled to sea level. A changing ice distribution will lead to a changing water distribution, and the deformation associated with this redistribution will alter the shape of the two surfaces that bound sea level – the solid surface of the Earth and the gravitational equipotential surface that defines the sea surface. The impact of the Earth's rotation must also be considered. The evolving surface mass load will perturb the Earth's moment of inertia both by the direct effect of mass redistribution and by the deformation driven by this redistribution. Therefore, the Earth's rotation rate will change in order to conserve the total angular momentum of the system. Such a change will result in deformation in both bounding surfaces of sea level. We therefore require a gravitationally and rotationally self-consistent way of modelling sea level change. It has also been shown that it is important to include the effects of shoreline migration in order to model GIA accurately (e.g., Mitrovica & Milne, 2003). Most studies of GIA solve the forward problem through use of the so-called sea level equation, which was introduced by Farrell & Clark (1976) with further developments by a number of authors (e.g., Johnston, 1993; Lambeck *et al.*, 1998; Milne &

The theory in this chapter is, in part, based on unpublished notes written by David Al-Attar and Jeroen Tromp prior to the commencement of this PhD.

Mitrovica, 1998; Milne *et al.*, 1999; Mitrovica & Milne, 2003; Kendall *et al.*, 2005). It is also common to solve the equations of motion in the Laplace transform domain (Peltier, 1974); however, this method is not well suited to Earth structures with lateral variations or continuous radial variations (e.g., Fang & Hager, 1995; Han & Wahr, 1995; Boschi *et al.*, 1999).

In this chapter, we present a method for forward modelling GIA in the time domain in compressible and heterogeneous earth models. The evolution equations we derive can be numerically integrated without requiring us to solve the sea level equation. We consider only a Maxwell rheology, but the method is applicable to transient linear rheologies and non-linear rheologies through extensions discussed in chapter 2. We note that in this chapter we do not include the rotation of the Earth; this extension will be the subject of future work. We build on the work of Al-Attar & Tromp (2014) by including gravitationally self-consistent sea level change. The method is illustrated with numerical examples calculated in a spherically symmetric earth model and those that allow lateral variations in viscosity.

We consider the viscoelastic deformation of an earth model possessing surface oceans and ice sheets. In doing so, we follow previous work (e.g., Mitrovica & Milne, 2003; Kendall *et al.*, 2005) in making several assumptions. Firstly, we assume that the oceans and ice sheets are sufficiently thin that their interaction with the solid earth can be accurately represented through an associated surface load. Furthermore, we assume that the water surface is defined everywhere by the same gravitational equipotential and so neglect the possibility of isolated bodies of water. We also assume that, prior to the commencement of the deformation, the Earth is in hydrostatic equilibrium. This assumption cannot strictly be valid if the earth model possesses lateral variations in its density structure or if there is aspherical topography on any internal or external boundaries (Dahlen & Tromp, 1998). In particular, a truly hydrostatic earth model would either have to be covered by a global ocean or none at all, and so could not possess both continental and oceanic regions on its surface. However, it is expected that the departure from hydrostatic equilibrium due to realistic lateral variations will be small, and we therefore neglect additional terms in the equations of motion associated with deviatoric pre-stress (Dahlen & Tromp, 1998).

The GIA problem is typically solved through the so-called sea level equation, which is generally solved iteratively. Here, however, we present a different approach; we derive coupled evolution equations that can be numerically integrated without iteratively solving the sea level equation. This is an advantage in itself; however, the main motivation for the development of this rate-formulation is its suitability to the application of adjoint methods. The forward method presented in this section is valid in compressible and laterally heterogeneous earth models. We calculate gravitationally self-consistent sea level change, and include shoreline migration.

4.2 Deformation of the solid Earth

We first consider the equations of motion governing the response of the solid Earth to a general surface load. In this context, the "solid Earth" is the part of the model that remains after removal of the oceans and ice sheets; in spite of its name, this can include fluid layers within the Earth, such as a fluid outer core. In what follows, we make extensive use of Al-Attar & Tromp (2014) and also Dahlen (1974), Dahlen & Tromp (1998) and Tromp & Mitrovica (1999).

4.2.1 Equations of motion

We consider the motion of the solid Earth relative to its initial, or reference, configuration at $t = t_0$, which we denote by $M \subseteq \mathbb{R}^3$ with external boundary ∂M. The material particles within this earth model are labelled by $\mathbf{x}$, their position at the initial time. The earth model has a number of fluid and solid regions that we write as M_F for the former and M_S for the latter. These regions are separated by smooth, non-intersecting, closed surfaces called internal boundaries which consist of four subsets – Σ_{SS}, Σ_{SF}, Σ_{FS} and Σ_{FF}, where the first (second) subscript indicates whether the region on the inside (outside) of the boundary is solid (S) or fluid (F). The union of all boundaries, both internal and external, is written Σ. For times $t \geq t_0$, the deformation of the solid earth is described by

$$\mathbf{r}(\mathbf{x}, t) = \mathbf{x} + \mathbf{u}(\mathbf{x}, t), \tag{4.1}$$

where $\mathbf{r}(\mathbf{x}, t)$ is the spatial point now occupied by the material particle $\mathbf{x}$ and we call $\mathbf{u}(\mathbf{x}, t)$ the displacement. We assume that the displacement is small and so, in what follows, will consider linearised equations of motion. We write $\phi^E(\mathbf{r}, t)$ for the Eulerian gravitational potential at the spatial point $\mathbf{r}(\mathbf{x}, t)$ and time t, and decompose this field as

$$\phi^E(\mathbf{r}, t) = \Phi(\mathbf{r}) + \phi(\mathbf{r}, t) \tag{4.2}$$

where $\Phi(\mathbf{r})$ is the gravitational potential of the reference earth model which satisfies Poisson's equation,

$$\nabla^2 \Phi = 4\pi G \rho. \tag{4.3}$$

ϕ is the gravitational potential perturbation and, to first order, $\phi(\mathbf{r}, t) = \phi(\mathbf{x}, t)$. Following Dahlen (1974), ϕ satisfies the modified Poisson's equation,

$$(4\pi G)^{-1} \nabla^2 \phi = \begin{cases} -\nabla \cdot (\rho \mathbf{u}), & \mathbf{x} \in M_S, \\ g^{-1} \phi \partial_n \rho, & \mathbf{x} \in M_F, \\ 0, & \mathbf{x} \in \mathbb{R}^3 \setminus M, \end{cases} \tag{4.4}$$

where ∂_n is the directional derivative along the outward normal to the level surfaces of density ρ and g is the magnitude of the gravitational acceleration. The latter is defined through

$$\nabla \Phi = g \hat{\boldsymbol{\nu}}, \tag{4.5}$$

where $\hat{\boldsymbol{\nu}}$ is thus the local vertical direction. We have the initial conditions $\mathbf{u}(\mathbf{x}, t_0) = 0$ and $\phi(\mathbf{r}, t_0) = 0$ which follow from the above definitions. As mentioned, we assume that the earth model is in hydrostatic equilibrium initially. In a non-rotating earth model, this assumption implies that the level surfaces of density ρ, pressure p and gravitational potential Φ are concentric spheres. This means that on internal or external boundaries, we must have

$$\nabla \Phi = g \hat{\mathbf{n}}, \tag{4.6}$$

where $\hat{\mathbf{n}}$ is the outward unit normal vector, and so the local vertical direction $\hat{\boldsymbol{\nu}}$ coincides with $\hat{\mathbf{n}}$ on such boundaries.

Neglecting inertial terms, the deformation due to a time-dependent surface loading, $\sigma(\mathbf{x}, \mathbf{t})$, satisfies the quasi-static momentum equation, given by

$$-\nabla \cdot \mathbf{T} + \nabla(\rho \mathbf{u} \cdot \nabla \Phi) - \nabla \cdot (\rho \mathbf{u}) \nabla \Phi + \rho \nabla \phi = \mathbf{0}, \tag{4.7}$$

where $\mathbf{T}$ is the incremental Lagrangian-Cauchy stress tensor and ρ is the density. We also have boundary conditions for the system, which, following Al-Attar & Tromp (2014), are

$$\hat{\boldsymbol{\nu}} \cdot \mathbf{T} = -\sigma \nabla \Phi, \quad \mathbf{x} \in \partial M, \tag{4.8}$$

$$[\hat{\boldsymbol{\nu}} \cdot \mathbf{T}]^+_- = \mathbf{0}, \quad \mathbf{x} \in \Sigma_{\mathrm{SS}}, \tag{4.9}$$

$$\hat{\boldsymbol{\nu}} \cdot \mathbf{T}^+ = \rho^-[\mathbf{u}^+ \cdot \nabla \Phi + \phi]\hat{\boldsymbol{\nu}}, \quad \mathbf{x} \in \Sigma_{\mathrm{FS}}, \tag{4.10}$$

$$\hat{\boldsymbol{\nu}} \cdot \mathbf{T}^- = \rho^+[\mathbf{u}^- \cdot \nabla \Phi + \phi]\hat{\boldsymbol{\nu}}, \quad \mathbf{x} \in \Sigma_{\mathrm{SF}}, \tag{4.11}$$

$$[\mathbf{u}]^+_- = \mathbf{0}, \quad \mathbf{x} \in \Sigma_{\mathrm{SS}}, \tag{4.12}$$

$$[\phi]^+_- = 0, \quad \mathbf{x} \in \Sigma, \tag{4.13}$$

$$\left[(4\pi G)^{-1} \hat{\boldsymbol{\nu}} \cdot \nabla \phi\right]^+_- - \rho^- \hat{\boldsymbol{\nu}} \cdot \mathbf{u}^- = 0, \quad \mathbf{x} \in \partial M, \tag{4.14}$$

$$\left[(4\pi G)^{-1} \hat{\boldsymbol{\nu}} \cdot \nabla \phi + \rho \hat{\boldsymbol{\nu}} \cdot \mathbf{u}\right]^+_- = 0, \quad \mathbf{x} \in \Sigma_{\mathrm{SS}}, \tag{4.15}$$

$$\left[(4\pi G)^{-1} \hat{\boldsymbol{\nu}} \cdot \nabla \phi\right]^+_- + [\rho]^+_- \hat{\boldsymbol{\nu}} \cdot \mathbf{u}^+ = 0, \quad \mathbf{x} \in \Sigma_{\mathrm{FS}}, \tag{4.16}$$

$$\left[(4\pi G)^{-1} \hat{\boldsymbol{\nu}} \cdot \nabla \phi\right]^+_- + [\rho]^+_- \hat{\boldsymbol{\nu}} \cdot \mathbf{u}^- = 0, \quad \mathbf{x} \in \Sigma_{\mathrm{SF}}, \tag{4.17}$$

where $^+$ and $^-$ indicate whether a term is evaluated on the outer or inner side of a discontinuity respectively. We note that the load, σ, appears only through equation (4.8), the equation for the traction on the surface of the Earth. We further require the gravity perturbation to tend to 0 as $\mathbf{x}$ tends to infinity.

4.2.2 Linear viscoelasticity

We require a constitutive equation to describe the rheology of the viscoelastic mantle. Following Al-Attar & Tromp (2014), for an isotropic and linear viscoelastic material with bulk modulus κ and time-dependent shear relaxation function $\mu(t)$ we can write

$$\mathbf{T}(t) = \kappa \nabla \cdot \mathbf{u}(t)\, \mathbf{I} + \int_{t_0}^{t} 2\mu(t - t') \dot{\mathbf{d}}(t')\, \mathrm{d}t', \tag{4.18}$$

where a dot over a symbol indicates differentiation with respect to time and

$$\mathbf{d} = \mathbf{e} - \frac{1}{3}\mathrm{tr}(\mathbf{e})\mathbf{I} \tag{4.19}$$

is the deviatoric part of the linearised strain tensor

$$\mathbf{e} = \frac{1}{2}[\nabla \mathbf{u} + (\nabla \mathbf{u})^T]. \tag{4.20}$$

In equation (4.19), tr$(\cdot)$ indicates the trace of the matrix. For a Maxwell solid, the shear relaxation function can be written as

$$\mu(t) = \mu_0 e^{-t/\tau}, \tag{4.21}$$

where μ_0 is the unrelaxed shear modulus and τ is the Maxwell relaxation time. It will be useful to define the internal variable

$$\mathbf{m}(t) = \frac{1}{\tau}\int_{t_0}^{t} e^{-(t-t')/\tau}\mathbf{d}(t')\,\mathrm{d}t', \tag{4.22}$$

which can be seen to satisfy

$$\dot{\mathbf{m}} + \frac{1}{\tau}(\mathbf{m} - \mathbf{d}) = \mathbf{0}. \tag{4.23}$$

We can therefore rewrite equation (4.18) as

$$\mathbf{T} = \kappa\nabla\cdot\mathbf{u}\,\mathbf{I} + 2\mu_0(\mathbf{d} - \mathbf{m}). \tag{4.24}$$

From this, we can see that the deviatoric stress, $\boldsymbol{\tau}$, is given by

$$\boldsymbol{\tau} = 2\mu_0(\mathbf{d} - \mathbf{m}). \tag{4.25}$$

These results can readily be extended to other linear viscoelastic materials as described in chapter 2 and non-linear viscoelastic materials as described in Crawford *et al.* (2017).

4.2.3 Rate formulation

In order to incorporate time dependence and a viscoelastic rheology into equation (4.7), we follow the method of Al-Attar & Tromp (2014). Differentiating equation (4.7) and using equations (4.23) and (4.24), we obtain

$$\nabla\cdot(\kappa\nabla\cdot\dot{\mathbf{u}} + 2\mu_0\dot{\mathbf{d}}) + \nabla\cdot\left[\frac{2\mu_0}{\tau}(\mathbf{m} - \mathbf{d})\right] - \nabla(\rho\dot{\mathbf{u}}\cdot\nabla\Phi) + \nabla\cdot(\rho\dot{\mathbf{u}})\nabla\Phi - \rho\nabla\dot{\phi} = \mathbf{0}. \tag{4.26}$$

We can also differentiate (4.4) and the boundary conditions (4.8) – (4.17). These, along with equation (4.26), constitute the rate formulation in strong form of the viscoelastic loading problem.

4.3 Sea level

We now require the form of the surface load for GIA and the equations governing the time evolution of sea level.

4.3.1 Sea level definitions

We first define ∂M_t to be the outer surface of the solid earth at time t and this is given by

$$\partial M_t = \{\mathbf{x} + \mathbf{u}(\mathbf{x}, t)\,|\,\mathbf{x} \in \partial M\}. \tag{4.27}$$

Sea level $SL(\mathbf{x}, t)$ is defined at every point on this surface. We assume that the oceans remain in hydrostatic equilibrium throughout the deformation and so the sea surface is an equipotential of the

gravitational field. We will write the value of the gravitational potential on this surface at a given time as $\Phi_G(t)$. $SL(\mathbf{x},t)$ is therefore determined implicitly for $\mathbf{x} \in \partial M$ through the equation

$$\phi^E(\mathbf{x} + \mathbf{u}(\mathbf{x},t) + SL(\mathbf{x},t)\hat{\boldsymbol{\nu}}(\mathbf{x},t),t) = \Phi_G(t), \tag{4.28}$$

i.e., sea level is the distance from the solid surface to the gravitational equipotential which defines the sea surface along the direction of the local vertical at the surface.

Above each point on the solid earth surface, there can be an ice sheet of height $I(\mathbf{x},t)$ and an ocean of height $S(\mathbf{x},t)$, where these heights are measured in the direction of the local vertical and cannot be negative. We note that, in the GIA literature, I is commonly taken to be the change in ice thickness from the initial value (e.g., Mitrovica & Milne, 2003), but we find our definition to be more convenient. The load at the surface comprises both the ocean and ice sheet; we can write

$$\sigma(\mathbf{x},t) = \rho_w S(\mathbf{x},t) + \rho_i I(\mathbf{x},t), \tag{4.29}$$

where ρ_w and ρ_i are the densities of water and ice respectively. Where $S(\mathbf{x},t)$ and $I(\mathbf{x},t)$ are simultaneously positive, the ice sheet (or, in this case, ice shelf) floats buoyantly on top of the ocean and so, assuming local isostatic equilibrium between the ocean and ice sheet, we must have

$$\rho_w S(\mathbf{x},t) + \rho_i I(\mathbf{x},t) = \rho_w SL(\mathbf{x},t). \tag{4.30}$$

We note that floating ice here is dynamically equivalent to the presence of the same mass of water. In the case $I(\mathbf{x},t) = 0$, this equation simplifies to $SL(\mathbf{x},t) = S(\mathbf{x},t)$.

Where there is an ocean present, $S(\mathbf{x},t) > 0$ and so, from equation (4.30), $\rho_w SL(\mathbf{x},t) > \rho_i I(\mathbf{x},t)$. Conversely, where there is no ocean present, $S(\mathbf{x},t) = 0$ and it must therefore hold that $\rho_w SL(\mathbf{x},t) \leq \rho_i I(\mathbf{x},t)$. We therefore define the ocean set by

$$\mathcal{O}_t = \{\mathbf{x} \in \partial M \,|\, \rho_w SL(\mathbf{x},t) > \rho_i I(\mathbf{x},t)\}, \tag{4.31}$$

which comprises all those locations where there is an ocean present (including an ocean covered by a buoyant ice sheet). We are then able to define the ocean function by

$$C(\mathbf{x},t) = \begin{cases} 1, & \mathbf{x} \in \mathcal{O}_t, \\ 0, & \mathbf{x} \notin \mathcal{O}_t, \end{cases} \tag{4.32}$$

which is equivalent to that of Mitrovica & Milne (2003) and reduces to that of Farrell & Clark (1976) in the absence of floating ice sheets. Using the ocean function, we can now write

$$S(\mathbf{x},t) = C(\mathbf{x},t)\left[SL(\mathbf{x},t) - \frac{\rho_i}{\rho_w} I(\mathbf{x},t)\right], \tag{4.33}$$

which holds at all locations. We can also rewrite equation (4.29) as

$$\sigma = \rho_w C\, SL + \rho_i (1 - C) I, \tag{4.34}$$

and so, recalling that the ocean function itself depends on SL and I, we see explicitly the non-linear

dependence of the surface load on sea level and ice height in the GIA problem. We note again that this is the only non-linear term included, as we neglect those due to, for example, the time dependence of the local vertical direction. The inclusion of shoreline migration has been shown to be important (Mitrovica & Milne, 2003) and the neglect of other terms is consistent with all other forward methods.

It will be useful to consider the form of the boundary of the ocean set, which we will write as $\partial\mathcal{O}_t$. From equation (4.31), we can see that this is defined by

$$\partial\mathcal{O}_t = \{\mathbf{x} \in \partial M \,|\, \rho_w SL(\mathbf{x}, t) = \rho_i I(\mathbf{x}, t)\}. \tag{4.35}$$

Writing ∇_1 for the tangential gradient operator on ∂M, we shall assume that

$$\forall \mathbf{x} \in \partial\mathcal{O}_t : \nabla_1[\rho_w SL(\mathbf{x}, t) - \rho_i I(\mathbf{x}, t)] \neq \mathbf{0}. \tag{4.36}$$

It then follows from the regular value theorem (e.g, Spivak, 1970) that $\partial\mathcal{O}_t$ forms a one-dimensional submanifold on ∂M. Physically, this result means that the ocean basins have well-defined boundaries on which the ocean locally lies on one side. We can decompose $\partial\mathcal{O}_t$ into locations for which $I(\mathbf{x}, t) = 0$ or for which $I(\mathbf{x}, t) > 0$. In the former case, the boundary to the ocean basin is where the gravitational equipotential that describes the sea surface intersects the solid surface, while for the latter, the boundary lies at the grounding line of the ice sheet. While this simple isostatic relation for the grounding line position is not strictly consistent with ice dynamics (e.g., Schoof, 2007), it will be sufficient for our purposes.

4.3.2 The evolution of sea level

In the forward GIA problem, the evolution of the ice sheets is prescribed. It will prove useful to write this as

$$I(\mathbf{x}, t_0) = I_0(\mathbf{x}), \tag{4.37}$$

$$\dot{I}(\mathbf{x}, t) = \dot{I}_1(\mathbf{x}, t), \tag{4.38}$$

i.e., we have the initial ice distribution and the time derivative of the ice sheet thickness at all times. This uniquely defines $I(\mathbf{x}, t)$. Given the initial earth model and ice distribution, we can, in principle, calculate the initial sea level from equation (4.28) with no deformation and so

$$\Phi(\mathbf{x} + SL(\mathbf{x}, t)\hat{\boldsymbol{\nu}}, t) = \Phi_G(t), \tag{4.39}$$

where Φ itself depends on SL. In practice, however, our knowledge of the initial earth model can never be perfect and the above procedure need not lead to sensible values for the initial sea level. We therefore choose to prescribe the initial sea level, and we will write this as

$$SL(\mathbf{x}, t_0) = SL_0(\mathbf{x}). \tag{4.40}$$

We could also, by iteration, find an initial sea level which gives a suitably correct present day sea level (Kendall *et al.*, 2005). We discuss how to perform such calculations using the adjoint method in section 5.5.3.

We now wish to calculate how the sea level evolves with time due to variations in ice thickness. In doing so, we will relate the rate of change of sea level to the deformation of the solid Earth. Differentiating equation (4.28) with respect to time, and retaining only first-order terms in $\mathbf{u}$ and ϕ, we find

$$\dot{SL} = -\frac{1}{g}(\dot{\mathbf{u}} \cdot \nabla\Phi + \dot{\phi}) + \frac{\dot{\Phi}_G}{g}. \tag{4.41}$$

To determine the second term on the right hand side in this equation, we will use the fact that the total mass of water and ice on the surface of the Earth must be conserved. This can be written as

$$\int_{\partial M} \left(\rho_w \dot{S} + \rho_i \dot{I}\right) \mathrm{d}S = 0, \tag{4.42}$$

where we have neglected the difference between the local vertical $\hat{\boldsymbol{\nu}}$ and the outward unit normal vector $\hat{\mathbf{n}}$, which is consistent with our assumption that the reference earth model is in a state of hydrostatic equilibrium, and we ignore the time dependence of these directions. From equation (4.33), we see that

$$\dot{S} = C\left(\dot{SL} - \frac{\rho_i}{\rho_w}\dot{I}\right) + \dot{C}\left(SL - \frac{\rho_i}{\rho_w}I\right). \tag{4.43}$$

In Crawford *et al.* (2018), it was shown that $\dot{C}$ is given by

$$\dot{C} = \frac{\rho_\mathrm{w}\dot{SL} - \rho_\mathrm{i}\dot{I}}{\rho_\mathrm{w}\partial_\perp SL - \rho_\mathrm{i}\partial_\perp I}\delta_{\partial\mathcal{O}_t}, \tag{4.44}$$

where $\partial\mathcal{O}_t$ is the boundary of the ocean set given by equation (4.35), $\partial_\perp$ is a derivative in the direction perpendicular to this boundary, pointing into the ocean and $\delta_{\partial\mathcal{O}_t}$ is the Dirac line distribution which is only non-zero on the ocean set boundary. This is defined such that

$$\int_{\partial M} f\,\delta_{\partial\mathcal{O}_t}\,\mathrm{d}S = \int_{\partial\mathcal{O}_t} f\,\mathrm{d}l, \tag{4.45}$$

for a function f defined on the surface of the Earth.

Equation (4.44) is only non-zero on $\partial\mathcal{O}_t$, but this is, by definition, where $SL - \frac{\rho_i}{\rho_w}I = 0$. Therefore, the second term on the right hand side of equation (4.43) vanishes and so

$$\dot{S} = C\left(\dot{SL} - \frac{\rho_i}{\rho_w}\dot{I}\right). \tag{4.46}$$

Substituting equation (4.46) into equation (4.42), we find

$$\int_{\partial M} \left[\rho_w C\dot{SL} + \rho_i(1-C)\dot{I}\right] \mathrm{d}S = 0. \tag{4.47}$$

Using equation (4.34), this can also be written

$$\int_{\partial M} \dot{\sigma}\,\mathrm{d}S = 0, \tag{4.48}$$

where, as above, the terms in $\dot{\sigma}$ involving $\dot{C}$ vanish, and so we can see that the rate of change of load has a mean value of zero. Substituting equation (4.41) into equation (4.47) and rearranging, we see

that

$$\frac{\dot{\Phi}_G}{g} = \frac{1}{gA}\int_{\partial M} C(\dot{\mathbf{u}}\cdot\nabla\Phi + \dot{\phi})\,\mathrm{d}S - \frac{\rho_i}{\rho_w A}\int_{\partial M}(1-C)\dot{I}\,\mathrm{d}S, \tag{4.49}$$

where A is the surface area of the ocean basin, which is given by

$$A = \int_{\partial M} C\,\mathrm{d}S. \tag{4.50}$$

Substituting this result into equation (4.41), we find

$$\dot{SL} = -\frac{1}{g}(\dot{\mathbf{u}}\cdot\nabla\Phi + \dot{\phi}) + \frac{1}{gA}\int_{\partial M} C(\dot{\mathbf{u}}\cdot\nabla\Phi + \dot{\phi})\,\mathrm{d}S - \frac{\rho_i}{\rho_w A}\int_{\partial M}(1-C)\dot{I}\,\mathrm{d}S, \tag{4.51}$$

and, from equation (4.34)

$$\dot{\sigma} = -\frac{\rho_w C}{g}(\dot{\mathbf{u}}\cdot\nabla\Phi + \dot{\phi}) + \frac{\rho_w C}{gA}\int_{\partial M} C(\dot{\mathbf{u}}\cdot\nabla\Phi + \dot{\phi})\,\mathrm{d}S + \rho_i(1-C)\dot{I} - \frac{\rho_i C}{A}\int_{\partial M}(1-C)\dot{I}\,\mathrm{d}S. \tag{4.52}$$

These equations explicitly relate the time derivatives of the sea level and surface load to the deformation of the solid Earth. In obtaining these results, we have fully accounted for shoreline migration, but this is expressed simply through the dependence of the ocean function on SL and I. This dependence introduces non-linearity into the problem.

4.4 Weak formulation of the GIA problem

It will be useful to derive the weak form of the GIA problem. This enables us to implement the forward equations using a finite-element-type method and is necessary in deriving the adjoint equations, which we will need later when considering the inverse problem.

From Al-Attar & Tromp (2014), the weak form of the viscoelastic loading problem can be written as

$$\mathcal{A}(\dot{\mathbf{u}},\dot{\phi}\,|\,\mathbf{u}',\phi') - \int_{M_S} 2\mu_0\left[\dot{\mathbf{m}}:\mathbf{m}' + \frac{1}{\tau}(\mathbf{d}-\mathbf{m}):(\mathbf{d}'-\mathbf{m}')\right]\mathrm{d}V + \int_{\partial M}(\mathbf{u}'\cdot\nabla\Phi + \phi')\dot{\sigma}\,\mathrm{d}S = 0, \tag{4.53}$$

which must hold for all sufficiently smooth test functions $\mathbf{u}'$, ϕ' and $\mathbf{m}'$ that satisfy

$$\left[\mathbf{u}'\right]_-^+ = \mathbf{0}, \quad \mathbf{x}\in\Sigma_{\mathrm{SS}}, \tag{4.54}$$

$$\left[\phi'\right]_-^+ = 0, \quad \mathbf{x}\in\Sigma, \tag{4.55}$$

and

$$\lim_{\|\mathbf{x}\|\to\infty}\phi' = 0. \tag{4.56}$$

Here, $\mathcal{A}$ is the bilinear form

$$\begin{aligned}\mathcal{A}(\mathbf{u},\phi|\mathbf{u}',\phi') = &\int_{M_S} \kappa\nabla\cdot\mathbf{u}\,\nabla\cdot\mathbf{u}'\ \mathrm{d}V + \int_{M_S} 2\mu_0\mathbf{d}:\mathbf{d}'\,\mathrm{d}V + \frac{1}{2}\int_{M_S}\rho\left[\nabla(\mathbf{u}\cdot\nabla\Phi)\cdot\mathbf{u}' + \nabla(\mathbf{u}'\cdot\nabla\Phi)\cdot\mathbf{u}\right]\mathrm{d}V\\ &-\frac{1}{2}\int_{M_S}\rho\left(\nabla\cdot\mathbf{u}\nabla\Phi\cdot\mathbf{u}' + \nabla\cdot\mathbf{u}'\nabla\Phi\cdot\mathbf{u}\right)\mathrm{d}V + \int_{M_S}\rho(\nabla\phi\cdot\mathbf{u}' + \mathbf{u}\cdot\nabla\phi')\,\mathrm{d}V\\ &+\frac{1}{4\pi G}\int_{\mathbb{R}^3}\nabla\phi\cdot\nabla\phi'\,\mathrm{d}V + \int_{M_F} g^{-1}\phi\phi'\partial_n\rho\,\mathrm{d}V + \int_{\Sigma_{\mathrm{FS}}}\rho^- g\hat{\boldsymbol{\nu}}\cdot\mathbf{u}\,\hat{\boldsymbol{\nu}}\cdot\mathbf{u}'\,\mathrm{d}S\\ &-\int_{\Sigma_{\mathrm{SF}}}\rho^+ g\hat{\boldsymbol{\nu}}\cdot\mathbf{u}\,\hat{\boldsymbol{\nu}}\cdot\mathbf{u}'\,\mathrm{d}S + \int_{\Sigma_{\mathrm{FS}}}\rho^-(\phi\mathbf{u}' + \mathbf{u}\phi')\cdot\hat{\boldsymbol{\nu}}\,\mathrm{d}S - \int_{\Sigma_{\mathrm{SF}}}\rho^+(\phi\mathbf{u}' + \mathbf{u}\phi')\cdot\hat{\boldsymbol{\nu}}\,\mathrm{d}S.\end{aligned} \tag{4.57}$$

This weak form of the problem is completely equivalent to the rate formulation of the linear viscoelastic problem described in section 4.2.3, including all associated boundary conditions.

We now wish to combine the equations for the surface load and the evolution of sea level with this weak form. Firstly, we can substitute equation (4.52) for the surface load term, $\dot{\sigma}$, into the above weak form to find

$$\begin{aligned}&\mathcal{A}(\dot{\mathbf{u}},\dot{\phi}\,|\,\mathbf{u}',\phi') - \int_{M_S} 2\mu_0\left[\dot{\mathbf{m}}:\mathbf{m}' + \frac{1}{\tau}(\mathbf{d}-\mathbf{m}):(\mathbf{d}'-\mathbf{m}')\right]\mathrm{d}V\\ &-\frac{\rho_w}{g}\int_{\partial M}\left[\dot{\mathbf{u}}\cdot\nabla\Phi + \dot{\phi} - \frac{1}{A}\int_{\partial M} C(\dot{\mathbf{u}}\cdot\nabla\Phi + \dot{\phi})\,\mathrm{d}S\right]C(\mathbf{u}'\cdot\nabla\Phi + \phi')\,\mathrm{d}S\\ &+\rho_i\int_{\partial M}(1-C)\dot{I}\left[\mathbf{u}'\cdot\nabla\Phi + \phi' - \frac{1}{A}\int_{\partial M} C(\mathbf{u}'\cdot\nabla\Phi + \phi')\,\mathrm{d}S\right]\mathrm{d}S = 0.\end{aligned} \tag{4.58}$$

We will now derive the weak form of equation (4.51) and combine it with equation (4.58). We introduce the test function SL' which is defined on ∂M, multiply equation (4.51) by this test function and then integrate over the surface to find

$$\rho_w g\int_{\partial M}\dot{S}LSL'\,\mathrm{d}S + \int_{\partial M}\left\{\rho_w\left[\dot{\mathbf{u}}\cdot\nabla\Phi + \dot{\phi} - \frac{1}{A}\int_{\partial M} C(\dot{\mathbf{u}}\cdot\nabla\Phi + \dot{\phi})\,\mathrm{d}S\right] + \frac{\rho_i g}{A}\int_{\partial M}(1-C)\dot{I}\,\mathrm{d}S\right\}SL'\,\mathrm{d}S = 0, \tag{4.59}$$

where a factor of $\rho_w g$ has been introduced for convenience. Adding this to equation (4.58), the weak form becomes

$$\begin{aligned}&\mathcal{A}(\dot{\mathbf{u}},\dot{\phi}|\mathbf{u}',\phi') - \int_{M_S} 2\mu_0\left[\dot{\mathbf{m}}:\mathbf{m}' + \frac{1}{\tau}(\mathbf{d}-\mathbf{m}):(\mathbf{d}'-\mathbf{m}')\right]\mathrm{d}V - \rho_w g\int_{\partial M}\dot{S}L\,SL'\,\mathrm{d}S\\ &-\frac{\rho_w}{g}\int_{\partial M}\left[\dot{\mathbf{u}}\cdot\nabla\Phi + \dot{\phi} - \frac{1}{A}\int_{\partial M} C(\dot{\mathbf{u}}\cdot\nabla\Phi + \dot{\phi})\,\mathrm{d}S\right]\left[gSL' + C(\mathbf{u}'\cdot\nabla\Phi + \phi')\right]\mathrm{d}S\\ &+\rho_i\int_{\partial M}(1-C)\dot{I}_1\left[\mathbf{u}'\cdot\nabla\Phi + \phi' - \frac{1}{A}\int_{\partial M}\left[gSL' + C(\mathbf{u}'\cdot\nabla\Phi + \phi')\right]\mathrm{d}S\right]\mathrm{d}S = 0,\end{aligned} \tag{4.60}$$

and we also require the initial condition given by equation (4.40). We will finally add the weak form of equation (4.38), which, introducing the test function I' defined on ∂M, is

$$\rho_i g\int_{\partial M}(\dot{I} - \dot{I}_1)I'\,\mathrm{d}S = 0, \tag{4.61}$$

where, again, we have introduced a factor of $\rho_i g$ for convenience. We also have the initial condition

from equation (4.37). Therefore, the overall weak form for the GIA problem, which we recall must hold for all $\mathbf{u}'$, ϕ', $\mathbf{m}'$, SL' and I', is

$$\mathcal{A}(\dot{\mathbf{u}}, \dot{\phi}|\mathbf{u}', \phi') - \int_{M_S} 2\mu_0 \left[\dot{\mathbf{m}} : \mathbf{m}' + \frac{1}{\tau}(\mathbf{d} - \mathbf{m}) : (\mathbf{d}' - \mathbf{m}')\right] \mathrm{d}V - \rho_w g \int_{\partial M} \dot{SL}\, SL' \,\mathrm{d}S$$
$$- \frac{\rho_w}{g} \int_{\partial M} \left[\dot{\mathbf{u}} \cdot \nabla\Phi + \dot{\phi} - \frac{1}{A}\int_{\partial M} C(\dot{\mathbf{u}} \cdot \nabla\Phi + \dot{\phi})\,\mathrm{d}S\right] [gSL' + C(\mathbf{u}' \cdot \nabla\Phi + \phi')]\,\mathrm{d}S - \rho_i g \int_{\partial M} (\dot{I}_1 - \dot{I}) I' \,\mathrm{d}S$$
$$+ \rho_i \int_{\partial M} (1 - C)\dot{I}_1 \left[\mathbf{u}' \cdot \nabla\Phi + \phi' - \frac{1}{A}\int_{\partial M} [gSL' + C(\mathbf{u}' \cdot \nabla\Phi + \phi')]\,\mathrm{d}S\right] \mathrm{d}S = 0, \tag{4.62}$$

with the initial conditions

$$\mathbf{u}(\mathbf{x}, 0) = \mathbf{0}, \tag{4.63}$$
$$\phi(\mathbf{x}, 0) = 0, \tag{4.64}$$
$$\mathbf{m}(\mathbf{x}, 0) = \mathbf{0}, \tag{4.65}$$
$$SL(\mathbf{x}, 0) = 0, \tag{4.66}$$
$$I(\mathbf{x}, 0) = I_0(\mathbf{x}). \tag{4.67}$$

The equations are equivalent to the formulation using the sea level equation, but are expressed independently of any numerical or iterative scheme. Through equation (4.62), the time derivatives of the variables of the forward problem ($\mathbf{u}$, ϕ, $\mathbf{m}$, SL, I) are related to the current state of the system. In order to solve the forward problem, the current state of the system is used to calculate the time derivatives of the variables and combined with some time-stepping scheme to find the state of the system at the next time step.

4.5 Numerical implementation in spherically symmetric earth models

We now have the equations of motion for the GIA problem and can implement them numerically in order to solve the forward problem. Given the current state of the system, it is possible to calculate the time derivatives of the forward variables and, along with some suitable time-stepping scheme, use them to update the system. In this section, we outline how to implement the forward problem numerically in spherically symmetric earth models and present some examples of forward calculations in such models.

For a spherically symmetric earth model, the outward unit normal vector will be in the radial direction. Therefore,

$$\nabla\Phi = g\hat{\mathbf{r}}, \tag{4.68}$$

and so

$$\mathbf{u} \cdot \nabla\Phi = g u_r, \tag{4.69}$$

where u_r is the component of the displacement in the radial direction.

4.5.1 Generalised spherical harmonics

We will find it useful to adopt a pseudo-spectral method in calculating the time derivatives – we transform back and forth between the spatial and spherical harmonic domains depending on which is most useful for the particular step. To do so, we will expand some fields in generalised spherical harmonics, as outlined in section 1.3.2.

In order to describe the displacement, we will find it useful to introduce coefficients U_{lm}, V_{lm} and W_{lm}, defined such that

$$u^0_{lm} = U_{lm}, \tag{4.70}$$

$$u^\pm_{lm} = \frac{k}{\sqrt{2}}(V_{lm} \pm iW_{lm}), \tag{4.71}$$

where $k = \sqrt{l(l+1)}$. The main tensor we wish to consider is $\mathbf{m}$; however, from equation (4.23), we can see that $\mathbf{m}$ is a symmetric second-order tensor with zero trace. We therefore will also find it useful to introduce the coefficients M_{lm}, N_{lm}, R_{lm}, S_{lm} and T_{lm}, defined such that

$$m^{\pm\pm}_{lm} = \frac{k\sqrt{k^2-2}}{2r}(M_{lm} \pm iN_{lm}), \tag{4.72}$$

$$m^{00}_{lm} = \frac{2}{3r}R_{lm}, \tag{4.73}$$

$$m^{0\pm}_{lm} = m^{\pm 0}_{lm} = \frac{k}{2\sqrt{2}r}(S_{lm} \pm iT_{lm}), \tag{4.74}$$

$$m^{\pm\mp}_{lm} = \frac{1}{3r}R_{lm}. \tag{4.75}$$

As shown in Al-Attar & Tromp (2014), the system naturally decouples into two sets of equations, the spheroidal system, which involves the coefficients U_{lm}, V_{lm}, ϕ_{lm}, M_{lm}, R_{lm} and S_{lm}, and the toroidal system, which involves W_{lm}, N_{lm} and T_{lm}. As our force term is purely in the radial direction, only the spheroidal system is excited in the spherically symmetric case.

4.5.2 Calculation of $\dot{\mathbf{m}}$

We can calculate $\dot{\mathbf{m}}$ using equation (4.23). The tensor components can be expanded using generalised spherical harmonics. As the spherical harmonics are orthogonal, the equations decouple for each l and m, and so each can be considered separately. We find that

$$\dot{M}_{lm} = \frac{1}{\tau}(V_{lm} - M_{lm}), \tag{4.76}$$

$$\dot{R}_{lm} = \frac{1}{\tau}\left(r\partial_r U_{lm} - U_{lm} + \frac{k^2}{2}V_{lm} - R_{lm}\right), \tag{4.77}$$

$$\dot{S}_{lm} = \frac{1}{\tau}\left(r\partial_r V_{lm} - V_{lm} + U_{lm} - S_{lm}\right). \tag{4.78}$$

4.5.3 Calculation of $\dot{\mathbf{u}}$ and $\dot{\phi}$

Given the current ice distribution and sea level, we first calculate the ocean function spatially. We then calculate the spherical harmonic coefficients of C and hence the ocean area, which is given by

$$A = \sqrt{4\pi} R^2 C_{00}. \tag{4.79}$$

In order to find $\dot{\mathbf{u}}$ and $\dot{\phi}$, we must solve

$$\begin{aligned}
&\mathcal{A}(\dot{\mathbf{u}}, \dot{\phi} \,|\, \mathbf{u}', \phi') - \frac{\rho_w}{g} \int_{\partial M} \left[\dot{\mathbf{u}} \cdot \nabla\Phi + \dot{\phi} - \frac{1}{A} \int_{\partial M} C(\dot{\mathbf{u}} \cdot \nabla\Phi + \dot{\phi}) \, \mathrm{d}S \right] C(\mathbf{u}' \cdot \nabla\Phi + \phi') \, \mathrm{d}S \\
&= \int_{M_S} \frac{2\mu_0}{\tau} (\mathbf{d} - \mathbf{m}) : \mathbf{d}' \, \mathrm{d}V - \rho_i \int_{\partial M} (1 - C) \dot{I} \left[\mathbf{u}' \cdot \nabla\Phi + \phi' - \frac{1}{A} \int_{\partial M} C(\mathbf{u}' \cdot \nabla\Phi + \phi') \, \mathrm{d}S \right] \mathrm{d}S,
\end{aligned} \tag{4.80}$$

where we have written all terms that are independent of $\dot{\mathbf{u}}$ and $\dot{\phi}$ on the right hand side, whereas those on the left hand side are linear in these time derivatives. However, we will first find it useful to consider the simpler equation

$$\mathcal{A}(\dot{\mathbf{u}}, \dot{\phi} \,|\, \mathbf{u}', \phi') = \int_{M_S} \frac{2\mu_0}{\tau} (\mathbf{d} - \mathbf{m}) : \mathbf{d}' \, \mathrm{d}V - \rho_i \int_{\partial M} (1 - C) \dot{I} \left[\mathbf{u}' \cdot \nabla\Phi + \phi' - \frac{1}{A} \int_{\partial M} C(\mathbf{u}' \cdot \nabla\Phi + \phi') \, \mathrm{d}S \right] \mathrm{d}S. \tag{4.81}$$

We recall that the equations of motion must hold for all choices of the test functions $\mathbf{u}'$ and ϕ'. We will find it useful to choose

$$u'^{\alpha} = u'^{\alpha *}_{lm} Y^{\alpha *}_{lm}, \tag{4.82}$$

$$\phi' = \phi'^{*}_{lm} Y^{*0}_{lm}, \tag{4.83}$$

for a particular l and m. As shown in Al-Attar & Tromp (2014), this choice results in the decoupling of the spherical harmonic components of $\dot{\mathbf{u}}$ and $\mathbf{u}$ for each different l and m. We can write these equations schematically as

$$\mathbf{A}_l \dot{\mathbf{w}}^0_{lm} = \mathbf{f}_{lm}. \tag{4.84}$$

For a model with no fluid regions and N radial nodes, $\mathbf{A}_l$ is a matrix of size $3N \times 3N$ and $\mathbf{w}^0_{lm}$ and $\mathbf{f}_{lm}$ are vectors of length $3N$. $\dot{\mathbf{w}}^0_{lm}$ contains, for particular values of l and m, the coefficients $\dot{\phi}^0_{lm}$, $\dot{U}^0_{lm}$ and $\dot{V}^0_{lm}$ at each radial node that satisfy equation (4.81), so that

$$(\mathbf{w}^0_{lm})_{3n-2} = \dot{\phi}^0_{lm}(r_n), \tag{4.85}$$

$$(\mathbf{w}^0_{lm})_{3n-1} = \dot{U}^0_{lm}(r_n), \tag{4.86}$$

$$(\mathbf{w}^0_{lm})_{3n} = \dot{V}^0_{lm}(r_n). \tag{4.87}$$

$\mathbf{A}_l$ and $\mathbf{f}_{lm}$ are constructed by taking U'^{*}_{lm}, V'^{*}_{lm} and ϕ'^{*}_{lm} to be equal to one at each radial node in turn and zero elsewhere. We note that in fluid regions, this formulation requires some modification as only the gravitational potential coefficients are defined. In either case, the solution to equation (4.81) is

$$\dot{\mathbf{w}}^0_{lm} = [\mathbf{A}_l]^{-1} \mathbf{f}_{lm}, \tag{4.88}$$

for each l and m.

With the addition of the remaining terms on the left hand side of equation (4.80), the system no longer has the form of equation (4.84). The extra terms mean the equations no longer decouple for each l and m. Equation (4.80) can be written

$$\mathbf{A}_l \dot{\mathbf{w}}_{lm} + \mathbf{g}_{lm}(\dot{u}_r, \dot{\phi}) = \mathbf{f}_{lm}, \tag{4.89}$$

where $\mathbf{g}_{lm}(\dot{u}_r, \dot{\phi})$ is a vector of length 3N formed by taking U'^{*}_{lm}, V'^{*}_{lm} and ϕ'^{*}_{lm} to be equal to one at each radial node in turn and zero elsewhere. We can therefore see that the components of $\mathbf{g}_{lm}$ are

$$g^{3N-2}_{lm}(\dot{u}_r, \dot{\phi}) = \frac{\rho_w}{gA}\left[C(g\dot{u}_r + \dot{\phi})\right]_{00} C_{lm} - \frac{\rho_w}{g}\left[C(g\dot{u}_r + \dot{\phi})\right]_{lm}, \tag{4.90}$$

$$g^{3N-1}_{lm}(\dot{u}_r, \dot{\phi}) = \frac{\rho_w}{A}\left[C(g\dot{u}_r + \dot{\phi})\right]_{00} C_{lm} - \rho_w\left[C(g\dot{u}_r + \dot{\phi})\right]_{lm}, \tag{4.91}$$

and $g^{n}_{lm}(\dot{u}_r, \dot{\phi}) = 0$ for $n \neq 3N-2, 3N-1$. Here we can explicitly see how $\mathbf{g}_{lm}$ depends on the total $\dot{u}_r$ and $\dot{\phi}$ fields, not just the coefficients for l and m. We can therefore not solve equation (4.80) by simply acting a matrix on a vector. Instead, we will use an iterative method, the steps of which are

1. use equation (4.88) to find $\dot{\mathbf{w}}^0_{lm}$, an initial estimate of $\dot{U}_{lm}$, $\dot{V}_{lm}$ and $\dot{\phi_{lm}}$, for all l and m;
2. find the current estimate of the spatial fields $\dot{\mathbf{u}}$ and $\dot{\phi}$;
3. construct the product $C(g\dot{u}_r + \dot{\phi})$ and take its spherical harmonic transform;
4. calculate $\mathbf{g}^i_{lm}(\dot{u}_r, \dot{\phi})$, the current estimate of $\mathbf{g}(\dot{u}_r, \dot{\phi})$;
5. calculate $\dot{\mathbf{w}}^{i+1}_{lm}$ by rearranging equation (4.89) to find

$$\dot{\mathbf{w}}^{i+1}_{lm} = A_l^{-1}[\mathbf{f}_{lm} - \mathbf{g}_{lm}(\dot{u}^i_r, \dot{\phi}^i)] = \dot{\mathbf{w}}^0_{lm} - \mathbf{A}_l^{-1}\mathbf{g}_{lm}(\dot{u}^i_r, \dot{\phi}^i); \tag{4.92}$$

6. repeat steps (ii) - (v) until a suitable level of convergence is reached.

This method looks somewhat like the iteration required to solve the sea level equation; however, shoreline migration is handled trivially and a separate iteration would not be required in a fully numerical method with a three-dimensional model.

4.5.4 Calculation of $\dot{SL}$

We finally calculate $\dot{SL}$ in the spatial domain using equation (4.41). In order to do so, we must

1. calculate the spatial variation of $\dot{\mathbf{u}}$ and $\dot{\phi}$ at the surface from their spherical harmonic coefficients;
2. construct the products $C(\dot{\mathbf{u}} \cdot \nabla\Phi + \dot{\phi})$ and $(1-C)\dot{I}$;
3. transform these products to the spherical harmonic domain in order to find $[C(\dot{\mathbf{u}} \cdot \nabla\Phi + \dot{\phi})]_{00}$ and $[(1-C)\dot{I}]_{00}$;
4. calculate $\dot{SL}$, which is given by

$$\dot{SL} = -\left(\dot{u}_r + \frac{\dot{\phi}}{g}\right) + \frac{\sqrt{4\pi}R^2}{A}\left[C\left(\dot{u}_r + \frac{\dot{\phi}}{g}\right)\right]_{00} - \frac{\sqrt{4\pi}R^2\rho_i}{\rho_w A}[(1-C)\dot{I}]_{00}. \tag{4.93}$$

4.5.5 Details of implementation

Within the forward problem, we require a model of ice sheet history and of earth structure. We use the ice model ICE-5G (Peltier, 2004), which gives the ice thickness globally at 500 or 1000 year intervals for the last 21000 years. However, our formulation of the forward problem takes the rate of change of ice thickness, and so we assume that this is constant between time slices. The earth model has the elastic structure of the Preliminary Reference Earth Model (PREM; Dziewonski & Anderson, 1981) and a simple three-layer viscosity structure – there is a 120km thick elastic lid on top of an upper mantle with a viscosity of 5×10^{20} Pa s and a lower mantle (below 670 km depth) with a viscosity of 5×10^{21} Pa s. We also require the initial sea level – this is again taken from ICE-5G and is shown in figure 4.2.

4.5.6 Comparison with Laplace domain sea level equation code

We benchmarked our implementation against a code which calculates post-glacial sea level in the Laplace domain using a Love number approach and the sea level equation (Peltier, 1974; Kendall *et al.*, 2005). In figure 4.3 we show the difference between the change in sea level from 21000 years ago to the present day calculated using the two methods. The maximum difference in sea level change calculated is two metres which, as these differences are in regions of large sea level change, is less than 0.5 percent of the change in sea level at these locations. We also plot the sea level change as a function of time using the two methods at two locations (as marked in figure 4.3) in figure 4.4, and can see that the differences are negligible.

4.5.7 Numerical examples

In figure 4.5, we show the change in sea level from 21000 years ago calculated using the method described in this chapter and with the implementation details described in section 4.5.5.

4.6 Numerical implementation in earth models with a laterally varying viscosity

As mentioned in section 4.1, we expect there to be lateral variations in viscosity within the Earth, of several orders of magnitude. The theory presented in this chapter is fully valid in such earth models; however, thus far, we have presented only numerical examples calculated in spherically symmetric earth models. Earth structures with lateral variations in both elastic and viscous structure can be modelled using a three-dimensional finite element (e.g., Paulson *et al.*, 2005) or finite volume (e.g., Latychev *et al.*, 2005) method; however, such methods require significant computational resources and there are difficulties with modelling gravity correctly. In this section, we discuss a simple extension of the method described in the previous section to earth models with a laterally varying viscosity structure but spherically symmetric elastic structure. As lateral variations in the elastic parameters in the Earth are on the order of a few percent, this is likely a good approximation of the Earth for modelling viscoelastic processes, where the significantly larger viscosity variations will probably dominate. The method is based on one described in Martinec (2000). We also present examples of calculations performed with such structures.

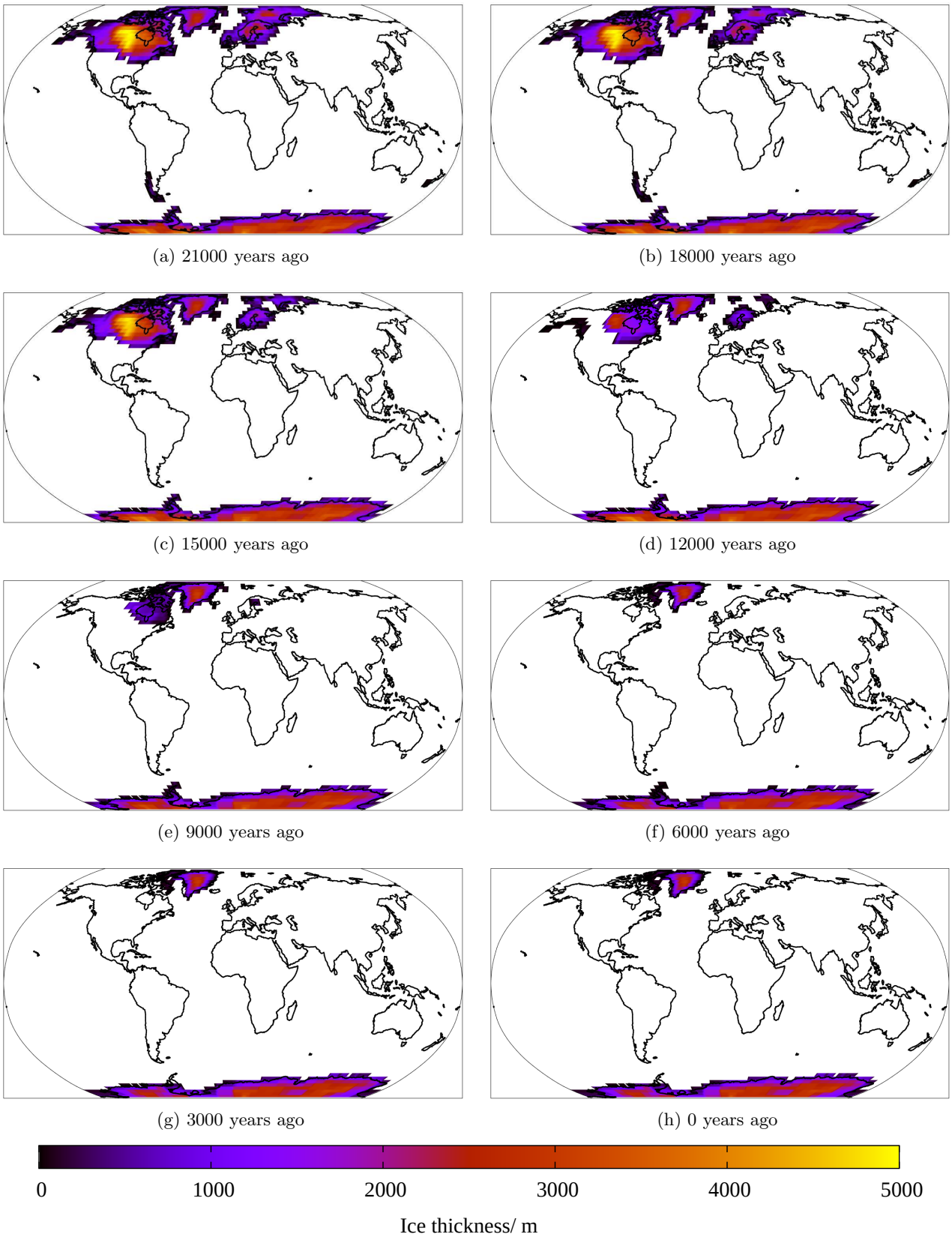

(a) 21000 years ago

(b) 18000 years ago

(c) 15000 years ago

(d) 12000 years ago

(e) 9000 years ago

(f) 6000 years ago

(g) 3000 years ago

(h) 0 years ago

Figure 4.1: The ice thickness at different times from the model ICE5G, as used for all calculations in this chapter and chapter 5. The ice thickness is shown (a) 21000 years ago, (b) 18000 years ago, (c) 15000 years ago, (d) 12000 years ago, (e) 9000 years ago, (f) 6000 years ago, (g) 3000 years ago and (h) at the present day. Where there is no ice present, the colour has been set to white.

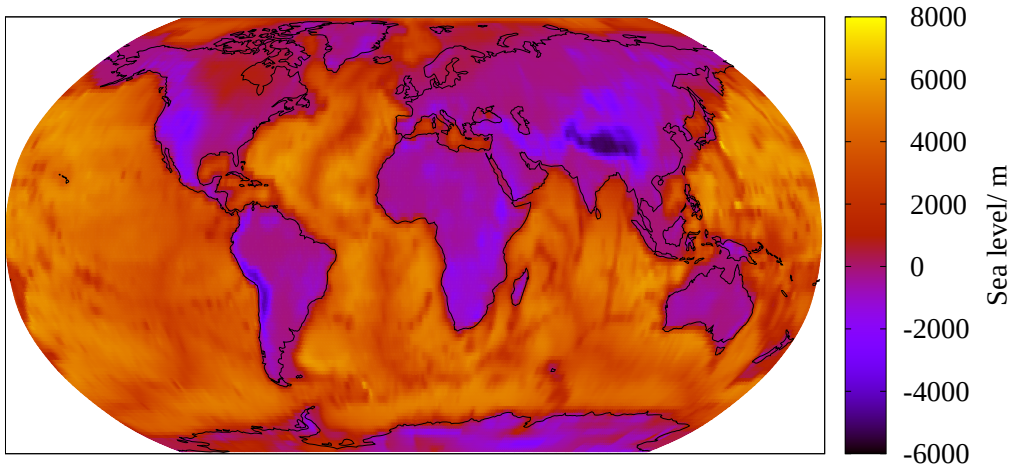

Figure 4.2: The initial sea level used for calculations in this chapter and chapter 5.

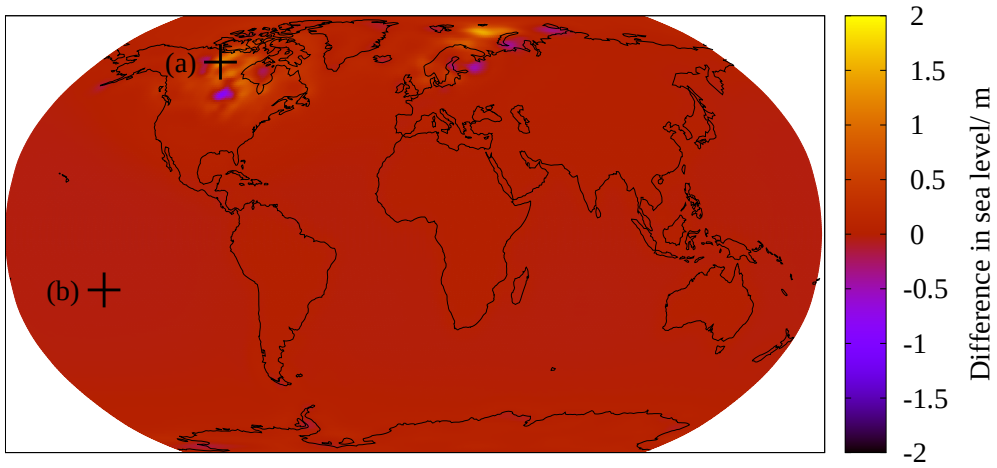

Figure 4.3: Difference in sea level change from 21000 years ago to the present calculated using the two methods. The crosses indicate the locations of the two time series plotted in figure 4.4.

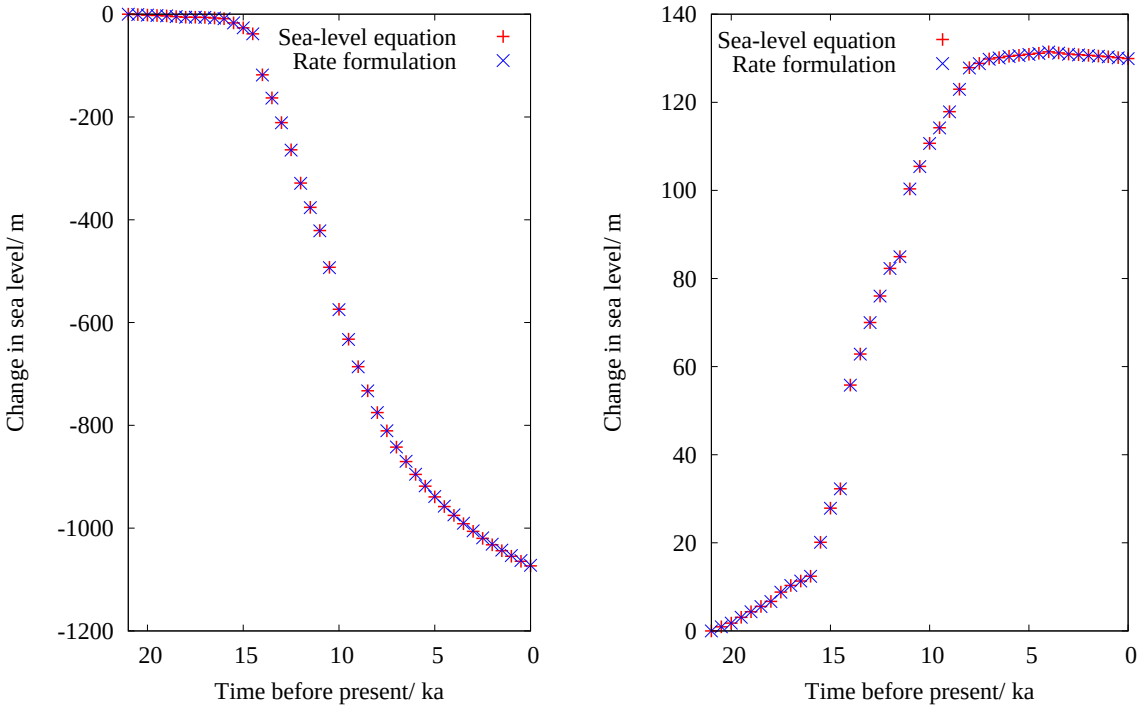

(a) Canada (b) Tahiti

Figure 4.4: Time series showing the change in sea level from 21000 years ago at two locations for the two methods. The locations of the measurements are marked by crosses in figure 4.3.

In order to model such earth structures, we must make some changes to the details of numerical implementation discussed in section 4.5 for spherically symmetric earth models. The viscosity appears in the equation for the displacement, $\mathbf{u}$, and gravitational potential perturbation, ϕ, and also the equation for the memory variables, $\mathbf{m}$, and so we must make changes to the method for calculating the time derivative of these variables. Calculation of sea level is performed as described in section 4.5.4. The method has been tested to check that in the case of a one-dimensional viscosity structure the results are the same as those calculated using the method presented in the previous section.

4.6.1 Calculation of $\dot{\mathbf{m}}$

We no longer expand $\mathbf{m}$ in terms of spherical harmonics, but calculate it purely spatially. From equation (4.23), we simply have

$$\dot{m}^{\alpha\beta} = \frac{1}{\tau}(d^{\alpha\beta} - m^{\alpha\beta}), \tag{4.94}$$

where $m^{\alpha\beta}$ are the contravariant components of $\mathbf{m}$ and $d^{\alpha\beta}$ are the contravariant components of $\mathbf{d}$, the deviatoric strain tensor given by equation (4.19). To form the right hand side of this equation, we must take the product of two spatially varying fields. This is very easy in the spatial domain, but harder in the spherical harmonic domain; it is for this reason that we calculate the components of $\mathbf{m}$ spatially. As discussed below, we still calculate the spherical harmonic coefficients of $\mathbf{u}$, and so we must calculate the spatial contravariant components $d^{\alpha\beta}$ from these spherical harmonic coefficients.

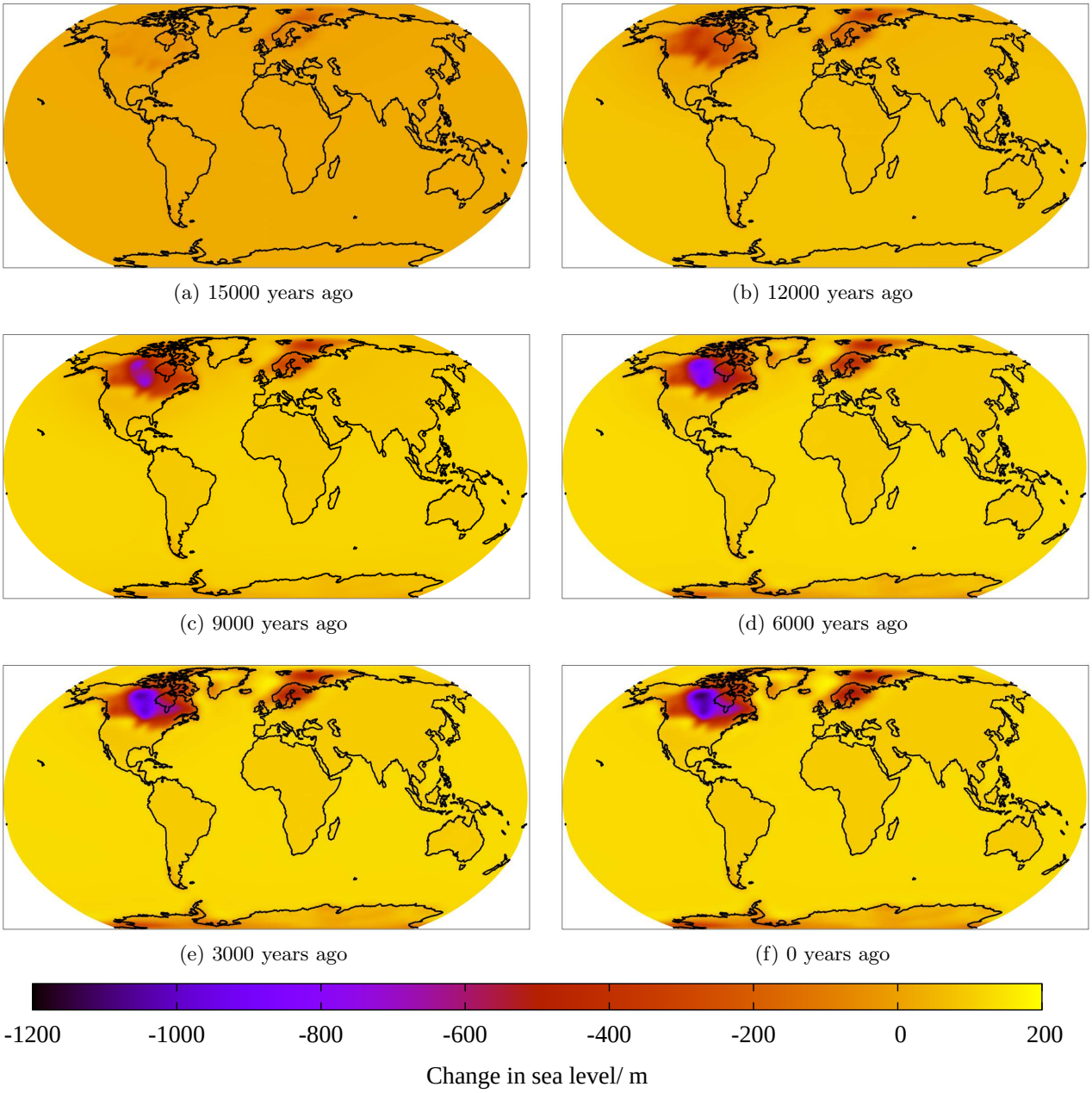

(a) 15000 years ago

(b) 12000 years ago

(c) 9000 years ago

(d) 6000 years ago

(e) 3000 years ago

(f) 0 years ago

Figure 4.5: The change in sea level from 21000 years ago at different times as calculated using the method described in this chapter. The change in sea level is shown (a) 15000 years ago, (b) 12000 years ago, (c) 9000 years ago, (d) 6000 years ago, (e) 3000 years ago and (f) at the present day. We note that, whilst the sea level appears to change discontinuously at the coast lines, the change is in fact continuous but occurs over a small distance.

4.6.2 Calculation of $\dot{\mathbf{u}}$ and $\dot{\phi}$

We recall that the equation for $\dot{\mathbf{u}}$ and $\dot{\phi}$ is

$$\begin{aligned}&\mathcal{A}(\dot{\mathbf{u}}, \dot{\phi} \,|\, \mathbf{u}', \phi') - \frac{\rho_w}{g} \int_{\partial M} \left[\dot{\mathbf{u}} \cdot \nabla\Phi + \dot{\phi} - \frac{1}{A} \int_{\partial M} C(\dot{\mathbf{u}} \cdot \nabla\Phi + \dot{\phi}) \, \mathrm{d}S \right] C(\mathbf{u}' \cdot \nabla\Phi + \phi') \, \mathrm{d}S \\ &= \int_{M_S} \frac{2\mu_0}{\tau} (\mathbf{d} - \mathbf{m}) : \mathbf{d}' \, \mathrm{d}V - \rho_i \int_{\partial M} (1 - C) \dot{I} \left[\mathbf{u}' \cdot \nabla\Phi + \phi' - \frac{1}{A} \int_{\partial M} C(\mathbf{u}' \cdot \nabla\Phi + \phi') \, \mathrm{d}S \right] \mathrm{d}S,\end{aligned} \tag{4.95}$$

and that it was convenient to introduce the spherical harmonic coefficients U_{lm}, V_{lm} and W_{lm} for the displacement, as defined in equations (4.70) and (4.71). We further recall that, in the spherically symmetric case, the system decouple into two sets of equations – the spheroidal equations involving U_{lm}, V_{lm} and ϕ_{lm} and the toroidal equations involving W_{lm}. As the load is in the vertical direction, the toroidal system is not excited when the structure is spherically symmetric. However, once we allow the viscosity to vary laterally, the two systems of equations no longer decouple and so the toroidal system is also excited. Schematically, we can write the two systems as

$$\mathbf{A}_l^s \dot{\mathbf{w}}_{lm}^s + \mathbf{g}_{lm}(\dot{u}_r, \dot{\phi}) = \mathbf{f}_{lm}^s \tag{4.96}$$

$$\mathbf{A}_l^t \dot{\mathbf{w}}_{lm}^t = \mathbf{f}_{lm}^t \tag{4.97}$$

where the s and t superscripts indicate the spheroidal and toroidal terms respectively. The terms in the spheroidal equation are as defined in section 4.5.3. $\dot{\mathbf{w}}_{lm}^t$ contains, for particular values of l and m, the coefficient $\dot{W}_{lm}$ at each radial node in turn. $\mathbf{A}_l^t$ and $\mathbf{f}_{lm}^t$ are constructed by taking $W_{lm}'^*$ to be equal to one at each radial node in turn and zero elsewhere.

Let us consider the forms of $\mathbf{f}_{lm}^s$ and $\mathbf{f}_{lm}^t$, which come from the terms on the right hand side of equation (4.95), in more detail. The second term, due to the surface load, has only spheroidal components and, as it is independent of the viscosity, is the same for both the spherically symmetric and laterally varying cases. However, the first term on the right hand side is dependent on the viscosity (through τ) and so, in order to work out the components of $\mathbf{f}_{lm}^s$ and $\mathbf{f}_{lm}^t$, we require the spherical harmonic coefficients of $\frac{1}{\tau}(\mathbf{d} - \mathbf{m})$.

Therefore, to calculate $\dot{\mathbf{u}}$ and $\dot{\phi}$ we:

1. find the spherical harmonic coefficients of the tensor $\frac{1}{\tau}(\mathbf{d} - \mathbf{m})$ from the tensor as a function of space, which was constructed in order to calculate $\dot{\mathbf{m}}$;

2. calculate $\mathbf{f}_{lm}^s$ and $\mathbf{f}_{lm}^t$;

3. find $\dot{\mathbf{w}}_{lm}^t$ by evaluating
$$\dot{\mathbf{w}}_{lm}^t = [\mathbf{A}_l^t]^{-1} \mathbf{f}_{lm}^t; \tag{4.98}$$

4. find $\dot{\mathbf{w}}_{lm}^s$ iteratively, as discussed in section 4.5.3.

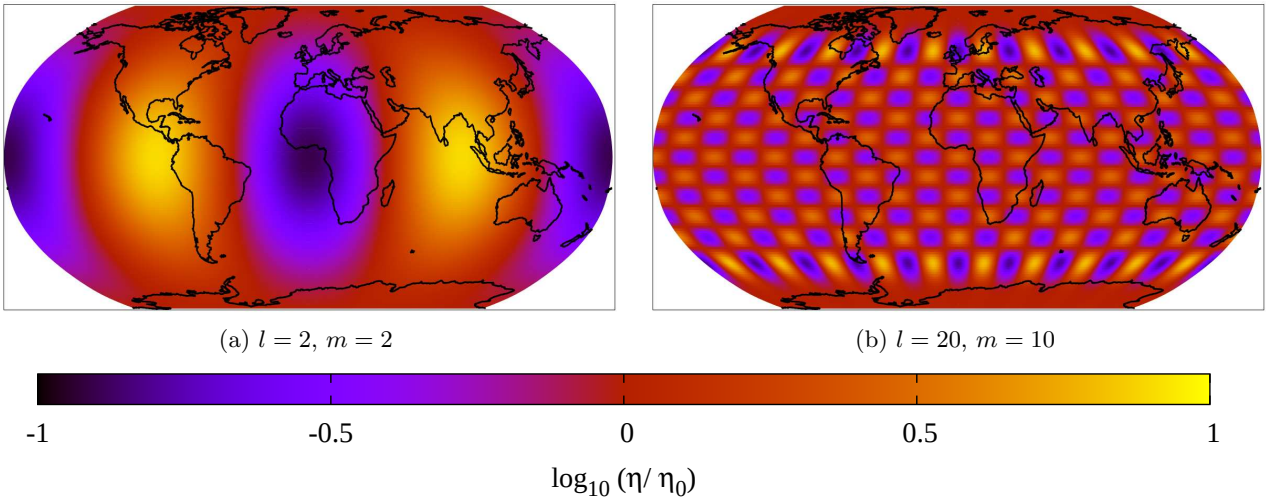

(a) $l = 2$, $m = 2$ (b) $l = 20$, $m = 10$

Figure 4.6: The lateral variations in viscosity, at all depths in the mantle, relative to a spherically symmetric background structure, η_0, due to a spherical harmonic perturbation as given in equation (4.99). The spherical harmonic perturbations have (a) $l = 2$ and $m = 2$, and (b) $l = 20$ and $m = 10$. We note that, in our case, in the upper mantle $\eta_0 = 5 \times 10^{20}$ Pa s while in the lower mantle $\eta_0 = 5 \times 10^{21}$ Pa s. The difference in sea level change from 21000 years ago at different times between that calculated with a spherically symmetric viscosity structure as in figure 4.5 and that calculated with these structures is shown in (a) figure 4.7 and (b) figure 4.8.

4.6.3 Numerical examples – spherical harmonic viscosity variation

We first consider a simple viscosity perturbation with the form of a single real spherical harmonic of degree l and order m. The laterally varying viscosity is given by

$$\eta(r, \theta, \phi) = \eta_0(r) e^{A[Y^0_{lm}(\theta,\phi) + (-1)^m Y^0_{l-m}(\theta,\phi)]}, \tag{4.99}$$

where A is a constant which determines the magnitude of the variations and the combination of Y^0_{lm} and Y^0_{l-m} is chosen so as to make the perturbation real. We present two examples of forward calculations performed with such a viscosity structure. One has $l = 2$ and $m = 2$ while the other has $l = 20$ and $m = 10$. In both cases, A was chosen so that the viscosity varies by approximately one order of magnitude on either side of the radial viscosity structure, η_0, which is the same structure as used in the spherically symmetric calculations (section 4.5.5). The resulting perturbations relative to η_0 are shown in figure 4.6. In figure 4.7, we plot the difference in sea level change from 21000 years ago at different times between that calculated with the spherically symmetric viscosity structure, η_0, as shown in figure 4.5 and that calculated with the laterally varying viscosity structure given in equation (4.99) with $l = 2$ and $m = 2$. Figure 4.8 is the corresponding figure for the viscosity variation with $l = 20$ and $m = 10$.

4.6.4 Numerical examples – viscosity variation scaled from S20RTS

We now present numerical examples calculated with a viscosity structure obtained by scaling the shear wave velocity model S20RTS (Ritsema *et al.*, 1999). We note that the form of this scaling in the Earth is not well known; however, in this case, we simply wish to have a three-dimensional viscosity structure with which to perform calculations and so the physicality of the scaling is unimportant. In order to

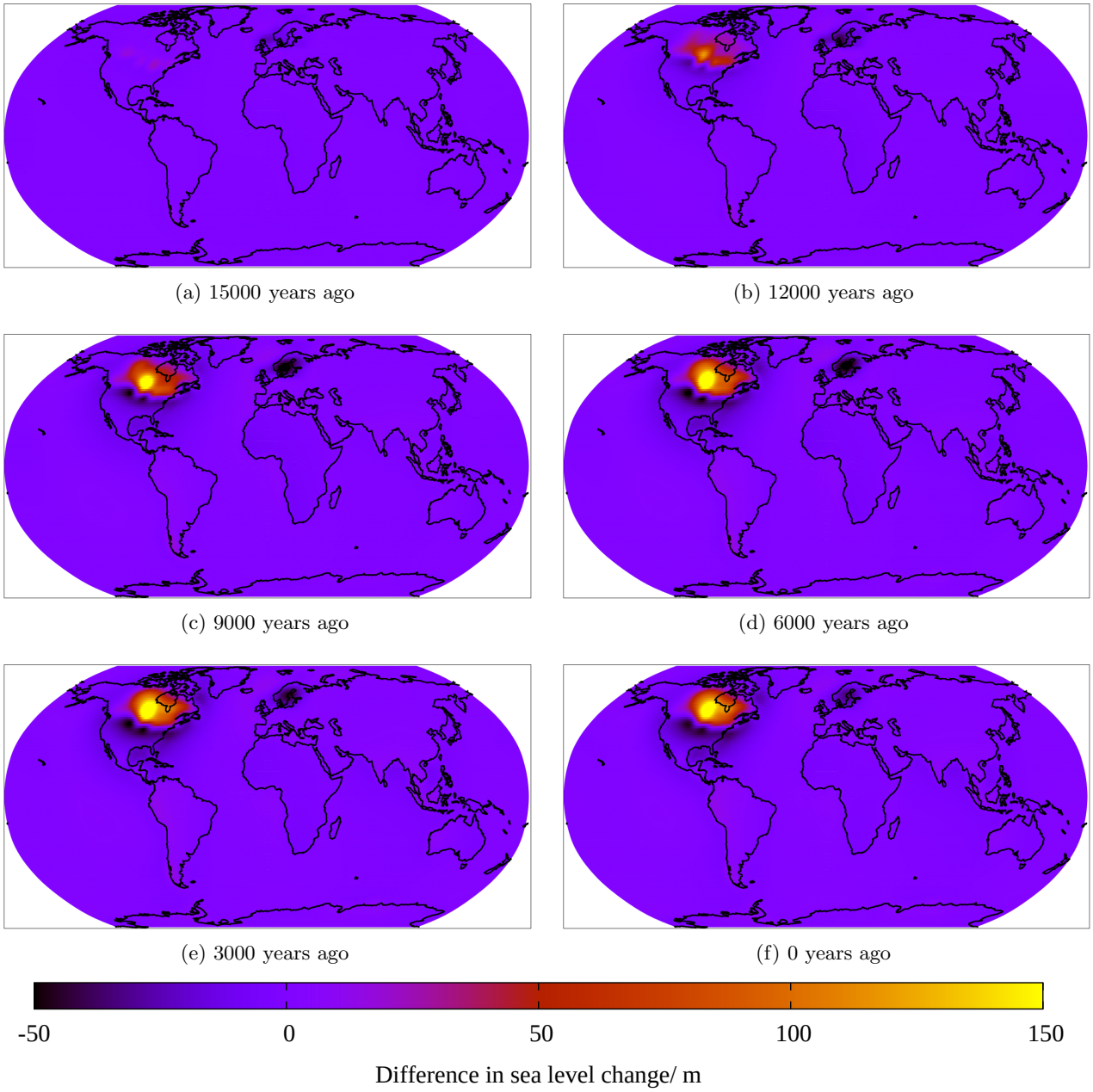

Figure 4.7: The difference in sea level change from 21000 years ago at different times between that calculated with a spherically symmetric viscosity structure as in figure 4.5 and that calculated with the laterally varying viscosity structure given in equation (4.99) with $l = 2$ and $m = 2$. The difference in sea level change is shown (a) 15000 years ago, (b) 12000 years ago, (c) 9000 years ago, (d) 6000 years ago, (e) 3000 years ago and (f) at the present day.

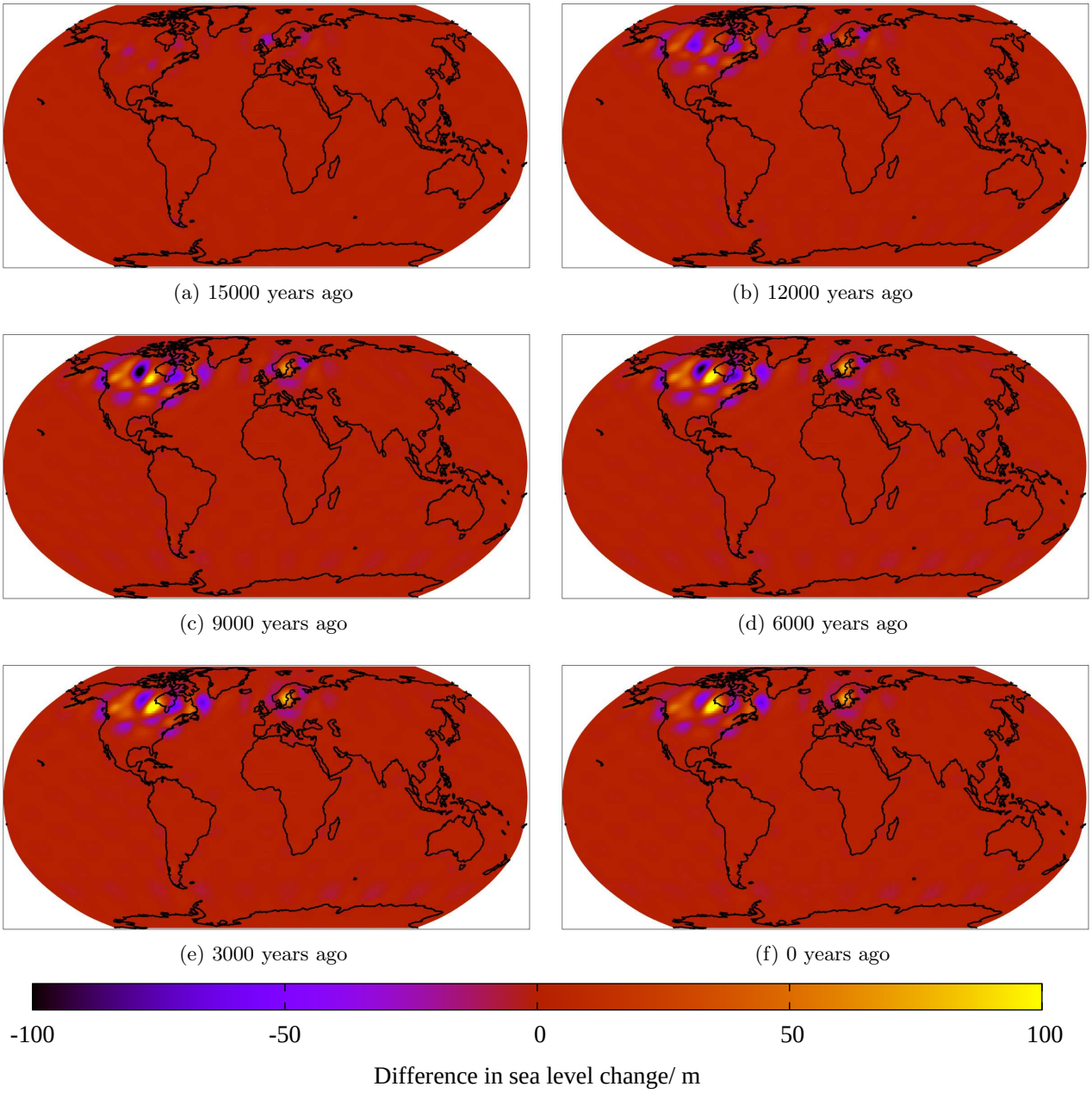

(a) 15000 years ago

(b) 12000 years ago

(c) 9000 years ago

(d) 6000 years ago

(e) 3000 years ago

(f) 0 years ago

Figure 4.8: The difference in sea level change from 21000 years ago at different times between that calculated with a spherically symmetric viscosity structure as in figure 4.5 and that calculated with the laterally varying viscosity structure given in equation (4.99) with $l = 20$ and $m = 10$. The difference in sea level change is shown (a) 15000 years ago, (b) 12000 years ago, (c) 9000 years ago, (d) 6000 years ago, (e) 3000 years ago and (f) at the present day.

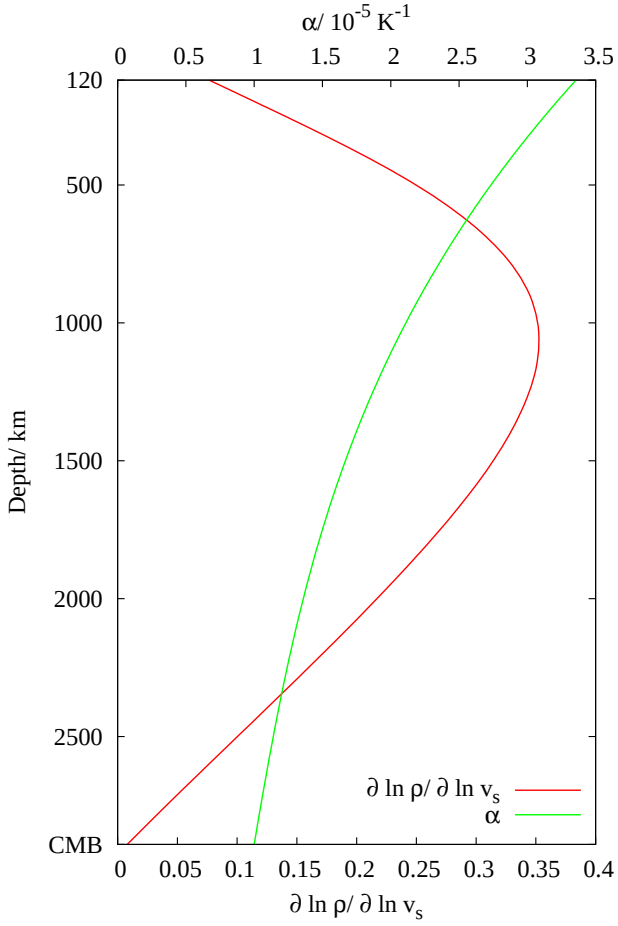

Figure 4.9: Coefficients $\frac{\partial \ln \rho}{\partial \ln v_s}$ and α, used to calculate viscosity perturbations from shear wave velocity perturbations, plotted as a function of depth in the mantle.

obtain a suitable relationship between the shear wave velocity and the viscosity, we follow Latychev *et al.* (2005). Firstly, the relative density variation from the spherical background is calculated from the relative shear wave velocity variation through

$$\delta \ln \rho(r, \theta, \phi) = \frac{\partial \ln \rho}{\partial \ln v_s}(r) \delta \ln v_s(r, \theta, \phi). \tag{4.100}$$

For the depth-dependent scaling from velocity to density, $\frac{\partial \ln \rho}{\partial \ln v_s}(r)$, Latychev *et al.* (2005) follow Forte & Woodward (1997). We show this scaling as a function of depth in figure 4.9. The percentage variations in density are then scaled to temperature variations through

$$\delta T(r, \theta, \phi) = -\frac{1}{\alpha(r)} \delta \ln \rho(r, \theta, \phi), \tag{4.101}$$

where the depth-dependent coefficient of thermal expansion, $\alpha(r)$, is taken from Chopelas & Boehler (1992) and is plotted in figure 4.9.

Finally, the lateral variations in viscosity are calculated from the temperature variations so that

$$\eta(r, \theta, \phi) = \eta_0(r) e^{-\epsilon \delta T(r, \theta, \phi)}, \tag{4.102}$$

where η_0 is the spherically symmetric background viscosity structure and ϵ is a parameter which controls the magnitude of the viscosity variations. In the examples that follow, we choose η_0 to be the viscosity structure used in the section 4.5 and $\epsilon = 0.01K^{-1}$.

Several depth slices of the resulting viscosity structure are shown in figure 4.10. In figure 4.11, we show the difference between the change in sea level due to this three-dimensional structure and the change in sea level due to a spherically symmetric viscosity, as shown in figure 4.5.

4.7 Conclusion

In this chapter, we have presented a new method for modelling glacial isostatic adjustment in compressible and heterogeneous earth models. We derive evolution equations which can be numerically integrated; this formulation means we avoid the need to solve the sea level equation and we accommodate shoreline migration more easily. We also present numerical examples calculated in both spherically symmetric earth models and those that allow lateral variations in viscosity structure. Our main motivation for this forward method is that it allows us to apply the adjoint method to the inverse problem. This is discussed in the next chapter.

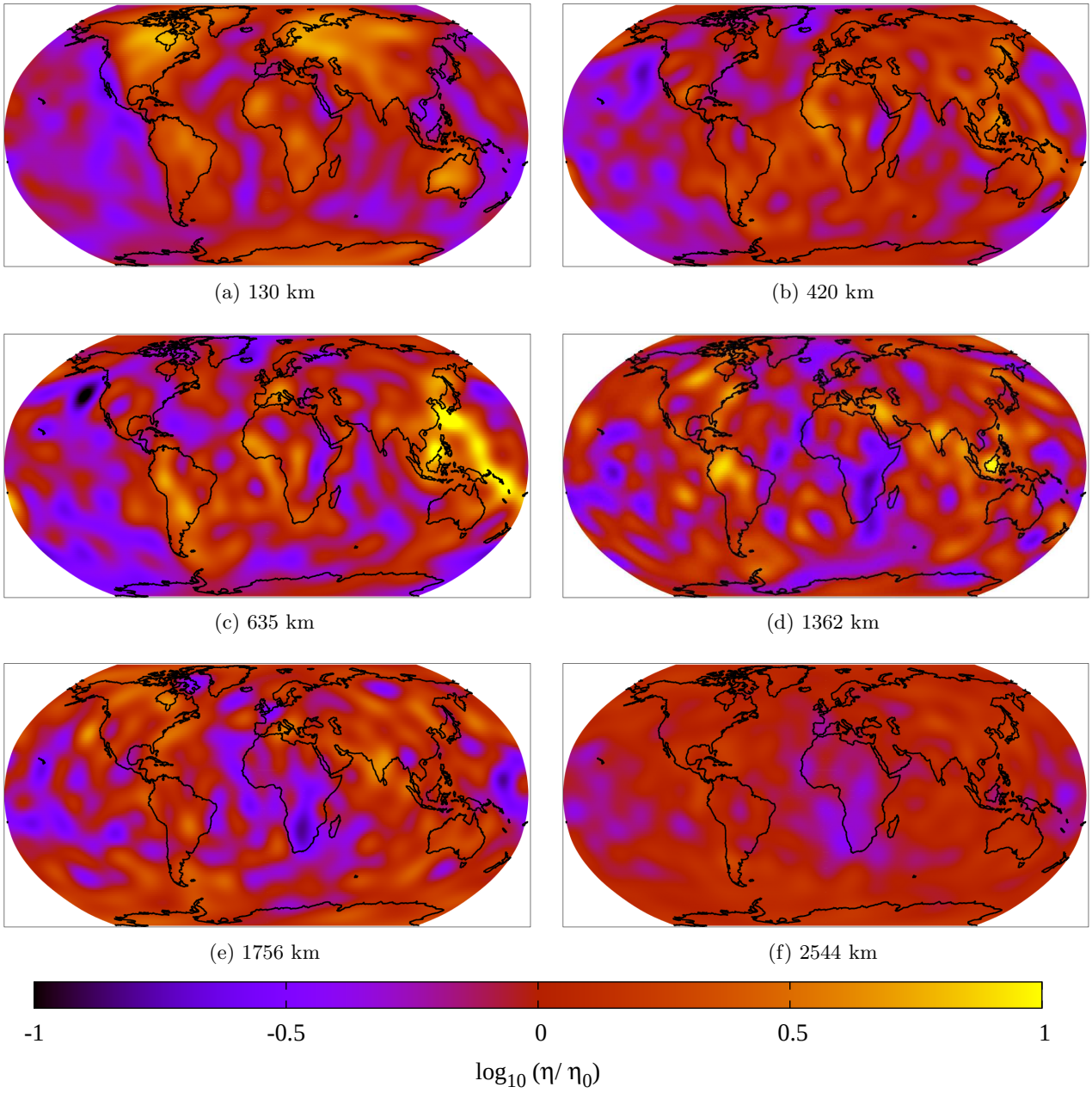

(a) 130 km

(b) 420 km

(c) 635 km

(d) 1362 km

(e) 1756 km

(f) 2544 km

Figure 4.10: The lateral variations in viscosity relative to a spherically symmetric background structure, η_0, due to scaling the shear wave velocity model S20RTS. We note that, in our case, in the upper mantle $\eta_0 = 5 \times 10^{20}$ Pa s while in the lower mantle $\eta_0 = 5 \times 10^{21}$ Pa s. The variation is shown at depths of (a) 130 km, (b) 420 km, (c) 635 km, (d) 1362 km, (e) 1756 km and (f) 2544 km. The difference in sea level change from 21000 years ago at different times between that calculated with a spherically symmetric viscosity structure as in figure 4.5 and that calculated with this structure is shown in figure 4.11.

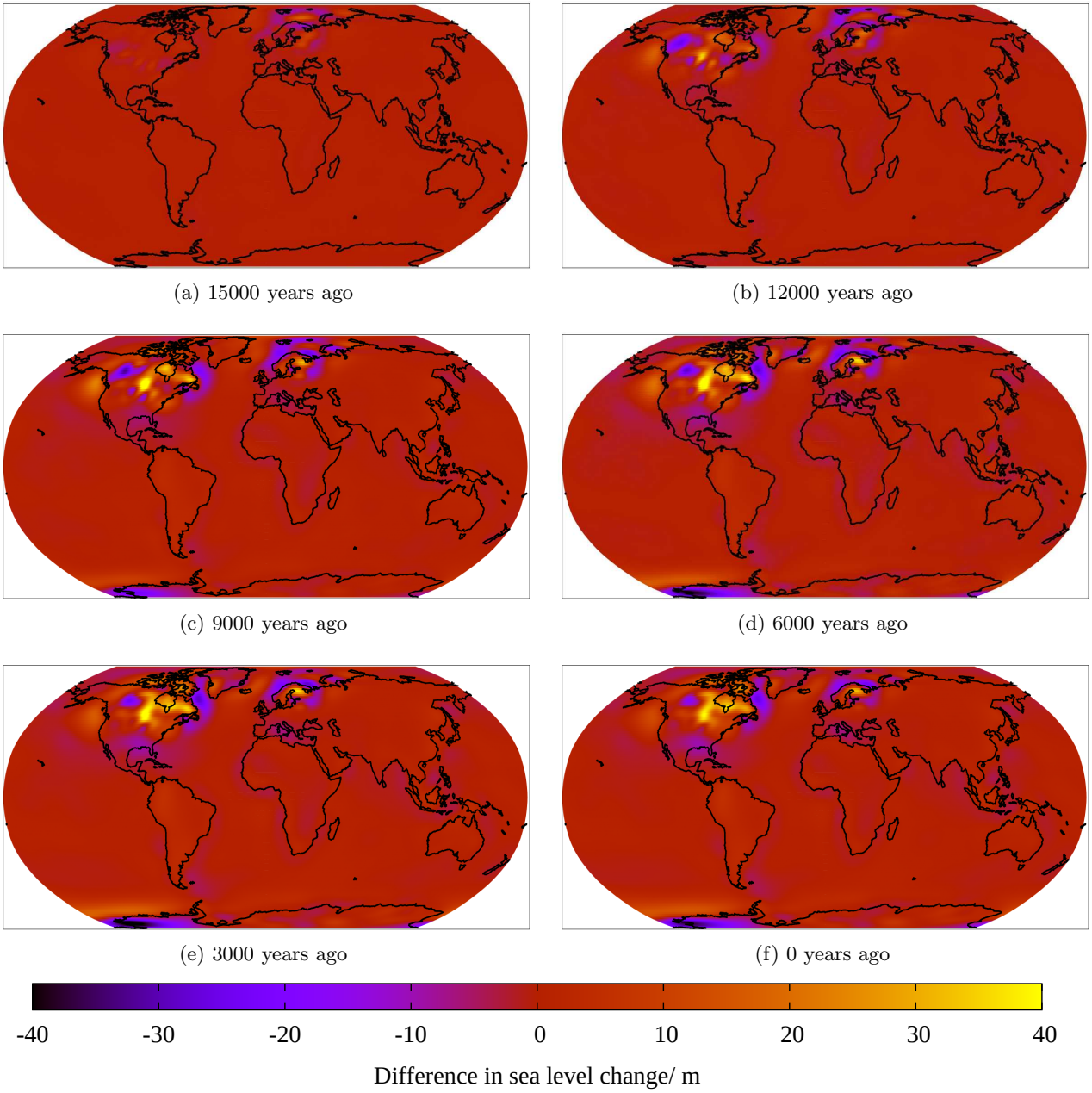

(a) 15000 years ago

(b) 12000 years ago

(c) 9000 years ago

(d) 6000 years ago

(e) 3000 years ago

(f) 0 years ago

Figure 4.11: The difference in sea level change from 21000 years ago at different times between that calculated with a spherically symmetric viscosity structure as in figure 4.5 and that calculated with the laterally varying viscosity structure discussed in section 4.6.4 and shown in figure 4.10. The difference in sea level change is shown (a) 15000 years ago, (b) 12000 years ago, (c) 9000 years ago, (d) 6000 years ago, (e) 3000 years ago and (f) at the present day.

Chapter 5

Inverse modelling of post-glacial deformation

5.1 Introduction

We now wish to turn our attention to the glacial isostatic inverse problem, that is, using measurements of GIA to learn about the model parameters – the viscosity, the ice sheet variation and the initial sea level. When considering the inverse problem, it would be useful to have a way of calculating the derivatives of measurements with respect to the parameters we wish to determine. Such derivatives provide a measure of the sensitivity of a given measurement to the model and have a number of potential applications within the inverse problem. Firstly, they could be used within a gradient-based optimisation method to find a model that minimises some data misfit function (e.g., Nocedal & Wright, 1999). The derivatives could also be used to quantify the uncertainty in such a model and hence to provide understanding of which parts of the model are well constrained. Finally, the derivatives could enable construction of measurements which provide sensitivity to a particular part of the model space in the manner of Backus & Gilbert (1968).

We would expect the Earth's viscosity to vary continuously, both radially and laterally, and there is increasing evidence that the neglect of lateral variations is incompatible with observations and can lead to significant errors within inferences of paleo-climatological interest (e.g., Lambeck & Chappell, 2001; A *et al.*, 2013; Van der Wal *et al.*, 2015; Creveling *et al.*, 2017). We would therefore like to be able to calculate derivatives of measurements with respect to continuous, three-dimensional variations in viscosity structure. Furthermore, we would like to be able to calculate derivatives with respect to ice sheet history. While there now exist a range of computational tools for modelling GIA within laterally heterogeneous Earth models (e.g., Zhong *et al.*, 2003; Wu, 2004; Latychev *et al.*, 2005), it is less clear how they can be used effectively within inverse studies to investigate Earth structure and ice sheet history. Forward calculations within three-dimensional models are sufficiently time consuming and involve such a large number of parameters that methods based on trial-and-error or grid-searches are unfeasible.

The theory in this chapter is, in part, based on unpublished notes written by David Al-Attar and Jeroen Tromp prior to the commencement of this PhD.

As an alternative, the adjoint method (e.g., Lions, 1970) provides an efficient way of calculating the derivatives we desire and has been used in a number of geophysical applications (e.g., Bunge *et al.*, 2003; Tromp *et al.*, 2005; Li *et al.*, 2011). The first application of adjoint methods to GIA was Al-Attar & Tromp (2014), who considered the sensitivity of viscoelastic deformation to surface loads and the viscosity structure. Since then, Martinec *et al.* (2015) applied the method in order to calculate the sensitivity of measurements to viscosity for GIA including sea level. Furthermore, Larour *et al.* (2017) have recently calculated the sensitivity of specific locations to present-day mass loss, but address only elastic, and not viscoelastic, deformation. This paper also makes use of a technique known as automatic differentiation as opposed to deriving the adjoint equations.

In this chapter, we make use of the forward formulation presented in the previous chapter, which allows us to apply the adjoint method (see section 1.3.3) to the inverse problem. We use this method to derive equations for the sensitivity of measurements of GIA to both the viscosity structure of the Earth and to the ice sheet history. Our formulation is entirely independent of that of Martinec *et al.* (2015), and is more general and and convenient for practical GIA applications. In particular, we present kernels for three-dimensional viscosity perturbations and with respect to ice sheet history. Furthermore, in contrast to Larour *et al.* (2017), we derive the exact adjoint equations, an approach that is more elegant and flexible than, and offers numerical advantages over, automatic differentiation. The method is illustrated with numerical examples calculated in a spherically symmetric earth model.

5.2 Example objective functionals

There are a variety of measurements of which we might wish to calculate the derivative. In general, for the GIA problem, we can write $J(\mathbf{u}, \phi, SL)$ and so the first-order perturbation of the objective functional with respect to the forward variables is

$$\delta J = \int_{t_0}^{t_1} \int_{\partial M} \left(\dot{\mathbf{h}}_{\mathbf{u}} \cdot \delta \mathbf{u} + \dot{h}_{\phi} \, \delta \phi + \dot{h}_{SL} \, \delta SL \right) \mathrm{d}S \, \mathrm{d}t, \tag{5.1}$$

where $\dot{\mathbf{h}}_{\mathbf{u}}$, $\dot{h}_{\phi}$ and $\dot{h}_{SL}$ are the Fréchet derivatives of J with respect to $\mathbf{u}$, ϕ and SL respectively. We note that these are written as time derivatives for later convenience. We are ignoring any possible explicit dependence of the objective functional on the model parameters, as might be introduced through regularisation, but its addition would be trivial.

In this section, we will consider two example objective functionals – a point sea level measurement and a spherical harmonic gravitational potential measurement. Further examples of objective functionals are considered in appendix C of Al-Attar & Tromp (2014).

5.2.1 Point sea level measurement

Firstly, we will consider the case of a sea level point measurement – the sea level at a particular time and location. In this case, the objective functional can be written as

$$J(SL) = \int_{t_0}^{t_1} \int_{\partial M} SL(\mathbf{x}, t) \, \delta(\mathbf{x} - \mathbf{x}_d) \, \delta(t - t_d) \, \mathrm{d}S \, \mathrm{d}t, \tag{5.2}$$

where $\mathbf{x}_d$ and t_d are the location and time of the measurement respectively. Therefore,

$$\delta J = \int_{t_0}^{t_1} \int_{\partial M} \delta SL(\mathbf{x}, t)\, \delta(\mathbf{x} - \mathbf{x}_d)\, \delta(t - t_d)\, \mathrm{d}S\, \mathrm{d}t, \tag{5.3}$$

and so the Fréchet derivatives are

$$\dot{\mathbf{h}}_{\mathbf{u}} = \mathbf{0}, \quad \dot{h}_\phi = 0, \quad \dot{h}_{SL} = \delta(\mathbf{x} - \mathbf{x}_d)\, \delta(t - t_d). \tag{5.4}$$

5.2.2 Spherical harmonic gravitational potential measurement

We will now consider a measurement of a particular spherical harmonic component of the Earth's gravitational potential. This is akin to the measurements made by the Gravity Recovery and Climate Experiment (GRACE) satellites.

The gravitational potential field, ϕ^E, can be expanded in terms of spherical harmonics as

$$\phi^E = \sum_{l,m} \phi^E_{lm} \mathcal{Y}_{lm}, \tag{5.5}$$

where $\mathcal{Y}_{lm}$ is the real spherical harmonic of degree l and order m as defined in appendix B of Dahlen & Tromp (1998). These spherical harmonics are orthonormal so that

$$\int_\Omega \mathcal{Y}_{lm} \mathcal{Y}_{l'm'}\, \mathrm{d}\Omega = \delta_{ll'} \delta_{mm'}. \tag{5.6}$$

Therefore, the objective functional for a measurement of a particular component of the gravitational potential at time t_d, $\phi^E_{l_d m_d}(t_d)$ is

$$J = \int_{t_0}^{t_1} \int_{\partial M} \phi^E(\mathbf{x}, t)\, \mathcal{Y}_{l_d m_d}\, \delta(t - t_d)\, \mathrm{d}S\, \mathrm{d}t. \tag{5.7}$$

Therefore

$$\delta J = \int_{t_0}^{t_1} \int_{\partial M} \delta\phi(\mathbf{x}, t)\, \mathcal{Y}_{l_d m_d}\, \delta(t - t_d)\, \mathrm{d}S\, \mathrm{d}t \tag{5.8}$$

and so

$$\dot{\mathbf{h}}_{\mathbf{u}} = \mathbf{0}, \quad \dot{h}_\phi = \mathcal{Y}_{l_d m_d}\, \delta(t - t_d), \quad \dot{h}_{SL} = 0. \tag{5.9}$$

5.3 The Lagrangian

We now need to construct the Lagrangian, as in equation (1.20), for the GIA problem. We find that it is

$$\begin{aligned} L = & J(\mathbf{u}, \phi, SL) - \rho_w g \int_{\partial M} [SL(t_0) - SL_0] SL_0' \, \mathrm{d}S + \rho_i g \int_{\partial M} [I(t_0) - I_0] I_0' \, \mathrm{d}S \\ & + \int_{t_0}^{t_1} \left\{ \mathcal{A}(\dot{\mathbf{u}}, \dot{\phi} | \mathbf{u}', \phi') - \int_{M_S} 2\mu_0 \left[\dot{\mathbf{m}} : \mathbf{m}' + \frac{1}{\tau} (\mathbf{d} - \mathbf{m}) : (\mathbf{d}' - \mathbf{m}') \right] \mathrm{d}V \right. \\ & - \rho_w g \int_{\partial M} \dot{SL} \, SL' \, \mathrm{d}S - \rho_i g \int_{\partial M} (\dot{I}_1 - \dot{I}) I' \, \mathrm{d}S \\ & - \frac{\rho_w}{g} \int_{\partial M} \left[\dot{\mathbf{u}} \cdot \nabla \Phi + \dot{\phi} - \frac{1}{A} \int_{\partial M} C(\dot{\mathbf{u}} \cdot \nabla \Phi + \dot{\phi}) \, \mathrm{d}S \right] [g SL' + C(\mathbf{u}' \cdot \nabla \Phi + \phi')] \, \mathrm{d}S \\ & \left. + \rho_i \int_{\partial M} (1 - C) \dot{I}_1 \left[\mathbf{u}' \cdot \nabla \Phi + \phi' - \frac{1}{A} \int_{\partial M} [g SL' + C(\mathbf{u}' \cdot \nabla \Phi + \phi')] \, \mathrm{d}S \right] \mathrm{d}S \right\} \mathrm{d}t, \end{aligned} \tag{5.10}$$

where $J(\mathbf{u}, \phi, SL)$ is the chosen observable, the weak form is inside the time integral and we have introduced the test functions SL_0' and I_0' to impose the initial conditions given by equations (4.40) and (4.37).

5.4 Deriving the adjoint equations

By solving the forward problem as described in the previous chapter, we have found the solution to equation (1.23). In order to construct the derivative of our measurement, we must also find the solution of (1.22), that is, solve the adjoint equations. We must first derive the adjoint equations by perturbing the Lagrangian with respect to each of the forward variables and setting the perturbations equal to zero. Our forward variables are $\mathbf{u}$, ϕ, $\mathbf{m}$, SL and I. In doing so, it will be useful to write

$$\delta J = \int_{t_0}^{t_1} \int_{\partial M} (\dot{\mathbf{h}}_{\mathbf{u}} \cdot \delta \mathbf{u} + \dot{h}_\phi \delta \phi + \dot{h}_{SL} \delta SL) \, \mathrm{d}S \, \mathrm{d}t, \tag{5.11}$$

where we are assuming the objective functional is a function of displacement, gravitational potential and sea level only.

5.4.1 Perturbation of the Lagrangian with respect to SL

We first consider perturbations of the Lagrangian with respect to SL, and find

$$\begin{aligned}
\delta L = &\int_{t_0}^{t_1}\int_{\partial M} \dot{h}_{SL}\delta SL\,\mathrm{d}S\;\mathrm{d}t - \rho_w g\int_{\partial M}\delta SL(t_0)\,SL_0'\,\mathrm{d}S - \rho_w g\int_{\partial M}\delta\dot{SL}\,SL'\,\mathrm{d}S\\
&+\int_{t_0}^{t_1}\Bigg\{\frac{\rho_w}{g}\left[\int_{\partial M}\delta C(\dot{\mathbf{u}}\cdot\nabla\Phi+\dot{\phi})\,\mathrm{d}S\right]\left[\int_{\partial M}\frac{1}{A}[gSL'+C(\mathbf{u}'\cdot\nabla\Phi+\phi')]\,\mathrm{d}S\right]\\
&\quad-\frac{\rho_w}{g}\left[\int_{\partial M}C(\dot{\mathbf{u}}\cdot\nabla\Phi+\dot{\phi})\,\mathrm{d}S\right]\left[\int_{\partial M}\frac{1}{A^2}[gSL'+C(\mathbf{u}'\cdot\nabla\Phi+\phi')]\,\mathrm{d}S\right]\left[\int_{\partial M}\delta C\,\mathrm{d}S\right]\\
&\quad-\frac{\rho_w}{g}\int_{\partial M}\left[\dot{\mathbf{u}}\cdot\nabla\Phi+\dot{\phi}-\frac{1}{A}\int_{\partial M}C(\dot{\mathbf{u}}\cdot\nabla\Phi+\dot{\phi})\,\mathrm{d}S\right]\delta C(\mathbf{u}'\cdot\nabla+\phi')\,\mathrm{d}S\\
&\quad-\rho_i\int_{\partial M}\delta C\,\dot{I}_1\left[\mathbf{u}'\cdot\nabla\Phi+\phi'-\frac{1}{A}\int_{\partial M}[gSL'+C(\mathbf{u}'\cdot\nabla\Phi+\phi')]\,\mathrm{d}S\right]\mathrm{d}S\\
&\quad-\rho_i\left[\int_{\partial M}\frac{(1-C)}{A}\dot{I}_1\,\mathrm{d}S\right]\left[\int_{\partial M}\delta C(\mathbf{u}'\cdot\nabla\Phi+\phi')\,\mathrm{d}S\right]\\
&\quad+\rho_i\left[\int_{\partial M}\frac{(1-C)}{A^2}\dot{I}_1\,\mathrm{d}S\right]\left[\int_{\partial M}[gSL'+C(\mathbf{u}'\cdot\nabla\Phi+\phi')]\,\mathrm{d}S\right]\left[\int_{\partial M}\delta C\,\mathrm{d}S\right]\Bigg\}\,\mathrm{d}t, \qquad (5.12)
\end{aligned}$$

where δC denotes the first order perturbation of C with respect to SL. Collecting terms and integrating by parts with respect to time to remove the time derivative of the perturbation, we find

$$\begin{aligned}
\delta L =&\rho_w g\int_{\partial M}\{\delta SL(t_0)[SL'(t_0)-SL_0']-\delta SL(t_1)SL'(t_1)\}\,\mathrm{d}S+\int_{t_0}^{t_1}\Bigg\{\int_{\partial M}\delta SL(\dot{h}_{SL}+\rho_w g\dot{SL}')\,\mathrm{d}S\\
&-\int_{\partial M}\delta C\left[\frac{\rho_w}{g}(\dot{\mathbf{u}}\cdot\nabla\Phi+\dot{\phi})-\frac{\rho_w}{gA}\int_{\partial M}C(\dot{\mathbf{u}}\cdot\nabla\Phi+\dot{\phi})\,\mathrm{d}S+\rho_i\dot{I}_1+\frac{\rho_i}{A}\int_{\partial M}(1-C)\dot{I}_1\,\mathrm{d}S\right]\\
&\left[\mathbf{u}'\cdot\nabla\Phi+\phi'-\frac{1}{A}\int_{\partial M}[gSL'+C(\mathbf{u}'\cdot\nabla\Phi+\phi')]\,\mathrm{d}S\right]\mathrm{d}S\Bigg\}\,\mathrm{d}t. \qquad (5.13)
\end{aligned}$$

In order to eliminate the terms outside the time integral, we impose the conditions

$$SL'(t_1)=0,\quad SL_0'=SL'(t_0). \qquad (5.14)$$

We recall that

$$\dot{SL}=-\frac{1}{g}(\dot{\mathbf{u}}\cdot\nabla\Phi+\dot{\phi})+\frac{1}{gA}\int_{\partial M}C(\dot{\mathbf{u}}\cdot\nabla\Phi+\dot{\phi})\,\mathrm{d}S-\frac{\rho_i}{\rho_w}\int_{\partial M}(1-C)\dot{I}_1\,\mathrm{d}S, \qquad (5.15)$$

and so equation (5.13) can be written as

$$\begin{aligned}
\delta L = &\int_{t_0}^{t_1}\Bigg\{\int_{\partial M}(\dot{h}_{SL}+\rho_w g\dot{SL}')\delta SL\,\mathrm{d}S\\
&-\int_{\partial M}\delta C(\rho_i\dot{I}_1-\rho_w\dot{SL})\left[\mathbf{u}'\cdot\nabla\Phi+\phi'-\frac{1}{A}\int_{\partial M}[gSL'+C(\mathbf{u}'\cdot\nabla\Phi+\phi')]\,\mathrm{d}S\right]\mathrm{d}S\Bigg\}\,\mathrm{d}t.
\end{aligned} \qquad (5.16)$$

From equation (4.44), we can see that

$$\delta C=\frac{\rho_{\mathrm{w}}\delta SL-\rho_{\mathrm{i}}\delta I}{\rho_{\mathrm{w}}\partial_\perp SL-\rho_{\mathrm{i}}\partial_\perp I}\delta_{\partial\mathcal{O}_t}. \qquad (5.17)$$

Using this along with equations (4.38) and (4.44), we can write

$$(\rho_w \dot{SL} - \rho_i \dot{I}_1)\delta C = (\rho_w \dot{SL} - \rho_i \dot{I})\delta C = \rho_w \dot{C} \delta SL \tag{5.18}$$

and so

$$\delta L = \int_{t_0}^{t_1} \int_{\partial M} \left\{ \dot{h}_{SL} + \rho_w g \dot{SL}' + \rho_w \dot{C} \left[\mathbf{u}' \cdot \nabla\Phi + \phi' - \frac{1}{A} \int_{\partial M} [gSL' + C(\mathbf{u}' \cdot \nabla\Phi + \phi')] \, \mathrm{d}S \right] \right\} \mathrm{d}S \, \mathrm{d}t. \tag{5.19}$$

Therefore, setting the variation of L with respect to SL to be equal to zero, we have

$$\dot{SL}' + \frac{\dot{h}_{SL}}{\rho_w g} + \frac{\dot{C}}{g} \left[\mathbf{u}' \cdot \nabla\Phi + \phi' - \frac{1}{A} \int_{\partial M} [gSL' + C(\mathbf{u}' \cdot \nabla\Phi + \phi')] \, \mathrm{d}S \right] = 0. \tag{5.20}$$

5.4.2 Perturbation of the Lagrangian with respect to I

We now consider perturbations of the Lagrangian with respect to I. In this case,

$$\begin{aligned} \delta L =& \rho_i g \int_{\partial M} \{\delta I(t_0)[I_0' - I'(t_0)] + \delta I(t_1) I'(t_1)\} \, \mathrm{d}S \\ & - \rho_i g \int_{t_0}^{t_1} \int_{\partial M} \delta I \, \dot{I}' \, \mathrm{d}S \, \mathrm{d}t \\ & - \int_{t_0}^{t_1} \int_{\partial M} \delta C (\rho_i \dot{I}_1 - \rho_w \dot{SL}) \left[\mathbf{u}' \cdot \nabla\Phi + \phi' - \frac{1}{A} \int_{\partial M} [gSL' + C(\mathbf{u}' \cdot \nabla\Phi + \phi')] \, \mathrm{d}S \right] \mathrm{d}S \, \mathrm{d}t. \end{aligned} \tag{5.21}$$

where δC denotes the first order perturbation of C with respect to I, we have used equation (5.15) and we have integrated by parts with respect to time. In order to eliminate the terms outside the time integral, we impose the conditions

$$I'(t_1) = 0, \quad I_0' = I'(t_0). \tag{5.22}$$

Using equations (4.38), (4.44) and (5.17), we can write

$$(\rho_w \dot{SL} - \rho_i \dot{I}_1)\delta C = (\rho_w \dot{SL} - \rho_i \dot{I})\delta C = -\rho_i \dot{C} \delta I, \tag{5.23}$$

and so

$$\delta L = \int_{t_0}^{t_1} \left\{ -\rho_i g \int_{\partial M} \delta I \, \dot{I}' \, \mathrm{d}S - \int_{\partial M} \rho_i \dot{C} \delta I \left[\mathbf{u}' \cdot \nabla\Phi + \phi' - \frac{1}{A} \int_{\partial M} [gSL' + C(\mathbf{u}' \cdot \nabla\Phi + \phi')] \, \mathrm{d}S \right] \mathrm{d}S \right\} \mathrm{d}t. \tag{5.24}$$

Setting the variation of L with respect to I to be equal to zero, we therefore have

$$\dot{I}' + \frac{\dot{C}}{g} \left[\mathbf{u}' \cdot \nabla\Phi + \phi' - \frac{1}{A} \int_{\partial M} [gSL' + C(\mathbf{u}' \cdot \nabla\Phi + \phi')] \, \mathrm{d}S \right] = 0. \tag{5.25}$$

5.4.3 Perturbation of the Lagrangian with respect to u, ϕ and m

Finally, we consider perturbations of the Lagrangian with respect to $\mathbf{u}$, ϕ and $\mathbf{m}$, and so find

$$\delta L = \int_{t_0}^{t_1} \left\{ \int_{\partial M} (\dot{\mathbf{h}}_{\mathbf{u}} \cdot \delta\mathbf{u} + \dot{h_\phi}\delta\phi)\,\mathrm{d}S + \mathcal{A}(\delta\dot{\mathbf{u}}, \delta\dot{\phi}|\mathbf{u}', \phi') - \int_{\partial M} 2\mu_0 \left[\delta\dot{\mathbf{m}} : \mathbf{m}' + \frac{1}{\tau}(\delta\mathbf{d} - \delta\mathbf{m}) : (\mathbf{d}' - \mathbf{m}') \right] \mathrm{d}V \right.$$
$$\left. -\frac{\rho_w}{g} \int_{\partial M} \left[\delta\dot{\mathbf{u}} \cdot \nabla\Phi + \delta\dot{\phi} - \frac{1}{A}\int_{\partial M} C(\delta\dot{\mathbf{u}} \cdot \nabla\Phi + \delta\dot{\phi})\,\mathrm{d}S \right] [gSL' + C(\mathbf{u}' \cdot \nabla\Phi + \phi')]\,\mathrm{d}S \right\} \mathrm{d}t. \tag{5.26}$$

To eliminate the time derivatives of the perturbations, we can integrate this equation by parts with respect to time. We find

$$\delta L = \int_{t_0}^{t_1} \left\{ \int_{\partial M} (\dot{\mathbf{h}}_{\mathbf{u}} \cdot \delta\mathbf{u} + \dot{h}_\phi\delta\phi)\,\mathrm{d}S - \mathcal{A}(\delta\mathbf{u}, \delta\phi|\dot{\mathbf{u}}', \dot{\phi}') + \int_{\partial M} 2\mu_0 \left[\delta\mathbf{m} : \dot{\mathbf{m}}' - \frac{1}{\tau}(\delta\mathbf{d} - \delta\mathbf{m}) : (\mathbf{d}' - \mathbf{m}') \right] \mathrm{d}V \right.$$
$$+\frac{\rho_w}{g} \int_{\partial M} \left[\delta\mathbf{u} \cdot \nabla\Phi + \delta\phi - \frac{1}{A}\int_{\partial M} C(\delta\mathbf{u} \cdot \nabla\Phi + \delta\phi)\,\mathrm{d}S \right] [g\dot{S}L' + C(\dot{\mathbf{u}}' \cdot \nabla\Phi + \dot{\phi}') + \dot{C}(\mathbf{u}' \cdot \nabla\Phi + \phi')]\,\mathrm{d}S$$
$$\left. -\frac{\rho_w}{gA} \int_{\partial M} \dot{C} \left[\delta\mathbf{u} \cdot \nabla\Phi + \delta\phi - \frac{1}{A}\int_{\partial M} C(\delta\mathbf{u} \cdot \nabla\Phi + \delta\phi)\,\mathrm{d}S \right] [gSL' + C(\mathbf{u}' \cdot \nabla\Phi + \phi')]\,\mathrm{d}S \right\} \mathrm{d}t, \tag{5.27}$$

where we have imposed the terminal conditions

$$\mathbf{u}'(t_1) = \mathbf{0}, \quad \phi'(t_1) = 0, \quad \mathbf{m}'(t_1) = \mathbf{0}. \tag{5.28}$$

The terms in the second and third rows of equation (5.27) arise because

$$\int_{t_0}^{t_1} \left[\delta\dot{\mathbf{u}} \cdot \nabla\Phi + \delta\dot{\phi} - \frac{1}{A}\int_{\partial M} C(\delta\dot{\mathbf{u}} \cdot \nabla\Phi + \delta\dot{\phi})\,\mathrm{d}S \right] \mathrm{d}t$$
$$= \left[\delta\mathbf{u} \cdot \nabla\Phi + \delta\phi - \frac{1}{A}\int_{\partial M} C(\delta\mathbf{u} \cdot \nabla\Phi + \delta\phi)\,\mathrm{d}S \right]_{t_0}^{t_1}$$
$$+ \int_{t_0}^{t_1} \frac{1}{A}\int_{\partial M} \dot{C} \left[\delta\mathbf{u} \cdot \nabla\Phi + \delta\phi - \frac{1}{A}\int_{\partial M} C(\delta\mathbf{u} \cdot \nabla\Phi + \delta\phi)\,\mathrm{d}S \right] \mathrm{d}S\,\mathrm{d}t. \tag{5.29}$$

Using equation (5.20), we can write

$$g\dot{S}L' + \dot{C}(\mathbf{u}' \cdot \nabla\Phi + \phi') = -\frac{\dot{h}_{SL}}{\rho_w} + \frac{\dot{C}}{A}\int_{\partial M} [gSL' + C(\mathbf{u}' \cdot \nabla\Phi + \phi')]\,\mathrm{d}S. \tag{5.30}$$

Substituting this into equation (5.27), and after some rearrangement and cancelling of terms, we find

$$\delta L = \int_{t_0}^{t_1} \left\{ \int_{\partial M} (\dot{\mathbf{h}}_{\mathbf{u}} \cdot \delta\mathbf{u} + \dot{h}_\phi\delta\phi)\,\mathrm{d}S - \mathcal{A}(\delta\mathbf{u}, \delta\phi|\dot{\mathbf{u}}', \dot{\phi}') \right.$$
$$+ \int_{\partial M} 2\mu_0 \left[\delta\mathbf{m} : \dot{\mathbf{m}}' - \frac{1}{\tau}(\delta\mathbf{d} - \delta\mathbf{m}) : (\mathbf{d}' - \mathbf{m}') \right] \mathrm{d}V$$
$$\left. -\frac{\rho_w}{g} \int_{\partial M} \left[\delta\mathbf{u} \cdot \nabla\Phi + \delta\phi - \frac{1}{A}\int_{\partial M} C(\delta\mathbf{u} \cdot \nabla\Phi + \delta\phi)\,\mathrm{d}S \right] \left[\frac{\dot{h}_{SL}}{\rho_w} - C(\dot{\mathbf{u}}' \cdot \nabla\Phi + \dot{\phi}') \right] \mathrm{d}S \right\} \mathrm{d}t, \tag{5.31}$$

and so, setting this variation equal to zero, we have

$$\int_{\partial M}(\dot{\mathbf{h}}_{\mathbf{u}}\cdot\delta\mathbf{u}+\dot{h}_{\phi}\delta\phi)\,\mathrm{d}S-\mathcal{A}(\delta\mathbf{u},\delta\phi|\dot{\mathbf{u}}',\dot{\phi}')+\int_{\partial M}2\mu_0\left[\delta\mathbf{m}:\dot{\mathbf{m}}'-\frac{1}{\tau}(\delta\mathbf{d}-\delta\mathbf{m}):(\mathbf{d}'-\mathbf{m}')\right]\mathrm{d}V$$
$$+\frac{\rho_w}{g}\int_{\partial M}\left[\dot{\mathbf{u}}'\cdot\nabla\Phi+\dot{\phi}'-\frac{1}{A}\int_{\partial M}C(\dot{\mathbf{u}}'\cdot\nabla\Phi+\dot{\phi}')\,\mathrm{d}S\right]C(\delta\mathbf{u}\cdot\nabla\Phi+\delta\phi)\,\mathrm{d}S$$
$$-\frac{1}{g}\int_{\partial M}\dot{h}_{SL}\left[\delta\mathbf{u}\cdot\nabla\Phi+\delta\phi-\frac{1}{A}\int_{\partial M}C(\delta\mathbf{u}\cdot\nabla\Phi+\delta\phi)\,\mathrm{d}S\right]\mathrm{d}S=0. \tag{5.32}$$

This equation is left in the weak form as this is all that is needed for numerical calculations.

5.4.4 The adjoint equations

It is convenient to introduce adjoint variables, defined by

$$\mathbf{u}^{\dagger}(t)=\mathbf{u}'(t_1-t+t_0), \tag{5.33}$$
$$\phi^{\dagger}(t)=\phi'(t_1-t+t_0), \tag{5.34}$$
$$\mathbf{m}^{\dagger}(t)=\mathbf{m}'(t_1-t+t_0), \tag{5.35}$$
$$SL^{\dagger}(t)=SL'(t_1-t+t_0), \tag{5.36}$$
$$I^{\dagger}(t)=I'(t_1-t+t_0), \tag{5.37}$$

which satisfy the initial conditions

$$\mathbf{u}^{\dagger}(t_0)=\mathbf{0},\quad \phi^{\dagger}(t_0)=0,\quad \mathbf{m}^{\dagger}(t_0)=\mathbf{0},\quad SL^{\dagger}(t_0)=0,\quad I^{\dagger}(t_0)=0. \tag{5.38}$$

Similarly, we define the adjoint ocean function and adjoint ocean area through

$$C^{\dagger}(t)=C(t-t_1+t_0), \tag{5.39}$$
$$A^{\dagger}(t)=A(t-t_1+t_0), \tag{5.40}$$

and finally define adjoint sources as

$$\mathbf{h}^{\dagger}_{\mathbf{u}}(t)=\mathbf{h}_{\mathbf{u}}(t_1-t+t_0), \tag{5.41}$$
$$h^{\dagger}_{\phi}(t)=h_{\phi}(t_1-t+t_0), \tag{5.42}$$
$$h^{\dagger}_{SL}(t)=h_{SL}(t_1-t+t_0). \tag{5.43}$$

Using these definitions, we can rewrite equations (5.20), (5.25) and (5.32) as

$$\dot{SL}^\dagger = -\frac{\dot{h}^\dagger_{SL}}{\rho_w g} - \frac{\dot{C}^\dagger}{g}\left[\mathbf{u}^\dagger\cdot\nabla\Phi + \phi^\dagger - \frac{1}{A^\dagger}\int_{\partial M}[gSL^\dagger + C^\dagger(\mathbf{u}^\dagger\cdot\nabla\Phi+\phi^\dagger)]\,\mathrm{d}S\right], \tag{5.44}$$

$$\dot{I}^\dagger = -\frac{\dot{C}^\dagger}{g}\left[\mathbf{u}^\dagger\cdot\nabla\Phi + \phi^\dagger - \frac{1}{A^\dagger}\int_{\partial M}[gSL^\dagger + C^\dagger(\mathbf{u}^\dagger\cdot\nabla\Phi+\phi^\dagger)]\,\mathrm{d}S\right] = \dot{SL}^\dagger + \frac{\dot{h}^\dagger_{SL}}{\rho_w g}, \tag{5.45}$$

$$\begin{aligned}&\mathcal{A}(\dot{\mathbf{u}}^\dagger,\dot{\phi}^\dagger|\mathbf{u},\phi) - \int_{\partial M} 2\mu_0\left[\dot{\mathbf{m}}^\dagger:\mathbf{m} + \frac{1}{\tau}(\mathbf{d}^\dagger-\mathbf{m}^\dagger):(\mathbf{d}-\mathbf{m})\right]\mathrm{d}V - \int_{\partial M}(\dot{\mathbf{h}}^\dagger_{\mathbf{u}}\cdot\mathbf{u} + \dot{h}^\dagger_\phi\phi)\,\mathrm{d}S\\ &- \frac{\rho_w}{g}\int_{\partial M}\left[\dot{\mathbf{u}}^\dagger\cdot\nabla\Phi + \dot{\phi}^\dagger - \frac{1}{A^\dagger}\int_{\partial M} C^\dagger(\dot{\mathbf{u}}^\dagger\cdot\nabla\Phi+\dot{\phi}^\dagger)\,\mathrm{d}S\right]C^\dagger(\mathbf{u}\cdot\nabla\Phi+\phi)\,\mathrm{d}S\\ &+ \frac{1}{g}\int_{\partial M}\dot{h}^\dagger_{SL}\left[\mathbf{u}\cdot\nabla\Phi+\phi - \frac{1}{A^\dagger}\int_{\partial M}C^\dagger(\mathbf{u}\cdot\nabla\Phi+\phi)\,\mathrm{d}S\right]\mathrm{d}S = 0,\end{aligned} \tag{5.46}$$

where we have also written the test functions $\delta\mathbf{u}$, $\delta\phi$ and $\delta\mathbf{m}$ as $\mathbf{u}$, ϕ and $\mathbf{m}$. These equations, along with the initial conditions given in equation (5.38), constitute the adjoint problem.

5.4.5 Solving the adjoint sea level and ice equations

Equations (5.44) and (5.45) are singular and so cannot be straightforwardly numerically integrated. Instead, we define a new variable, $Q^\dagger$, which satisfies

$$Q^\dagger = SL^\dagger + \frac{h^\dagger_{SL}}{\rho_w g} + \frac{C^\dagger}{g}\left[\mathbf{u}^\dagger\cdot\nabla\Phi+\phi^\dagger - \frac{1}{A^\dagger}\int_{\partial M}[gSL^\dagger + C^\dagger(\mathbf{u}^\dagger\cdot\nabla\Phi+\phi^\dagger)]\,\mathrm{d}S\right]. \tag{5.47}$$

Therefore,

$$\begin{aligned}\dot{Q}^\dagger =& \dot{SL}^\dagger + \frac{\dot{h}^\dagger_{SL}}{\rho_w g} + \frac{\dot{C}^\dagger}{g}\left[\mathbf{u}^\dagger\cdot\nabla\Phi+\phi^\dagger - \frac{1}{A^\dagger}\int_{\partial M}[gSL^\dagger + C^\dagger(\mathbf{u}^\dagger\cdot\nabla\Phi+\phi^\dagger)]\,\mathrm{d}S\right]\\ &+ \frac{C^\dagger}{g}\left[\dot{\mathbf{u}}^\dagger\cdot\nabla\Phi+\dot{\phi}^\dagger - \frac{1}{A^\dagger}\int_{\partial M}[g\dot{SL}^\dagger + C^\dagger(\dot{\mathbf{u}}^\dagger\cdot\nabla\Phi+\dot{\phi}^\dagger) + \dot{C}^\dagger(\mathbf{u}^\dagger\cdot\nabla\Phi+\phi^\dagger)]\,\mathrm{d}S\right]\\ &+ \frac{C^\dagger}{gA^\dagger}\left[\int_{\partial M}\dot{C}^\dagger\,\mathrm{d}S\right]\left[\frac{1}{A^\dagger}\int_{\partial M}[gSL^\dagger + C^\dagger(\mathbf{u}^\dagger\cdot\nabla\Phi+\phi^\dagger)]\,\mathrm{d}S\right],\end{aligned} \tag{5.48}$$

which, using equation (5.15), simplifies to

$$\dot{Q}^\dagger = \frac{C^\dagger}{g}\left[\dot{\mathbf{u}}^\dagger\cdot\nabla\Phi+\dot{\phi}^\dagger + \frac{1}{\rho_w A^\dagger}\int_{\partial M}\dot{h}^\dagger_{SL}\,\mathrm{d}S - \frac{1}{A^\dagger}\int_{\partial M}C^\dagger(\dot{\mathbf{u}}^\dagger\cdot\nabla\Phi+\dot{\phi}^\dagger)\,\mathrm{d}S\right]. \tag{5.49}$$

We also note that

$$Q^\dagger(t_0) = \frac{h^\dagger_{SL}(t_0)}{\rho_w g}. \tag{5.50}$$

We further define $P^\dagger$ to be

$$P^\dagger = \frac{1}{gA^\dagger}\int_{\partial M}[gSL^\dagger + C^\dagger(\mathbf{u}^\dagger\cdot\nabla\Phi+\phi^\dagger)]\,\mathrm{d}S, \tag{5.51}$$

which satisfies

$$\begin{aligned}\dot{P}^\dagger =&\frac{1}{A^\dagger}\int_{\partial M}\dot{SL}^\dagger\,\mathrm{d}S-\frac{1}{gA^\dagger}\left[\int_{\partial M}\dot{C}\,\mathrm{d}S\right]\left[\frac{1}{A^\dagger}\int_{\partial M}[gSL^\dagger+C^\dagger(\mathbf{u}^\dagger\cdot\nabla\Phi+\phi^\dagger)]\,\mathrm{d}S\right]\\&+\frac{1}{gA^\dagger}\int_{\partial M}\dot{C}^\dagger(\mathbf{u}^\dagger\cdot\nabla\Phi+\phi^\dagger)\,\mathrm{d}S+\frac{1}{gA^\dagger}\int_{\partial M}C^\dagger(\dot{\mathbf{u}}^\dagger\cdot\nabla\Phi+\dot{\phi}^\dagger)\,\mathrm{d}S,\end{aligned}\tag{5.52}$$

and, again using equation (5.15), this simplifies to

$$\dot{P}^\dagger=\frac{1}{gA^\dagger}\int_{\partial M}C^\dagger(\dot{\mathbf{u}}^\dagger\cdot\nabla\Phi+\dot{\phi}^\dagger)\,\mathrm{d}S-\frac{1}{\rho_w gA^\dagger}\int_{\partial M}\dot{h}^\dagger_{SL}\,\mathrm{d}S.\tag{5.53}$$

We also see that

$$P^\dagger(t_0)=0.\tag{5.54}$$

Both equation (5.49) and equation (5.53) can be straightforwardly integrated. It is therefore useful to write $SL^\dagger$ in terms of these two fields, and so we find

$$SL^\dagger=Q^\dagger+C^\dagger P^\dagger-\frac{h^\dagger_{SL}}{\rho_w g}-\frac{C^\dagger}{g}(\mathbf{u}^\dagger\cdot\nabla\Phi+\phi^\dagger).\tag{5.55}$$

Using equation (5.45), we can also write

$$I^\dagger=Q^\dagger+C^\dagger P^\dagger-\frac{C^\dagger}{g}(\mathbf{u}^\dagger\cdot\nabla\Phi+\phi^\dagger)-\frac{h^\dagger_{SL}(t_0)}{\rho_w g}.\tag{5.56}$$

5.4.6 Elastic adjoint equations

It will also be useful to form the equations for when there is a jump in adjoint load. In this case, the equations become

$$\Delta Q^\dagger=\frac{C^\dagger}{g}\left[\Delta\mathbf{u}^\dagger\cdot\nabla\Phi+\Delta\phi^\dagger+\frac{1}{\rho_w A^\dagger}\int_{\partial M}\Delta h^\dagger_{SL}\,\mathrm{d}S-\frac{1}{A^\dagger}\int_{\partial M}C^\dagger(\Delta\mathbf{u}^\dagger\cdot\nabla\Phi+\Delta\phi^\dagger)\,\mathrm{d}S\right],\tag{5.57}$$

$$\Delta P^\dagger=\frac{1}{gA^\dagger}\int_{\partial M}C^\dagger(\Delta\mathbf{u}^\dagger\cdot\nabla\Phi+\Delta\phi^\dagger)\,\mathrm{d}S-\frac{1}{\rho_w gA^\dagger}\int_{\partial M}\Delta h^\dagger_{SL}\,\mathrm{d}S,\tag{5.58}$$

$$\begin{aligned}&\mathcal{A}(\Delta\mathbf{u}^\dagger,\Delta\phi^\dagger|\delta\mathbf{u},\delta\phi)-\int_{\partial M}(\Delta\mathbf{h}^\dagger_{\mathbf{u}}\cdot\delta\mathbf{u}+\Delta h^\dagger_\phi\delta\phi)\,\mathrm{d}S\\&-\frac{\rho_w}{g}\int_{\partial M}\left[\Delta\mathbf{u}^\dagger\cdot\nabla\Phi+\Delta\phi^\dagger-\frac{1}{A^\dagger}\int_{\partial M}C^\dagger(\Delta\mathbf{u}^\dagger\cdot\nabla\Phi+\Delta\phi^\dagger)\,\mathrm{d}S\right]C^\dagger(\delta\mathbf{u}\cdot\nabla\Phi+\delta\phi)\,\mathrm{d}S\\&+\frac{1}{g}\int_{\partial M}\Delta h^\dagger_{SL}\left[\delta\mathbf{u}\cdot\nabla\Phi+\delta\phi-\frac{1}{A^\dagger}\int_{\partial M}C^\dagger(\delta\mathbf{u}\cdot\nabla\Phi+\delta\phi)\,\mathrm{d}S\right]\mathrm{d}S=0,\end{aligned}\tag{5.59}$$

and we can calculate $SL^\dagger$ and $I^\dagger$ using equations (5.55) and (5.56) respectively.

5.5 Sensitivity kernels

Given the solutions of the forward and adjoint problems, we are able to calculate the sensitivity of particular measurements (such as the example given in section 5.2) to the parameters. We now need to derive the form of the sensitivity kernels for the different parameters using equation (1.21). In doing

so, we will find it useful to use the adjoint definitions to rewrite the Lagrangian in equation (5.10) as

$$
\begin{aligned}
L = J + \int_{t_0}^{t_1} \Bigg\{ & \mathcal{A}(\dot{\mathbf{u}}, \dot{\phi} | \mathbf{u}^\dagger, \phi^\dagger) - \int_{M_S} 2\mu_0 \left[\dot{\mathbf{m}} : \mathbf{m}^\dagger + \frac{1}{\tau}(\mathbf{d} - \mathbf{m}) : (\mathbf{d}^\dagger - \mathbf{m}^\dagger) \right] \mathrm{d}V \\
& - \rho_w g \int_{\partial M} \dot{SL}\, SL^\dagger \, \mathrm{d}S - \rho_i g \int_{\partial M} (\dot{I}_1 - \dot{I}) I^\dagger \, \mathrm{d}S \\
& - \frac{\rho_w}{g} \int_{\partial M} \left[\dot{\mathbf{u}} \cdot \nabla\Phi + \dot{\phi} - \frac{1}{A} \int_{\partial M} C(\dot{\mathbf{u}} \cdot \nabla\Phi + \dot{\phi}) \, \mathrm{d}S \right] [g SL^\dagger + C^\dagger (\mathbf{u}^\dagger \cdot \nabla\Phi + \phi^\dagger)] \, \mathrm{d}S \\
& + \rho_i \int_{\partial M} (1 - C) \dot{I}_1 \left[\mathbf{u}^\dagger \cdot \nabla\Phi + \phi^\dagger - \frac{1}{A^\dagger} \int_{\partial M} [g SL^\dagger + C^\dagger (\mathbf{u}^\dagger \cdot \nabla\Phi + \phi^\dagger)] \, \mathrm{d}S \right] \mathrm{d}S \Bigg\} \, \mathrm{d}t \\
& - \rho_w g \int_{\partial M} [SL(t_0) - SL_0] SL^\dagger(t_1) \, \mathrm{d}S + \rho_i g \int_{\partial M} [I(t_0) - I_0] I^\dagger(t_1) \, \mathrm{d}S,
\end{aligned} \tag{5.60}
$$

where, within the time integral, it is understood that all forward variables are evaluated at time t and all adjoint variables are evaluated at time $t_1 - t + t_0$. In what follows, we write the kernel for the model parameter p as K_p. We calculate the form of the kernels for viscosity, ice sheet thickness and initial sea level, but we could also consider the kernels for other parameters. For example, we could calculate the sensitivity to boundary perturbations, such as the thickness of the elastic lid, using a method similar to Liu & Tromp (2008) or through a so-called particle relabelling transformation (Al-Attar & Crawford, 2016).

5.5.1 Viscosity kernel

Perturbing the Lagrangian in equation (5.60) with respect to η, we find

$$
\delta \hat{J} = \int_{t_0}^{t_1} \int_{M_S} \frac{2\mu_0}{\tau} (\mathbf{d} - \mathbf{m}) : (\mathbf{d}^\dagger - \mathbf{m}^\dagger) \frac{\delta\eta}{\eta} \, \mathrm{d}V \, \mathrm{d}t. \tag{5.61}
$$

It will be useful to consider relative changes in viscosity, and so we define the viscosity sensitivity kernel such that

$$
\delta \hat{J} = \int_{M_S} K_\eta \frac{\delta\eta}{\eta} \, \mathrm{d}V. \tag{5.62}
$$

We therefore see that

$$
K_\eta = \int_{t_0}^{t_1} \frac{2\mu_0}{\tau} (\mathbf{d} - \mathbf{m}) : (\mathbf{d}^\dagger - \mathbf{m}^\dagger) \, \mathrm{d}t = \int_{t_0}^{t_1} \frac{1}{2\eta} \boldsymbol{\tau}(t) : \boldsymbol{\tau}^\dagger(t_1 - t + t_0) \, \mathrm{d}t, \tag{5.63}
$$

where we recall that the deviatoric stress, $\boldsymbol{\tau}$, is given by equation (4.25). It will also be useful to define the radial viscosity sensitivity kernel, $\overline{K}_\eta$, which is given by

$$
\overline{K}_\eta = \int_{\mathbb{S}^2} r^2 K_\eta \, \mathrm{d}S = \int_{t_1}^{t_2} \int_{\mathbb{S}^2} \frac{1}{2\eta} \boldsymbol{\tau}(t) : \boldsymbol{\tau}^\dagger(t_1 - t + t_0) \; r^2 \; \mathrm{d}S \; \mathrm{d}t, \tag{5.64}
$$

where $\mathbb{S}^2$ is the unit two-sphere. These equations have the same form as the equivalents in Al-Attar & Tromp (2014) and the post-seismic case discussed in chapter 3.

5.5.2 Ice kernels

We can first calculate the sensitivity of the objective functional to the initial ice thickness. This is defined such that

$$\delta\hat{J} = \int_{\partial M} K_{I_0}\delta I_0 \,\mathrm{d}S. \tag{5.65}$$

Perturbing the Lagrangian with respect to I_0, we find

$$\delta\hat{J} = -\rho_i g \int_{\partial M} I^\dagger(t_1)\delta I_0 \,\mathrm{d}S, \tag{5.66}$$

and so

$$K_{I_0} = -\rho_i g I^\dagger(t_1). \tag{5.67}$$

As discussed in Al-Attar & Tromp (2014), the kernel for the ice thickness at later times will be singular whenever there is a jump in the adjoint loads (as is the case when considering, for example, a point sea level measurement). However, the kernel for the rate of change of ice thickness remains non-singular with such loads. In deriving the kernel for ice coverage at later times, it is therefore most convenient to define it with respect to the rate of change of ice thickness, and so we write

$$\delta\hat{J} = \int_{t_0}^{t_1}\int_{\partial M} K_{\dot{I}_1}\delta\dot{I}_1 \,\mathrm{d}S\,\mathrm{d}t. \tag{5.68}$$

Perturbing the Lagrangian with respect to $\dot{I}_1$, we find

$$\delta\hat{J} = \int_{t_0}^{t_1}\int_{\partial M} \rho_i \left\{(1-C)\left[\mathbf{u}^\dagger\cdot\nabla\Phi + \phi^\dagger - \frac{1}{A}\int_{\partial M}[gSL^\dagger + C^\dagger(\mathbf{u}^\dagger\cdot\nabla\Phi+\phi^\dagger)]\,\mathrm{d}S\right] - gI^\dagger\right\}\delta\dot{I}_1 \,\mathrm{d}S\,\mathrm{d}t, \tag{5.69}$$

and so

$$K_{\dot{I}_1} = \rho_i(1-C)\left[\mathbf{u}^\dagger\cdot\nabla\Phi + \phi^\dagger - \frac{1}{A^\dagger}\int_{\partial M}[gSL^\dagger + C^\dagger(\mathbf{u}^\dagger\cdot\nabla\Phi+\phi^\dagger)]\,\mathrm{d}S\right] - \rho_i g I^\dagger, \tag{5.70}$$

where we again recall that forward variables are evaluated at time t whereas adjoint variables are evaluated at time $t_1 - t + t_0$.

5.5.3 Initial sea level kernel

Finally, we consider the sensitivity of the objective functional to the initial sea level. Perturbing the Lagrangian with respect to SL_0, we find that

$$\delta\hat{J} = \int_{\partial M} \rho_w g SL^\dagger(t_1)\delta SL_0 \,\mathrm{d}S, \tag{5.71}$$

and so

$$K_{SL_0} = \rho_w g SL^\dagger(t_1), \tag{5.72}$$

where we have chosen to define the kernel such that

$$\delta\hat{J} = \int_{\partial M} K_{SL_0}\delta SL_0 \,\mathrm{d}S. \tag{5.73}$$

One possible application of this kernel is to find the initial sea level such that the final sea level matches present day sea level as closely as possible. We define a misfit

$$J(SL) = \int_{\partial M} \frac{1}{2}[SL(\mathbf{x}, t_p) - SL_p(\mathbf{x})]^2 \, \mathrm{d}S, \tag{5.74}$$

where t_p is the time at the present day and SL_p is the measured sea level at this time. We would like to find the initial sea level, SL_0, that minimises this misfit. In order to do so, we require the gradient of equation (5.74) combined with some gradient-based optimisation method. We can use the adjoint method in order to calculate this gradient. Equation (5.74) is the objective functional and, perturbing it with respect to the forward variables, we see that

$$\delta J(SL) = \int_{\partial M} [SL(\mathbf{x}, t_p) - SL_p(\mathbf{x})] \, \delta SL(\mathbf{x}, t_p) \, \mathrm{d}S = \int_{t_0}^{t_1} \int_{\partial M} [SL(\mathbf{x}, t) - SL_p(\mathbf{x})] \, \delta SL(\mathbf{x}, t) \delta(t - t_p) \, \mathrm{d}S \, \mathrm{d}t, \tag{5.75}$$

and so,

$$\dot{\mathbf{h}}_{\mathbf{u}} = \mathbf{0}, \quad \dot{h}_{\phi} = 0, \quad \dot{h}_{SL} = [SL(\mathbf{x}, t_p) - SL_p(\mathbf{x})] \, \delta(t - t_p). \tag{5.76}$$

Therefore, in order to calculate the initial sea level which best fits the present day sea level, we

1. choose some first estimate of the initial sea level;
2. solve the forward problem to find the final sea level;
3. calculate the misfit given by equation (5.74) and the adjoint loads given by equation (5.76);
4. solve the elastic adjoint equations for the given load, as the kernel in equation (5.72) only requires the adjoint solution at time t_1;
5. construct the derivative given by equation (5.72);
6. using the derivative and some gradient-based optimisation method (e.g., the conjugate gradient method), calculate an updated initial sea level;
7. repeat steps (ii) to (vi) until the misfit in equation (5.74) is sufficiently small.

We present an example of this initial sea level inversion in section 5.6.8, and find the process converges in only a few iterations.

5.6 Numerical implementation in spherically symmetric earth models

In this section, we discuss an implementation of the adjoint equations in spherically symmetric earth models and present examples of sensitivity kernels calculated in such models.

5.6.1 Generalised spherical harmonic expansions

We can expand the adjoint fields in an analogous manner to the forward fields. Introducing coefficients $\phi^{\dagger}_{lm}$, $U^{\dagger}_{lm}$, $V^{\dagger}_{lm}$ and $W^{\dagger}_{lm}$, we write

$$\phi^{\dagger} = \sum_{l,m} \phi^{\dagger}_{lm} Y^0_{lm}, \tag{5.77}$$

and

$$u^{\dagger 0}_{lm} = U^{\dagger}_{lm}, \tag{5.78}$$

$$u^{\dagger \pm}_{lm} = \frac{k}{\sqrt{2}}(V^{\dagger}_{lm} \pm iW^{\dagger}_{lm}). \tag{5.79}$$

We can also write

$$m^{\dagger \pm\pm}_{lm} = \frac{k\sqrt{k^2-2}}{2r}(M^{\dagger}_{lm} \pm iN^{\dagger}_{lm}), \tag{5.80}$$

$$m^{\dagger 00}_{lm} = \frac{2}{3r}R^{\dagger}_{lm}, \tag{5.81}$$

$$m^{\dagger 0\pm}_{lm} = m^{\dagger \pm 0}_{lm} = \frac{k}{2\sqrt{2}r}(S^{\dagger}_{lm} \pm iT^{\dagger}_{lm}), \tag{5.82}$$

$$m^{\dagger \pm\mp}_{lm} = \frac{1}{3r}R^{\dagger}_{lm}, \tag{5.83}$$

where we have introduced the coefficients $M^{\dagger}_{lm}$, $N^{\dagger}_{lm}$, $R^{\dagger}_{lm}$, $S^{\dagger}_{lm}$ and $T^{\dagger}_{lm}$. As in the forward case, the spheroidal and toroidal systems of equations decouple. In what follows, we will assume that only the spheroidal system is excited. For a measurement with no toroidal component (such as a sea level measurement), this is a valid assumption. However, if we were, for example, to make a measurement of the horizontal displacement, we would need to solve the toroidal system of equations. This is considered in chapter 3.

5.6.2 Calculation of $\dot{\mathbf{m}}^{\dagger}$

We find that the components of $\dot{\mathbf{m}}^{\dagger}$ satisfy

$$\dot{M}^{\dagger}_{lm} = \frac{1}{\tau}(V^{\dagger}_{lm} - M^{\dagger}_{lm}), \tag{5.84}$$

$$\dot{R}^{\dagger}_{lm} = \frac{1}{\tau}\left(r\partial_r U^{\dagger}_{lm} - U^{\dagger}_{lm} + \frac{k^2}{2}V^{\dagger}_{lm} - R^{\dagger}_{lm}\right), \tag{5.85}$$

$$\dot{S}^{\dagger}_{lm} = \frac{1}{\tau}\left(r\partial_r V^{\dagger}_{lm} - V^{\dagger}_{lm} + U^{\dagger}_{lm} - S^{\dagger}_{lm}\right). \tag{5.86}$$

These equations have exactly the same form as those for the forward variables, and so we can use the same numerical code.

5.6.3 Calculation of $\dot{\mathbf{u}}^{\dagger}$ and $\dot{\phi}^{\dagger}$

In order to find $\dot{\mathbf{u}}^{\dagger}$ and $\dot{\phi}^{\dagger}$, we must solve

$$\begin{aligned}
&\mathcal{A}(\dot{\mathbf{u}}^{\dagger}, \dot{\phi}^{\dagger} | \mathbf{u}, \phi) - \int_{\partial M} 2\mu_0 \left[\dot{\mathbf{m}}^{\dagger} : \mathbf{m} + \frac{1}{\tau}(\mathbf{d}^{\dagger} - \mathbf{m}^{\dagger}) : (\mathbf{d} - \mathbf{m})\right] \mathrm{d}V - \int_{\partial M} (\dot{\mathbf{h}}^{\dagger}_{\mathbf{u}} \cdot \mathbf{u} + \dot{h}^{\dagger}_{\phi}\phi)\, \mathrm{d}S \\
&- \frac{\rho_w}{g}\int_{\partial M}\left[\dot{\mathbf{u}}^{\dagger} \cdot \nabla\Phi + \dot{\phi}^{\dagger} - \frac{1}{A^{\dagger}}\int_{\partial M} C^{\dagger}(\dot{\mathbf{u}}^{\dagger} \cdot \nabla\Phi + \dot{\phi}^{\dagger})\, \mathrm{d}S\right] C^{\dagger}(\mathbf{u} \cdot \nabla\Phi + \phi)\, \mathrm{d}S \\
&= -\frac{1}{g}\int_{\partial M} \dot{h}^{\dagger}_{SL}\left[\mathbf{u} \cdot \nabla\Phi + \phi - \frac{1}{A^{\dagger}}\int_{\partial M} C^{\dagger}(\mathbf{u} \cdot \nabla\Phi + \phi)\, \mathrm{d}S\right] \mathrm{d}S,
\end{aligned} \tag{5.87}$$

where we have simply rearranged equation (5.46) to have the terms independent of $\dot{\mathbf{u}}^\dagger$ and $\dot{\phi}^\dagger$ on the right hand side. Comparing this to equation (4.80), we see that the two differ only in the terms on the right hand side. We recall that in equation (5.87), $\mathbf{u}$ and ϕ are now the time-independent test functions, and the equation must hold for all choices. As in the forward case, we define the test functions in terms of the complex conjugates of the generalised spherical harmonics. We can now find $\dot{\mathbf{u}}^\dagger$ and $\dot{\phi}^\dagger$ by following the same method as outlined in section 4.5.3. We will find that the vector $\mathbf{f}_{lm}$ will be different in the adjoint case, but that it can be constructed in exactly the same way as in the forward case. With the exception of the calculation of this vector, we can use exactly the same numerical routines to solve the equations for the adjoint variables $\dot{\mathbf{u}}^\dagger$ and $\dot{\phi}^\dagger$ as for the forward variables $\dot{\mathbf{u}}$ and $\dot{\phi}$.

5.6.4 Calculation of $I^\dagger$ and $SL^\dagger$

As described in section 5.4.5, we do not calculate $\dot{I}^\dagger$ and $\dot{SL}^\dagger$. We instead calculate $\dot{P}^\dagger$ and $\dot{Q}^\dagger$, the time derivatives of two different functions and, having time-stepped the system, calculate $SL^\dagger$ and $I^\dagger$ from $P^\dagger$ and $Q^\dagger$.

$\dot{P}^\dagger$ and $\dot{Q}^\dagger$ are given by equations (5.53) and (5.49) respectively. We calculate them spatially and so simply calculate $\dot{\mathbf{u}}$ and $\dot{\phi}$ from their spherical harmonic coefficients and construct the required terms. Having time-stepped the system, we then calculate $SL^\dagger$ and $I^\dagger$ in the spatial domain using equations (5.55) and (5.56) respectively.

5.6.5 Details of implementation

In figure 5.1, we show the total sea level change from 21000 years ago to the present day calculated using the method discussed in chapter 4 and also mark the locations of sea level measurements that are used when considering the inverse problem; these are (1) a formerly glaciated location to the north on the border between Alberta and Saskatchewan in Canada, (2) on the peripheral bulge (the area just outside the former ice extent which sees the largest increases in sea level) in north west Nebraska in the US and (3) in the far-field of the ice melt in Tahiti.

5.6.6 Viscosity sensitivity kernels

We calculated the radial sensitivity kernels, given by equation (5.64) for the sea level at locations in Canada, the US and Tahiti at three different times since the Last Glacial Maximum (as indicated in figure 5.1). These are shown in figure 5.2. A positive (negative) value of the kernel at a particular depth means that an increase in viscosity at this depth would lead to an increase (decrease) in the sea level measurement. We note that the magnitude of the sensitivity is much smaller in Tahiti than it is for the North American measurements – as the Laurentide ice sheet has melted from North America, there has been a significant fall in sea level due to rebound and the magnitude of this rebound will depend quite strongly on the viscosity structure of the model. However, relative to the values in the upper mantle, we can see that the measurement in Tahiti has greater sensitivity in the lower mantle. This is because the ocean load which affects deformation in Tahiti has a larger spatial scale than the ice load over North America.

The laterally varying sensitivities, given by equation (5.63), have also been calculated for sea level measurements at different times and at the above locations to the viscosity at depths of 635 km and

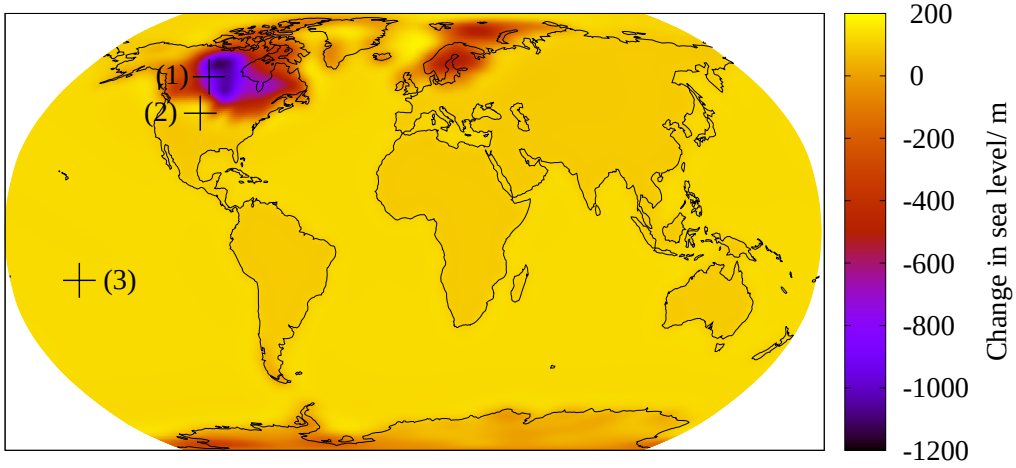

Figure 5.1: Sea level change from 21000 years ago to present calculated using the new rate formulation method presented in this chapter. The crosses indicate locations of sea level measurements that are used when considering the inverse problem. Location (1) is in Canada (near-field site), (2) is in the US (peripheral bulge site) and (3) is in Tahiti (far-field site).

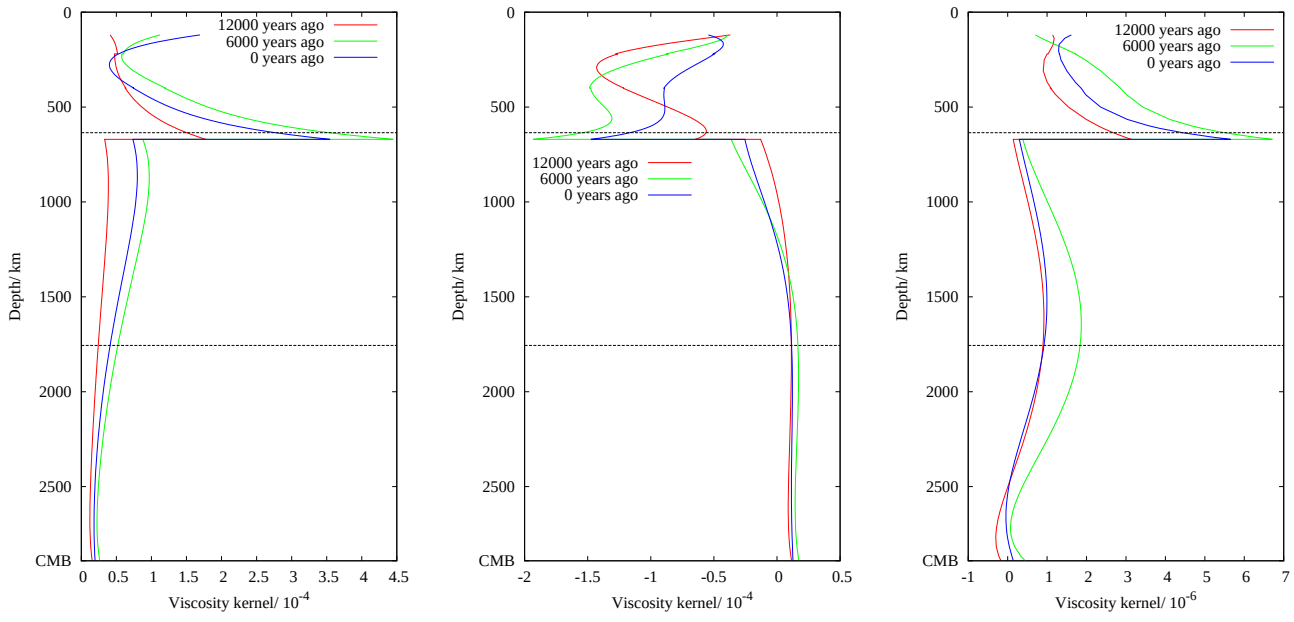

(a) Canada (b) The US (c) Tahiti

Figure 5.2: The radial sensitivity kernels for the sea level at three different times since the LGM at locations in (a) Canada (indicated by (1) in figure 5.1), (b) the US (indicated by (2) in figure 5.1) and (c) Tahiti (indicated by (3) in figure 5.1). There is a discontinuity in the kernels at a depth of 670 km due to the jump in viscosity structure at this depth. The kernels are not defined at depths shallower than 120 km as the earth model is elastic in this region. The horizontal black dashed lines indicate the depths at which we plot the laterally varying sensitivity kernels for the same measurements in figures 5.3 and 5.4 for Canada, 5.5 and 5.6 for the US and 5.7 and 5.8 for Tahiti.

1756 km. These depths are indicated on the radial kernels in figure 5.2 with black dashed lines. A positive (negative) value of the kernel at a particular location means that an increase in viscosity at this location would lead to an increase (decrease) in the sea level measurement. Figures 5.3 and 5.4 show the kernels for measurements at a location in Canada which was under the ice sheet at the LGM. The sensitivity broadens with depth, as we would expect. We note that the sensitivity to viscosity structure is small until approximately 12000 years ago. This is in part due to the ice sheet model, as ICE-5G has only a small amount of ice melt from the Laurentide ice sheet until this time. There is a small amount of sensitivity outside the region shown, particularly in northern Europe while the Fennoscandian ice sheet is melting. Figures 5.5 and 5.6 show the equivalent kernels for measurements at a location in the US which is on the peripheral bulge, the region of land just outside the edge of the former ice sheet that has seen the greatest increase in sea level. We see similar features in these kernels.

We also present figures for the sensitivity of the sea level in Tahiti (figures 5.7 and 5.8). At both depths, we see that the magnitude of the sensitivity is similar at the measurement location as it is in the regions of ice melt and, again, broadens with depth. However, as in figure 5.2, we see that the maximum amplitude of the sensitivity is much smaller here than for measurements in North America.

We can also calculate sensitivity kernels for gravity measurements, such as those made by GRACE as discussed in section 5.2.2. In figures 5.9 and 5.10, we show the sensitivity of the real spherical harmonic component of the gravity perturbation with $l = 2$ and $m = 2$ at depths of 635 km and 1756 km respectively. Similar calculations are shown in figures 5.11 and 5.12 for the real spherical harmonic component with $l = 20$ and $m = 9$. We see that, in both cases, the sensitivity at 635 km depth is largely concentrated in regions where ice has melted but becomes more widespread, particularly for the lower degree measurement, as the depth increases.

As mentioned above, the kernels give the linearised sensitivity of a measurement, and we would like to examine the magnitude of perturbations for which this is a good approximation of the total sensitivity. In figure 5.13, we show the magnitude of the calculated change in sea level at a location in the US and that predicted by the kernels for viscosity perturbations of different magnitudes and sea level measurements made at different times. We can see that the kernels predict the change very well for perturbations of up to 10 percent, and this is true for sea level measurements at all times and perturbations at all depths shown. For perturbations of a larger magnitude, the change predicted is still of the right sign and order of magnitude.

5.6.7 Ice sensitivity kernels

In figures 5.14 and 5.15 we show the sensitivity of the present-day sea level in central North America and Tahiti respectively to the rate of change of ice thickness at different times. These sensitivities are given by equation (5.70). The kernels presented in panel (f) of each figure are equivalent to the results presented in Larour *et al.* (2017); however, we are also able to account fully for viscoelasticity in our kernel calculations, as required for the other figure panels. A positive (negative) value of the ice kernel at a particular location means that an increase in the rate of change of ice thickness at this location would result in an increase (decrease) in the present-day sea level at the measurement location. We note that, in both of these figures, we do not place any restrictions on where the ice sheet thickness can change.

From figure 5.14, we can firstly see that the sensitivity of present day sea level to the rate of

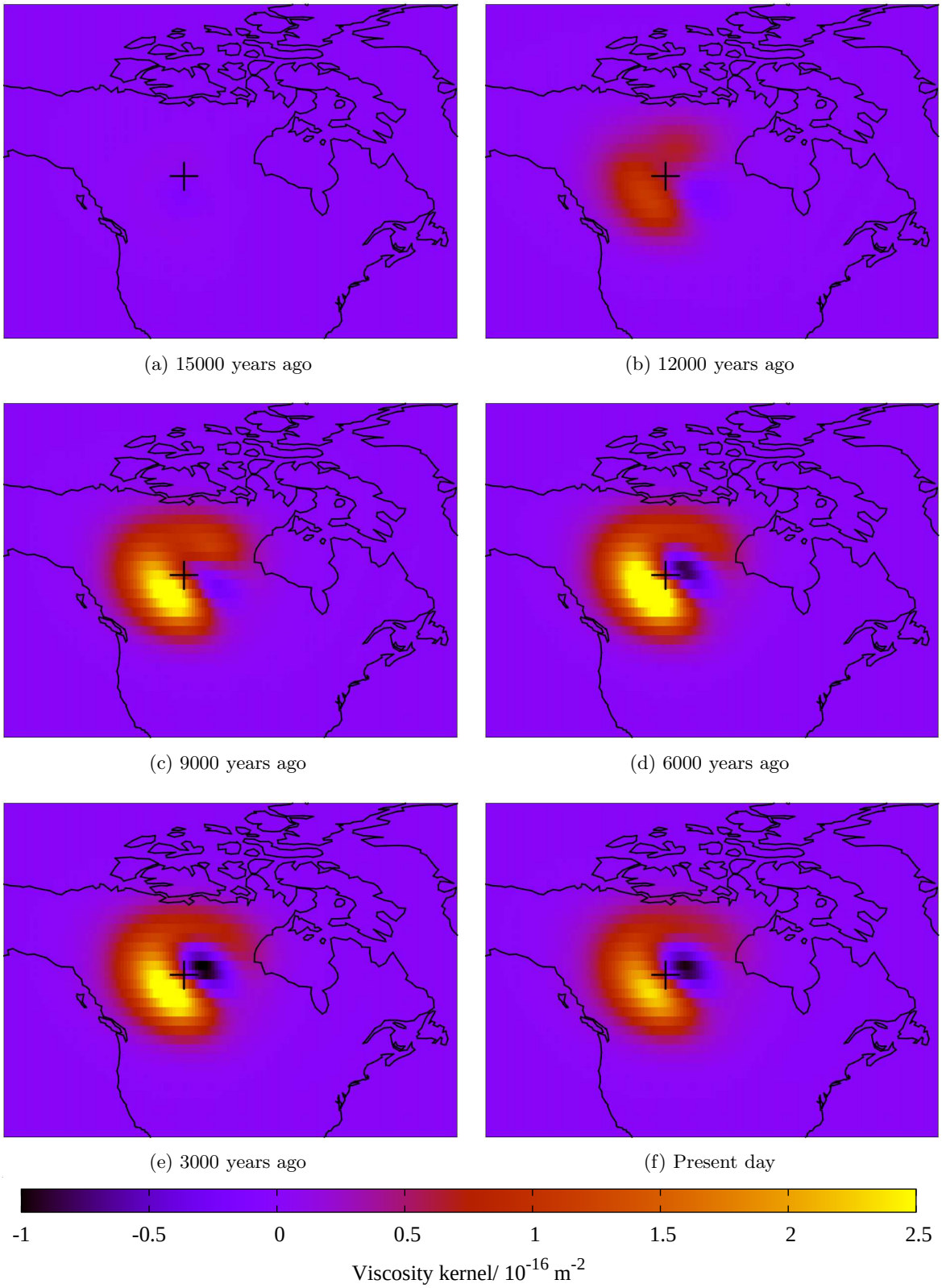

Figure 5.3: The sensitivity of the sea level at a location in Canada (as marked by the cross here and labelled (1) in figure 5.1) at different times to the viscosity at a depth of 635 km. The sensitivity is shown for sea level measurements (a) 15000 years ago, (b) 12000 years ago, (c) 9000 years ago, (d) 6000 years ago, (e) 3000 years ago and (f) at the present day.

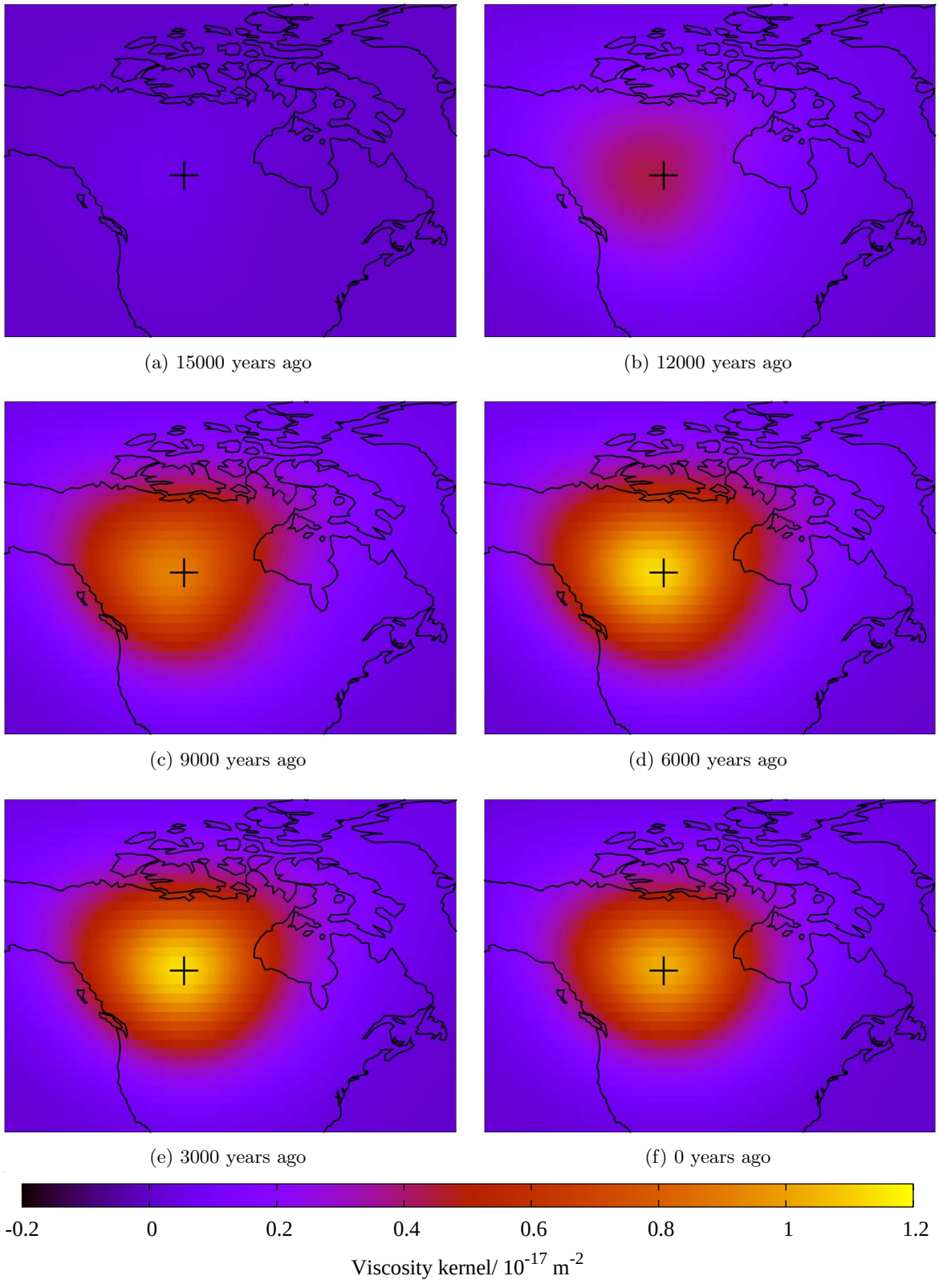

Figure 5.4: The sensitivity of the sea level at a location in Canada (as marked by the cross here and labelled (1) in figure 5.1) at different times to the viscosity at a depth of 1756 km. The sensitivity is shown for sea level measurements (a) 15000 years ago, (b) 12000 years ago, (c) 9000 years ago, (d) 6000 years ago, (e) 3000 years ago and (f) at the present day.

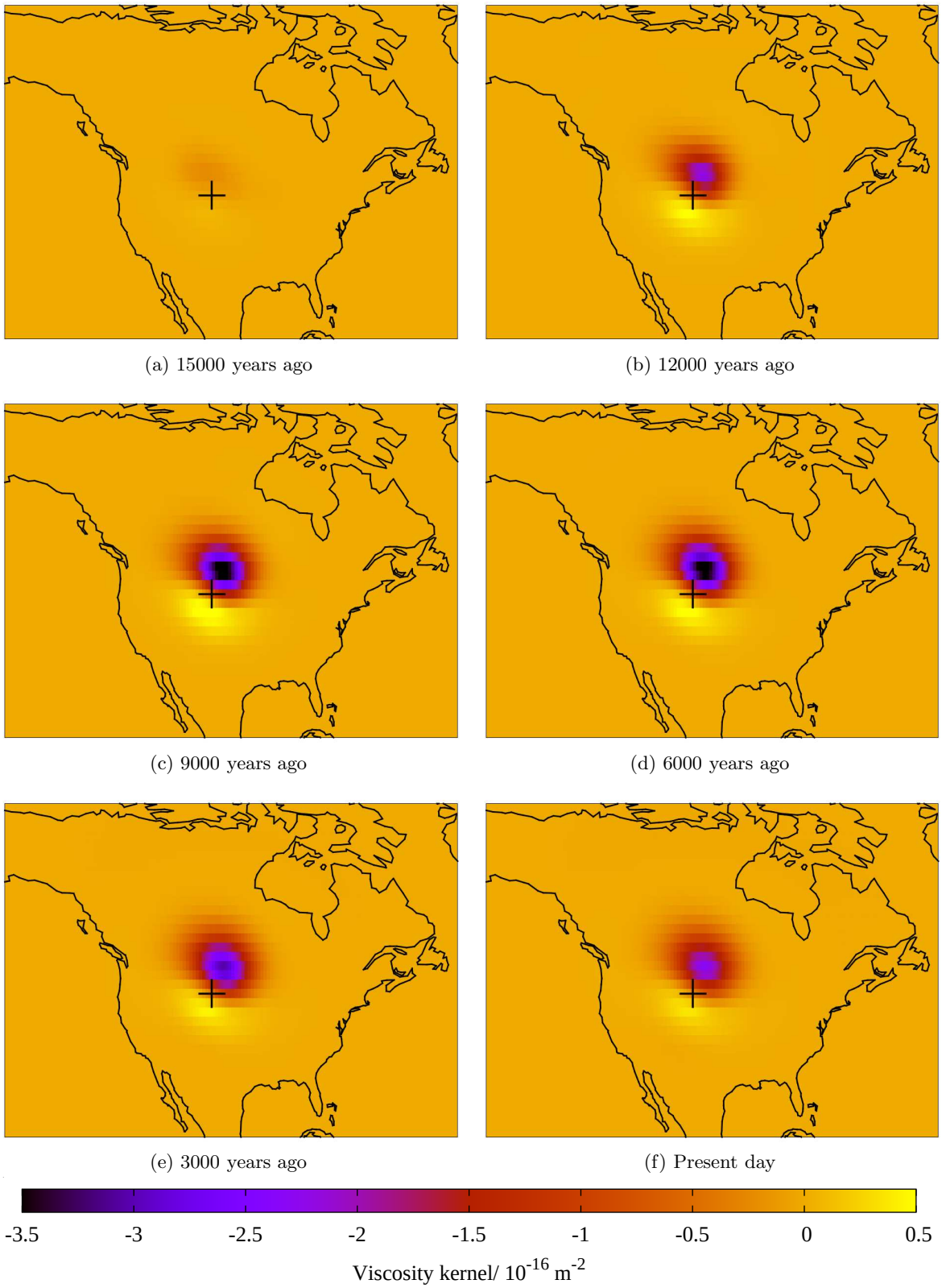

Figure 5.5: The sensitivity of the sea level at a location in the US (as marked by the cross here and labelled (2) in figure 5.1) at different times to the viscosity at a depth of 635 km. The sensitivity is shown for sea level measurements (a) 15000 years ago, (b) 12000 years ago, (c) 9000 years ago, (d) 6000 years ago, (e) 3000 years ago and (f) at the present day.

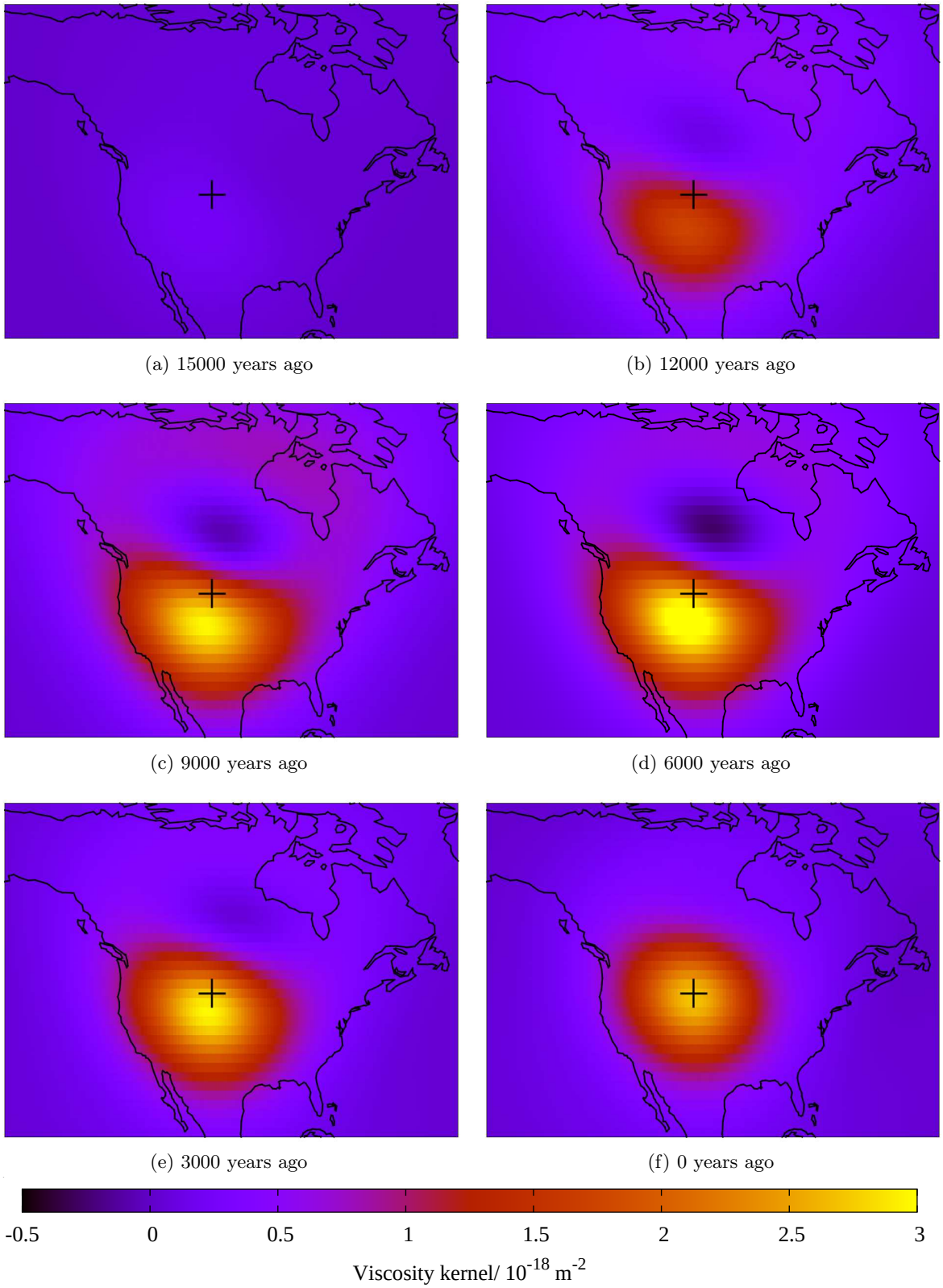

Figure 5.6: The sensitivity of the sea level at a location in the US (as marked by the cross here and labelled (2) in figure 5.1) at different times to the viscosity at a depth of 1756 km. The sensitivity is shown for sea level measurements (a) 15000 years ago, (b) 12000 years ago, (c) 9000 years ago, (d) 6000 years ago, (e) 3000 years ago and (f) at the present day.

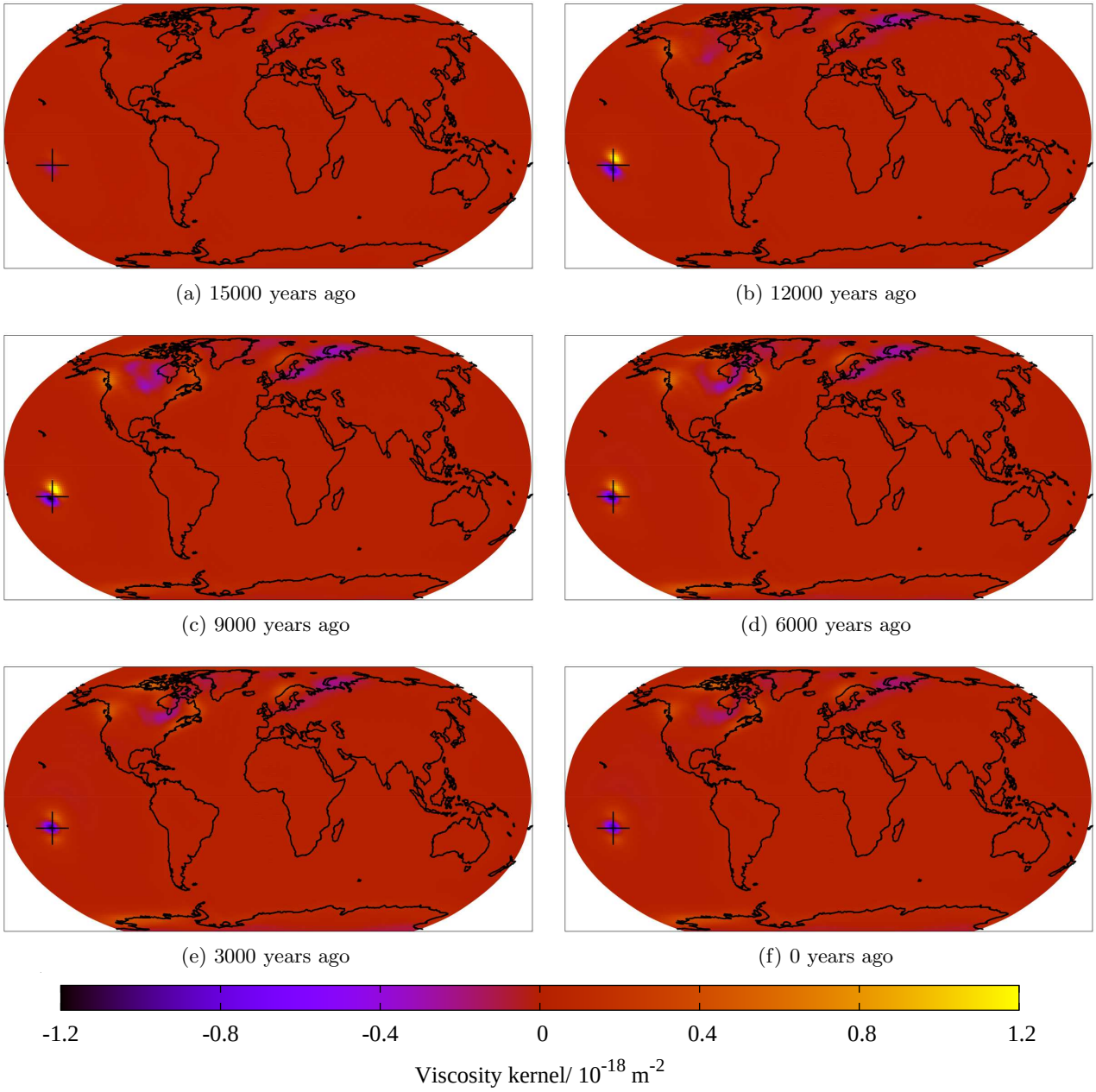

Figure 5.7: The sensitivity of the sea level in Tahiti (as marked by the cross here and labelled (3) in figure 5.1) at different times to the viscosity at a depth of 635 km. The sensitivity is shown for sea level measurements (a) 15000 years ago, (b) 12000 years ago, (c) 9000 years ago, (d) 6000 years ago, (e) 3000 years ago and (f) at the present day.

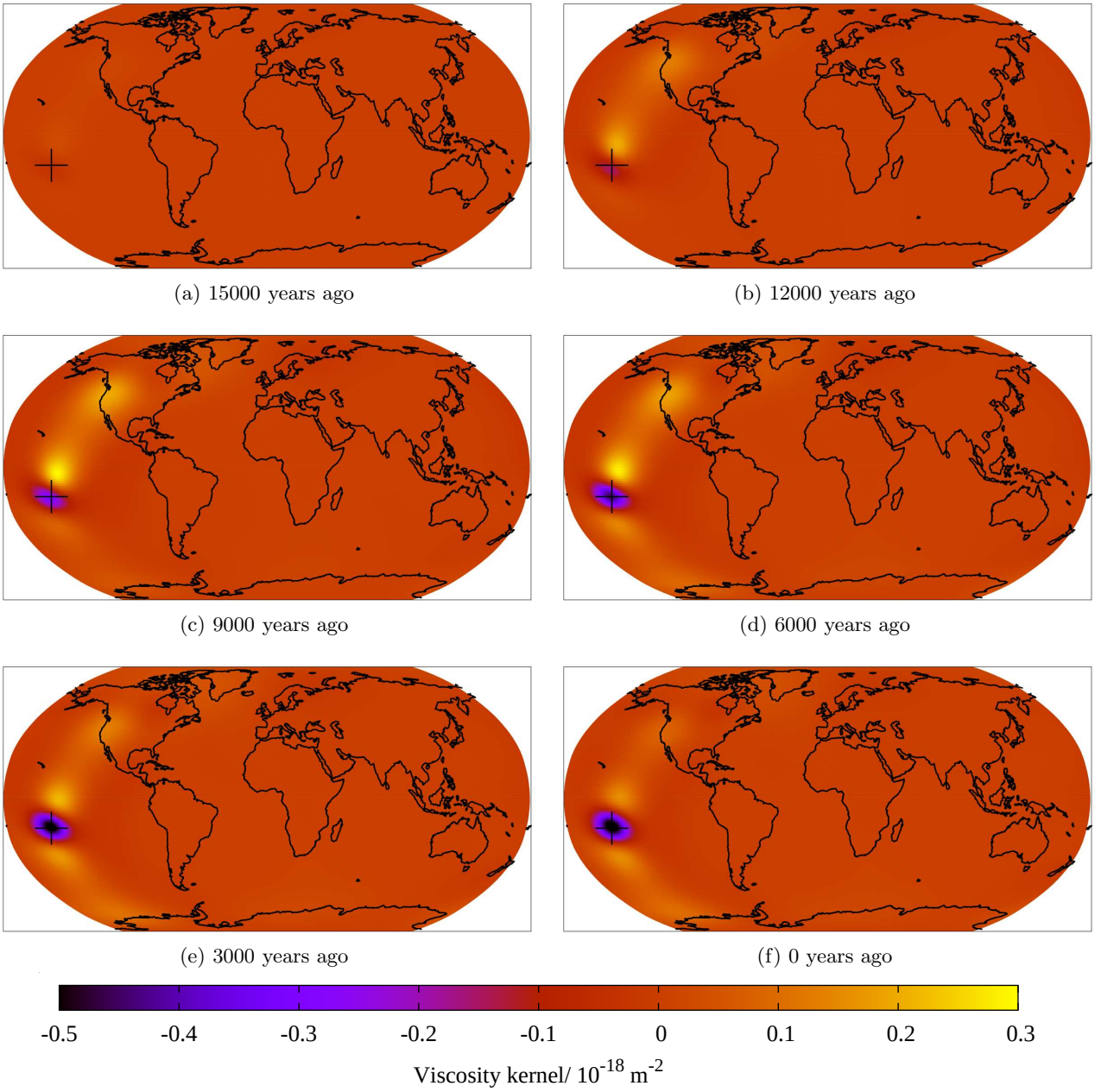

Figure 5.8: The sensitivity of the sea level in Tahiti (as marked by the cross here and labelled (3) in figure 5.1) at different times to the viscosity at a depth of 1756 km. The sensitivity is shown for sea level measurements (a) 15000 years ago, (b) 12000 years ago, (c) 9000 years ago, (d) 6000 years ago, (e) 3000 years ago and (f) at the present day.

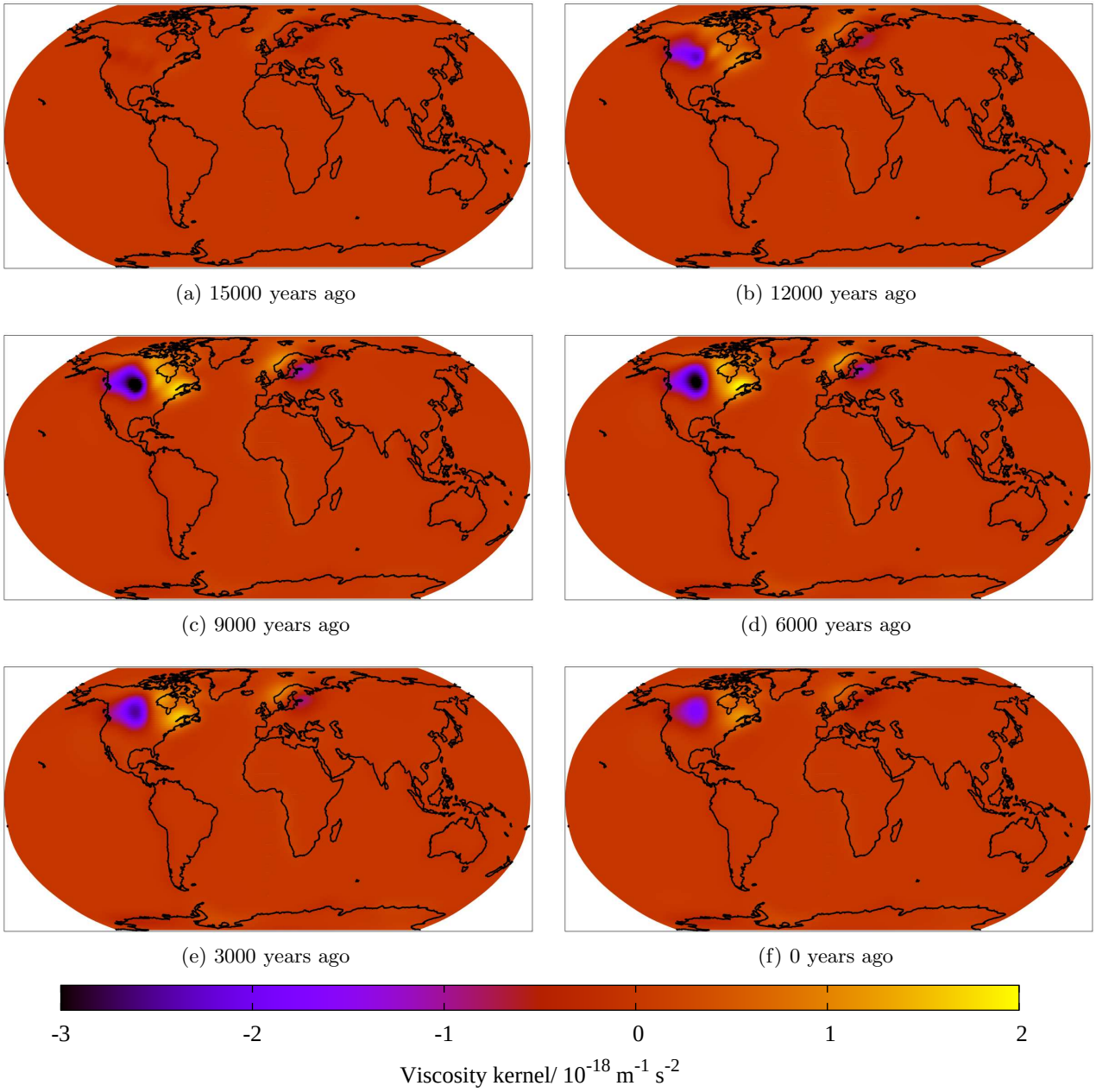

Figure 5.9: The sensitivity of the $l = 2$ and $m = 2$ component of the surface gravitational potential at different times to the viscosity at a depth of 635 km. The sensitivity is shown for sea level measurements (a) 15000 years ago, (b) 12000 years ago, (c) 9000 years ago, (d) 6000 years ago, (e) 3000 years ago and (f) at the present day.

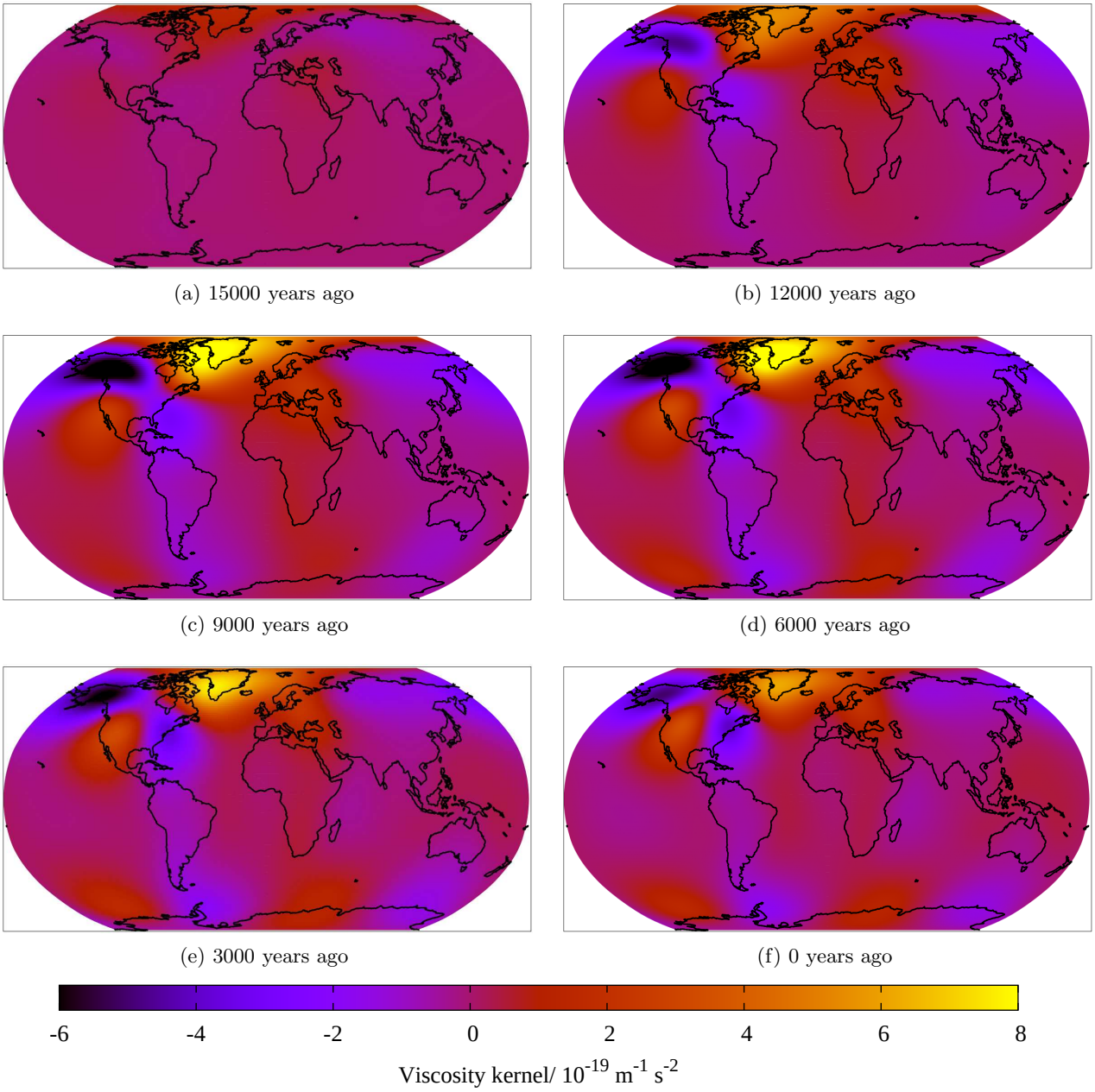

(a) 15000 years ago

(b) 12000 years ago

(c) 9000 years ago

(d) 6000 years ago

(e) 3000 years ago

(f) 0 years ago

Figure 5.10: The sensitivity of the $l = 2$ and $m = 2$ component of the surface gravitational potential at different times to the viscosity at a depth of 1756 km. The sensitivity is shown for sea level measurements (a) 15000 years ago, (b) 12000 years ago, (c) 9000 years ago, (d) 6000 years ago, (e) 3000 years ago and (f) at the present day.

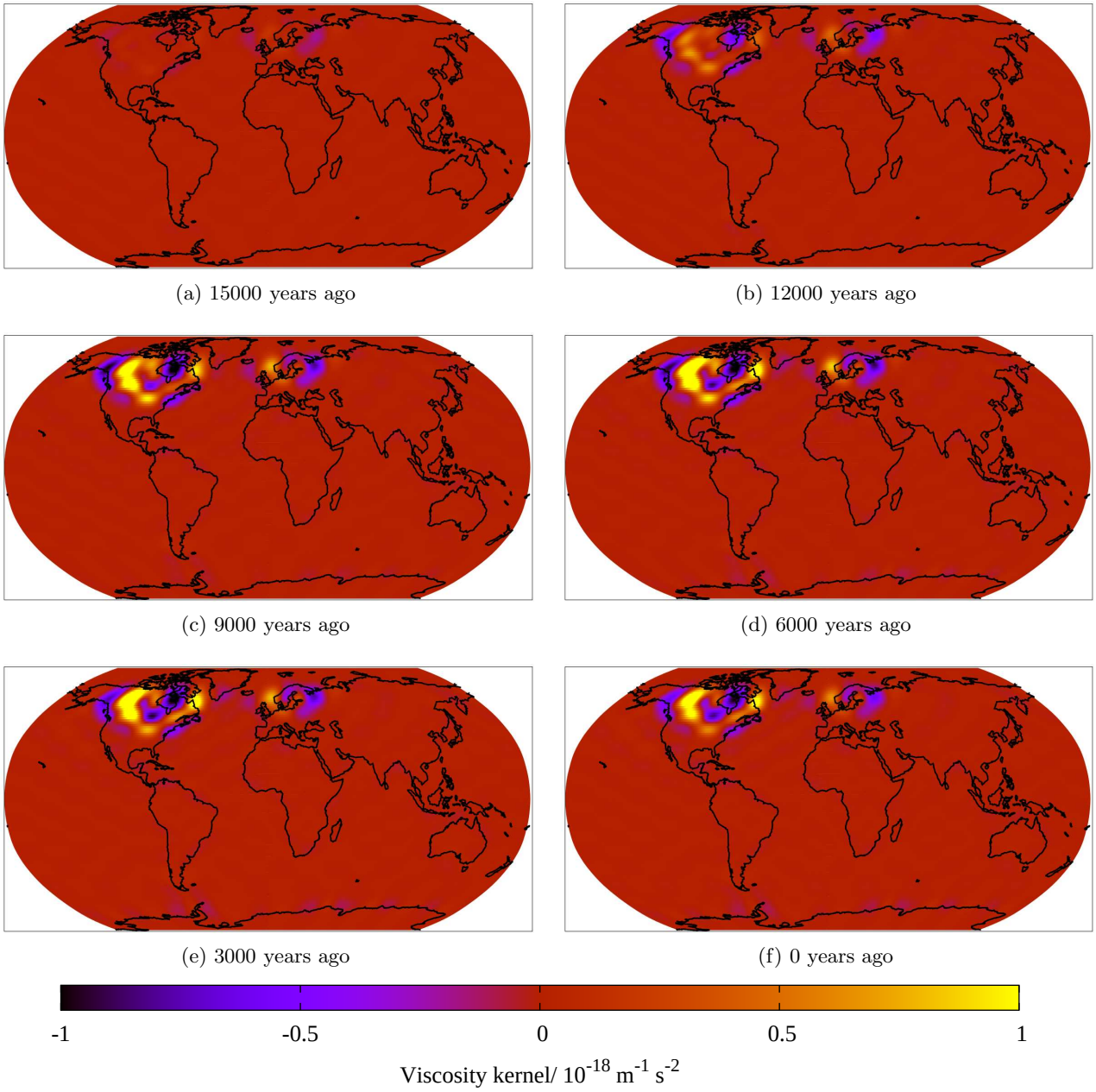

Figure 5.11: The sensitivity of the $l = 20$ and $m = 9$ component of the surface gravitational potential at different times to the viscosity at a depth of 635 km. The sensitivity is shown for sea level measurements (a) 15000 years ago, (b) 12000 years ago, (c) 9000 years ago, (d) 6000 years ago, (e) 3000 years ago and (f) at the present day.

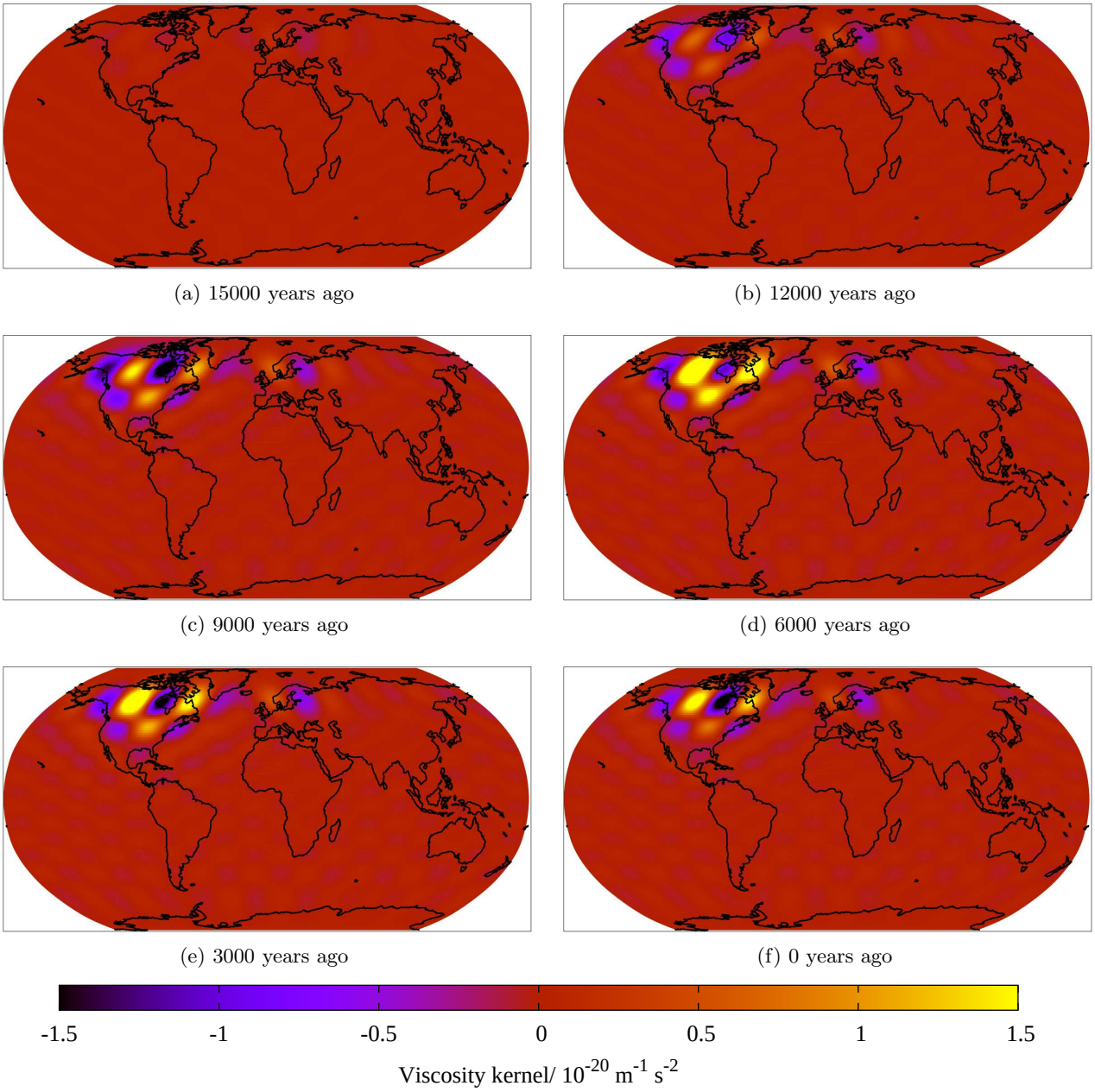

Figure 5.12: The sensitivity of the $l = 20$ and $m = 9$ component of the surface gravitational potential at different times to the viscosity at a depth of 1756 km. The sensitivity is shown for sea level measurements (a) 15000 years ago, (b) 12000 years ago, (c) 9000 years ago, (d) 6000 years ago, (e) 3000 years ago and (f) at the present day.

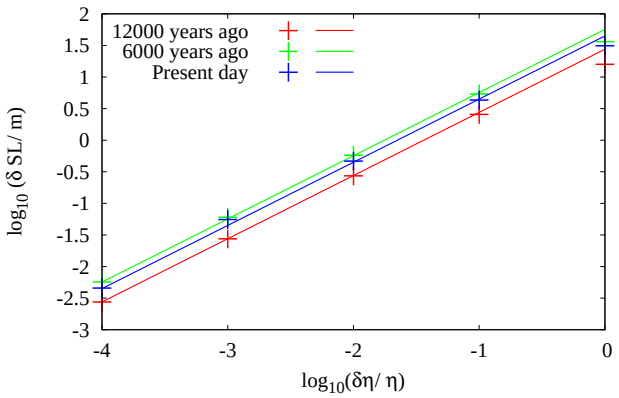

(a) Perturbation of the bottom part of the lower mantle

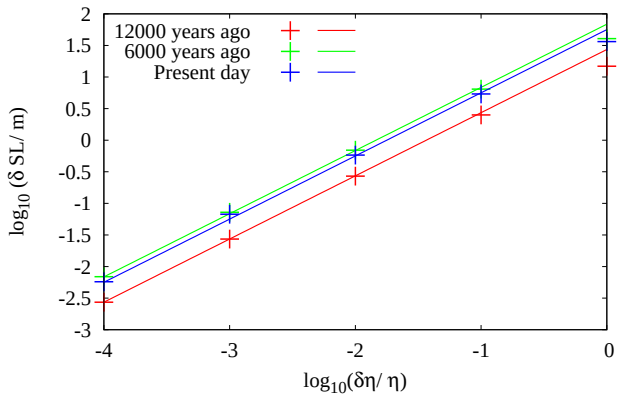

(b) Perturbation of the top part of the lower mantle

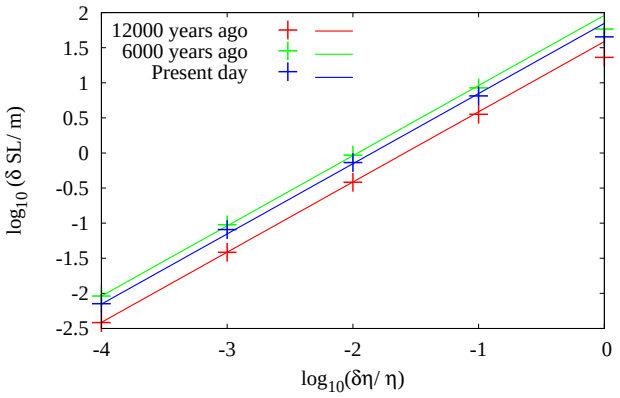

(c) Perturbation of the upper mantle

Figure 5.13: Comparison of the magnitude of the change in sea level at a location in Canada (indicated by (1) in figure 5.1) predicted by the kernels to the magnitude of the actual change for several different viscosity perturbations and sea level measurement times. We consider the sea level 12000 years ago (shown in red), 6000 years ago (shown in green) and at the present day (shown in blue) and examine how they respond to viscosity perturbations of different magnitudes in three different regions of the mantle. We perturb the viscosity between (a) 1428 and the core-mantle boundary at 2891 km depth (bottom part of the lower mantle), (b) 670 km and 1428 km depth (top part of the lower mantle) and (c) 120 km and 670 km depth (the upper mantle). The calculated changes in sea level are plotted in crosses of the appropriate colour, whilst the linearised changes predicted by the kernels are shown with the straight lines. At all times, all perturbations in the viscosity lead to an increase in sea level. We see that the kernels predict the change in sea level very well up to a perturbation of about 10%, and for perturbations larger than this still predict a change of the correct sign and order of magnitude.

change of ice thickness in the past is roughly constant until about 9000 years before the present. This is because, for the viscosity model we have adopted, the Earth has essentially relaxed in response to any ice melting or growth prior to this time. Thus melting of a given amount prior to 9000 years ago will contribute the same sea level change regardless of the precise timing of the melt. As we get closer to the present day, the sensitivity to the rate of change of ice thickness decreases in magnitude because the level of relaxation in response to the change progressively decreases. The largest positive sensitivity is evident at the location of the sea level measurement. As ice melts (forms) here, the ground rebounds (subsides) and sea level falls (rises). On land away from the measurement location, the kernel is negative. The dominant effect in these locations is simply the change in water volume in the oceans due to a change in ice thickness. For example, ice melting in the far-field adds water to the oceans, increasing sea level at the measurement location.

The pattern of sensitivity for a present day sea level measurement in Tahiti, as shown in figure 5.15, is quite different. As the sea level measurement is on a small island in the ocean, there is essentially no sensitivity in the vicinity of the measurement. As before, the sensitivity does not vary with time for changes in ice volume more than 9000 years before the measurement. The sensitivity is negative everywhere – wherever ice melts (forms) on land, the volume of water in the oceans will increase (decrease) and sea level will rise (fall). The largest amplitude negative sensitivity is on the shorelines as, if ice forms at these locations, the shoreline will subside, increasing the volume of the ocean basin and hence lowering sea level even further. In contrast, the smallest amplitude negative sensitivity is slightly in land of the coast. If ice forms in such a location, the ground under the ice will subside, causing uplift on the coast and so the volume of the ocean basin will decrease; this effect will negate some of the fall in sea level due to the formation of ice. As we get closer to the present day, the solid Earth has had less time to rebound due to the change in ice load, and so the kernel is dominated by gravitational effects.

In figure 5.16, we show the sensitivity of the sea level at the Sunda Shelf (figure 5.16a) and Barbados (figure 5.16b) 14200 years ago to the rate of change of ice thickness at this time, only in locations where there was ice present. This is the time of Melt Water Pulse 1A, when a large increase in sea level is observed due to a sudden ice melting event (Clark *et al.*, 2002). From our sensitivity kernels, we can see that the sea level at the two locations has similar sensitivity to the rate of change of ice thickness in Antarctica, but quite different sensitivity to that in North America. Clark *et al.* (2002) calculated the sea level change at the Sunda Shelf and Barbados due to ice melting in different regions and, in agreement with our kernels, found that the change at the two locations would be similar for an Antarctic source but different for a North American source. However, they only considered melting of entire ice sheets, while our kernels reveal the full spatial dependence. Using these kernels, we can also construct a measurement that is relatively insensitive to the rate of change of ice thickness in Antarctica. In figure 5.16c, we show the ice sensitivity kernel for the measurement that is equal to the sea level at the Sunda Shelf minus 0.95 times the sea level in Barbados. We can see that this measurement is most sensitive to the rate of change of ice sheet thickness in the south-eastern part of the Laurentide ice sheet. This is an example of how we can use the sensitivity kernels to find a combination of measurements that localises the sensitivity in a particular way. In this case, the value of 0.95 was chosen by trial and error; in practice, a combination of data which minimises or maximises sensitivity in a particular region could be found more systematically using Backus-Gilbert methods (Backus & Gilbert, 1967, 1968; Backus, 1970).

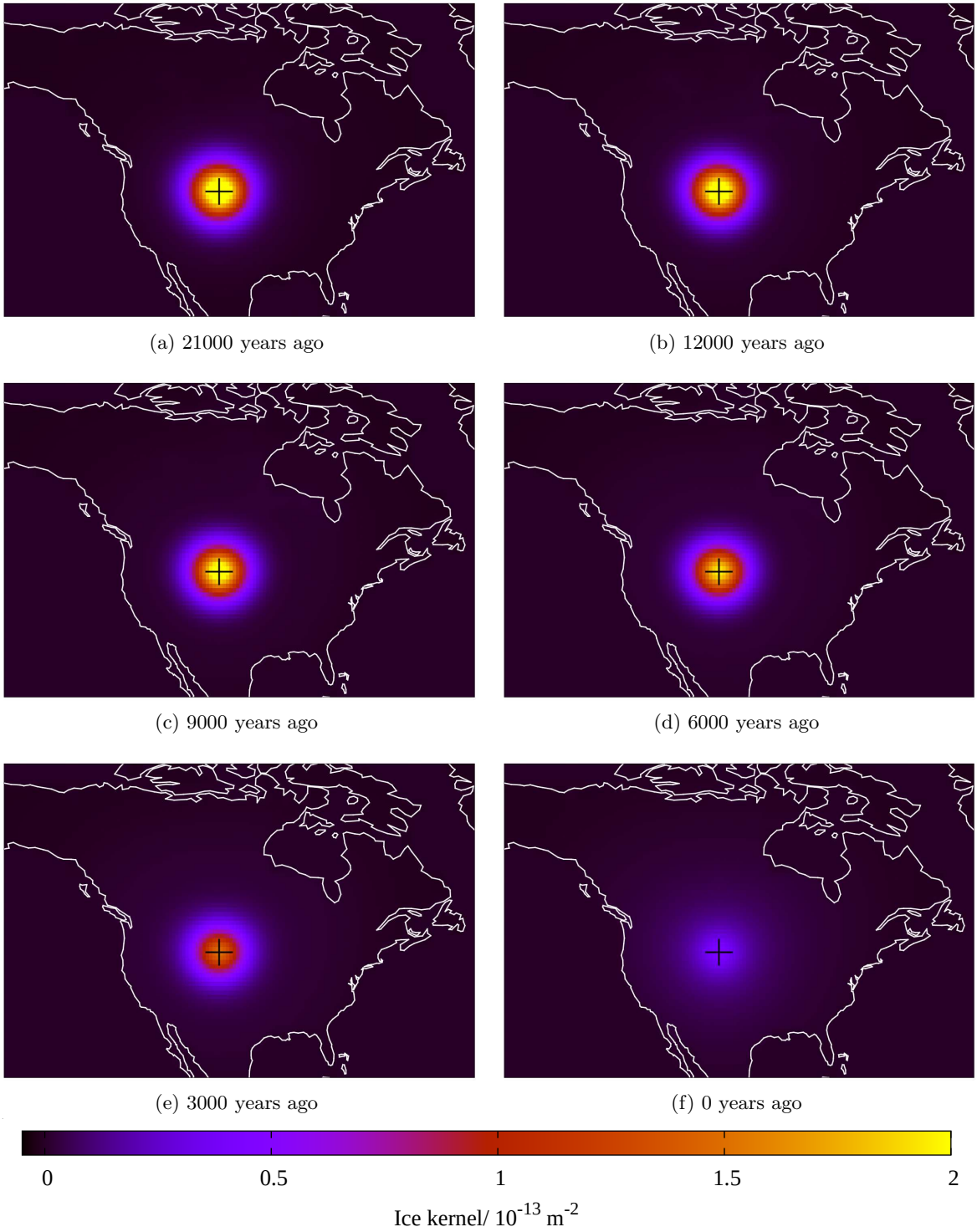

(a) 21000 years ago

(b) 12000 years ago

(c) 9000 years ago

(d) 6000 years ago

(e) 3000 years ago

(f) 0 years ago

Figure 5.14: The sensitivity of the sea level at a location in the US (as marked by the cross here and labelled (2) in figure 5.1) at the present day to the rate of change of ice thickness at several times since the LGM. The sensitivity is shown to the rate of change of ice thickness (a) 21000 years ago, (b) 12000 years ago, (c) 9000 years ago, (d) 6000 years ago, (e) 3000 years ago and (f) at the present day. We show only the sensitivity in the vicinity of North America; however, there is a small negative sensitivity on the rest of the continents.

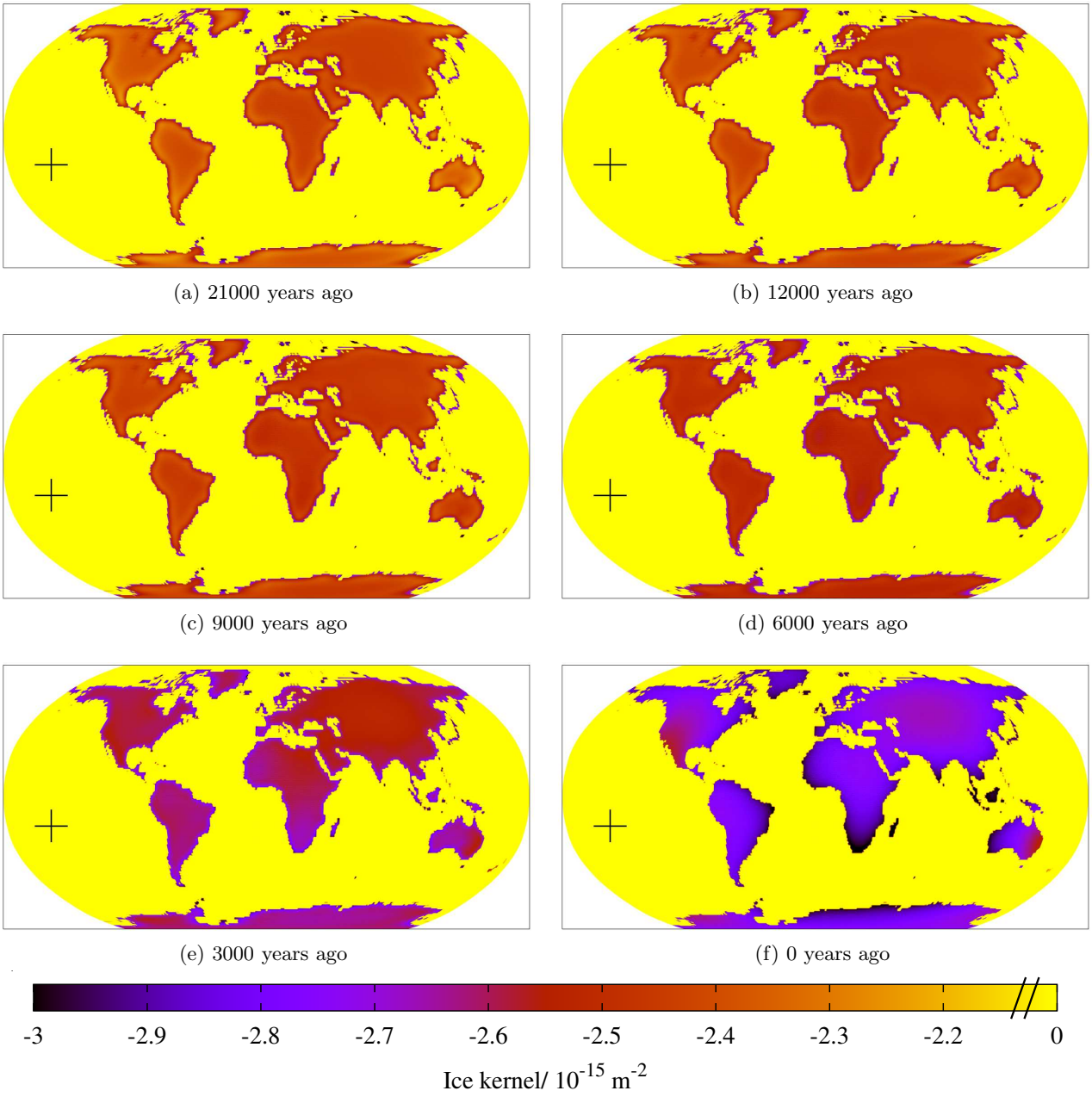

(a) 21000 years ago

(b) 12000 years ago

(c) 9000 years ago

(d) 6000 years ago

(e) 3000 years ago

(f) 0 years ago

Figure 5.15: The sensitivity of the sea level in Tahiti (as marked by the cross here and labelled (3) in figure 5.1) at the present day to the rate of change of ice thickness at several times since the LGM. The sensitivity is shown to the rate of change of ice thickness (a) 21000 years ago, (b) 12000 years ago, (c) 9000 years ago, (d) 6000 years ago, (e) 3000 years ago and (f) at the present day.

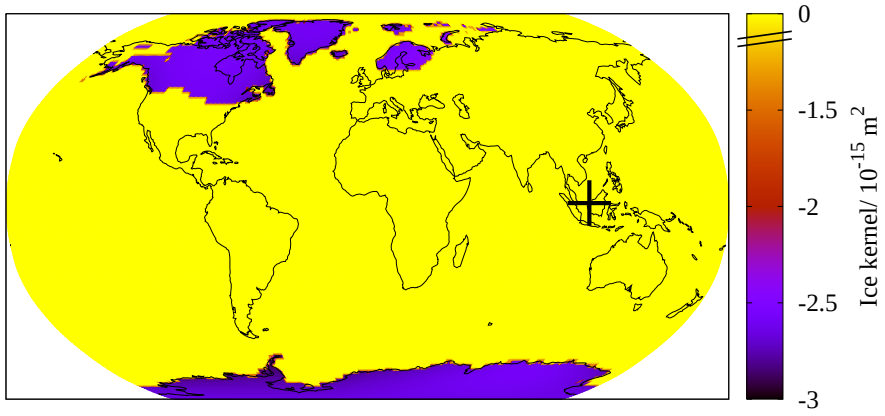

(a) Measurement in the Sunda Shelf

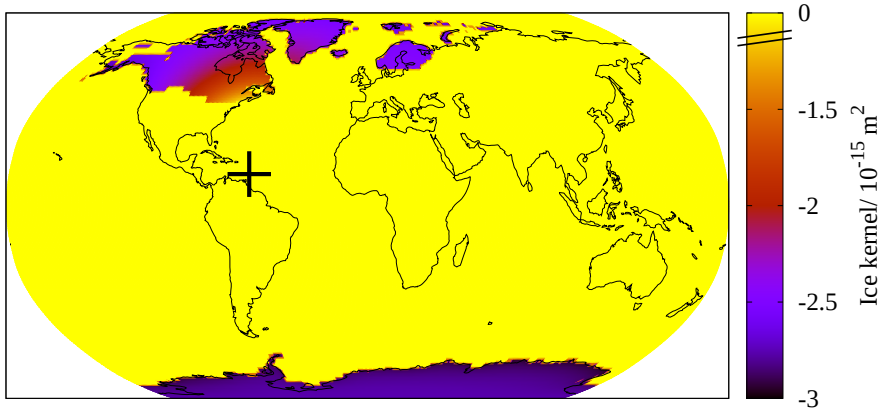

(b) Measurement in Barbados

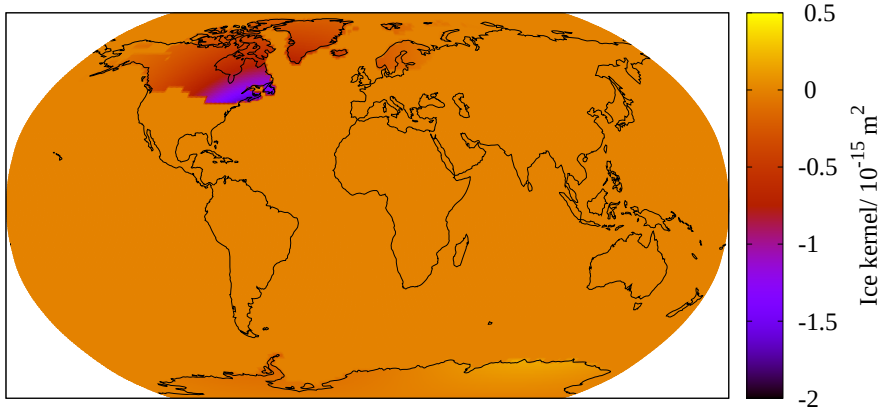

(c) Composite measurement – the sea level in the Sunda Shelf minus 95% of the sea level in Barbados

Figure 5.16: The sensitivity of the sea level 14200 years ago to the rate of change of ice thickness at that time in locations where there was ice present. We show the sensitivities for (a) the Sunda Shelf and (b) Barbados, which are indicated by the crosses. We also show (c) the sensitivity of a composite measurement, constructed to be relatively insensitive to the rate of change of ice thickness in Antarctica, which is 95% of the sea level in Barbados subtracted from the sea level in the Sunda Shelf.

5.6.8 Initial sea level inversion

We performed a synthetic inversion for the initial sea level as described in section 5.5.3. Using some known initial sea level, we calculated the final sea level to give the synthetic data, SL_p, and then found the best fitting initial sea level for this data.

The true initial sea level was generated by adding a perturbation to the sea level shown in figure 5.17a of the form

$$\sum_{l=1}^{l_{max}} \sum_{m=-l}^{l} A_{lm} Y_{lm}^0, \tag{5.88}$$

for some constants A_{lm}. So that the perturbation is real, we require $A_{l\,-m} = (-1)^m A_{lm}^*$. The real and imaginary parts of the A_{lm} were chosen at random from a Gaussian distribution with standard deviation $\frac{200}{l(l+1)}$ m. The resulting perturbation is shown in figure 5.17a.

The difference between the true sea levels and the sea levels before (top row) and after (bottom row) the inversion are shown in figure 4.2. The inversion took four iterations. On the left is the difference between the initial sea level and the true initial sea level, and on the right is the difference between the final sea level and the true final sea level, the synthetic data. At the start of the inversion, the initial sea level was chosen to be that shown in figure 4.2. We can see that the maximum sea level difference after the inversion is 1%, for both the initial and final sea levels, of what it was initially, and that these differences are concentrated in the locations of highest sea level change overall.

5.7 Numerical implementation in earth models with a laterally varying viscosity

We will now consider performing inverse calculations in models with a spherically symmetric elastic structure but a laterally varying viscosity structure. In order to do so, we must solve the forward and adjoint equations in such models. The method for solving the forward equations is discussed in section 4.5; in order to solve the adjoint equation, we make the same changes to the method for solving the adjoint equations in a spherically symmetric structure discussed in section 5.6.

5.7.1 Viscosity sensitivity kernels

For comparison, we calculated equivalent kernels to some of those presented in section 5.6.6 but with respect to a three dimensional background viscosity structure. In all the examples presented in this section, the background viscosity structure was scaled from S20RTS as described in section 4.6.4 and shown in figure 4.10. We present the sensitivity of the sea level at different times since the Last Glacial Maximum in Canada (figures 5.18 and 5.19), the US (figures 5.20 and 5.21) and Canada (figures 5.22 and 5.23) to the viscosity at depths of 635 km and 1756 km. In all cases, the main features of the kernels are similar to those in figures 5.3 to 5.8; however, the kernels here have more small scale lateral variations.

5.7.2 Viscosity inversion

Using the sensitivity kernels, it is possible to perform an inversion for the three-dimensional viscosity structure of the Earth. Given some data, a viscosity structure which fits the data can be found. In

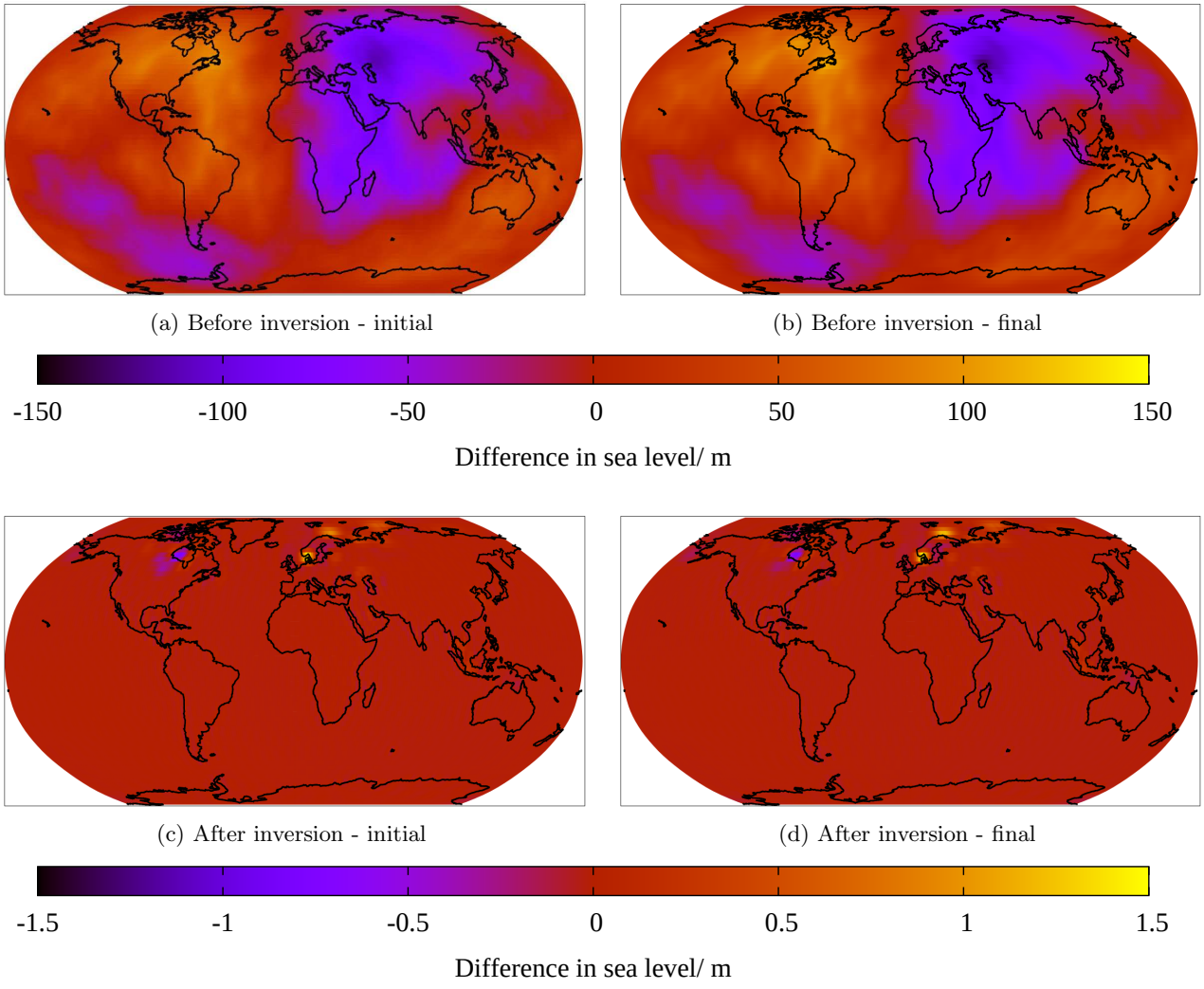

Figure 5.17: Initial sea level inversion, as discussed in section 5.6.8. We show the difference between the (a) initial sea levels before the inversion, (b) final sea levels before the inversion, (c) initial sea levels after the inversion and (b) final sea levels after the inversion.

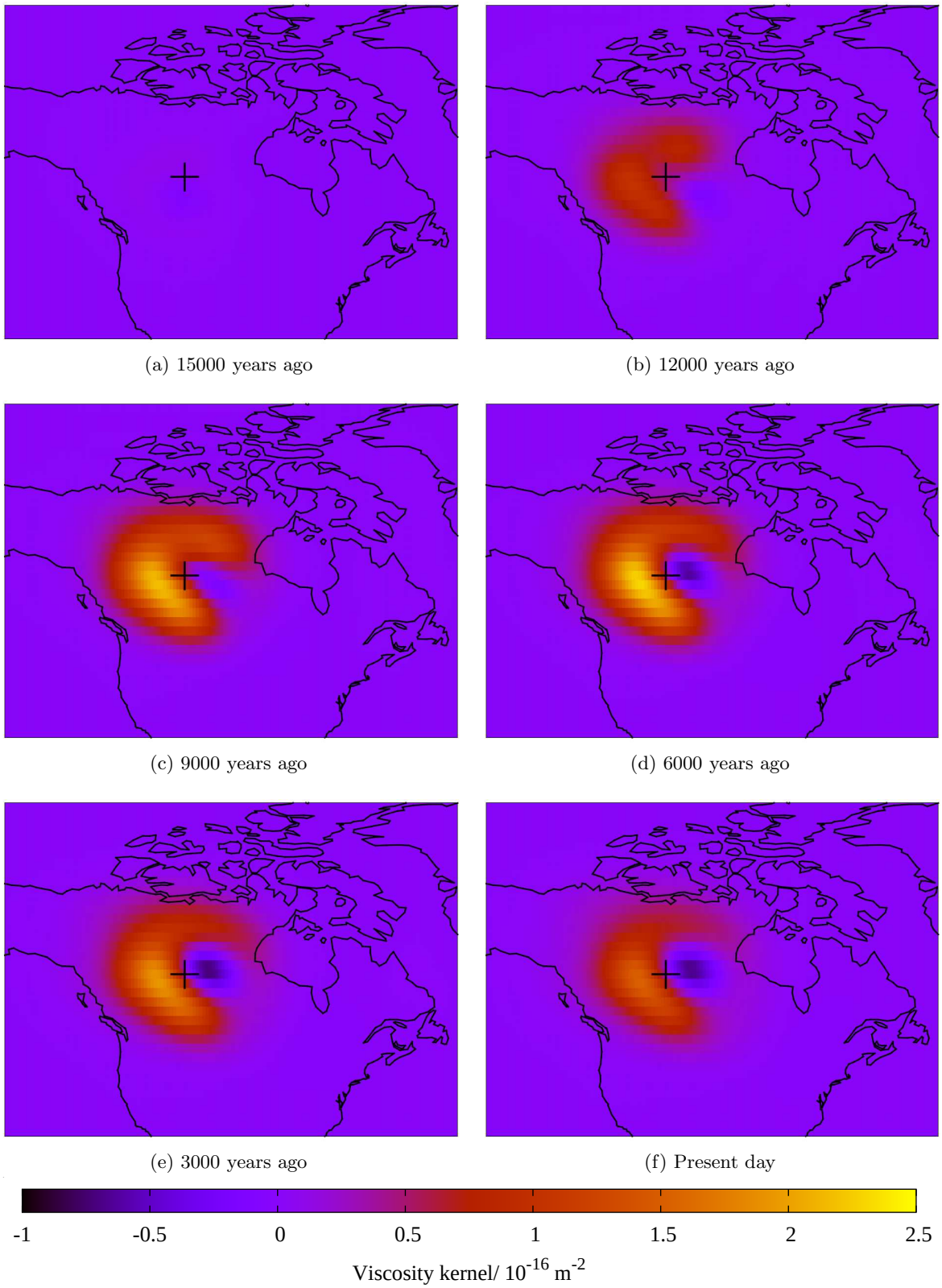

Figure 5.18: The sensitivity of the sea level at a location in Canada (as marked by the cross here and labelled (1) in figure 5.1) at different times to the viscosity at a depth of 635 km. The background viscosity structure is scaled from S20RTS, as discussed in section 4.6.4 and shown in figure 4.10. The sensitivity is shown for sea level measurements (a) 15000 years ago, (b) 12000 years ago, (c) 9000 years ago, (d) 6000 years ago, (e) 3000 years ago and (f) at the present day.

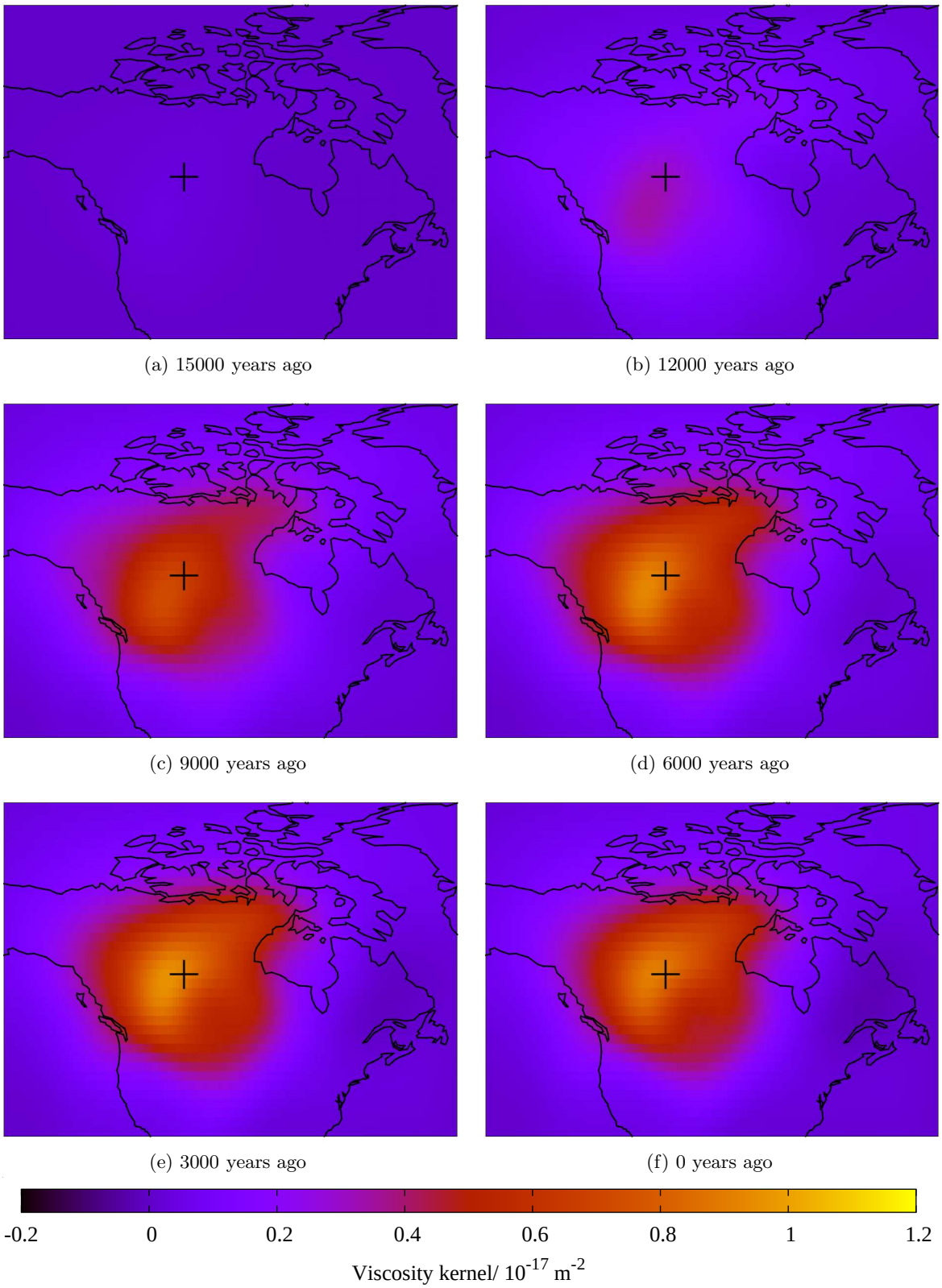

Figure 5.19: The sensitivity of the sea level at a location in Canada (as marked by the cross here and labelled (1) in figure 5.1) at different times to the viscosity at a depth of 1756 km. The background viscosity structure is scaled from S20RTS, as discussed in section 4.6.4 and shown in figure 4.10. The sensitivity is shown for sea level measurements (a) 15000 years ago, (b) 12000 years ago, (c) 9000 years ago, (d) 6000 years ago, (e) 3000 years ago and (f) at the present day.

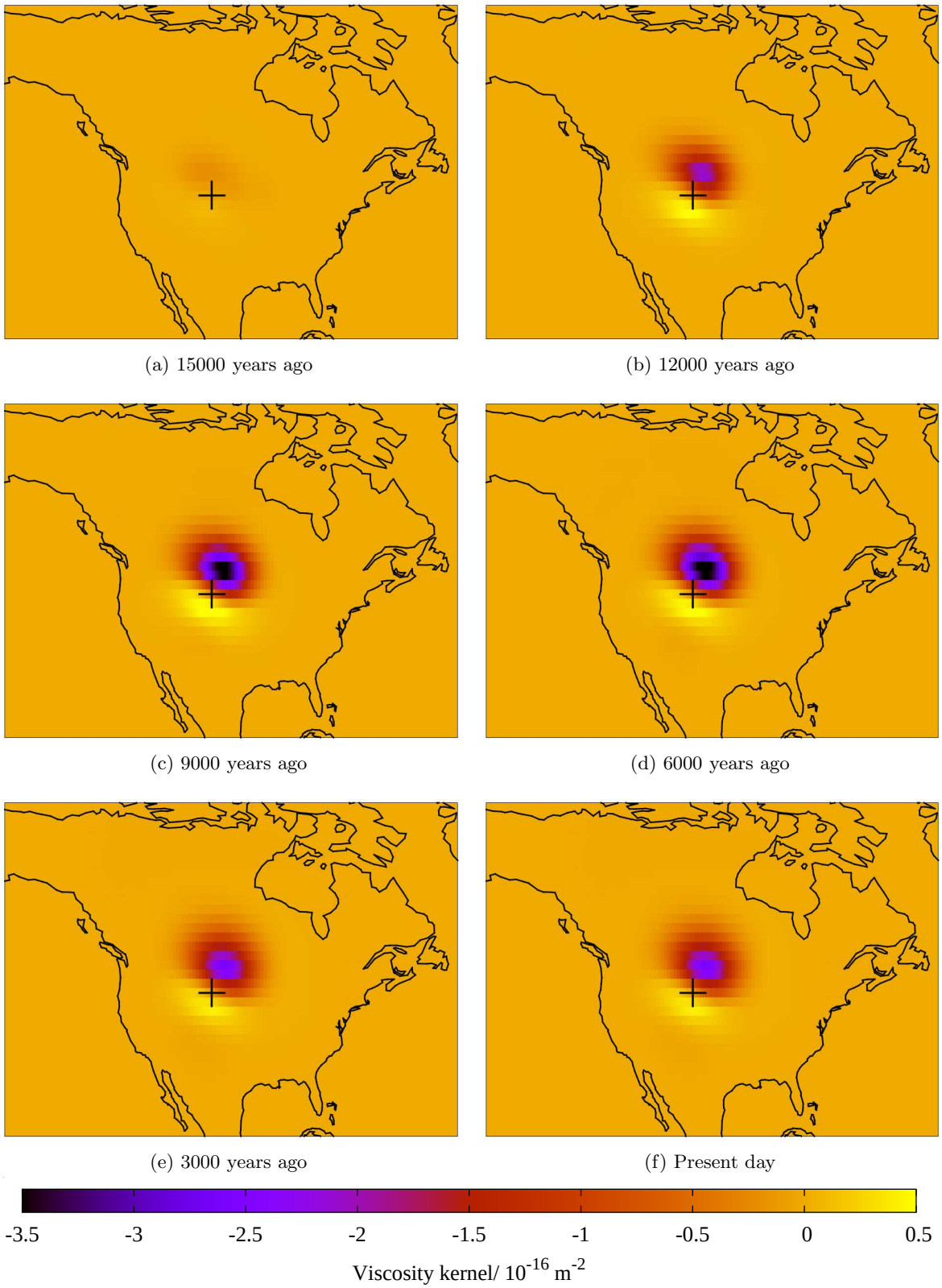

Figure 5.20: The sensitivity of the sea level at a location in the US (as marked by the cross here and labelled (2) in figure 5.1) at different times to the viscosity at a depth of 635 km. The background viscosity structure is scaled from S20RTS, as discussed in section 4.6.4 and shown in figure 4.10. The sensitivity is shown for sea level measurements (a) 15000 years ago, (b) 12000 years ago, (c) 9000 years ago, (d) 6000 years ago, (e) 3000 years ago and (f) at the present day.

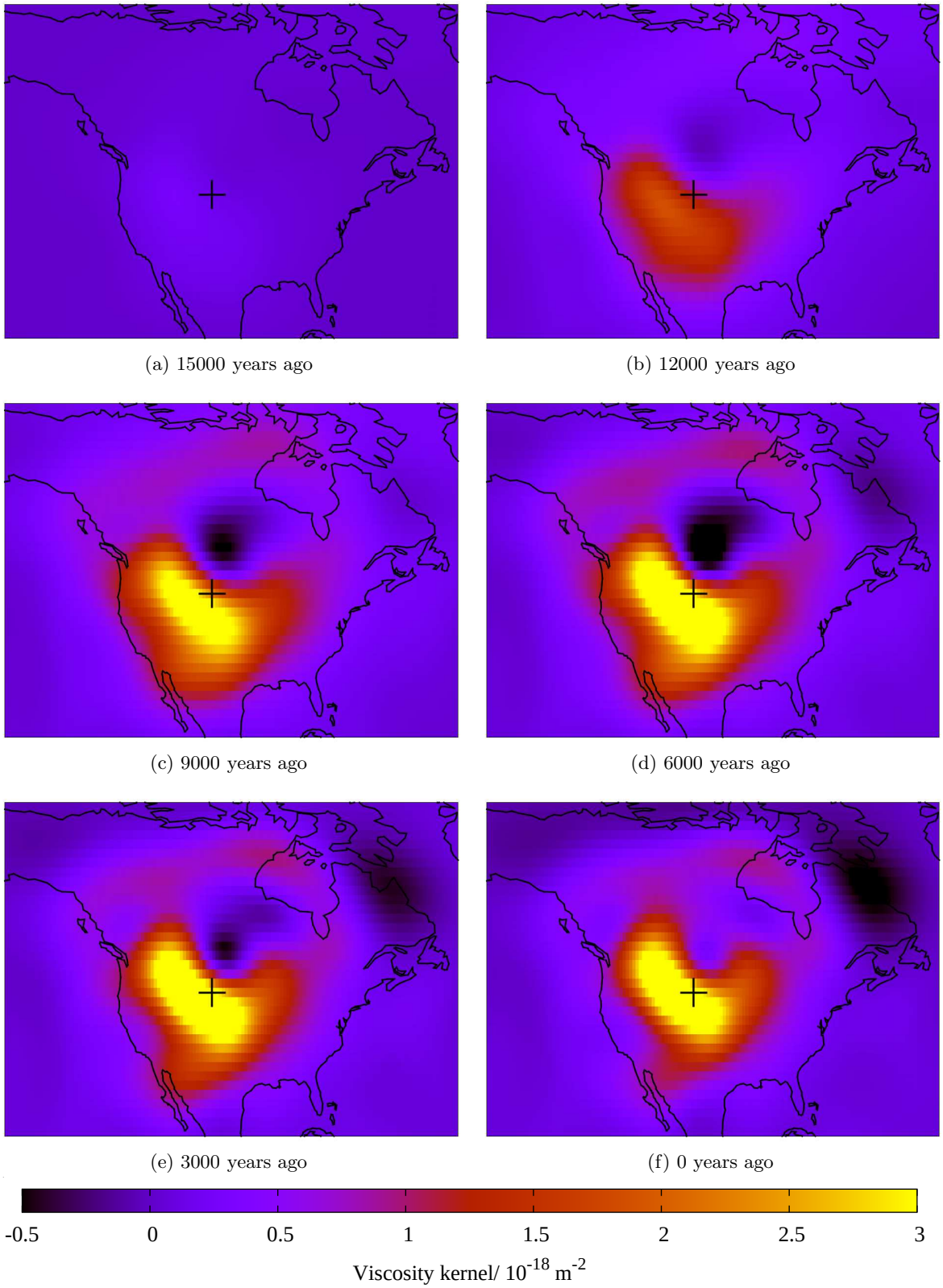

Figure 5.21: The sensitivity of the sea level at a location in the US (as marked by the cross here and labelled (2) in figure 5.1) at different times to the viscosity at a depth of 1756 km. The background viscosity structure is scaled from S20RTS, as discussed in section 4.6.4 and shown in figure 4.10. The sensitivity is shown for sea level measurements (a) 15000 years ago, (b) 12000 years ago, (c) 9000 years ago, (d) 6000 years ago, (e) 3000 years ago and (f) at the present day.

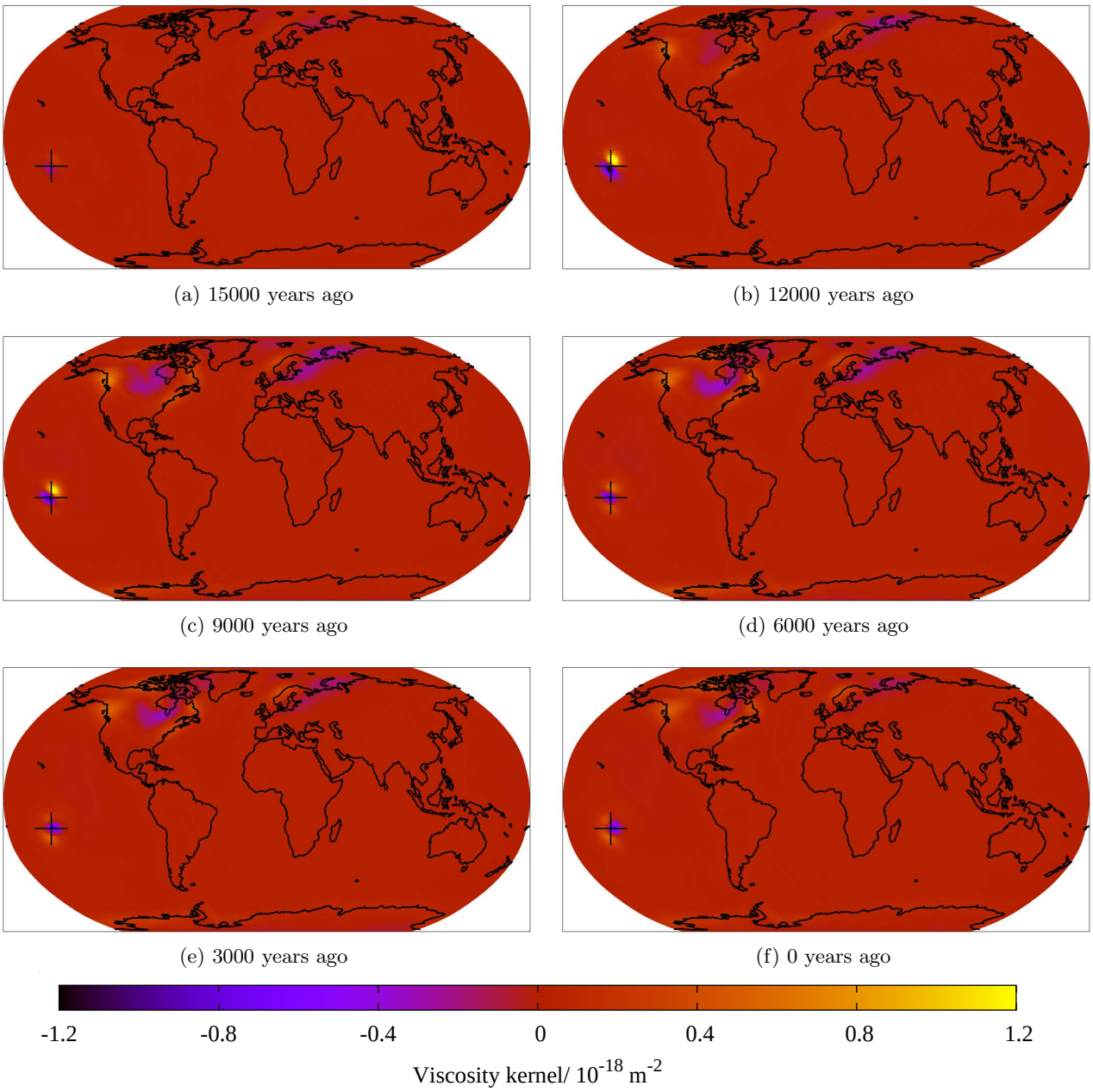

(a) 15000 years ago

(b) 12000 years ago

(c) 9000 years ago

(d) 6000 years ago

(e) 3000 years ago

(f) 0 years ago

Figure 5.22: The sensitivity of the sea level in Tahiti (as marked by the cross here and labelled (3) in figure 5.1) at different times to the viscosity at a depth of 635 km. The background viscosity structure is scaled from S20RTS, as discussed in section 4.6.4 and shown in figure 4.10. The sensitivity is shown for sea level measurements (a) 15000 years ago, (b) 12000 years ago, (c) 9000 years ago, (d) 6000 years ago, (e) 3000 years ago and (f) at the present day.

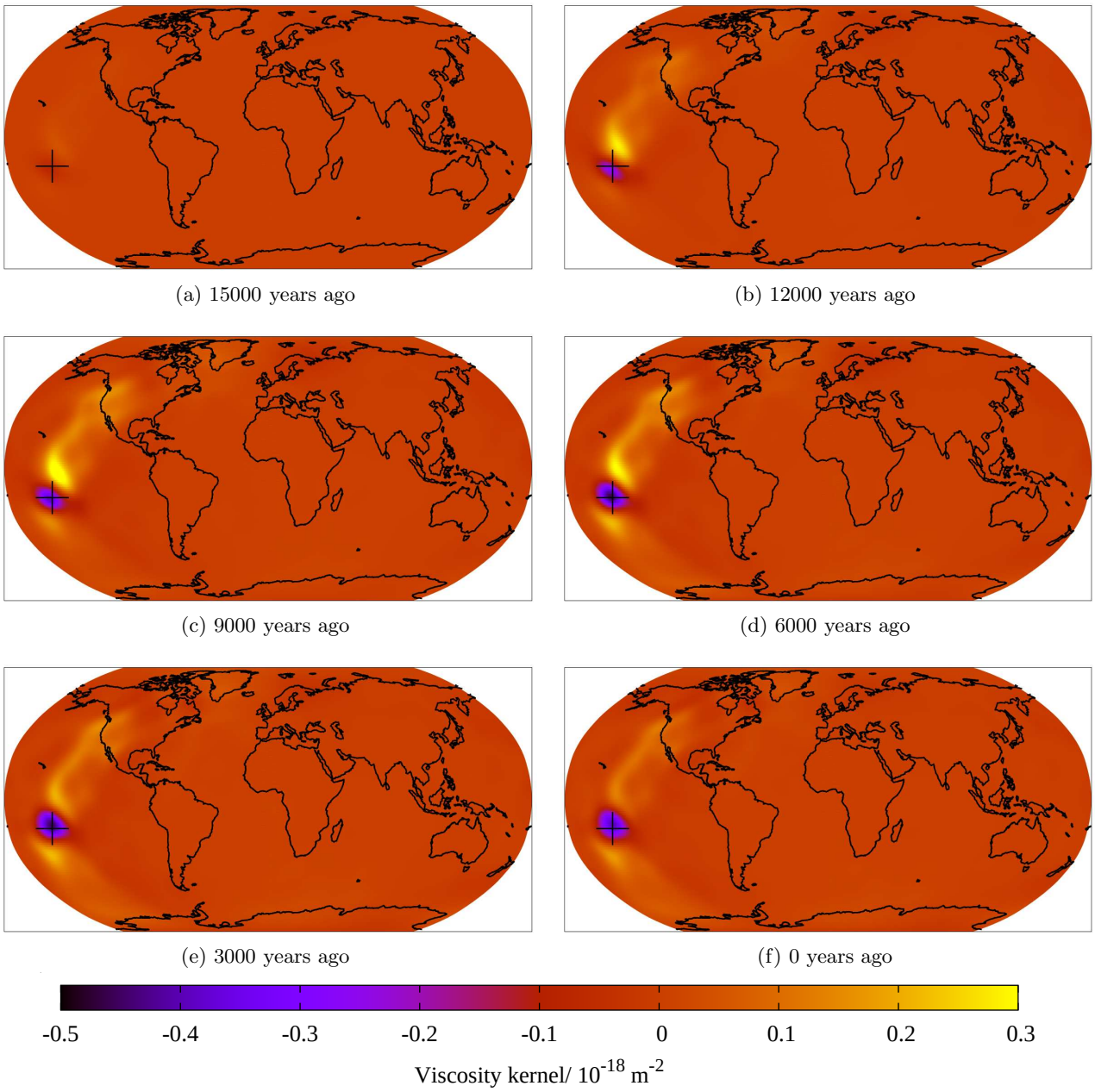

Figure 5.23: The sensitivity of the sea level in Tahiti (as marked by the cross here and labelled (3) in figure 5.1) at different times to the viscosity at a depth of 1756 km. The background viscosity structure is scaled from S20RTS, as discussed in section 4.6.4 and shown in figure 4.10. The sensitivity is shown for sea level measurements (a) 15000 years ago, (b) 12000 years ago, (c) 9000 years ago, (d) 6000 years ago, (e) 3000 years ago and (f) at the present day.

the kernel calculations shown above, we use measurements of sea level relative to the 21000 years ago. However, it is not possible to extract such measurements from real data, unless there happens to be a record of the sea level at both times. What is recorded is the sea level relative to the present day, typically known simply as the relative sea level, or RSL. It is clear that this is defined such that

$$RSL(t) = SL(t) - SL(t_p), \tag{5.89}$$

where t_p is the time at the present day. We shall use measurements of relative sea level to perform the viscosity inversion.

Let us assume that we have sea level measurements at N locations, $\mathbf{x}_i$ for $1 \leq i \leq N$. At each location, we have N_i past sea level measurements, which we will write as RSL_{ij}, made at times t_{ij} where $1 \leq j \leq N_i$ for a particular i. RSL_{ij} has an associated error σ_{ij}. We also have the present day sea level, SL_{ip} at each location $\mathbf{x}_i$. We can define the least squares misfit between the actual data and synthetic data to be

$$J(SL) = \sum_{i=1}^{N}\sum_{j=1}^{N_i} \frac{1}{2\sigma_{ij}^2}[RSL(\mathbf{x}_i, t_{ij}) - RSL_{ij}]^2 + \sum_{i=1}^{N} \frac{1}{2}[SL(\mathbf{x}_i, t_p) - SL_{ip}]^2 \tag{5.90}$$

$$= \sum_{i=1}^{N}\sum_{j=1}^{N_i} \frac{1}{2\sigma_{ij}^2}[SL(\mathbf{x}_i, t_{ij}) - SL(\mathbf{x}_i, t_p) - RSL_{ij}]^2 + \sum_{i=1}^{N} \frac{1}{2}[SL(\mathbf{x}_i, t_p) - SL_{ip}]^2. \tag{5.91}$$

We then find that

$$\delta J = \sum_{i=1}^{N}\sum_{j=1}^{N_i} \frac{1}{\sigma_{ij}^2}[SL(\mathbf{x}_i, t_{ij}) - SL(\mathbf{x}_i, t_p) - RSL_{ij}][\delta SL(\mathbf{x}_i, t_{ij}) - \delta SL(\mathbf{x}_i, t_p)]$$
$$+ \sum_{i=1}^{N}[SL(\mathbf{x}_i, t_p) - SL_{ip}]\delta SL(\mathbf{x}_i, t_p) \tag{5.92}$$

$$= \sum_{i=1}^{N}\sum_{j=1}^{N_i} \frac{1}{\sigma_{ij}^2}[RSL(\mathbf{x}_i, t_{ij}) - RSL_{ij}][\delta SL(\mathbf{x}_i, t_{ij}) - \delta SL(\mathbf{x}_i, t_p)]$$
$$+ \sum_{i=1}^{N}[SL(\mathbf{x}_i, t_p) - SL_{ip}]\delta SL(\mathbf{x}_i, t_p) \tag{5.93}$$

$$= \sum_{i=1}^{N}\sum_{j=1}^{N_i} \frac{1}{\sigma_{ij}^2}[RSL(\mathbf{x}_i, t_{ij}) - RSL_{ij}] \int_{t_0}^{t_1}\int_{\partial M} \delta SL(\mathbf{x}, t)\delta(\mathbf{x} - \mathbf{x}_i)[\delta(t - t_{ij}) - \delta(t - t_p)]\,\mathrm{d}S\,\mathrm{d}t$$
$$+ \sum_{i=1}^{N}[SL(\mathbf{x}_i, t_p) - SL_{ip}] \int_{t_0}^{t_1}\int_{\partial M} \delta SL(\mathbf{x}, t)\delta(\mathbf{x} - \mathbf{x}_i)\delta(t - t_p)\,\mathrm{d}S\,\mathrm{d}t, \tag{5.94}$$

and so

$$\dot{h}_{SL} = \sum_{i=1}^{N}\sum_{j=1}^{N_i} \frac{1}{\sigma_{ij}^2}[RSL(\mathbf{x}_i, t_{ij}) - RSL_{ij}]\delta(\mathbf{x} - \mathbf{x}_i)[\delta(t - t_{ij}) - \delta(t - t_p)]$$
$$+ \sum_{i=1}^{N}[SL(\mathbf{x}_i, t_p) - SL_{ip}]\delta(\mathbf{x} - \mathbf{x}_i)\delta(t - t_p), \tag{5.95}$$

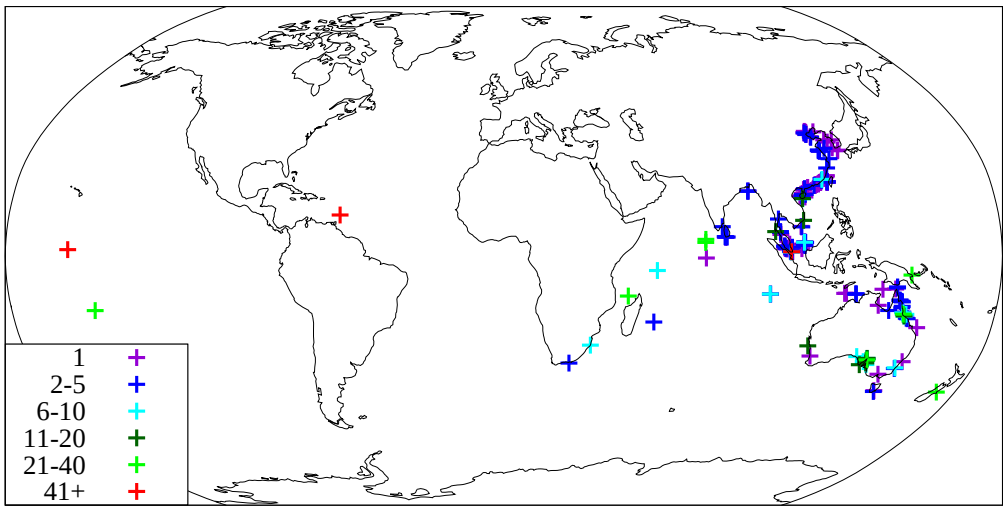

Figure 5.24: The locations of sea level measurements used in the viscosity inversion discussed in section 5.7.2. The colour of the points shows the number of measurements at each location.

and $\dot{\mathbf{h}}_{\mathbf{u}} = \mathbf{0}$ and $\dot{h}_\phi = 0$. By solving the forward equations and using this adjoint load within the adjoint equations, we can calculate the derivative of the misfit given in equation (5.91) with respect to the viscosity structure. We can then use this derivative, along with some gradient based optimisation method to find the viscosity structure that minimises the misfit. Therefore, in order to perform such an inversion we:

1. Choose some initial viscosity structure;
2. Solve the forward equations and calculate the misfit given by equation (5.91);
3. Calculate the adjoint load given by equation (5.95) and solve the adjoint equations;
4. Calculate the viscosity sensitivity kernel given by equation (5.63);
5. Use the conjugate gradient method (outlined in section 1.3.4) to update the viscosity structure;
6. Repeat steps 2 to 5 until some termination criteria are satisfied.

We performed an inversion as described above for three-dimensional viscosity structure using synthetic sea level data. The true model was scaled from S20RTS as described in section 4.6.4 and shown in figure 4.10. We took the locations of the sea level measurements to be the 187 locations used in Lambeck *et al.* (2014). We also took the N_i, the number of measurements at location $\mathbf{x}_i$, to be equal to those in the paper; however, we randomly selected the times from those at 50 year increments between 21000 years ago and the present day. For this example, we did not add any errors to the data; this could have been done and we would simply converge to a different model. The locations are shown in figure 5.24, with the colour indicating the number of measurements at each location. The initial viscosity was chosen to be the spherically symmetric structure described in section 4.5.5.

The viscosity structure after ten inversion iterations is shown in figure 5.25. As one would expect, the perturbations are concentrated in regions where there are measurements, particularly at shallow depths. In the lower mantle, the perturbations are broader in scale and there is also significant viscosity change under where the ice sheets have melted. In figure 5.26, we show the misfit, given by

equation (5.91), at each iteration of the inversion. We can see that it has reduced by about a factor of 30 overall, and reached close to its minimum value after seven iterations.

In order to make an assessment of how well the inverted viscosity matches the true viscosity, we can consider the correlation between the two models. Let η_t be the true viscosity model, η_i be the inverted viscosity model and η_0 be the spherically symmetric background model. We then define the correlation between the relative perturbations with respect to the background model to be

$$C = \frac{\left\langle \log_{10}\left(\frac{\eta_t}{\eta_0}\right), \log_{10}\left(\frac{\eta_i}{\eta_0}\right) \right\rangle}{\left\| \log_{10}\left(\frac{\eta_t}{\eta_0}\right) \right\| \left\| \log_{10}\left(\frac{\eta_i}{\eta_0}\right) \right\|}, \tag{5.96}$$

where $\langle \cdot, \cdot \rangle$ is the appropriate inner product and $\| \cdot \|$ the corresponding norm. If η_t and η_i are perfectly correlated, we will have $C = 1$, if they are perfectly anti-correlated we will have $C = -1$ and if they are not correlated at all we will have $C = 0$. We will consider two different inner products in order to present two different correlations. We will first consider the correlation as a function of depth. In this case, the inner product will be the average of the integral over the unit sphere at each depth, that is

$$\langle f, g \rangle = \frac{1}{4\pi} \int_{\mathbb{S}^2} f\, g \, \mathrm{d}S, \tag{5.97}$$

where $\mathbb{S}^2$ is the unit two-sphere. We plot this correlation in figure 5.27 along with the norms of the true and inverted viscosities. We can see that the correlation is approximately 0.3 throughout much of the mantle. The correlation becomes much larger at the base of the mantle, but this is because the norm of the true model has become very small. We would not expect the correlation as a function of depth to be very close to one because we know that large parts of the viscosity structure were not updated during the inversion due to the lack of data coverage. It would therefore be informative to consider the correlation as a function of position so that we can see how well the inversion performed in regions of high data coverage. In this case, we take the inner product to be

$$\langle f, g \rangle = \frac{1}{h_M} \int_{I_S} f\, g \, \mathrm{d}r, \tag{5.98}$$

where h_M is the thickness of the mantle. The correlation as a function of lateral position is shown in figure 5.28a. Again, there are some areas of the Earth to which the data have very little sensitivity and so the inverted viscosity structure is very similar to that at the start of the inversion. In these regions, it is essentially chance as to the value of the correlation. We are more interested in the correlation in regions which have been updated by the model. In figures 5.28b to 5.28d, we therefore present further plots where the correlation is only shown if the norm of the inverted viscosity model is above a certain value. We can see that the correlation is largely very good in these regions, particularly for the largest norm value.

5.8 Conclusion

In this chapter, we presented a method for calculating the sensitivity of measurements of glacial isostatic adjustment to the viscosity structure of the Earth and the ice sheet history. We use the adjoint method, which enables the linearised sensitivities, or kernels, to be calculated quickly and

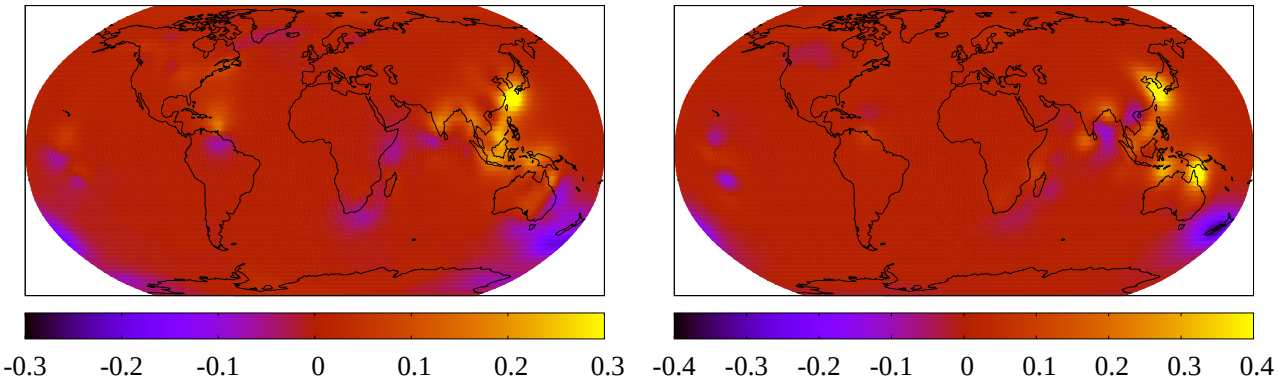

(a) 130 km

(b) 420 km

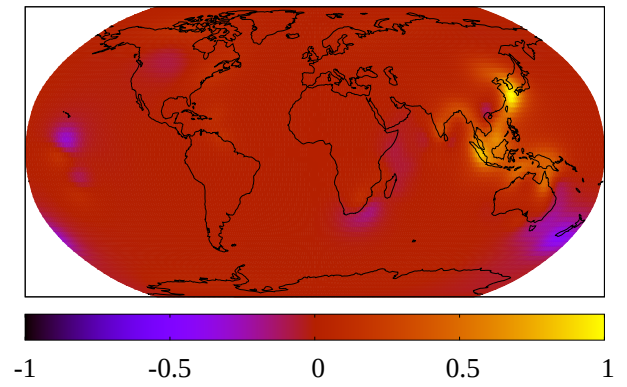

(c) 635 km

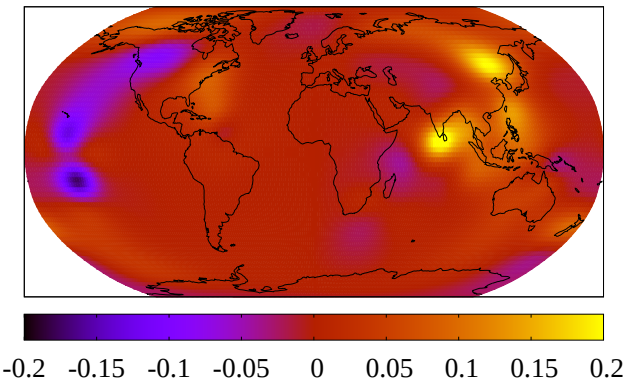

(d) 1362 km

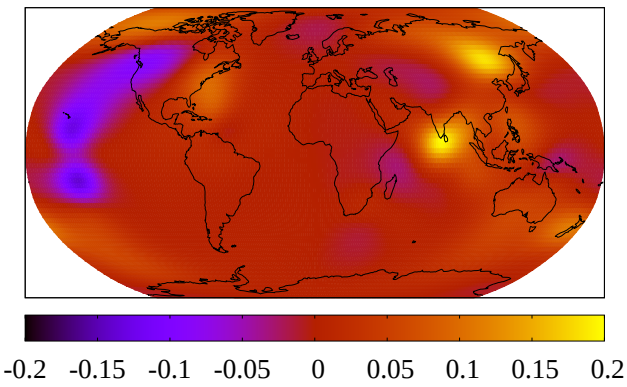

(e) 1756 km

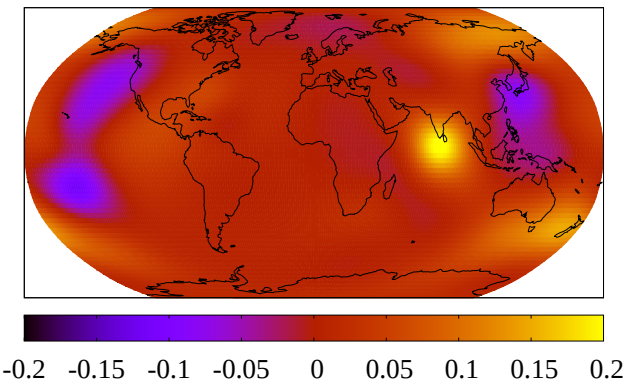

(f) 2544 km

Figure 5.25: The final viscosity structure after performing the inversion described in section 5.7.2. The viscosity is shown at depths of (a) 130 km, (b) 420 km, (c) 635 km, (d) 1362 km, (e) 1756 km and (f) 2544 km. Note that each figure has its own colour scale.

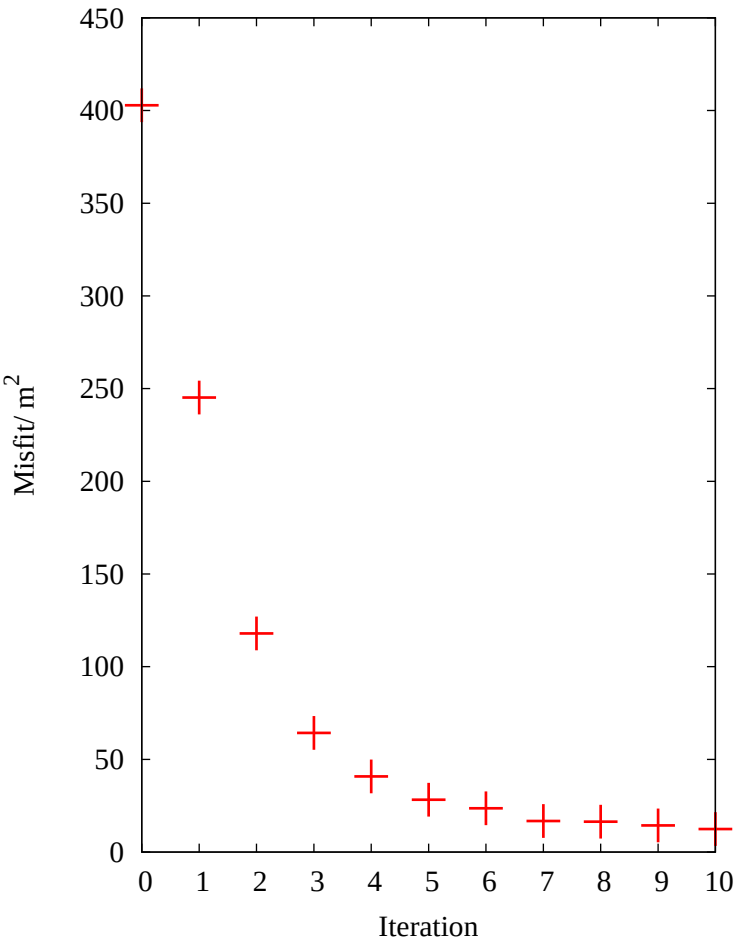

Figure 5.26: The misfit given by equation (5.91) at each stage of the inversion described in section 5.7.2.

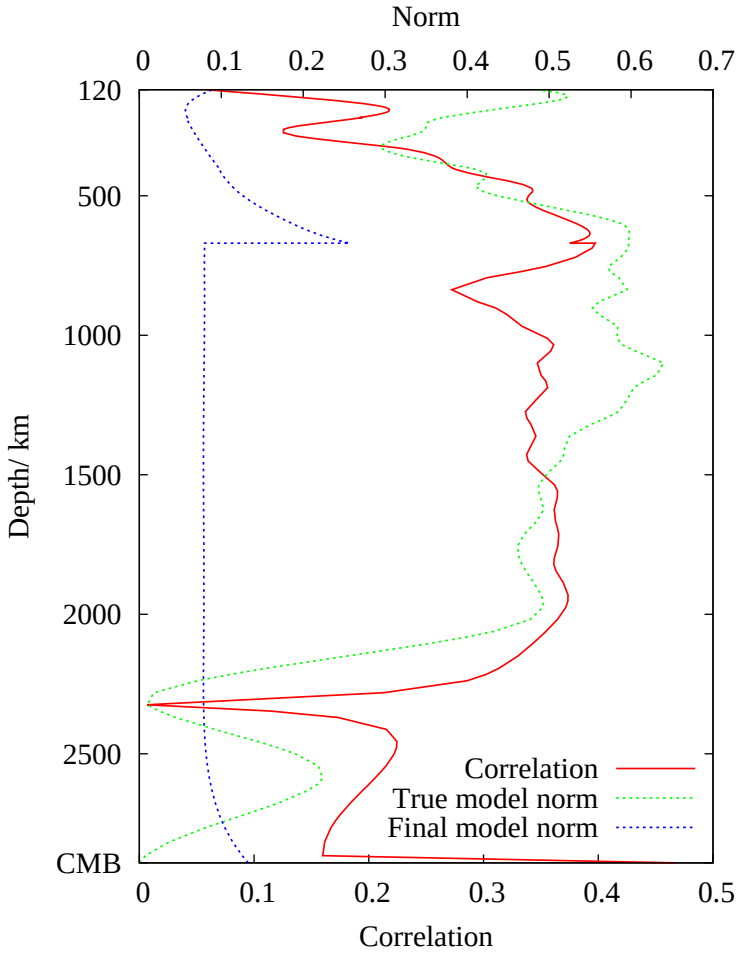

Figure 5.27: The correlation as a function of depth between the true and inverted viscosity models, as given by equation (5.96) with the inner product defined in equation (5.97). The norms for the two structures are also plotted.

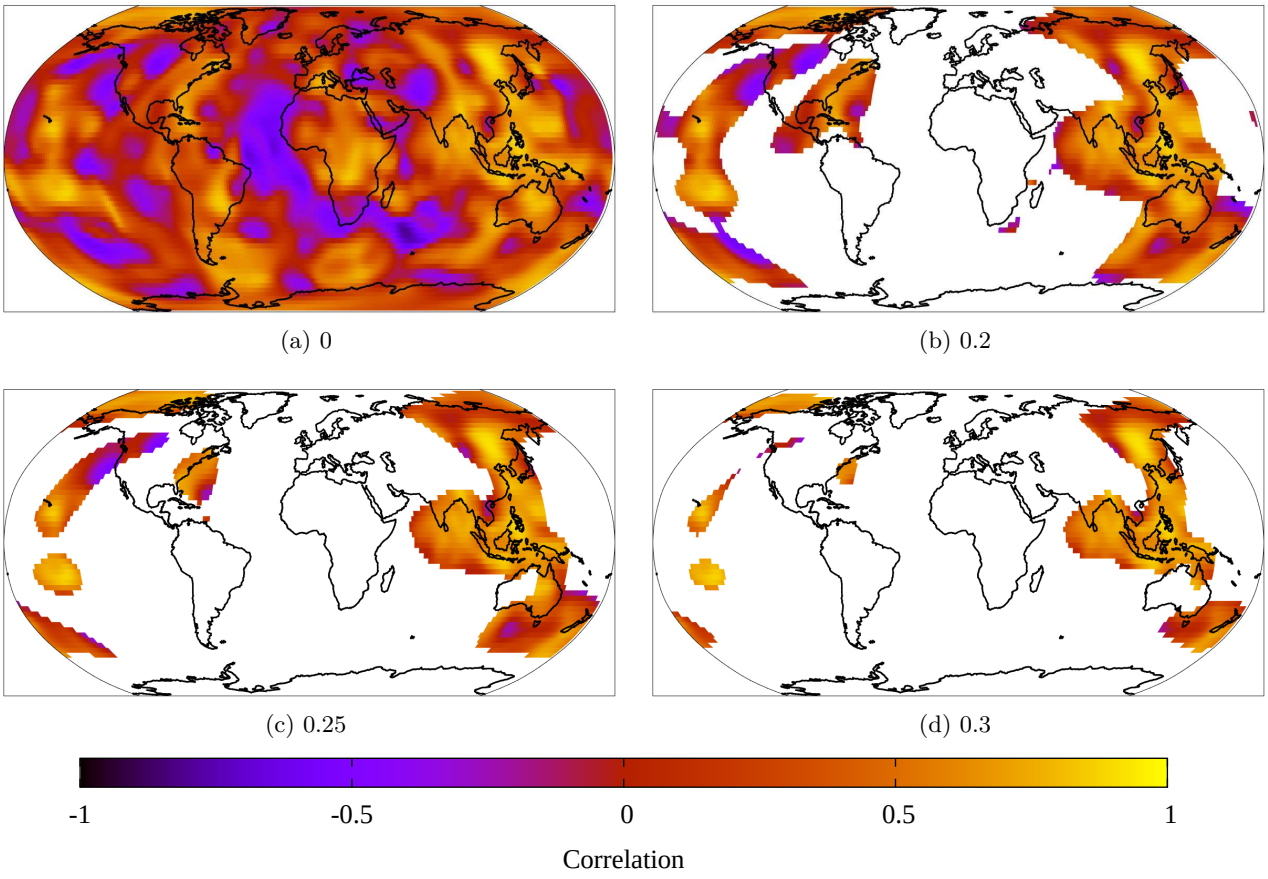

Figure 5.28: The correlation as a function of lateral position between the true and inverted viscosity models, as given by equation (5.96) with the inner product defined in equation (5.98). We show (a) the full correlation, as well as the correlation only where the norm of the inverted viscosity is above a certain value. These values are (b) 0.2, (c) 0.25 and (d) 0.3.

efficiently, even in the case of laterally heterogeneous earth models. Through application of this approach, we have also presented the first three-dimensional examples of such sensitivities in both spherically symmetric and laterally varying background models, and used the kernels to perform a synthetic inversion for three-dimensional viscosity structure. We have also presented sensitivities to ice sheet history.

Chapter 6

Conclusions and Future Work

6.1 Conclusions

In this dissertation, new methods for forward and inverse modelling post-seismic deformation and glacial isostatic adjustment have been presented. In both cases, the forward formulation allows the processes to be modelled in a self-gravitating, compressible, laterally heterogeneous Earth, with a variety of linear rheologies. Non-linear rheologies can also be considered through extensions discussed in Crawford *et al.* (2017). The forward problem is formulated in the time domain, which avoids difficulties associated with continously varying structures exhibited by Laplace domain methods (e.g., Fang & Hager, 1995; Han & Wahr, 1995; Boschi *et al.*, 1999). The adjoint method is applied to the inverse problem, which allows efficient calculation of derivatives of meausurements with respect to model parameters. Such derivatives, or kernels, quantify the sensitivity of measurements to the model parameters, and hence provide insight into what can be learnt from them. For both post-seismic and post-glacial deformation, numerical examples were presented in models with a spherically symmetric structure as well as model with laterally varying viscosity structure in the post-glacial case. The kernels were also used to perform synthetic inversions for viscosity structure – one-dimensional in the post-seismic case and three-dimensional in the post-glacial case.

6.2 Future Work

The examples contained within this dissertation illustrate some of the potential applications of the work. There exist many further uses in both the post-seismic and post-glacial contexts and some of these are discussed here.

6.2.1 Post-seismic deformation

In this work, we have considered the deformation of the whole Earth. However, post-seismic deformation is largely localised to the vicinity of the seismic source and so we could increase computational efficiency by modelling the deformation in a plane layer geometry. One possible method would be to use a cylindrical coordinate equivalent of the generalised spherical harmonics introduced by Burridge (1984). It is not, however, straightforward to include self-gravitation in a plane layer (e.g., Rundle, 1980), but its effect is arguably not vital in some situations.

In section 3.5.4, we performed several synthetic inversions for depth-dependent viscosity structure. The method could also be applied to some real situations, and a similar resolution analysis undertaken to quantify how well obtained viscosity structure is constrained. Earthquakes which have previously been considered suitable for such studies include the 1999 Hector Mine, California earthquake (e.g., Pollitz *et al.*, 2001; Freed & Bürgmann, 2004; Pollitz & Thatcher, 2010) and the 2002 Denali, Alaska earthquake (e.g., Pollitz, 2005; Freed *et al.*, 2006; Johnson *et al.*, 2009). We could also consider inverting for a more complicated rheology, such as a Burgers body, which has previously been proposed in the case of, for example, the aforementioned Hector Mine earthquake (Pollitz, 2003); however, the addition of more parameters naturally raises questions about how well they can be constrained.

In chapters 2 and 3, all numerical examples were calculated in a spherically symmetric earth model. However, the theory presented is applicable to fully heterogeneous models. Calculations with laterally varying viscosity could be performed in a similar manner to those in chapters 4 and 5 and implementation using a three-dimensional finite-element method would permit laterally varying elastic structure too. This would allow, for example, inversions for laterally varying viscosity structure, and there is evidence that such structures are required in some circumstances (e.g., Li *et al.*, 2017b). However, it is not clear if post-seismic data could usefully constrain any three-dimensional viscoelastic structure in the Earth, but the kernels could be used to quantify what can be learnt.

We derived the form of the viscosity kernels and stress glut kernels, but only gave examples of the former. Using kernels for the time-dependence of the source, we could perform a joint inversion for afterslip and viscosity structure, and investigate the resolution in the case that the particular cause of the time-dependent displacement is unknown. It would also be possible to calculate the kernels for other model components, such as the elastic parameters or thickness of the elastic lid.

6.2.2 Glacial isostatic adjustment

Before applying the methods presented in this dissertation to GIA data, it will be necessary to include the rotation of the Earth in the forward method. The gravity equipotential which describes the sea surface is controlled by both gravitation and rotation. As water and ice mass are redistributed, the moment of inertia of the Earth changes resulting in a change in rotation rate to conserve angular momentum and therefore a change in shape of the equipotential surfaces. It is therefore necessary to have a gravitationally and rotationally self-consistent theory for modelling sea level change. In practice, this would be achieved by coupling the current system of equations to Euler's rotation equations, and should not require substantial changes to the numerical implementation. Once this has been done, there are many ways in which the adjoint sensitivity kernels can be used to probe GIA data and enhance our understanding of the Earth and its past climate.

In section 5.6.7, we showed an example of constructing a measurement with sensitivity limited to a particular part of the model space. However, in this instance the measurement was constructed purely through trial and error. A more systematic approach would be to use Backus-Gilbert methods (Backus & Gilbert, 1967, 1968; Backus, 1970), and there are many localised sensitivities it could be useful to construct. In the example presented, the sensitivity was limited to a particular area of ice – the ice sheet over North America. Other ice sheets could be considered as well as looking for measurements with sensitivity to the ice history in any location, but with limited sensitivity to the viscosity structure. Conversely, measurements with limited ice sheet sensitivity could be constructed in order to examine only the viscosity structure and the sensitivity could be further limited to just

one region of the Earth for a local viscosity study.

When performing a viscosity inversion using measurements of GIA, there are some combinations of data that are typically used as they are thought to have little sensitivity to the ice sheet history. One such type of measurement are so-called decay times. In formerly glaciated regions, the relative sea level is observed to take the form of a decaying exponential (Andrews, 1970; Cathles, 1975), and the time scale of this decay is thought to be relatively independent of the ice sheet history (e.g., Mitrovica & Peltier, 1995). Using the sensitivity kernels, we could first examine whether such assumptions are correct. We could also investigate, again using Backus-Gilbert methods, whether there are other combinations of the same data which could be used to extract more information about the viscosity structure, or which decrease the sensitivity to the ice sheet history even further.

Information obtained from such investigations could be used to guide inversions for model parameters. As a first study, an inversion for one-dimensional viscosity structure could be performed, in the manner of, for example, Lau *et al.* (2016). The radial viscosity kernels presented in section 5.6.6 could be used to perform the inversion. Once a best fitting structure is found, the laterally varying kernels could be used to investigate which parts of the viscosity the measurements are sensitive to, and hence in what sense the one-dimensional structure is an average of a three-dimensional structure.

The laterally varying kernels could also be used to perform an inversion for three-dimensional structure, as illustrated by the example in section 5.7.2. However, as suggested by the difference in starting and inverted viscosity structures found in this synthetic example, it is unlikely that the data is able to constrain much of the full three-dimensional viscosity structure of the Earth and so a more specific problem should be considered. One possibility would be to investigate the so-called missing ice problem. In order to fit far-field sea level change since the LGM, a larger change in ice volume seems to be required than is suggested by the palaeo constraints on ice sheet geometry (e.g., Lambeck *et al.*, 2014). Whilst there is a degree of trade-off between the ice sheet history and viscosity structure, GIA studies have thus far been unable to find a viscosity structure that allows the ice volume to match independent constraints. However, such studies have considered only one-dimensional viscosity structures. It would therefore be desirable to investigate whether three-dimensional viscosity structures could reconcile some of the difference; indeed, lateral viscosity variations have been shown to have a significant impact on estimates of sea level change associated with ice volume change (Austermann *et al.*, 2013). This could be achieved by fixing the ice sheet history to have a smaller ice volume change and then inverting for three-dimensional viscosity structure using the adjoint sensitivity kernels. Any inverted viscosity structure would not necessarily be close to that of the Earth; however, if a structure can be found that fits both GIA data and other ice sheet constraints, it gives a direction for future investigations and provides a possible resolution to the missing ice problem.

An inversion for ice sheet history could also be performed using the ice sensitivity kernels. In this case, thought must be given to ensuring any ice history obtained is physically sensible. One option would be to take a viscosity model obtained from a previous GIA study and an ice model from another study and update the ice model until it fits the data. If an ice model cannot be found to fit the data with a particular viscosity structure, an inversion for viscosity could first be performed. This study would give some idea of the range of ice models that fit the data. The changes to previous ice sheet models would hopefully be sufficiently small so as not to render the resulting models unphysical. Physically realistic ice models could also be ensured through regularisation or by coupling ice sheet dynamics to the problem (e.g., Gomez *et al.*, 2012).

Bibliography

A, G., Wahr, J., & Zhong, S. (2013). Computations of the viscoelastic response of a 3-D compressible Earth to surface loading: an application to Glacial Isostatic Adjustment in Antarctica and Canada. *Geophys. J. Int.*, **192**(2), 557–572. doi:10.1093/gji/ggs030.

Al-Attar, D. & Crawford, O. (2016). Particle relabelling transformations in elastodynamics. *Geophys. J. Int.*, **205**(1), 575–593. doi:10.1093/gji/ggw032.

Al-Attar, D., Crawford, O., Valentine, A. P., & Trampert, J. (2018). Hamilton's principle and normal mode coupling in an aspherical planet. *Geophys. J. Int.*, **214**(1), 485–507. doi:10.1093/gji/ggy141.

Al-Attar, D. & Tromp, J. (2014). Sensitivity kernels for viscoelastic loading based on adjoint methods. *Geophys. J. Int.*, **196**(1), 34–77. doi:10.1093/gji/ggt395.

Al-Attar, D. & Woodhouse, J. H. (2008). Calculation of seismic displacement fields in self-gravitating earth models - applications of minor vectors and symplectic structure. *Geophys. J. Int.*, **175**(3), 1176–1208. doi:10.1111/j.1365-246X.2008.03961.x.

Anderson, D. L., Kanamori, H., Hart, R. S., & Liu, H.-P. (1977). The Earth as a seismic absorption band. *Science*, **196**(4294), 1104–1106. doi:10.1126/science.196.4294.1104.

Andrews, J. T. (1970). Present and postglacial rates of uplift for glaciated northern and eastern North America derived from postglacial uplift curves. *Can. J. Earth Sci.*, **7**(2), 703–715. doi:10.1139/e70-069.

Argus, D. F., Peltier, W. R., Drummond, R., & Moore, A. W. (2012). The Antarctica component of postglacial rebound model ICE-6G_C (VM5a) based on GPS positioning, exposure age dating of ice thicknesses, and relative sea level histories. *Geophys. J. Int.*, **198**(1), 537–563. doi:10.1093/gji/ggu140.

Austermann, J., Mitrovica, J. X., Latychev, K., & Milne, G. A. (2013). Barbados-based estimate of ice volume at Last Glacial Maximum affected by subducted plate. *Nat. Geosci.*, **6**, 553–557. doi:10.1038/ngeo1859.

Backus, G. (1970). Inference from inadequate and inaccurate data, I. *P. Natl. Acad. Sci. U.S.A.*, **65**(1), 1–7. doi:10.1073/pnas.65.1.1.

Backus, G. & Gilbert, F. (1968). The resolving power of gross Earth data. *Geophys. J. Int.*, **16**(2), 169–205. doi:10.1111/j.1365-246X.1968.tb00216.x.

Backus, G. & Mulcahy, M. (1976). Moment tensors and other phenomenological descriptions of seismic sources - I. Continuous displacements. *Geophys. J. Int.*, **46**(2), 341–361. doi:10.1111/j.1365-246X.1976.tb04162.x.

Backus, G. E. & Gilbert, J. F. (1967). Numerical applications of a formalism for geophysical inverse problems. *Geophys. J. Int.*, **13**(1-3), 247–276. doi:10.1111/j.1365-246X.1967.tb02159.x.

Barbot, S., Fialko, Y., & Bock, Y. (2009). Postseismic deformation due to the M_W 6.0 2004 Parkfield earthquake: stree-driven creep on a fault with spatially variable rate-and-state friction parameters. *J. Geophys. Res.*, **114**(B7). doi:10.1029/2008JB005748.

Bard, E., Hamelin, B., Fairbanks, R. G., & Zindler, A. (1990). Calibration of the ^{14}C timescale over the past 30,000 years using mass spectrometric U-Th ages from Barbados corals. *Nature*, **345**, 405–410. doi:10.1038/345405a0.

Bassett, S. E., Milne, G. A., Bentley, M. J., & Huybrechts, P. (2007). Modelling Antarctic sea-level data to explore te possibility of a dominant Antarctic contribution to meltwater pulse 1A. *Quaternary Sci. Rev.*, **26**(17-18), 2113–2127. doi:10.1016/j.quascirev.2007.06.011.

Boschi, L., Piersanti, A., & Spada, G. (2000). Global postseismic deformation: Deep earthquakes. *J. Geophys. Res.*, **105**(B1), 631–652. doi:10.1029/1999JB900278.

Boschi, L., Tromp, J., & O'Connell, R. J. (1999). On Maxwell singularities in postglacial rebound. *Geophys. J. Int.*, **136**(2), 492–498. doi:10.1046/j.1365-246X.1999.00644.x.

Bunge, H. P., Hagelberg, C. R., & Travis, B. J. (2003). Mantle circulation models with variational data assimilation: inferring past mantle flow and structure from plate motion histories and seismic tomography. *Geophys. J. Int.*, **152**(2), 280–301. doi:10.1046/j.1365-246X.2003/01923.x.

Bunge, H. P., Richards, M. A., & Baumgardner, J. R. (1996). Effect of depth-dependent viscosity on the planform of mantle convection. *Nature*, **379**, 436–438. doi:10.1038/379436a0.

Burridge, R. (1984). The group of motions in the plane and separation of variables in cylindrical coordinates. In *Mathematical Methods in Energy Research*. Society for Industrial and Applied Mathematics.

Čadek, O. & Fleitout, L. (2003). Effect of lateral viscosity variations in the top 300 km on the geoid and dynamic topography. *Geophys. J. Int.*, **152**(3), 566–580. doi:10.1046/j.1365-246X.2003.01859.x.

Carlson, A. E. (2009). Geochemical constraints on the Laurentide Ice Sheet contribution to Meltwater Pulse 1A. *Quaternary Sci. Rev.*, **28**(17-18), 1625–1630. doi:10.1016/j.quascirev.2009.02.011.

Carlson, A. E., Ullman, D. J., Anslow, F. S., He, F., Clark, P. U., Liu, Z., & Otto-Bliesner, B. L. (2012). Modeling the surface mass-balance response of the Laurentide Ice Sheet to Bølling warming and its contribution to Meltwater Pulse 1A. *Earth Planet. Sci. Lett.*, **315-316**, 24–29. doi:10.1016/j.epsl.2011.07.008.

Cathles, L. M. (1975). *The viscosity of the Earth's mantle*. Princeton University Press.

Chen, J. L., Wilson, C. R., Blakenship, D., & Tapley, B. D. (2009). Accelerated Antarctic ice loss from satellite gravity measurements. *Nat. Geosci.*, **2**, 859–862. doi:10.1038/ngeo694.

Chen, M., Huang, H., Yao, H., van der Hilst, R., & Niu, F. (2013). Low wave speed zones in the crust beneath SE Tibet revealed by ambient noise adjoint tomography. *Geophys. Res. Lett.*, **41**(2), 334–340. doi:10.1002/2013GL058476.

Chopelas, A. & Boehler, R. (1992). Thermal expansivity in the lower mantle. *Geophys. Res. Lett.*, **19**(19). doi:10.1029/92GL02144.

Clark, P. U., Licciardi, J. M., MacAyeal, D. R., & Jenson, J. W. (1996). Numerical reconstruction of a soft-bedded Laurentide Ice Sheet during the last glacial maximum. *Geology*, **24**(8), 679–682. doi:10.1130/0091-7613(1996)024¡0679:NROASB¿2.3.CO;2.

Clark, P. U., Mitrovica, J. X., Milne, G. A., & Tamisiea, M. E. (2002). Sea-level fingerprinting as a direct test for the source of Global Meltwater Pulse 1A. *Science*, **295**(5564), 2438–2441. doi:10.1126/science.1068797.

Corrieu, V., Ricard, Y., & Froidevaux, C. (1994). Converting mantle tomography into mass anomalies to predict the Earth's radial viscosity. *Phys. Earth Planet. In.*, **84**(1-4), 3–13. doi:10.1016/0031-9201(94)90031-0.

Crase, E., Pica, A., Noble, M., McDonald, J., & Tarantola, A. (1990). Robust elastic nonlinear waveform inversion: Application to real data. *Geophysics*, **55**(5), 527–538. doi:10.1190/1.1442864.

Crawford, O., Al-Attar, D., Tromp, J., & Mitrovica, J. X. (2017). Forward and inverse modelling of post-seismic deformation. *Geophys. J. Int.*, **208**(2), 845–876. doi:10.1093/gji/ggw414.

Crawford, O., Al-Attar, D., Tromp, J., Mitrovica, J. X., Austermann, J., & Lau, H. C. P. (2018). Quantifying the sensitivity of post-glacial sea level change to laterally varying viscosity. *Geophys. J. Int.*, **214**(2), 1324–1363. doi:10.1093/gji/ggy184.

Creveling, J. R., Mitrovica, J. X., Clark, P. U., Waelbroeck, C., & Pico, T. (2017). Predicted bounds on peak global mean sea level during marine isotope stages 5a and 5c. *Quaternary Sci Rev*, **163**, 193–208. doi:10.1016/j.quascirev.2017.03.003.

Cserepesa, L., Yuen, D. A., & Schroederb, B. A. (2000). Effect of the mid-mantle viscosity and phase-transition structure on 3D mantle convection. *Phys. Earth Planet. In.*, **118**(1-2), 135–148. doi:10.1016/S0031-9201(99)00140-5.

Dahlen, F. A. (1974). On the static deformation of an earth model with a fluid core. *Geophys. J. Int.*, **36**(2), 461–485. doi:10.1111/j.1365-246X.1974.tb03649.

Dahlen, F. A. & Tromp, J. (1998). *Theoretical Global Seismology*. Princeton University Press.

Deschamps, P., Durand, N., Bard, E., Hamelin, B., Camoin, G., Thomas, A. L., Henderson, G. M., Okuno, J., & Yokoyama, Y. (2012). Ice-sheet collapse and sea-level rise at the Bølling warming 14,600 years ago. *Nature*, **483**, 559–564. doi:10.1038/nature10902.

Diao, F., Xiong, X., Wang, R., Zheng, Y., Walter, T. R., Weng, H., & Li, J. (2014). Overlapping post-seismic deformation processes: afterslip and viscoelastic relaxation following the 2011 M_W 9.0 Tohoku (Japan) earthquake. *Geophys. J. Int.*, **196**(1), 218–229. doi:10.1093/gji/ggt376.

Dziewonski, A. M. & Anderson, D. L. (1981). Preliminary reference Earth model. *Phys. Earth Planet. In.*, **25**(4), 297–356. doi:10.1016/0031-9201(81)90046-7.

Fang, M. & Hager, B. H. (1995). The singularity mystery associated with a radially continuous Maxwell viscoelastic structure. *Geophys. J. Int.*, **123**(3), 849–865. doi:j.1365-246X.1995.tb06894.x.

Farrell, W. E. & Clark, J. A. (1976). On postglacial sea level. *Geophys. J. Int.*, **46**(3), 647–667. doi:j.1365-246X.1976.tb01252.x.

Fichtner, A., Kennett, B. L. N., Igel, H., & Bunge, H. P. (2009). Full seismic waveform tomography for upper-mantle structure in the Australasian region using adjoint methods. *Geophys. J. Int.*, **179**(3), 1703–1725. doi:10.1111/j.1365-246X.2009.04368.x.

Forte, A. M. & Mitrovica, J. X. (1996). New inferences of mantle viscosity from joint inversion of long-wavelength mantle convection and post-glacial rebound data. *Geophys. Res. Lett.*, **23**(10), 1147–1150. doi:10.1029/96GL00964.

Forte, A. M. & Peltier, W. R. (1987). Plate tectonics and aspherical Earth structure: the importance of poloidal-toroidal coupling. *J. Geophys. Res.*, **92**(B5), 3645–3679. doi:10.1029/JB092iB05p03645.

Forte, A. M. & Woodward, R. L. (1997). Seismic-geodynamic constraints on three-dimensional structure, vertical flow, and heat transfer in the mantle. *J. Geophys. Res.*, **102**(B8). doi:10.1029/97JB01276.

Freed, A. M. & Bürgmann, R. (2004). Evidence of power-law flow in the Mojave desert mantle. *Nature*, **430**, 548–551. doi:10.1038/nature02784.

Freed, A. M., Bürgmann, R., Calais, E., Freymuller, J., & Hreinsdóttir, S. (2006). Implications of deformation following the 2002 Denali, Alaska, earthquake for postseismic relaxation processes and lithospheric rheology. *J. Geophys. Res.*, **111**(B1). doi:10.1029/2005JB003894.

Freed, A. M., Hashima, A., Becker, T. W., Okaya, D. A., Sato, H., & Hatanaka, Y. (2017). Resolving depth-dependent subduction zone viscosity and afterslip from postseismic displacements following the 2011 Tohoku-oki, Japan earthquake. *Earth Planet. Sci. Lett.*, **459**. doi:10.1016/j.epsl.2016.11.040.

Gilbert, F. (1971). Ranking and winnowing gross Earth data for inversion and resolution. *Geophys. J. Int.*, **23**(1), 125–128. doi:10.1111/j.1365-246X.1971.tb01807.

Gilbert, F. & Backus, G. E. (1966). Propagator matrices in elastic wave and vibration problems. *Geophysics*, **31**(2), 326–332. doi:10.1190/1.1439771.

Golub, G. H. & van Loan, C. F. (1983). *Matrix Computations*. The Johns Hopkins University Press.

Gomez, N., Gregoire, L. J., Mitrovica, J. X., & Payne, A. J. (2015). Laurentide-Cordilleran Ice Sheet collapse as a contribution to meltwater pulse 1A. *Geophys. Res. Lett.*, **42**(10), 3954–3962. doi:10.1002/2015GL063960.

Gomez, N., Pollard, D., Mitrovica, J. X., Huybers, P., & Clark, P. U. (2012). Evolution of a coupled marine ice sheet-sea level model. *J. Geophys. Res.*, **117**(F1).

Gregoire, L. J., Payne, A. J., & Waldes, P. J. (2012). Deglacial rapid sea level rises caused by ice-sheet saddle collapses. *Nature*, **487**(219-222), 219–222. doi:10.1038/nature11257.

Hager, B. H. (1984). Subducted slabs and the geoid: contraints on mantle rheology and flow. *J. Geophys. Res.*, **89**(B7), 6003–6015.

Han, D. & Wahr, J. (1995). The viscoelastic relaxation of a realistically stratified earth, and a further analysis of postglacial rebound. *Geophys. J. Int.*, **120**(2), 287–311. doi:10.1111/j.1365-246X.1995.tb01819.x.

Han, S.-C., Sauber, J., & Pollitz, F. (2016). Postseismic gravity change after the 2006-2007 great earthquake doublet and constraints on the asthenosphere structure in the central Kuril Islands. *Geophys. Res. Lett.*, **43**(7), 3169–3177. doi:10.1002/2016GL068167.

Hanyk, L., Moser, J., Yuen, D. A., & Matyska, C. (1995). Time-domain approach for the transient responses in stratified viscoelastic Earth models. *Geophys. Res. Lett.*, **22**(10), 1285–1288. doi:10.1029/95GL01087.

Haskell, N. A. (1935). The motion of a viscous fluid under a surface load. *J. Appl. Phys.*, **6**(8), 265–269. doi:10.1063/1.1745329.

Hines, T. T. & Hetland, E. A. (2016). Rapid and simultaneous estimation of fault slip and heterogeneous lithospheric viscosity from post-seismic deformation. *Geophys. J. Int.*, **204**(1), 569–582. doi:10.1093/gji/ggv477.

Huang, M. H., Bürgmann, R., & Pollitz, F. (2016). Lithospheric rheology constrained from twenty-five years of postseismic deformation following the 1989 M_W 6.9 Loma Prieta earthquake. *Earth Planet. Sci. Lett.*, **435**, 147–158. doi:10.1016/j.epsl.2015.12.018.

Ivins, E. R., James, T. S., Wahr, J., Schrama, E. J. O., Landerer, F. W., & Simon, K. M. (2013). Antarctic contribution to sea level rise observed by GRACE with improved GIA correction. *J. Geophys. Res.*, **118**(6), 3126–3141. doi:10.1002/jgrb.50208.

Johnson, K. M., Bürgmann, R., & Freymueller, J. T. (2009). Coupled afterslip and viscoelastic flow following the 2002 Denali Fault, Alaska earthquake. *Geophys. J. Int.*, **176**(3), 670–682. doi:10.1111/j.1365-246X.2008.04029.x.

Johnston, P. (1993). The effect of spatially non-uniform water loads on prediction of sea-level change. *Geophys. J. Int.*, **114**(1), 615–634. doi:10.1111/j.1365-246X.1993.tb06992.x.

Kendall, R. A., Mitrovica, J. X., & Milne, G. A. (2005). On post-glacial sea level – II. Numerical formulation and comparative results on spherically symmetric models. *Geophys. J. Int.*, **161**(3), 679–706. doi:10.1111/j.1365-246X.2005.02553.x.

King, M. A., Bingham, R. J., Moore, P., Whitehouse, P. L., Bentley, M. J., & Milne, G. A. (2012). Lower satellite-gravimetry estimates of Antarctic sea-level contribution. *Nature*, **491**, 586–589. doi:10.1038/nature11621.

King, S. D. & Masters, G. (1992). An inversion for radial viscosity structure using seismic tomography. *Geophys. Res. Lett.*, **19**(15), 1551–1554. doi:10.1029/92GL01700.

Komatitsch, D. & Tromp, J. (1999). Introduction to the spectral element method for three-dimensional seismic wave propagation. *Geophys. J. Int.*, **139**(3), 806–822. doi:10.1046/j.1365-246x.1999.00967.x.

Lambeck, K. & Chappell, J. (2001). Sea level change through the last glacial cycle. *Science*, **292**(5517), 679–686. doi:10.1126/science.1059549.

Lambeck, K., Rouby, H., Purcell, A., Sun, Y., & Sambridge, M. (2014). Sea level and global ice volumes from the Last Glacial Maximum to the Holocene. *P. Natl. Acad. Sci. U.S.A.*, **111**(43), 15296–15303. doi:10.1073/pnas.1411762111.

Lambeck, K., Smither, C., & Johnston, P. (1998). Sea-level change, glacial rebound and mantle viscosity for northern Europe. *Geophys. J. Int.*, **134**(1), 102–144. doi:10.1046/j.1365-246x.1998.00541.x.

Larour, E., Ivins, E., & Adhikari, S. (2017). Should coastal planners have concern over where land ice is melting? *Sci Adv*, **3**(11). doi:10.1029/2010JB007405.

Latychev, K., Mitrovica, J. X., Tromp, J., Tamisiea, M. E., Komatitsch, D., & Christara, C. C. (2005). Glacial isostatic adjustment of 3-D Earth models: a finite-volume formulation. *Geophys. J. Int.*, **161**(1), 421–444. doi:10.1111/j.1365-246X.2005.02536.x.

Lau, H. C. P., Austermann, J., Mitrovica, J. X., Crawford, O., Al-Attar, D., & Latychev, K. (2018). Inferences of mantle viscosity based on ice age data sets: the bias in radial viscosity profiles due to neglect of laterally heterogeneous viscosity structure. *J. Geophys. Res.*, **123**(9), 7237–7252. doi:10.1029/2018JB015740.

Lau, H. C. P., Mitrovica, J. X., Austermann, J., Crawford, O., Al-Attar, D., & Latychev, K. (2016). Inferences of mantle viscosity based on ice age data sets: Radial structure. *J. Geophys. Res.*, **121**(10), 6991–7012. doi:10.1002/2016JB013043.

Li, D., Gurnis, M., & Stadler, G. (2017a). Towards adjoint-based inversion of time-dependent mantle convection with nonlinear viscosity. *Geophys. J. Int.*, **209**(1), 86–105. doi:10.1093/gji/ggw493.

Li, K., Jackson, A., & Livermore, P. W. (2011). Variational data assimilation for the initial-value dynamo problem. *Phys. Rev. E.*, **84**(5), 056321. doi:10.1103/PhysRevE.84.056321.

Li, S., Moreno, M., Bedford, J., Rosenau, M., Heidback, O., Melnick, D., & Oncken, O. (2017b). Postseismic uplift of the Andes following the 2010 Maule earthquake: Implications for mantle rheology. *Geophys. Res. Lett.*, **44**, 1768–1776. doi:10.1002/2016GL071995.

Li, T., Wu, P., Steffen, H., & Wang, H. (2018). In search of laterally heterogeneous viscosity models of glacial isostatic adjustment with the ICE-6G_C global ice model. *Geophys. J. Int.*, **214**(2), 1191–1205. doi:10.1093/gji/ggy181.

Lions, J. L. (1970). *Optimal Control of Systems Governed by Partial Differential Equations*. Springer-Verlag.

Liu, J., Milne, G. A., Kopp, R. E., Clark, P. U., & Shennan, I. (2016). Sea-level constraints on the amplitude and source distribution of Meltwater Pulse 1A. *Nat. Geosci.*, **9**, 130–134. doi:10.1038/ngeo2616.

Liu, Q. & Tromp, J. (2008). Finite-frequency sensitivity kernels for global seismic wave propagation based upon adjoint methods. *Geophys. J. Int.*, **174**(1), 265–286. doi:10.1111/j.1365-246X.2009.03798.x.

Martinec, Z. (2000). Spectral-finite element approach to three-dimensional viscoelastic relaxation in a spherical earth. *Geophys. J. Int.*, **142**(1), 117–141. doi:10.1046/j.1365-246x.2000.00138.x.

Martinec, Z., Sasgen, I., & Velímský, J. (2015). The forward sensitivity and adjoint-state methods of glacial isostatic adjustment. *Geophys. J. Int.*, **200**(1), 77–105. doi:10.1093/gji/ggu378.

Milne, G. A., Latychev, K., Schaeffer, A., Crowley, J. W., Lecavalier, B. S., & Audette, A. (2018). The influence of lateral Earth structure on glacial isostatic adjustment in Greenland. *Geophys. J. Int.*, **214**(2), 1252–1266. doi:10.1093/gji/ggy189.

Milne, G. A. & Mitrovica, J. X. (1998). Postglacial sea-level change on a rotating Earth. *Geophys. J. Int.*, **133**(1), 1–19. doi:10.1046/j.1365-246X.1998.1331455.x.

Milne, G. A., Mitrovica, J. X., & Davis, J. L. (1999). Near-field hydro-isostasy: the implementation of a revised sea-level equation. *Geophys. J. Int.*, **139**(2), 464–482. doi:10.1046/j.1365-246x.1999.00971.x.

Mitrovica, J. X. (1996). Haskell [1935] revisited. *J. Geophys. Res.*, **101**(B1), 555–569. doi:10.1029/95JB03208.

Mitrovica, J. X., Hay, C. C., Kopp, R. E., Harig, C., & Latychev, K. (2018). Quantifying the sensitivity of sea level change in coastal localities to the geometry of polar ice mass flux. *J. Climate*, **31**(9), 3701–3709. doi:10.1175/JCLI-D_17-0465.1.

Mitrovica, J. X. & Milne, G. A. (2003). On post-glacial sea level: I. General theory. *Geophys. J. Int.*, **154**(2), 253–267. doi:10.1046/j.1365-246X.2003.01942.x.

Mitrovica, J. X. & Peltier, W. R. (1991). A complete formalism for the inversion of post-glacial rebound data: resolving power analysis. *Geophys. J. Int.*, **104**(2), 267–288. doi:10.1111/j.1365-246X.1991.tb02511.x.

Mitrovica, J. X. & Peltier, W. R. (1995). Constraints on mantle viscosity based upon the inversion of post-glacial uplift data from the Hudson Bay region. *Geophys. J. Int.*, **122**(2), 353–377.

Miyazaki, S., Segall, P., Fukuda, J., & Kato, T. (2004). Space time distribution of afterslip following the 2003 Tokachi-oki earthquake: implications for variations in fault zone properties. *Geophys. Res. Lett.*, **31**(6). doi:10.1029/2003GL019410.

Mora, P. (1987). Nonlinear two-dimensional elastic inversion of multioffset seismic data. *Geophysics*, **52**(9), 1211–1228. doi:10.1190/1.1442384.

Müller, G. (1986). Generalized Maxwell bodies and estimates of mantle viscosity. *Geophys. J. Int.*, **87**(3), 1113–1141. doi:10.1111/j.1365-246X.1986.tb01986.x.

Nakada, M. & Lambeck, K. (1989). Late Pleistocene and Holocene sea-level change in the Australian region and mantle rheology. *Geophys. J. Int.*, **96**(3), 497–517. doi:10.1111/j.1365-246X.1989.tb06010.x.

Nakada, M., Okuno, J., Lambeck, K., & Purcell, A. (2015). Viscosity structure of Earth's mantle inferred from rotational variations due to GIA process and recent melting events. *Geophys. J. Int.*, **202**(2), 976–992. doi:10.1093/gji/ggv198.

Nakagawa, T. & Tackley, P. J. (2004). Effects of thermo-chemical mantle convection on the thermal evolution of the Earth's core. *Earth. Planet. Sci. Lett.*, **220**(1-2), 107–119. doi:10.1016/S0012-821X(04)00055-X.

Nakagawa, T. & Tackley, P. J. (2011). Effects of low-viscosity post-perovskite on thermo-chemical mantle convection in a 3-D spherical shell. *Geophys. Res. Lett.*, **38**(4). doi:10.1029/2010GL046494.

Nishimura, T. & Thatcher, W. (2003). Rheology of the lithosphere inferred from postseismic uplift following the 1959 Hebden Lake earthquake. *J. Geophys. Res.*, **108**(B8). doi:10.1029/2002JB002191.

Nissen-Meyer, T., Dahlen, F. A., & Fournier, A. (2007). Spherical-earth Fréchet sensitivity kernels. *Geophys. J. Int.*, **168**(3), 1051–1066. doi:10.1111/j.1365-246X.2006.03123.x.

Nocedal, J. & Wright, S. J. (1999). *Numerical Optimization*. Springer-Verlag.

Panasyuk, S. V. & Hager, B. H. (2000). Inversion for mantle viscosity profiles constrained by dynamic topography and the geoid, and their estimated errors. *Geophys. J. Int.*, **143**(3), 821–836. doi:10.1046/j.0956-540X.2000.01286.x.

Parker, R. L. (1994). *Geophysics Inverse Theory*. Princeton University Press.

Patera, A. T. (1984). A spectral element method for fluid dynamics: Laminar flow in a channel expansion. *J. Comput. Phys.*, **54**(3), 468–488. doi:10.1016/0021-9991(84)90128-1.

Paulson, A., Zhong, S., & Wahr, J. (2005). Modelling post-glacial rebound with lateral viscosity variations. *Geophys. J. Int.*, **163**(1), 357–371. doi:10.1111/j.1365-246X.2005.02645.x.

Peltier, W. R. (1974). The impulse response of a Maxwell Earth. *Rev. Geophys.*, **12**(4), 649–669. doi:10.1029/RG012i004p00649.

Peltier, W. R. (2004). Global glacial isostasy and the surface of the ice-age Earth: The ICE-5G (VM2) model and GRACE. *Annu. Rev. Earth Pl. Sc.*, **32**, 111–149. doi:10.1146/annurev.earth.32.082503.144359.

Peltier, W. R. (2005). On the hemispheric origins of meltwater pulse 1a. *Quaternary Sci. Rev.*, **24**(14-15), 1655–1671. doi:10.1016/j.quascirev.2004.06.023.

Phinney, R. A. & Burridge, R. (1973). Representation of the elastic-gravitational excitation of a spherical earth model by generalised spherical harmonics. *Geophys. J. Int.*, **34**(4), 451–487. doi:10.1111/j.1365-246X.1973.tb02407.x.

Piersanti, A., Spada, G., Sabadini, R., & Bonafede, M. (1995). Global post-seismic deformation. *Geophys. J. Int.*, **120**(3), 544–566. doi:10.1111/j.1365-246X.1995.tb01838.x.

Pollitz, F. F. (1997). Gravitational viscoelastic postseismic relaxation on a layered spherical Earth. *J. Geophys. Res.*, **102**(B8), 17921–17941. doi:10.1029/97JB01277.

Pollitz, F. F. (2003). Transient rheology of the uppermost mantle beneath the Mojave Desert, California. *Earth Planet. Sci. Lett.*, **215**(1-2), 89–104. doi:10.1016/S0012-821X(03)00432-1.

Pollitz, F. F. (2005). Transient rheology of the upper mantle beneath central Alaska inferred from the crustal velocity field following the 2002 Denali earthquake. *J. Geophys. Res.*, **110**(B8). doi:10.1029/2005JB003672.

Pollitz, F. F. (2015). Postearthquake relaxation evidence for laterally variable viscoelastic structure and water content in the Southern California mantle. *J. Geophys. Res.*, **120**(4), 2672–2696. doi:10.1002/2014JB011603.

Pollitz, F. F., Bürgmann, R., & Banerjee, P. (2006). Post-seismic relaxation following the great 2004 Sumatra-Andaman earthquake on a compressible self-gravitating Earth. *Geophys. J. Int.*, **167**(1), 397–420. doi:10.1111/j.1365-246X.2006.03018.x.

Pollitz, F. F. & Thatcher, W. (2010). On the resolution of shallow mantle viscosity structure using postearthquake relaxation data: Application to the 1999 Hector Mine, California, earthquake. *J. Geophys. Res.*, **115**(B10). doi:10.1029/2010JB007405.

Pollitz, F. F., Wicks, C., & Thatcher, W. (2001). Mantle flow beneath a continental strike-slip fault: Postseismic deformation after the 1999 Hector Mine earthquake. *Science*, **293**(5536), 1814–1818. doi:10.1126/science.1061361.

Pratt, R. G. (1999). Seismic waveform inversion in the frequency domain, Part 1: Theory and verification in a physical scale model. *Geophysics*, **64**(3), 888–901. doi:10.1190/1.1444597.

Press, W. H., Teukolsky, S. A., Vetterling, W. T., & Flannery, B. P. (1986). *Numerical Recipes*. Cambridge University Press.

Ritsema, J., van Heijst, H. J., & Woodhouse, J. H. (1999). Complex shear wave velocity structure imaged beneath Africa and Iceland. *Science*, **286**(5446), 1925–1928. doi:10.1126/science.286.5446.1925.

Rohling, E. J., Marsh, R., Wells, N. C., Siddall, M., & Edwards, N. R. (2004). Similar meltwater contributions to glacial sea level changes from Antarctic and northern ice sheets. *Nature*, **430**, 1016–1021.

Rolf, T., Capitanio, F. A., & Tackley, P. J. (in press). Constraints of mantle viscosity structure from continental drift histories in spherical mantle convection models. *Tectonophysics*. doi:10.1016/j.tecto.2017.04.031.

Rudolph, M. L., Lekić, V., & Lithgow-Bertelloni, C. (2015). Viscosity jump in Earth's mid-mantle. *Science*, **350**(6266), 1349–1352. doi:10.1126/science.aad1929.

Rundle, J. B. (1980). Static elastic-gravitational deformation of a layered half space by point couple sources. *J. Geophys. Res.*, **85**(B10), 5355–5363. doi:10.1029/JB085iB10p05355.

Schoof, C. (2007). Ice sheet grounding line dynamics: Steady states, stability, and hysteresis. *J. Geophys. Res.*, **112**(F3). doi:10.1029/2006JF000664.

Simo, J. C. & Hughes, T. J. R. (1998). *Computational Inelasticity*. Springer-Verlag.

Spivak, M. (1970). *A Comprehensive Introduction to Differential Geometry*, volume 1. Publish or Perish, Inc.

Stadler, G., Gurnis, M., Burstedde, C., Wilcox, L. C., & Alisic, L. (2010). The dynamics of plate tectonics and mantle flow: from local to global scales. *Science*, **329**(5995), 1033:1038. doi:10.1126/science.1191223.

Tackley, P. J. (2000). Mantle convection and plate tectonics: toward an integrated physical and chemical theory. *Science*, **288**(5473), 2002–2007. doi:10.1126/science.288.5473.2002.

Tape, C., Liu, Q., Maggi, A., & Tromp, J. (2009). Adjoint tomography of the southern California crust. *Science*, **325**(5943), 988–992. doi:10.1126/science.1175298.

Tape, C., Liu, Q., & Tromp, J. (2007). Finite-frequency tomography using adjoint methods - Methodology and examples using membrane surface waves. *Geophys. J. Int.*, **168**(3), 1105–1129. doi:10.1111/j.1365-246X.2006.03191.x.

Tarantola, A. (1984). Inversion of seismic reflection data in the acoustic approximation. *Geophysics*, **49**(8), 1259–1266. doi:10.1190/1.1441754.

Tarasov, L. & Peltier, W. R. (2004). A geophysically constrained large ensemble analysis of the deglacial history of the North American ice-sheet complex. *Quaternary Sci. Rev.*, **23**(3-4). doi:10.1016/j.quascirev.2003.08.004.

Tröltzsch, F. (2005). *Optimal Control of Partial Differential Equations*. American Mathematical Society.

Tromp, J. & Mitrovica, J. X. (1999). Surface loading of a viscoelastic earth - I. General theory. *Geophys. J. Int.*, **137**(3), 847–855. doi:10.1046/j.1365-246x.1999.00838.x.

Tromp, J., Tape, C., & Liu, Q. (2005). Seismic tomography, adjoint methods, time reversal and banana-doughnut kernels. *Geophys. J. Int.*, **160**(1), 195–216. doi:10.1111/j.1365-246X.2004.02453.x.

van den Berg, A. P., Rainey, E. S. G., & Yuen, D. A. (2005). The combined influences of variable thermal conductivity, temperature- and pressure-dependent viscosity and core-mantle couple on thermal evolution. *Phys. Earth Planet. In.*, **149**(3-4), 259–278. doi:10.1016/j.pepi.2004.10.008.

Van der Wal, W., Whitehouse, P., & Schrama, E. J. O. (2015). Effect of GIA models with 3D composite mantle viscosity on GRACE mass balance estimates for Antarctica. *Earth Planet. Sc. Lett.*, **414**, 134–143. doi:10.1016/j.epsl.2015.01.001.

Velicogna, I. (2009). Increasing rates of ice mass loss from the Greenland and Antarctic ice sheets revealed by GRACE. *Geophys. Res. Lett.*, **36**(19). doi:10.1029/2009GL040222.

Wang, R., Lorenzo-Martin, F., & Roth, F. (2006). PSGRN/PSCMP - a new code for calculating co- and post-seismic deformation, geoid and gravity changes based on the viscoelastic-gravitational dislocation theory. *Comput. Geosci.*, **32**(4), 527–541. doi:10.1016/j.cageo.2005.08.006.

Weaver, A. J., Saenko, O. A., Clark, P. U., & Mitrovica, J. X. (2003). Meltwater Pulse 1A from Antarctica as a trigger of the Bølling-Allerød warm interval. *Science*, **299**(5613), 1709–1713. doi:10.1126/science.1081002.

Whitehouse, P. L., Bentley, M. J., & Le Brocq, A. M. (2012). A deglacial model for Antarctica: geological constraints and glaciological modelling as a basis for a new model of Antarctic glacial isostatic adjustment. *Quaternary Sci. Rev.*, **32**(1), 1–24. doi:10.1016/j.quascirev.2011.11.016.

Woodhouse, J. H. & Deuss, A. (2007). Earth's free oscillations. In *Treatise on Geophysics*, volume 1. Elsevier.

Wu, P. (2004). Using commercial finite element packages for the study of earth deformations, sea levels and the state of stress. *Geophys. J. Int.*, **158**(2), 401–408. 10.1111/j.1365-246X.2004.02338.x.

Wu, P. & Peltier, W. R. (1982). Viscous gravitational relaxation. *Geophys. J. Int.*, **70**(2), 435–485. doi:10.1111/j.1365-246X.1982.tb04976.x.

Zhong, S., Paulson, A., & Wahr, J. (2003). Three-dimensional finite-element modelling of Earth's viscoelastic deformation: effects of lateral variations in lithospheric thickness. *Geophys. J. Int.*, **155**(2), 679–695. doi:10.1046/j.1365-246X.2003.02084.x.

Zhong, S., Zuber, M. T., Moresi, L., & Gurnis, M. (2000). Role of temperature-dependent viscosity and surface plates in spherical shell models of mantle convection. *J. Geophys. Res.*, **105**(B5), 11063–11082. doi:10.1029/2000JB900003.

Zhu, H., Bozdag, E., Peter, D., & Tromp, J. (2012). Structure of the European upper mantle revealed by adjoint tomography. *Geophys. J. Int.*, **5**, 493–498. doi:10.1038/ngeo1501.

Zwally, H. & Giovinetto, M. B. (2011). Overview and assessment of Antarctic ice-sheet mass balance estimates: 1992-2009. *Surv. Geophys.*, **32**(4-5), 351–376. doi:10.1007/s10712-011-9123-5.